Dynamics and morphology of driven domain walls in magnetic thin films from the standpoint of statistical physics

Lucas Javier Albornoz

To cite this version:

Lucas Javier Albornoz. Dynamics and morphology of driven domain walls in magnetic thin films from the standpoint of statistical physics. Statistical Mechanics [cond-mat.stat-mech]. Université Paris-Saclay; Universidad nacional de Cuyo, 2021. English. NNT : 2021UPASP093 . tel-03579391

HAL Id: tel-03579391
https://theses.hal.science/tel-03579391v1

Submitted on 18 Feb 2022

université
PARIS-SACLAY

UNCUYO
UNIVERSIDAD
NACIONAL DE CUYO

Dynamics and morphology of driven domain walls in magnetic thin films from the standpoint of statistical physics

Dynamique et morphologie des parois des domaines magnétiques dans les films minces du point de vue de la physique statistique

Thèse de doctorat de l'Université Paris-Saclay
et l'Universidad Nacional de Cuyo

École doctorale n°572, Ondes et Matière (EDOM)
Spécialité de doctorat : Physique
Unité de recherche : Université Paris-Saclay, CNRS, Laboratoire de Physique des Solides, 91405, Orsay, France
Référent : Faculté des Sciences d'Orsay

Thèse présentée et soutenue à Bariloche, Argentine,
le 07/10/2021, par

Lucas Javier ALBORNOZ

Composition du Jury

Alejandro BUTERA Profesor del Instituto Balseiro, Investigador en CONICET, Universidad Nacional de Cuyo, Bariloche, Argentina	Président
Gabriela PASQUINI Profesora Departamento de Física, Universicad de Buenos Aires, Buenos Aires, Argentina	Rapporteure et Examinatrice
Jan VOGEL Directeur de recherches au CNRS, Institut Néel, Grenoble, France	Rapporteur et Examinateur
Thierry GIAMARCHI Professeur à l'Université de Genève, Department of Quantum Matter Physics, Genève, Suisse	Examinateur
Liza HERRERA DIEZ Chargée des recherches au CNRS, C2N CNRS, Université Paris-Saclay, Orsay, France	Examinatrice

Direction de la thèse

Vincent JEUDY Professeur des universités, LPS (UMR8502), Université Paris-Saclay, Orsay, France	Directeur de thèse
Javier CURIALE Investigador Independiente, INN, Universidad Nacional de Cuyo, Bariloche, Argentina	Co-directeur de thèse

Thèse de doctorat

NNT : 2021UPASP093

A mi madre, Laila, y a mi padre, Felipe.

Síntesis en castellano

La fabricación de nuevos materiales magnéticos nanoestructurados ha despertado un gran interés en la comunidad científica durante las últimas décadas debido a sus propiedades novedosas. En particular, el estudio de paredes de dominios magnéticos en láminas delgadas de espesores nanométricos es de importancia tanto desde el punto de vista de la física fundamental como para el desarrollo de nuevos dispositivos. Estas paredes, que separan regiones de magnetización uniforme en una lámina delgada magnética, pueden ser vistas como interfases unidimensionales que se mueven en un medio bidimensional. Debido a su energía asociada, las paredes de dominios son objetos elásticos, que tienden a minimizar su longitud. Además, la lámina delgada magnética puede ser considerada un medio desordenado debido a la presencia de inhomogeneidades en su estructura microscópica. En este contexto, la dinámica y la morfología de paredes de dominios magnéticos en láminas delgadas pueden estudiarse utilizando la teoría de interfases elásticas unidimensionales en medios desordenados bidimensionales. Este enfoque, que es parte del campo de la física estadística, permite estudiar una gran variedad de fenómenos en la naturaleza considerando sólo algunos elementos fundamentales: la elasticidad de la interfase, el desorden del medio, la energía térmica, y la acción de una fuerza externa uniforme.

Dos modelos paradigmáticos para el estudio de este tipo de interfases son el modelo de *quenched Edwards-Wilkinson* y el de *quenched Kardar-Parisi-Zhang*. Estos modelos predicen ciertos comportamientos críticos tanto para la dinámica como para la morfología de la interfase, con exponentes críticos característicos. Un ejemplo de comportamiento crítico predicho por el modelo es el que se da en la llamada transición de desanclaje o *depinning* de la interfase, en la que la fuerza externa supera a las fuerzas de anclaje debidas al desorden. En esta transición, si no consideramos a la energía térmica, la velocidad de la interfase v sigue una ley de potencia en función de la fuerza aplicada f, con un exponente crítico característico β. Esto es, $v \sim (f - f_d)^\beta$ para $f \to f_d^+$, donde f_d es la llamada fuerza de desanclaje.

Los valores numéricos de los exponentes críticos están definidos únicamente por el modelo utilizado y, por lo tanto, se dice que son exponentes universales, ya que se espera que distintos fenómenos descriptos por un mismo modelo presenten los mismos exponentes críticos. Para probar que uno de los modelos mencionados describe satisfactoriamente al fenómeno físico estudiado, es necesario realizar una cuantificación experimental de los exponentes críticos característicos para luego compararlos con los predichos por el modelo.

Utilizando el enfoque de la teoría de interfases elásticas en medios desordenados, en esta tesis estudiamos la dinámica y la morfología de paredes de dominios en dos tipos de láminas delgadas de gran interés en la actualidad: por un lado, una lámina ferrimagnética de GdFeCo de 10 nm de espesor; por otro lado, una lámina ferromagnética y semiconductora de (Ga,Mn)(As,P)/(Ga,Mn)As de 4 nm de espesor. La técnica experimental que utilizamos para observar la morfología y la dinámica de paredes de dominios magnéticos es la microscopía magneto-óptica por efecto Kerr polar (PMOKE).

Los resultados de nuestras investigaciones se dividen en cuatro temas fundamentales:

- Primero, el estudio de la dinámica de paredes de dominios en GdFeCo inducida por campo magnético en un amplio rango de temperatura (10-353 K), considerando temperaturas por encima y por debajo de la temperatura de compensación magnética T_M, característica de los materiales ferrimagnéticos. Estos estudios nos permitieron cuantificar, en función de la temperatura, parámetros que están fuertemente relacionados con las características de las fuerzas de anclaje sobre las paredes de dominios, observando el efecto de la compensación magnética. Encontramos una divergencia del campo de desanclaje H_d en T_M, de acuerdo a lo esperado, y un aumento de la energía característica $k_B T_d$ asociada a las fuerzas de anclaje al disminuir la temperatura en todo el rango estudiado. Este comportamiento es similar al observado en otros materiales, con la particularidad de que en la muestra estudiada, los valores de $k_B T_d$ son particularmente altos a bajas temperaturas ($\sim 100\,\mathrm{K}$).
- Segundo, la observación de la transición de desanclaje a bajas temperaturas en GdFeCo, que nos permitió caracterizar experimentalmente por primera vez dos de los exponentes críticos de la transición y compararlos con las predicciones teóricas. Esta caracterización fue posible gracias a que, en la muestra estudiada y en el rango de bajas temperaturas ($T < 100\,\mathrm{K}$), la energía térmica efectiva es prácticamente nula. Además de observar la ley de potencia $v \sim (H - H_d)^{\beta}$ para $H \to H_d^+$, que nos permitió obtener un exponente $\beta = 0.30 \pm 0.03$, pudimos cuantificar la longitud de correlación característica ℓ_{av} de la transición de desanclaje, que diverge en la transición como $\ell_{\mathrm{av}} \sim (H - H_d)^{-\nu_{\mathrm{dep}}}$ para $H \to H_d^+$ y $T \to 0$. Así, pudimos cuantificar al exponente crítico correspondiente, obteniendo $\nu_{\mathrm{dep}} = 1.3 \pm 0.3$. Estos valores de los exponentes críticos universales, obtenidos experimentalmente por primera vez, están en desacuerdo con las predicciones del modelo de *quenched Kardar-Parisi-Zhang*, mientras que están de acuerdo con las predicciones del modelo de *quenched Edwards-Wilkinson*. Por lo tanto, concluímos que la transición de desanclaje de paredes de dominios magnéticos en láminas delgadas está bien descrita por este modelo. En otras

palabras, decimos que las paredes de dominios pertenecen a la clase de universalidad de *quenched Edwards-Wilkinson*.

- Tercero, el estudio de la morfología de paredes de dominios en un amplio rango de temperaturas y campos magnéticos aplicados en la misma muestra de GdFeCo. En particular, cuantificamos cuidadosamente el valor del llamado exponente de rugosidad ζ. Este exponente se define, para el perfil de una pared ubicada en la dirección $\hat{x}$, descripto por una función $u(x)$, de acuerdo a la ley de escala $u(x) \sim x^{\zeta}$ que se espera que el perfil satisfaga en el marco de la teoría de interfases elásticas en medios desordenados. Observamos que los valores efectivos del exponente de rugosidad ζ_{eff} que obtenemos son dependientes de la temperatura y del campo magnético aplicado, y que sus valores no están de acuerdo con los valores de referencia esperados de acuerdo al modelo de *quenched Edwards-Wilkinson*, $\zeta_{\text{eq}} = 2/3$, $\zeta_{\text{dep}} = 1.25$ y $\zeta_{\text{th}} = 1/2$. De acuerdo a ideas teóricas previas, proponemos una interpretación de nuestros resultados teniendo en cuenta que los exponentes de rugosidad efectivos ζ_{eff} resultan de la acción conjunta de los tres exponentes esperados a distintas escalas de longitud, y que las longitudes características que separan estas escalas de longitud son las longitudes de correlación ℓ_{av} y ℓ_{opt}, que corresponden a la transición de desanclaje y al límite $H \to 0$, respectivamente. Además, y también de acuerdo a ideas teóricas previas para $T > 0$, consideramos que ℓ_{av} tiene valores finitos incluso por debajo de H_d. A partir de estas ideas, obtuvimos una interpretación plausible para los exponentes determinados experimentalmente, y cuantificamos la longitud de correlación ℓ_{av} en función de la temperatura T y el campo H.

- Cuarto, la investigación de la dinámica de paredes de dominios magnéticos impulsada tanto por campo (mediante la interacción Zeeman) como por corriente (mediante el torque por transferencia de spin, STT) en (Ga,Mn)(As,P)/(Ga,Mn)As. Nos enfocamos en el régimen térmicamente activado que se da por debajo de la transición de desanclaje, llamado régimen de reptación o *creep*. Nos basamos en investigaciones previas que encontraron que tanto el *creep* impulsado por campo como el impulsado por corriente presentan los mismos comportamientos universales, e investigamos los efectos de la aplicación simultánea de corriente J y campo H. Al analizar la acción de las fuerzas inducidas por campo y por corriente en direcciones opuestas, encontramos condiciones tales que la velocidad v de las paredes de dominios es nula, correspondiendo a un balance entre ambas fuerzas. En estas condiciones y para un amplio rango de temperaturas por debajo de la temperatura de Curie de la muestra, encontramos que existe una proporcionalidad entre las fuerzas inducidas por la corriente y el campo, con un factor $\epsilon = \mu_0 H/J = (1.3 \pm 0.2)\,\text{mT}/(\text{GA}/\text{m}^2)$. En base a esto, analizamos la acción separada de campo y corriente y la acción simultánea en condiciones de $v \neq 0$ considerando que existe un campo efectivo debido a los dos estímulos $\mu_0 H_{\text{eff}} = \mu_0 H + \epsilon J$. Esta expresión proporciona una interpretación satisfactoria de los datos experimentales para velocidades relativamente altas, pero observamos inconsistencias entre el modelo propuesto y los datos experimentales para velocidades bajas. Dos posibles fuentes de esta discrepancia son el carácter anisotrópico de la fuerza inducida por corriente, que depende del ángulo relativo entre la corriente y la orientación de la pared en cada punto, y la contribución adiabática del torque por transferencia de spin, que no fue tenida en cuenta en nuestro análisis.

Las investigaciones presentadas en esta tesis dan cuenta de los comportamientos universales de las paredes de dominios magnéticos en láminas delgadas y muestran que la teoría de interfases elásticas en medios desordenados es una herramienta muy poderosa para su estudio. El enfoque que utilizamos contribuye a nuestro conocimiento sobre las propiedades estadísticas de las paredes de dominios y aporta nuevas evidencias de que el modelo de *quenched Edwards-Wilkinson* describe satisfactoriamente su dinámica y su morfología. Además, aporta nuevas ideas sobre la naturaleza de la dinámica inducida tanto por campo como por corriente. Nuestros resultados motivan futuras investigaciones que permitan seguir profundizando en la comprensión de las propiedades estadísticas de las paredes de dominios magnéticos.

Synthèse en français

Les nouveaux matériaux magnétiques nano-structurés ont suscité un grand intérêt dans la communauté scientifique au cours des dernières décennies en raison de leurs propriétés inédites. En particulier, l'étude des parois de domaines magnétiques dans des films minces d'épaisseur nanométrique présente un intérêt tant du point de vue de la physique fondamentale que pour le développement de nouveaux dispositifs de spintronique. Ces parois, qui séparent des régions d'aimantation uniforme dans une film mince magnétique, peuvent être considérées comme des interfaces unidimensionnelles élastiques se déplaçant dans un milieu bidimensionnel inhomogène. Lorsque les vitesses sont suffisamment faibles, les parois sont très sensibles aux défauts des films minces qui tendent à les piéger et s'opposer à leur déplacement. Dans ce cas, une paroi de domaines se comporte comme un système élastique se déplaçant en milieu aléatoire. La dynamique et la morphologie de parois peuvent être décrites par un modèle minimal qui ne prend pas en compte l'évolution de leur structure magnétique interne. Cette approche, qui s'inscrit dans le domaine de la physique statistique, permet d'étudier une grande variété de phénomènes en ne considérant que quelques éléments fondamentaux : l'élasticité de l'interface, le désordre figé (*quenched*) de l'environnement, l'énergie thermique, et l'action d'une force appliquée.

Des modèles minimaux paradigmatiques pour l'étude de ce type d'interfaces sont les modèles de *quenched Edwards-Wilkinson* et de *quenched Kardar-Parisi-Zhang*. Ces modèles prédisent des comportements critiques à la fois pour la dynamique et pour la morphologie des interfaces, avec des exposants critiques caractéristiques. Un exemple de comportement critique est la transition de dépiégeage ou de *depinning* se produisant lorsque la force externe dépasse le seuil de dépiégeage des parois. Pour cette transition, si l'activation thermique peut être négligée, la vitesse de l'interface v suit une loi de puissance en fonction de la force appliquée f, avec un exposant critique β. Autrement dit, $v \sim (f - f_d)^\beta$ pour $f \to f_d^+$, où f_d est la force seuil de désancrage. Les valeurs numériques des exposants critiques sont universelles et différents phénomènes peuvent partager les mêmes exposants critiques. Pour prouver qu'un modèle minimal décrit de manière satisfaisante un phénomène physique, il est nécessaire de mesurer les valeurs des exposants critiques caractéristiques et de les comparer aux prédictions théoriques.

Dans cette thèse, nous analysons la dynamique et la morphologie des parois de domaines dans le cadre de la théorie des interfaces élastiques en milieux désordonnés. Deux types de films minces d'un grand intérêt ont été étudiés : un film ferrimagnétique de GdFeCo de 10 nm d'épaisseur et un film du semi-conducteur ferromagnétique de (Ga,Mn)(As,P)/(Ga,Mn)As de 4 nm d'épaisseur. La technique expérimentale que nous utilisons pour observer la morphologie et la dynamique des parois de domaines magnétiques est la microscopie magnéto-optique à effet Kerr polaire (PMOKE).

Les résultats de nos recherches font l'objet de quatre sujets principaux qui sont résumés ci-dessous.

- Tout d'abord, nous présentons des études de la dynamique de parois de domaines dans GdFeCo induite par un champ magnétique. Ces études sont effectuées sur une large gamme de températures (10-353 K), de part et d'autre de la température de compensation magnétique T_M, caractéristique des matériaux ferrimagnétiques. Nous avons pu quantifier, en fonction de la température, les paramètres qui caractérisent l'ancrage des parois notamment au voisinage de la compensation magnétique. Nous mettons en évidence une divergence du champ de désancrage H_d au voisinage de T_M, comme attendu, et nous observons une augmentation de l'énergie d'ancrage des parois $k_B T_d$ lorsque la température diminue dans toute la plage étudiée. Ce comportement est similaire à celui observé dans d'autres matériaux. Nous montrons en particulier qu'à basse température ($< 100\,\mathrm{K}$), l'énergie d'ancrage des parois $k_B T_d$ est très élevée par rapport à l'énergie d'activation thermique $k_B T$ ($T_d/T > 300$).
- L'observation de la transition de dépiégeage à basse température dans le film de GdFeCo nous permet de déterminer expérimentalement pour la première fois deux des exposants critiques de la transition et de les comparer aux prédictions théoriques. Cette détermination a été possible grâce au caractère quasi-athermique de la transition, observée à basse température. Nous avons pu mettre en évidence un bon accord avec la loi de puissance $v \sim (H - H_d)^{\beta}$ prédite pour $H \to H_d^+$ et obtenir une valeur pour l'exposant $\beta = 0.30 \pm 0.03$. D'autre part, nous avons pu quantifier la longueur de corrélation caractéristique ℓ_{av} de la transition de désancrage, qui diverge suivant la relation $\ell_{\mathrm{av}} \sim (H - H_d)^{-\nu_{\mathrm{dep}}}$ pour $H \to H_d^+$ et $T \to 0$. Nous avons pu en déduire la valeur de l'exposant critique correspondant $\nu_{\mathrm{dep}} = 1.3 \pm 0.3$. Ces valeurs des exposants critiques universels sont en désaccord avec les prédictions du modèle de *quenched Kardar-Parisi-Zhang* mais présentent un bon accord avec celle du modèle *quenched Edwards-Wilkinson*. Par conséquent, nous concluons que la transition de désancrage des parois des domaines magnétiques dans les films minces est bien décrite par ce modèle. En d'autres termes, le mouvement des parois de domaines appartiennent à la classe d'universalité *quenched Edwards-Wilkinson*.

- D'autre part, nous avons effectué une étude de la morphologie des parois de domaine sur une large gamme de températures et de champs magnétiques appliqués avec le même échantillon de GdFeCo. En particulier, nous quantifions soigneusement la valeur de l'exposant de rugosité ζ. Cet exposant est défini par la loi d'échelle $u(x) \sim x^{\zeta}$, pour une paroi alignée suivant la direction $\hat{x}$, dont le déplacement transverse est décrit par une fonction $u(x)$. Nous observons que les valeurs mesurées de l'exposant de rugosité ζ_{eff} dépendent de la température et du champ magnétique appliqué. Ces valeurs ne concordent pas avec aucune des valeurs de référence prédites par le modèle *quenched Edwards-Wilkinson*, $\zeta_{\mathrm{eq}} = 2/3$, $\zeta_{\mathrm{dep}} = 1.25$ et $\zeta_{\mathrm{th}} = 1/2$ pour différentes échelles de longueurs et gammes de champ magnétique. Nous proposons une interprétation de nos résultats qui suppose que les exposants de rugosité mesurés correspondent à des exposants effectifs. Nous supposons que les exposants effectifs ζ_{eff} résultent de la contribution conjointe des trois exposants attendus à différentes échelles de longueur. Les longueurs caractéristiques qui séparent ces échelles sont les longueurs de corrélation ℓ_{av} et ℓ_{opt}, qui correspondent respectivement à la transition de désancrage et à la limite $H \to 0$. De plus, et d'après les idées théoriques précédentes pour $T > 0$, on considère que ℓ_{av} a des valeurs finies même pour $H < H_d$. Sur la base de ces hypothèses, nous obtenons une interprétation plausible pour les exposants déterminés expérimentalement, et nous quantifions la longueur de corrélation ℓ_{av} en fonction de la température T et du champ H.

- Enfin, nous rapportons une étude sur la dynamique de parois de domaines magnétiques induite par champ magnétique et par courant électrique (transfert de spin) dans un film de (Ga,Mn)(As,P)/(Ga,Mn)As à aimantation perpendiculaire. Nous nous sommes concentré sur le régime thermiquement activé de reptation (*creep*) qui est observé au-dessous de la transition de dépiégeage. Pour l'analyse des résultats, nous nous sommes appuyé sur des recherches antérieures qui ont montré que la dynamique de *creep* sous champ et sous courant présentent de comportements universels communs. Nous avons étudié les effets de l'application simultanée du courant J et du champ H. Nous montrons qu'il est possible d'annuler la vitesse v des parois lorsque les contributions du champ et du courant à leur mouvement se compensent. Pour une large gamme de températures, nous mettons en évidence une proportionnalité entre les forces induites par le courant et le champ, avec un facteur de proportionnalité $\epsilon = \mu_0 H/J = (1.3 \pm 0.2)\,\mathrm{mT}/(\mathrm{GA/m^2})$. Sur cette base, nous analysons l'action séparée du champ et du courant et l'action simultanée, pour $v \neq 0$, en supposant qu'il existe un champ effectif qui prend en compte les deux contributions $\mu_0 H_{\mathrm{eff}} = \mu_0 H + \epsilon J$. Cette expression fournit une interprétation satisfaisante des données expérimentales pour des vitesses relativement élevées. Cependant, on observe des incohérences entre le modèle proposé et les données expérimentales pour des vitesses faibles. Des sources possibles de cet écart sont le caractère anisotrope de la force induite par le courant, qui dépend de l'angle relatif entre le courant et l'orientation de la paroi, et une contribution dite adiabatique du transfert de spin non prise en compte.

Les investigations présentées dans cette thèse rendent compte des comportements universels des parois de domaines magnétiques dans des films minces à aimantation perpen-

diculaire et montrent que la théorie des interfaces élastiques dans les milieux désordonnés est un outil très puissant pour leur étude. L'approche que nous utilisons contribue à notre compréhension des propriétés statistiques des parois de domaines et fournit de nouvelles preuves que le modèle *quenched Edwards-Wilkinson* décrit de manière satisfaisante leur dynamique et leur morphologie. En outre, il apporte de nouvelles informations sur la nature de la dynamique induite par champ magnétique et transfert de spin. Nos résultats motivent de futures recherches qui permettront de mieux comprendre les propriétés statistiques des parois de domaines magnétiques.

Agradecimientos

"Cuidamos la huerta con dedicación.
Sembramos albahaca alrededor
de los tomates y pimientos
para ahuyentar las moscas
y combatir las plagas
que lastiman el fruto.

A menudo las cosas
no ocurren como deberían.
Todo camino conduce
a un extravío.

Plantaría todas las hierbas
que sean necesarias
alrededor de los que amo."

Jimena Arnolfi, *La tierra es fértil*

HACER una tesis de doctorado es una experiencia de vida que no podría ser llevada a cabo sin el acompañamiento y el apoyo de seres humanos maravillosos. En estas líneas quiero agradecer a todas las personas que fueron parte de este trabajo colectivo y también a las que me acompañaron e hicieron que estos años de vida estén llenos de experiencias memorables. Gracias por ayudarme a terminar esta etapa con alegría y satisfacción.

En primer lugar, quiero agradecer a las personas que fueron parte del jurado de tesis, que se tomaron el tiempo y el trabajo de leer con atención este escrito. Recibí con mucha alegría sus comentarios sobre la tesis en la instancia de la defensa, y sus preguntas generaron un momento de intercambio y reflexión muy enriquecedor. Gracias Alejandro Butera, Gabriela Pasquini, Jan Vogel, Liza Herrera Diez y Thierry Giamarchi por sus valoraciones sobre este trabajo y por la discusión constructiva que tuvimos.

Llevar a cabo esta tesis en cotutela no hubiera sido posible sin el excelente trabajo de Natalia Cabuccio, secretaria del Consejo Académico del Instituto Balseiro, quien se ocupó de hacer todos los movimientos necesarios para que el convenio entre universidades para mi tesis se lleve a cabo. ¡Muchísimas gracias Natalia!

En estos años tuve tres personas que fueron mis mayores guías en mi trabajo de tesis: Javier Curiale, Vincent Jeudy y Sebastian Bustingorry. Gracias Javier por tu acompañamiento y apoyo, por la confianza, y por siempre estar atento, para que cada etapa del doctorado avance de la mejor manera, y para que mi estado anímico sea el mejor posible. Siempre supe que tenía un director de una calidad humana enorme, y eso fue fundamental para lidiar con las dificultades. Gracias Vincent por recibirme y ayudarme a adaptarme a la vida en París, por el apoyo y por tu trato sincero y humano. Fue fundamental tener un director tan amable en esas etapas de vida en Francia en las que la adaptación a veces no fue fácil. Gracias también por tu mirada crítica y por aportar nuevas perspectivas a mi trabajo. Gracias Sebastian por estar siempre ahí acompañando y haciendo aportes al trabajo aunque formalmente no fueras mi director. Por tu disposición para charlar siempre que fue necesario y por encarar el trabajo con entusiasmo y pasión. Para mí sos un ejemplo de compromiso por la investigación y la enseñanza con consciencia social.

El trabajo científico se hace en equipo, por eso escribí esta tesis en primera persona del plural. Quiero agradecer a los integrantes del Paredom, un grupo de personas fantásticas con conocimientos diversos que transmiten entusiasmo y que disfrutan de compartir ideas y también momentos festivos. Es un placer y un privilegio trabajar con un grupo humano tan lindo y tan consciente de la importancia de colaborar y sumar fuerzas. El Paredom es una muestra de que personas con trayectorias científicas diferentes puede unirse y crear líneas de investigación comunes de forma muy virtuosa. Además de Javier Curiale y Sebastian Bustingorry, Alejandro Kolton, Ezequiel Ferrero, Mara Granada, Nirvana Caballero, Iván Fernández Aguirre, Matías Grassi, Cynthia Quinteros, María José Cortés Burgos, Daniel Jordán, Pamela Guruciaga, Emilio De Biasi, Julián Milano, Dafne Goijman, Gerardo Ramírez y Víctor Purrello son o fueron parte de este grupo durante estos años. ¡Muchísimas gracias a ustedes!

Gracias a los integrantes del Laboratorio de Resonancias Magnéticas del Centro Atómico Bariloche, con quienes compartí el día a día en el laboratorio. Tengo la suerte de haber hecho el doctorado en una atmósfera de compañerismo, de apoyo mutuo, de interés por el trabajo de cada persona, y en el que me sentí cómodo para pedir ayuda porque siempre encontré gente dispuesta y contenta de poder ayudar. Quiero agradecer especialmente a las personas con las que hice parte del trabajo experimental en el laboratorio o que me ayudaron con cuestiones técnicas. Gracias Iván Fernández Aguirre y Matías Grassi por acompañarme en mis primeros pasos en el mundo de las mediciones por microscopía Kerr. Con ustedes obtuve las primeras imágenes allá por 2016, fue muy lindo compartir esos momentos y sumarme al trabajo que venían haciendo. Gracias Gerardo Ramírez y Julián Milano por el trabajo compartido en las mediciones de resonancia ferromagnética, que no prosperaron, pero me hicieron aprender mucho. Gracias Javier Gómez por ayudarme con las mediciones de magnetometría Kerr. Gracias Matías Guillén por estar siempre dispuesto a ayudar con la electrónica de los experimentos. Gracias Rubén Benavides y César Pérez por sus ayudas técnicas y por aportar su creatividad para resolver problemas experimentales. Fue muy divertida la etapa en la que diseñamos y construímos imanes y portamuestras con ustedes.

En mis estadías en Francia, compartí mis días de trabajo en el Laboratoire de Physique des Solides con el grupo IDMAG. Quiero agradecer a todos sus integrantes por recibirme amablemente y sumarme a sus rituales: los mediodías en los que nos buscábamos para compartir el almuerzo, los cafés, las delicias compartidas, las reuniones del grupo... ¡y también por el curso intensivo de francés! Gracias André Thiaville, Stanislas Rohart, Alexandra Mougin, por transmitir su pasión, por sus críticas constructivas y por su generosidad para enseñar. Gracias Raphael Weil por tu ayuda en el trabajo en la sala limpia. Gracias Léo Berges por enseñarme con entusiasmo a hacer las mediciones de efecto Hall anómalo y su análisis. Gracias Pierre Géhanne por enseñarme a usar tu microscopio, por los días compartidos en la oficina, y por invitarme a los eventos de tu banda. Gracias Rebeca Díaz Pardo por ser mi compañera de experimentos, por mostrarme el laboratorio y por ayudarme a no sentirme tan lejos de casa. Qué gusto esos días de trabajo hablando en castellano y compartiendo la cultura de nuestros países. Gracias Eloi Haltz, Sougata Mallick, Sachin Krishna, João Sampaio, por las ayudas en el laboratorio, las charlas inspiradoras, y los lindos momentos compartidos dentro y fuera del laboratorio.

En Francia también tuve intercambios científicos con otras personas a las que quiero agradecer por su gran predisposición para enseñarme y trabajar juntos y por los días enriquecedores que compartimos: por un lado, Loïc Rondin y Timothée de Guillebon, con quienes compartí más de un mes de trabajo en el Laboratoire Aimé-Cotton y aprendí muchísimo; por otro lado, Jon Gorchon y Juan Carlos Rojas Sánchez del Institut Jean Lamour, con quienes colaboramos en algunos trabajos y me recibieron en dos ocasiones en su laboratorio en Nancy.

Quiero agradecer también a las instituciones en donde estudié y trabajé en estos años. Especialmente al Instituto Balseiro, en donde elegí recorrer mis últimos 9 años de formación académica, al CONICET, que me dio la beca con la que viví durante el doctorado, y a la Université Paris-Saclay, que financió parte de mis estadías en Francia. Agradezco a quienes defienden y luchan por la educación pública gratuita y de calidad en Argentina, permitiendo que muchísimas personas podamos desarrollarnos y hacer investigación dentro del país.

Por último, quiero agradecer a todas las personas que me acompañaron en estos años. Gracias a todas mis amistades, que fueron mi mayor apoyo emocional y me ayudaron a ver con más claridad en los momentos de crisis. Especialmente, gracias Vattu, Fer, Mangu, Aguss, Luchi: son mi apoyo de todos los días. ¡Qué suerte que tengo de tener estos amigues! Gracias Fran, por el folklore cuyano, el vino y las charlas. Gracias David, por nuestros reencuentros y viajes en Europa, que nos recargaban las pilas para seguir adelante y soportar mejor el sabernos lejos de casa. Pocos momentos en la vida son tan hermosos como los reencuentros con grandes amigos en lugares soñados. Así que también gracias Pampa, gracias Chavo, y gracias Vattu de vuelta, porque esos reencuentros “al otro lado del charco” me van a quedar para toda la vida. Gracias Aguus, Luchi, Nacho y Nico por nuestros momentos de festichola en Buenos Aires. Gracias a mis compas de La Nube Percusión, la comunidad con la que compartí muchos de los momentos más felices de estos años. Gracias a mis amistades de la Casa Argentina en París: Chaleco, César, Emilio, Facu, Renzo, Mati, Héctor, Jime, Santi, Coco, Dalmiro, Nelly. ¡Cuántos momentos memorables con ustedes! Gracias Anstel por enseñarme un poquito de los ritmos de Guinea y por invitarme a esas juntadas hermosas en La Villette. Gracias Blandine, Nora, Gilbert, Fédé, por sumarme a sus bellos mundos y por hacerme conocer el maravilloso “lado B” de París. Gracias Trilce, por tu compañía amorosa en la primera parte de este doctorado. Gracias Vicu, por nuestros momentos hermosos, por la valentía para lanzarnos a la aventura, y porque nos acompañamos en los momentos más difíciles. Gracias a mis familiares que siempre estuvieron ahí apoyando con sus lindas palabras y su compañía. Gracias a mis tíos y tías, primos y primas, y a mis abuelas Cristina y Mirta. Gracias Laura, gracias Paddy, por estar siempre presentes para charlar y por el apoyo constante. Gracias Willy, por estar siempre atento y por tenerme en cuenta para proyectos musicales que llevan a experiencias inolvidables. Gracias Ana, porque acompañaste como una integrante más de mi familia cercana. Gracias a mi mamá Laila y a mi papá Felipe, siempre presentes y siempre apoyando con muchísimo amor. Este trabajo lo dedico a ustedes, porque son mi apoyo más fundamental.

Acknowledgments

"La clave está en la simpleza,
en los momentos reales,
en las cosas pequeñas,
en perseguir lo que sueñas."
Albano "Nano" Geliberti

Doing a doctoral thesis is a life experience that could not be carried out without the accompaniment and support of wonderful human beings. In these lines I want to thank all the people who were part of this collective work and also those who accompanied me and made these years of life full of memorable experiences. Thank you for helping me finish this stage with joy and satisfaction.

First of all, I want to thank the people who were part of the thesis jury, who took the time to read this writing carefully. I received with great joy your comments on the thesis in the defense instance, and your questions generated a very enriching moment of exchange and reflection. Thank you Alejandro Butera, Gabriela Pasquini, Jan Vogel, Liza Herrera Diez and Thierry Giamarchi for valuing this work and for the constructive discussion we had.

Carrying out this thesis in co-supervision would not have been possible without the excellent work of Natalia Cabuccio, secretary of the Academic Council of Instituto Balseiro, who took care of making all the necessary arrangements in order to write and sign the agreements between universities. Thank you very much Natalia!

In these years I had three people who were my greatest guides in my thesis work: Javier Curiale, Vincent Jeudy and Sebastian Bustingorry. Thanks Javier for your accompaniment and support, for your trust, and for always being attentive, so that each stage of the doctorate progresses in the best way, and so that my state of mind is the best possible. I always knew that I had a director of enormous human quality, and that was essential in order to deal with the difficulties. Thank you Vincent for receiving me and helping me to adapt to life in Paris, for the support and for your sincere and humane treatment. It was essential to have such a friendly director in those stages of life in France in which adaptation was not easy at times. Thank you also for your critical gaze and for bringing new perspectives to my work. Thank you Sebastian for always being there accompanying and making contributions to the work even though you were not formally my advisor. For your willingness to chat whenever necessary and for approaching work with enthusiasm and passion. For me you are an example of commitment to research and teaching with a social conscience.

Scientific work is done as a team, that is why I wrote this thesis in the first person plural. I want to thank the members of Paredom, a group of fantastic people with diverse backgrounds who transmit enthusiasm and who enjoy sharing ideas and also festive moments. It is a pleasure and a privilege to work with such a beautiful human group, so aware of the importance of collaborating and joining forces. The Paredom is an example that people with different scientific backgrounds can come together and create common lines of research in a very virtuous way. In addition to Javier Curiale and Sebastian Bustingorry, Alejandro Kolton, Ezequiel Ferrero, Mara Granada, Nirvana Caballero, Iván Fernández Aguirre, Matías Grassi, Cynthia Quinteros, María José Cortés Burgos, Daniel Jordán, Pamela Guruciaga, Emilio De Biasi, Julián Milano, Dafne Goijman, Gerardo Ramírez and Víctor Purrello are or were part of this group during these years. Many thanks to you!

Thanks to the members of Laboratorio de Resonancias Magnéticas at Centro Atómico Bariloche, with whom I shared the day to day in the laboratory. I am fortunate to have done my doctorate in an atmosphere of camaraderie, of mutual support, of interest in the work of each person, and in which I felt comfortable asking for help because I always found people willing and happy to help. I want to especially thank the people with whom I did part of the experimental work in the laboratory or who helped me with technical issues. Thank you Iván Fernández Aguirre and Matías Grassi for accompanying me in my first steps in the world of Kerr microscopy measurements. With you I obtained the first images back in 2016, it was very nice to share those moments and join in the work that you had been doing. Thank you Gerardo Ramírez and Julián Milano for the shared work in the ferromagnetic resonance measurements, which did not prosper, but made me learn a lot. Thanks Javier Gómez for helping me with the Kerr magnetometry measurements. Thanks Matías Guillén for always being ready to help with the electronics of the experiments. Thank you Rubén Benavides and César Pérez for your technical aids and for contributing your creativity to solve experimental problems. It was a lot of fun when we designed and built magnets and sample holders with you.

During my stays in France, I shared my working days at the Laboratoire de Physique des Solides with the IDMAG group. I want to thank all its members for receiving me kindly and joining their rituals: the noons when we would meet each other to share lunch, the coffees, the shared delicacies, the group meetings... and also for the intensive French course! Thank you André Thiaville, Stanislas Rohart, Alexandra Mougin, for conveying your passion, for your constructive criticism, and for your generosity in teaching. Thank you Raphael Weil for your help with the clean room work. Thank you Léo Berges for enthusiastically teaching me how to make anomalous Hall effect measurements and analysis. Thank you Pierre Géhanne for teaching me to use your microscope, for the days spent in the office, and for inviting me to your band events. Thank you Rebeca Díaz Pardo for being my experiment partner, for showing me the laboratory and for helping me not feel so far from home. What a pleasure those days of work speaking in Spanish and sharing the culture of our countries. Thank you Eloi Haltz, Sougata Mallick, Sachin Krishna, João Sampaio, for the helps in the laboratory, the inspiring talks, and the beautiful moments shared inside and outside the laboratory.

In France I also had scientific exchanges with other people whom I want to thank for their great willingness to teach me and work together and for the enriching days we shared: on the one hand, Loïc Rondin and Timothée de Guillebon, with whom I shared more than a month of work at Laboratoire Aimé-Cotton and I learned a lot; on the other hand, Jon Gorchon and Juan Carlos Rojas Sánchez from Institut Jean Lamour, with whom we collaborated on some works and who received me twice in their laboratory in Nancy.

I also want to thank the institutions where I studied and worked in these years. Especially to Instituto Balseiro, where I chose to go through my last 9 years of academic training, to CONICET, which gave me the scholarship with which I lived during the doctorate, and to the Université Paris-Saclay, which financed part of my stays in France. I thank those who defend and fight for free and quality public education in Argentina, allowing many people to develop and do research within the country.

Finally, I want to thank all the people who have accompanied me in these years. Thanks to all my friends, who were my greatest emotional support and helped me to see more clearly in times of crisis. Especially thanks Vattu, Fer, Mangu, Aguss, Luchi: you are my support every day. How lucky I am to have these friends! Thanks Fran, for the Cuyo folklore, the wine and the talks. Thanks David, for our reunions and trips in Europe, which recharged our batteries in order to move on and better bear knowing each other far from home. Few moments in life are as beautiful as reunions with great friends in dream places. So also thanks Pampa, thanks Chavo, and thanks again Vattu, because those reunions "on the other side of the pond" are going to stay with me for a lifetime. Thank you Aguus, Luchi, Nacho and Nico for our festive moments in Buenos Aires. Thanks to my compas from La Nube Percusión, the community with which I shared many of the happiest moments of these years. Thanks to my friends from Casa Argentina in Paris: Chaleco, César, Emilio, Facu, Renzo, Mati, Héctor, Jime, Santi, Coco, Dalmiro, Nelly. How many memorable moments with you! Thank you Anstel for teaching me a bit about the rhythms of Guinea and for inviting me to those beautiful gatherings at La Villette. Thank you Blandine, Nora, Gilbert, Fédé, for joining me in your beautiful worlds and for letting me know the wonderful "B-side" of Paris. Thank you Trilce, for your loving company in the first part of this doctorate. Thank you Vicu, for our beautiful moments, for the courage to embark on an adventure, and because we accompanied each other in the most difficult moments. Thanks to my relatives who were always there supporting with their nice words and their company. Thanks to my uncles and aunts, my cousins, and my grandmothers Cristina and Mirta. Thank you Laura, thank you Paddy, for always being there to chat and for your constant support. Thank you Willy, for always being attentive and for taking me into account for musical projects that lead to unforgettable experiences. Thank you Ana, because you accompanied as one more member of my close family. Thanks to my mother Laila and my father Felipe, always present and always supporting with a lot of love. I dedicate this work to you, because you are my most fundamental support.

Contents

1 Introduction **1**

2 General concepts and framework **5**

- 2.1 Magnetism . . . 6
  - 2.1.1 Types of magnetism in matter . . . 7
  - 2.1.2 Magnetic energies . . . 8
  - 2.1.3 Magnetic domains and domain walls . . . 12
- 2.2 Micromagnetism of domain walls . . . 14
  - 2.2.1 Domain wall static profile . . . 14
  - 2.2.2 Landau-Lifshitz-Gilbert equation . . . 16
  - 2.2.3 1D model for field-driven domain wall dynamics . . . 18
  - 2.2.4 Domain wall dynamics driven by field and current . . . 22
  - 2.2.5 Limitations of micromagnetic theory and alternative approaches . . . 25
- 2.3 Elastic interfaces in disordered media . . . 26
  - 2.3.1 Roughness characterization . . . 28

2.3.2 Dynamical regimes of driven interfaces . . . 32
2.4 Magnetic domain walls as driven elastic lines . . . 39
2.4.1 Experimental observation of creep and flow regimes . . . 39
2.4.2 Universal creep regime . . . 40
2.4.3 Universal depinning transition . . . 43
2.4.4 Length scales and roughness exponents . . . 45
2.5 Studied magnetic thin films . . . 49
2.5.1 Rare earth - transition metal ferrimagnetic alloys . . . 50
2.5.2 Diluted ferromagnetic semiconductors . . . 55
2.6 Chapter summary and thesis overview . . . 57

3 Experimental techniques and studied samples 59

3.1 Magneto-optical Kerr effect imaging . . . 60
3.1.1 Polar Kerr effect . . . 61
3.1.2 Magneto-optical contrast . . . 61
3.2 Polar magneto-optical Kerr effect microscope . . . 66
3.2.1 Optical setup . . . 66
3.2.2 Temperature control . . . 69
3.2.3 Domain wall velocity measurement . . . 71
3.2.4 Magnetic field pulses . . . 73
3.2.5 Domain wall profile detection . . . 77
3.3 Thin film of GdFeCo . . . 79
3.3.1 Magnetic characterization . . . 79
3.4 (Ga,Mn)(As,P)/(Ga,Mn)As bilayer . . . 85
3.5 Chapter summary . . . 87

4 Field-driven domain wall dynamics in a ferrimagnetic GdFeCo thin film 89

4.1 Motivation, framework and previous investigations 91

4.1.1 Thermally activated dynamics and depinning transition 91

4.1.2 Universal depinning critical exponents 93

4.2 Domain wall dynamics in a wide temperature range 94

4.2.1 General analysis of domain wall velocity curves 95

4.2.2 Domain wall dynamics above magnetic compensation 98

4.2.3 Domain wall dynamics below magnetic compensation 105

4.2.4 Temperature dependence of depinning parameters 115

4.3 Athermal depinning transition at low temperatures 117

4.3.1 Zero-temperature-like characteristics 118

4.3.2 General procedure for fitting the athermal depinning transition 119

4.3.3 Universal and non-universal depinning parameters 123

4.3.4 Critical behavior of the depinning correlation length 127

4.3.5 Universality class of magnetic domain wall depinning 134

4.4 Chapter summary and conclusions 136

5 Domain wall roughness in a ferrimagnetic GdFeCo thin film 139

5.1 Previous experimental roughness measurements 140

5.2 Statistically meaningful roughness measurement 142

5.2.1 Computing the displacement-displacement correlation function of a domain wall profile 142

5.2.2 Determining the roughness parameters and their uncertainties 144

5.2.3 Statistics of roughness parameters 146

5.2.4 Roughness parameters in the field-temperature diagram 148

5.3 Analysis in terms of crossover lengths . . . 150

5.3.1 Structure factor with two crossovers . . . 151

5.3.2 Larkin length and equilibrium correlation length . . . 154

5.3.3 Depinning correlation length and structure factor amplitude . . . 155

5.3.4 Resulting parameters and experimental crossover diagram . . . 158

5.4 Chapter summary and conclusions . . . 160

6 Field- and current-driven domain wall dynamics in (Ga,Mn)(As,P)/(Ga,Mn)As 163

6.1 Motivation and framework . . . 164

6.1.1 Universality class of field-driven and STT-driven domain wall motion 165

6.1.2 Combined effect of field and STT on domain wall motion . . . 166

6.2 Methods for velocity measurements . . . 169

6.2.1 Shape and simultaneity of applied pulses . . . 169

6.2.2 Left and right domain wall velocities . . . 171

6.3 Results and discussion . . . 172

6.3.1 Balance of field- and STT-driven forces . . . 173

6.3.2 Field-driven and STT-driven creep regimes . . . 177

6.3.3 Combined field- and STT-driven dynamics . . . 180

6.4 Chapter summary and conclusions . . . 185

7 General conclusions and perspectives 187

CHAPTER 1

Introduction

"Miré el arco y esquivé patadas."
Diego Armando Maradona

THIS thesis is attached to several different areas of Physics: Statistical Physics, Magnetism, and Materials Science of Nanostructured Systems. Throughout this work, we shall establish links between these disciplines in order to present a deep study of our main subject, domain walls in magnetic thin films, not only focusing on its fundamental aspects but also keeping an eye on its technological potential.

Magnetic domain walls are the boundaries or interfaces between magnetic domains, which are regions of uniform magnetization in a material [1]. Inside a domain wall, magnetization changes rapidly as a function of the position when passing from one domain to the other, i.e. when crossing the domain wall [2]. This abrupt variation of magnetization results on an energetic cost for domain wall formation which may be effectively treated as an elasticity. As a consequence, domain walls tend to be as flat as possible. In addition, they are immersed in a magnetic material with its intrinsic inhomogeneities, meaning that the elastic domain wall is also subject to the action of disorder. Its impact may be modelled as an effective disordered pinning potential which affects the shape of domain walls and tends to prevent their motion.

Given this context, our approach to the study of magnetic domain walls is framed on the theory of elastic manifolds in disordered media, which comes from the field of Statistical

Physics [3]. Therefore, we shall discuss the general statistical properties of elastic interfaces in nature, which are particularly rich when disorder plays a relevant role [4, 5]. Due to the interplay between elasticity, disorder and thermal activation, interfaces are rough and their dynamics under the action of a driving force constitutes a stochastic process.

The motivation to understand the physics of a variety of phenomena within the same theoretical framework, consisting on a bunch of several fundamental elements that permit to describe them, is one of the main incentives for the study of elastic interfaces in disordered media. Indeed, there exist several key features that many different interfaces in nature share, being domain walls one of these interfaces. Furthermore, we can classify them into several so-called universality classes, which are defined by small groups of general characteristics [3, 4]. Particularly, interfaces in disordered media may undergo a second-order dynamic phase transition, the so-called depinning transition, which is characterized by critical behaviors. For a given interface phenomena, the associated critical exponents have particular values which define the universality class to which that phenomena belongs.

As we are particularly interested on magnetic domain walls in thin films, we shall put our focus on the fascinating area of Magnetism and Magnetic Materials. This theme, which is nowadays amazingly broad, has inspired human curiosity for centuries, even before the development of the scientific method [6, 7]. In the last century and mainly during the last decades, our deeper understanding of the microscopic phenomena behind magnetism and our capability to create new materials with reduced dimensions boosted enormously the technological improvements related to magnetism and unveiled new, previously unknown phenomena. A flourishing area in this issue is Spintronics, which consists on the development of devices such as sensors, magnetic memories and logic gates which are based on the control of both the electronic charge and spin [8–12].

In the quest for new technologies, understanding the nature of magnetic switching and domain wall motion is crucial. A variety of mechanisms are responsible for the dynamics of magnetization, and therefore there exist several different driving forces which may act on domain walls. To summarize, we can mention the two driving forces which are studied in this work: magnetic field, which favors a particular orientation of the magnetization and therefore induces a force over domain walls [13–18], and the spin-transfer torque (STT), which is generated by spin polarized electrical currents that drive domain walls when interacting with their internal magnetization [19–27].

In this thesis, we deeply study how these forces act over domain walls, inducing their movement and changing their morphology. The main experimental technique that we implement is the magneto-optical Kerr effect (MOKE) microscopy, which permits a real-time observation of domain walls in thin films, their shape, and their movement under applied stimuli. We perform these studies in two particular magnetic systems: a ferrimagnetic rare earth - transition metal alloy, composed by gadolinium, iron and cobalt (GdFeCo), and a diluted ferromagnetic semiconductor, the gallium arsenide doped with manganese and phosphorus, (Ga,Mn)(As,P). The studied samples consist on thin films, with thicknesses of the order of several nanometers, which have perpendicular magnetic anisotropy [28–30].

Ferrimagnetic rare earth - transition metal alloys have become of huge interest in the last years due to their particular magnetic ordering, which results in very efficient magnetization dynamics and a big variability of magnetic properties when changing the temperature or composition [31–37]. Our experimental studies in GdFeCo, which is part of this group of materials, are focused on the dynamics and morphology of domain walls driven by field, with the particularity that we perform careful studies in a wide range of temperatures.

Particularly, we have deeply studied the different regimes of motion of domain walls to which we have experimental access at temperatures ranging from 10 to 353 K. This has allowed for the detailed description of the temperature-dependence of parameters that describe domain wall dynamics in these regimes of motion. One of our most striking observations is the almost complete suppression of thermal effects in a low temperature range, what resulted in an unprecedented observation of the depinning transition with zero-temperature-like characteristics. This has enabled the first experimental determination of the full set of critical exponents defining the universality class to which field-driven domain wall depinning in thin films belongs [4, 5, 38].

In addition, we have studied the morphology of domain walls driven by field in the same GdFeCo sample by performing statistically meaningful roughness measurements [39]. This has given us a deeper insight on the statistical properties of domain wall morphology, and has permitted us to readdress, with the power of new evidence, questions related to the length scales defining the statistical nature of domain wall motion [40]. Particularly, we demonstrate the consistence between experimental roughness determinations and recently proposed theoretical ideas [4, 41] and, furthermore, we perform the first experimental quantification of the characteristic correlation length of the depinning transition. Both the determination of critical exponents and the study of characteristic length scales, which are the main goals of our research regarding domain walls in GdFeCo, are of great importance as they shed light on the nature of the fundamental ingredients that dominate domain wall motion.

The other system under study, as mentioned above, is a diluted ferromagnetic semiconductor. Particularly, we perform domain wall dynamics measurements in a bilayer of (Ga,Mn)(As,P)/(Ga,Mn)As. In this system, the current-driven force over domain walls via spin-transfer torque (STT) is particularly efficient [24–27, 42], what permits an appropriate comparison between the two types of drive. We therefore study and compare their nature and effects over domain walls in the regimes of relatively low wall velocity. This comparison sheds light over the similarities and differences between these two drives and on the nature of wall motion under their separated or simultaneous action. Remarkably, we have found that the forces induced by field and current are proportional between each other, with a well-defined proportionality factor, in various experimental situations.

This thesis makes contributions to the understanding of domain wall motion in thin films, both metallic and semiconducting, and both ferromagnetic and ferrimagnetic. In addition to this fundamental motivation, these contributions could be also of technological interest due to the fact that the studied systems present properties that are suitable for device development [42–45]. Our approach is particular because our main tools are taken from the framework of statistical physics, with the goal of contributing from an interdisciplinary point of view. This approach complements with fully magnetic studies and has its own strengths and weaknesses, as we will discuss throughout this manuscript. A remarkable strength is the fact that disorder, a challenging ingredient in Physics, is put as a protagonist which must be considered in order to comprehensively understand the studied phenomena and its intrinsic complexity.

This work is organized as follows. In chapter 2, we present the main general concepts that we address in the framework of this thesis. We shall therefore discuss about magnetism, statistical properties of magnetic domain walls in thin films, and the characteristics of the magnetic materials that we study. In chapter 3, we present the experimental techniques that we have used and developed during this thesis, focusing on magnetic imaging and particularly on polar Kerr microscopy. In addition, we present a characterization of the studied samples. Next three chapters are devoted to the presentation and discussion of the main experimental results that we have obtained. In chapter 4 we focus on the domain wall dynamics in a ferrimagnetic GdFeCo thin film, and in chapter 5 we present and discuss our studies on the domain wall roughness in GdFeCo. Later, in chapter 6 we present our studies on the current- and field-driven domain wall dynamics in (Ga,Mn)(As,P)/(Ga,Mn)As. We conclude in chapter 7 with a synthesis of our main findings, a discussion on the strengths and weaknesses of our study, and some remarks about the perspectives for future research in this topic.

CHAPTER 2

General concepts and framework

"Nós todos sabemos alguma coisa.
Nós todos ignoramos alguma coisa.
É por isso que sempre aprendemos."
Paulo Freire

In this chapter, the main concepts that constitute the framework in which this thesis work was performed, are presented. We start in section 2.1 with an overview of the vast area of Magnetism, from a historical introduction to presenting the concepts of magnetic domains and domain walls. Then, we shall describe the fundamental properties of domain walls from a micromagnetic point of view in section 2.2, focusing both on their statics and dynamics. Afterwards, a detailed presentation of the statistical properties of driven elastic interfaces in disordered media will be done in section 2.3, as it constitutes the main theoretical framework for the study of domain walls that we develop throughout this thesis. In section 2.4, the main concepts that constitute the present knowledge of domain wall dynamics and morphology in the framework of the theory of driven interfaces in disordered media will be presented. Then, in section 2.5 we shall describe the main properties of the systems studied in this thesis, the ferrimagnet GdFeCo and the semiconductor (Ga,Mn)(As,P)/(Ga,Mn)As, focusing on their main properties and the reasons why they are particularly interesting for the study of magnetic domain walls. Finally, we conclude and summarize this chapter and its links with following chapters in section 2.6.

2.1 Magnetism

Even if Magnetism has been observed and experienced by humans during millennia, almost all of our current knowledge about this phenomena was achieved during the last two centuries. Primitive observations of the “magical” attraction between some kinds of stones (most of them containing magnetite, as we now know) had already inspired the fabrication of instruments allowing humans to orientate on Earth since two thousand years ago [6]. Nevertheless, the fact that magnetism is not approachable directly through our senses lead to a much more developed understanding of other broad areas as Mechanics, Heat and Light [7]. Even today, Magnetism is probably one of the less comprehended big areas of Physics.

Up to the seventeenth century, the Greek notion that magnets were animated persisted in Europe. It was René Descartes who put this idea away [6]. The nineteenth century was the beginning of an incredible story for our understanding of Magnetism and its close relationship with Electricity. Hans-Christian Oersted first observed in 1820 the appearance of magnetic forces close to a current-carrying wire [46]. Then, Michael Faraday discovered magnetic induction, demonstrated the principle of an electric motor, and intuited that electric and magnetic forces could be understood from the basis of extended electric and magnetic fields. The observation of the so-called Faraday effect showed that the properties of a light beam can be affected by the interaction with magnetic materials [47]. Inspired by all this experimental work, James Clerk Maxwell formulated in 1864 his unified theory of Electricity, Magnetism and Light [47]. The research performed during this thesis is closely related to these three concepts: the interaction between polarized light and magnetic materials is on the basis of our experimental approach, and magnetic domain walls are studied when interacting both with polarized electric currents and magnetic fields.

Before the end of nineteenth century, Electromagnetism was already the basis of many technological advances which gave practical solutions for issues as illumination, transport and communication. Despite the wonderful technical and intellectual triumphs of this discipline, humans still had no idea of which was the microscopic origin of magnetism in matter. The molecular field theory of Pierre Weiss [48] (1907) successfully described the phenomenology of paramagnetic and ferromagnetic states, and the existence of a phase transition between them, but could not explain the origin of this molecular field. The formulation of Relativity and Quantum Mechanics in the first decades of the twentieth century [50] and, particularly, the discovery of electron’s intrinsic spin by George Uhlenbeck and Samuel Goudsmit in 1925 [49] finally explained the microscopical origin of magnetism and the spontaneous magnetization present in the ferromagnetic state of magnetic materials. The main contribution to this phenomena was found to be the electronic magnetic moment, arising from its intrinsic angular momentum, i.e. the electron spin.

The magnetic nature of different materials is intimately related to how electrons fill the energetic levels of atoms following the Hund rules [51, 52]. Atoms with unfilled atomic shells present an unbalance of electrons in the two possible spin states, “up” and “down”, and therefore present a magnetic moment. Furthermore, electronic spins may interact between each other via exchange interactions, which arise due to the Pauli exclusion principle characterizing fermions [53]. These interactions lead to the existence of spontaneously ordered magnetic states which we will briefly discuss in the following.

2.1.1 Types of magnetism in matter

Magnetic materials or, more generally, the magnetic states in which they may be found, can be grouped in different categories, depending on the interactions between their magnetic moments and with an applied field. As main examples, we can mention the diamagnetic, paramagnetic, ferromagnetic, anti-ferromagnetic and ferrimagnetic states.

Diamagnetism is characterized by weak interactions between magnetic moments and a negative response to an applied magnetic field, i.e. the magnetization induced by an applied field is opposite to it. Paramagnetism also presents weak interactions but, in contrast to diamagnetism, a positive alignment of magnetic moments with applied field is induced. These two states do not present a spontaneous magnetic order.

Materials in a ferromagnetic state present a strong coupling between magnetic moments via exchange interactions [54] which favors a parallel orientation of magnetic moments (see figure 2.1(a)), generating a spontaneous magnetization of relatively high magnitude. In anti-ferromagnetic materials, there also exists a strong exchange coupling between adjacent magnetic moments which induces magnetically ordered states, but with anti-parallel configurations: half of the magnetic moments are oriented in one direction, and half in the opposite one, resulting in no spontaneous magnetization. An example of anti-ferromagnetic ordering is schematized in figure 2.1(b). In some cases, magnetic moments pointing in one direction do not have the same magnitude as those pointing in the opposite direction, resulting in a spontaneous magnetization even if the exchange interactions are anti-ferromagnetic. Materials that present this characteristic are classified as ferrimagnetic. This type of magnetic ordering may be seen as formed by two ferromagnetic sub-lattices of different magnetization which are anti-ferromagnetically coupled (see figure 2.1(c)). We will deeply talk about ferrimagnetic materials throughout this thesis, as one of the studied systems belongs to this group.

The kinds of magnetism that we have mentioned so far do not represent at all the complete set of magnetic states and phases that we can encounter. There exists a huge variety of magnetic interactions that result in more complex structures. For example, anti-symmetric exchange interactions such as the so-called Dzyaloshinskii-Moriya interaction [55, 56] favor twisted configurations of magnetic spins [57]. Moreover, as none of the possible interactions between magnetic moments exist completely alone, their competition results in many different states which are subject of present discussions [58, 59]. In addition, the fabrication of new materials continuously gives rise to previously unknown magnetic states.

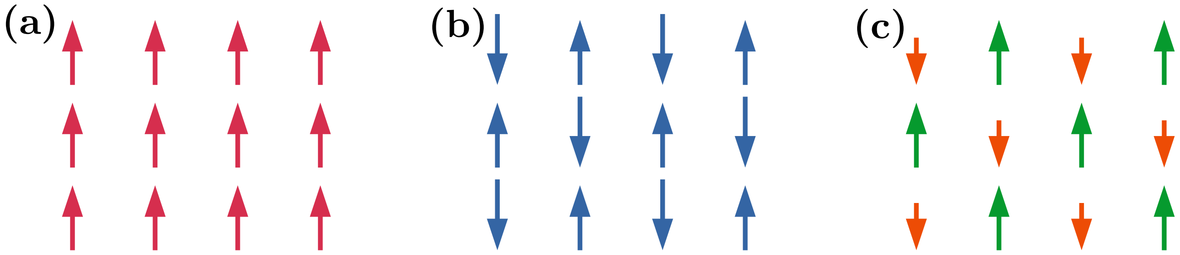

Figure 2.1: **Ferromagnetic, anti-ferromagnetic and ferrimagnetic configurations.** Schematic illustration of the magnetic ordering in (a) a ferromagnetic configuration, where all spins are parallel, (b) an anti-ferromagnetic configuration, in which adjacent spins are anti-parallel, resulting in a zero global magnetization, and (c) a ferrimagnetic configuration, in which adjacent spins are anti-parallel but, as the magnitudes of magnetic moments in each of the two sublattices are different, global magnetization is finite.

2.1.2 Magnetic energies

The variety of magnetic configurations that materials can experience result from the competition between different involved magnetic energies. These energy terms arise from interactions within the material or in its surfaces, or from the response to external stimulus as, for example, magnetic or electric field, strain, and temperature. In the following, we will briefly describe the main contributions to magnetic energy that are fundamental for the study of domains and domain walls in magnetized thin films.

Zeeman energy

A magnetic moment $\vec{\mu}$ is subject to a torque when a magnetic field $\vec{H}_a$ is applied. The energy of this interaction between field and moment is the Zeeman energy, and it is minimum when $\vec{H}_a$ and $\vec{\mu}$ are aligned. For a point magnetic moment in a space where $\vec{H}_a$ is applied [60],

$$E_Z = -\mu_0 \vec{H}_a \cdot \vec{\mu} \ , \tag{2.1}$$

where $\mu_0 = 4\pi \times 10^{-7}\,\mathrm{H/m}$ is the magnetic permeability of vacuum.

For an extended, continuous, magnetic material, we shall integrate over its volume, taking into account that the magnetic moment of an infinitesimal volume dV is $\vec{M}dV$, where $\vec{M}$ is the local magnetization. The Zeeman energy for a volume V immersed in a space where $\vec{H}_a$ is applied is then

$$E_Z = -\mu_0 \int_V \vec{H}_a \cdot \vec{M} dV \ . \tag{2.2}$$

Exchange energy

As we have mentioned above, magnetism of materials is originated mainly by the intrinsic spin of electrons. The intense spontaneous magnetization that arises in ferromagnetic materials is originated by the exchange interaction between electron spins, which is explained by the Pauli exclusion principle [53].

In an array of spins $\vec{S}_i$ interacting between pairs $\left(\vec{S}_i, \vec{S}_j\right)$ with interaction energies J_{ij}, the exchange energy is expressed by the Heisenberg Hamiltonian [54]

$$\mathcal{H} = -\sum_{i \neq j} J_{ij}\, \vec{S}_i \cdot \vec{S}_j \ . \tag{2.3}$$

If J_{ij} is positive, then the interaction between spins i and j will favor the parallel, ferromagnetic, orientation of these two spins. If J_{ij} is negative, the interactions will favor an anti-parallel, anti-ferromagnetic, orientation.

In a micromagnetic approach [1, 2], we consider that a magnetic material is a continuous medium with magnetization of uniform magnitude $|\vec{M}| = M_s$, where M_s is the saturation magnetization. In this context, the strength of the exchange interaction is quantified by the exchange stiffness A. For a ferromagnetic material, the exchange energy is lowest if magnetization direction is uniform and grows in regions where uniformity is not satisfied. The total exchange energy in a volume V of a magnetic material can be expressed as [2]

$$E_{ex} = \int_V A \left[(\nabla m_x)^2 + (\nabla m_y)^2 + (\nabla m_z)^2 \right] dV \ , \tag{2.4}$$

where $(m_x, m_y, m_z) = \vec{M}/M_s$. In this last expression, $\vec{m} = (m_x, m_y, m_z)$ is a unit vector, i.e. $|\vec{m}| = 1$.

The exchange interaction that we have just discussed, which favors uniform magnetic structures, is a symmetric interaction: its magnitude depends only on the absolute value of the angle between interacting spins and on a scalar quantity J_{ij} (see equation (2.3)). A higher order, antisymmetric exchange term playing an important role in the physics of magnetic thin films is the so-called Dzyaloshinskii-Moriya interaction (DMI) [55, 56]. This energy term is present in systems with low symmetry and favors not-uniform, chiral magnetic configurations [57, 59]. It can be expressed microscopically as [56]

$$E_{\mathrm{DMI}} = -\sum_{i<j} \vec{D}_{ij} \cdot \left(\vec{S}_i \times \vec{S}_j \right) \ , \tag{2.5}$$

where $\vec{D}_{ij}$ is an interaction vector whose magnitude is nonzero only if the magnetic system presents a broken spatial symmetry. The direction of $\vec{D}_{ij}$ depends on the symmetry properties of the system.

The Dzyaloshinskii-Moriya interaction is usually relevant in magnetic thin films with lack of inversion symmetry [57, 61, 62]. This affects strongly the internal structure and the behavior of magnetic domain walls under a driving force [63–66] and therefore has to be considered in the study of their dynamics and morphology.

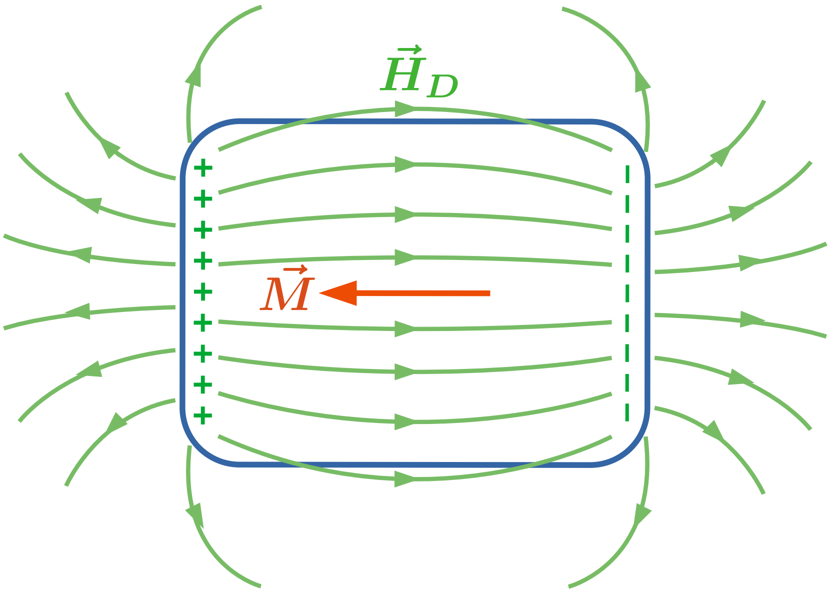

Figure 2.2: **Demagnetizing field in a uniformly magnetized material.** Schematic representation of a material with magnetization $\vec{M}$ which generates a demagnetizing field $\vec{H}_D$ due to the accumulation of magnetic charges in the two extremes, illustrated with signs $+$ and $-$.

Dipolar energy

The magnetization $\vec{M}$ in a magnetized sample generates itself a magnetic field $\vec{H}_D$, both outside (the so-called stray field) and inside the material (demagnetizing field). In an uniformly magnetized material the demagnetizing field is opposite to the magnetization and arises due to the accumulation of effective magnetic charges in the borders, as shown in figure 2.2.

The presence of a demagnetizing field and its Zeeman interaction with magnetization tends to prevent the existence of uniformly magnetized regions. The energy of this interaction is

$$E_D = -\frac{\mu_0}{2} \int_V \vec{H}_D \cdot \vec{M} dV \ , \tag{2.6}$$

where the factor 1/2 arises due to the fact that the field $\vec{H}_D$ is generated by $\vec{M}$ itself [6], and integration is performed in the volume of the magnetized sample.

The demagnetizing field magnitude and its distribution in space depends strongly in the shape of the magnetized volume. For example, if the effective negative and positive magnetic charges are relatively close to each other, its magnitude will be bigger, what favors the orientation of magnetization in the direction of the longest axis of a magnetic sample. This gives rise to the concept of shape anisotropy that we will discuss below.

For an ellipsoidal material uniformly magnetized in the direction of one of its axes, $\vec{H}_D$ is uniform [6]. In this context, we can easily calculate the magnetic dipolar energy. For a sphere, the demagnetizing field is $\vec{H}_D = -\vec{M}/3 = -(M_s/3)\vec{m}$. For an infinitely thin film, $\vec{H}_D = -\vec{M}\cos\theta$, where θ is the angle between $\vec{M}$ and the film's normal. Then, if $\vec{M}$ is out-of-plane, $\vec{H}_D = -\vec{M}$ and

$$E_D = \frac{\mu_0}{2} M_s^2 V \ , \tag{2.7}$$

where V is the total volume of the film. If $\vec{M}$ is in-plane, $H_D = 0$ and $E_D = 0$. Consequently, dipolar energy E_D favors an in-plane magnetization, as it is minimum if magnetization lies in the plane of the thin film, and maximum if it points normal to it. Similarly, for an infinitely long wire, $\vec{H}_D = -(\vec{M}/2)\sin\theta$, where θ is the angle between $\vec{M}$ and the wire. Then, dipolar energy E_D favors a magnetization orientation parallel to the wire. Later in this chapter, in sections 2.1.3 and 2.2.1, we shall recall these concepts for the energetical analysis of domain walls in thin films.

Anisotropy energy

The shape-dependent dipolar energy that we have just mentioned is an example of magnetic anisotropy called shape anisotropy. Generally, magnetic anisotropies consist on the existence of "easy" and "hard" directions for the magnetization. If the anisotropy is uniaxial, i.e. if the associated energy E_K can be expressed as a function of the angle between $\vec{M}$ and one particular direction, then we can write

$$E_K = \int_V K_u \sin^2\theta \, dV \ , \tag{2.8}$$

where K_u is the anisotropy energy per unit volume and θ is the angle between $\vec{M}$ and the anisotropy axis $\hat{k}$. If $K_u > 0$, then $\hat{k}$ is an easy axis. If $K_u < 0$, then $\hat{k}$ is a hard axis and $\vec{M}$ will tend to lie in the plane which is perpendicular to $\hat{k}$.

There are several possible origins of magnetic anisotropy, besides the shape dependent anisotropy that we have already discussed. Some examples are the crystallographic and surface properties, which may generate magnetic anisotropies due to mechanisms such as spin-orbit coupling and orbital hybridization [28, 52, 67].

The magnetic thin films that we study in this thesis present an out-of-plane magnetic anisotropy, this is $K_u > 0$ with $\hat{k} = \hat{z}$, where $\hat{z}$ is the film's normal direction. In the studied samples, this mechanism overcomes the shape anisotropy and therefore $\hat{z}$ is the effective easy axis [28, 68, 69]. In this context, the effective uniaxial anisotropy K_{eff} results from a competition between the energies corresponding to the out-of-plane anisotropy K_u and the dipolar energy corresponding to the thin film, given by equation (2.7), which favors an in-plane magnetization. Consequently, we may write

$$K_{\text{eff}} = K_u - \mu_0 M_s^2/2 \ , \tag{2.9}$$

with $K_u > \mu_0 M_s^2/2$ and therefore $K_{\text{eff}} > 0$.

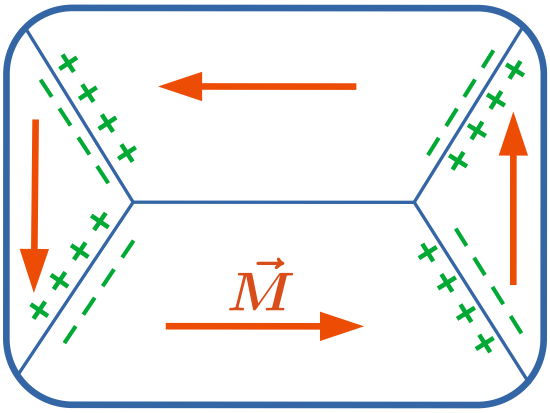

Figure 2.3: **Magnetic domains structure minimizing dipolar energy.** In this example, four uniformly magnetized regions are formed, resulting on zero global magnetization. Magnetic charges in the borders of domains are balanced and thus the demagnetizing field is minimum.

2.1.3 Magnetic domains and domain walls

The presence of different contributions to the total energy discussed above induces magnetic systems to adopt suitable configurations in order to minimize the total energy. In the following we will discuss how the competition between symmetric exchange, expressed by equation (2.4), and the magnetic dipolar energy, equation (2.6), leads to the formation of magnetic domains, i.e. to the appearance of several uniformly magnetized regions within a material.

Let us consider a uniformly magnetized sample, as it was shown in figure 2.2. Shape anisotropy induces magnetization to point in the sample's longest direction, and exchange energy favors the uniform magnetization. However, dipolar energy is considerable as unbalanced magnetic charges appear on the extremes, generating a demagnetizing field $\vec{H}_D$. This relevant energy contribution is significantly reduced if different regions of uniform magnetization are formed within the sample, as illustrated in figure 2.3. In this configuration, the sample's global magnetization is zero, what results in a minimum stray field. Magnetic charges are balanced in the borders of uniformly magnetized regions and thus the demagnetizing field is minimum.

Regions of uniform magnetization illustrated in figure 2.3 are the so-called magnetic domains, and the limiting surfaces between these regions are called domain walls. Magnetic domains may adopt a huge variety of shapes, according to the sample's geometry and to the role of all the mentioned magnetic energies [1, 2]. The internal structure of magnetic domain walls is also very rich, as they constitute regions in which magnetization is not uniform, changing rapidly as a function of position between configurations of adjacent domains. For

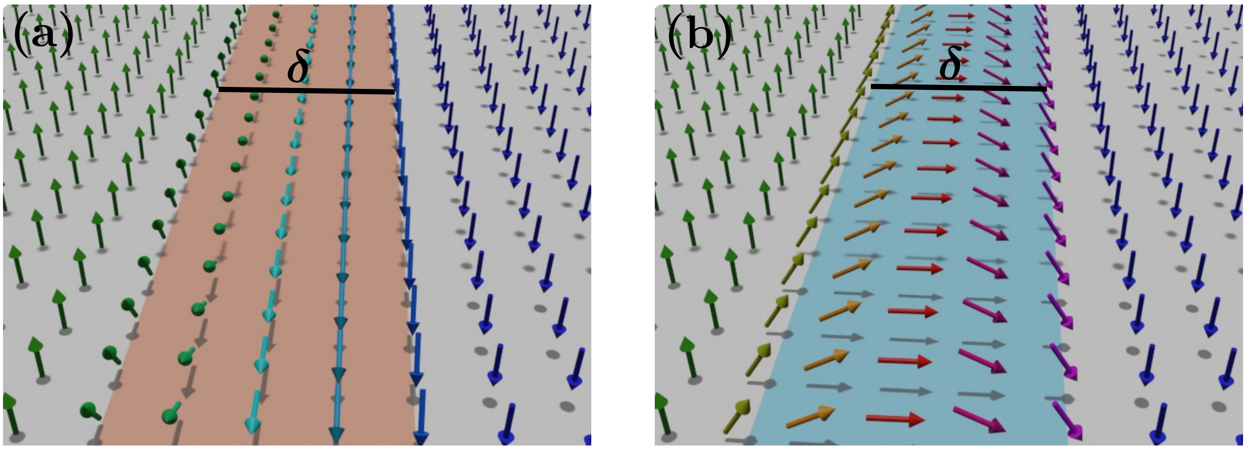

Figure 2.4: **Bloch and Néel Walls in a thin film with perpendicular anisotropy.** Schematic representation of the internal magnetization in (a) a Bloch wall and (b) a Néel wall. The region corresponding to the domain wall is indicated in both cases as a shaded area of width δ.

this reason, domain walls have an associated energetic cost corresponding both to exchange energy, equation (2.4), and anisotropy energy, equation (2.8).

Let us now consider the case of a magnetic thin film with perpendicular anisotropy, i.e. where magnetization points out of the sample's plane. As pointed out above, dipolar energy is reduced if several magnetic domains are formed. Their magnetization, due to the perpendicular magnetic anisotropy, may point "up" or "down" with respect to the sample's plane. In this context, magnetic domain walls are formed between these two types of domains. When crossing a domain wall, magnetization will progressively rotate in space. We may mention two particular ways in which this transition can occur, which are illustrated in figure 2.4. These two particular cases are the so-called Bloch and Néel walls.

The straight domain walls illustrated in figure 2.4 may be seen as vertical planes of width δ which separate the two adjacent domains. Within Bloch domain walls (fig. 2.4(a)), magnetization turns parallel to the plane of the domain wall when crossing from "up" to "down". In a Néel domain wall, in contrast, magnetization rotates in a plane which is perpendicular to the domain wall (fig. 2.4(b)).

In order to analyze the plausibility of each of these two particular domain wall configurations for a perpendicularly magnetized thin film, let us make some energetic considerations. The domain wall can be seen as a region of in-plane magnetization which has a length L, a height equal to the film thickness t and a width δ which corresponds to the distance in which magnetization turns between uniform configurations of the two domains, with $L \gg t$ and $L \gg \delta$ [70]. Consequently, shape anisotropy of the domain wall will favor a configuration in which its internal magnetization points along its long direction, i.e. it will favor a Bloch configuration. On the contrary, Néel configurations are not favored by the dipolar energy as magnetic charges are accumulated in both sides of the domain wall. However, evidences of the existence of Néel domain walls in magnetic thin films have been reported in many systems [63–65, 71, 72]. These observations are explained by the existence of relevant Dzyaloshinskii-Moriya interactions, which favor Néel domain walls of defined chirality affecting both their static and dynamic properties [66, 73].

We have just presented the concept of magnetic domain walls and discussed their basic static properties. In the following section, we will discuss in more detail the micromagnetic theory of domain walls. We shall start by presenting an analytical study on their internal structure which will permit us to quantify the domain wall energy and width. Afterwards, we shall thoroughly analyze the domain wall dynamics under the action of an external force in the framework of a simple micromagnetic model, which does not take into account the action of pinning and temperature.

2.2 Micromagnetism of domain walls

In this section, we will consider the case of a planar domain wall in a continuous medium of saturation magnetization M_s and effective uniaxial anisotropy K_{eff} in the $\hat{z}$ direction. We start by discussing the domain wall magnetization profile in a static situation. Afterwards, we shall present and discuss the dynamics of this domain wall when subject to an external driving force.

2.2.1 Domain wall static profile

Let us consider a domain wall which is centered at $y = 0$ (in the xz plane), separating the space in two semi-infinite regions, $y > 0$ and $y < 0$. Within the domain wall, magnetization $\vec{M}$ turns as a function of y, from $\vec{M} = +M_s\,\hat{z}$ to $\vec{M} = -M_s\,\hat{z}$ in a characteristic length δ that corresponds to the domain wall width. We will therefore describe the domain wall magnetization profile through a one-dimensional model, as a function of the coordinate y. As $|\vec{M}| = M_s$, we are only interested on the polar coordinates (θ, ϕ), defined relative to the z axis as shown in figure 2.5(a).

The local energy per unit volume of the one-dimensional domain wall may be written as the sum of the local exchange energy and the local anisotropy energy (see equations (2.4) and (2.8)), in the following way [2]

$$w = w_A + w_K = A\left[\left(\frac{\partial \theta}{\partial y}\right)^2 + \left(\sin\theta\,\frac{\partial \phi}{\partial y}\right)^2\right] + K_{\text{eff}}\sin^2\theta\ . \tag{2.10}$$

In order to find an analytical, static solution for $\theta(y)$ and $\phi(y)$, it is necessary to consider the condition of static equilibrium in which torques are zero or, equivalently, $\int w\,dy$ is stationary.

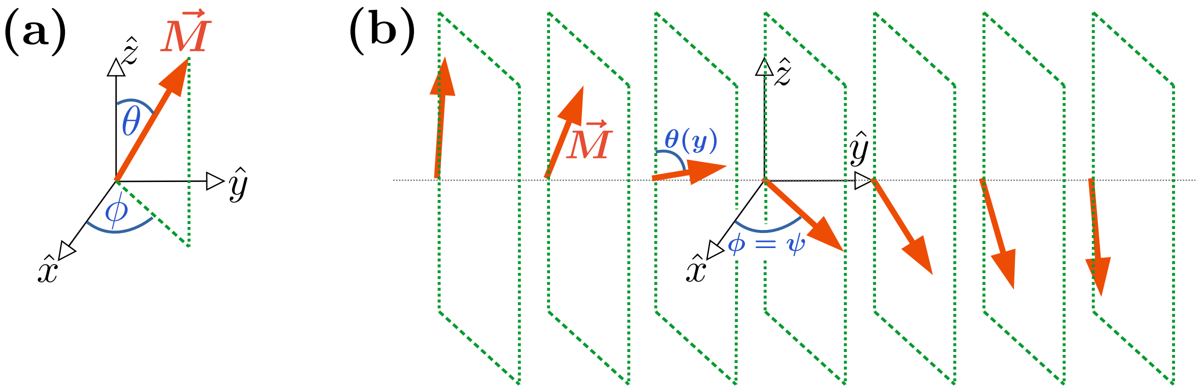

Figure 2.5: **Static profile of a one-dimensional domain wall.** (a) Polar coordinates (θ, ϕ), relative to the uniaxial anisotropy axis $\hat{z}$, for describing the magnetization direction. (b) Domain wall profile as a function of y in the one-dimensional model. The plane formed by $\vec{M}$ and $\hat{z}$ is fixed and therefore $\phi = \psi$ where ψ is a constant. The angle θ varies from 0 to π as a function of y according to equation (2.12).

The resulting analytical solution is [2]

$$\phi(y) = \psi = \text{constant} \tag{2.11}$$
$$\theta(y) = 2\arctan\left[\exp(y/\Delta)\right] , \tag{2.12}$$

where

$$\Delta = \sqrt{A/K_{\text{eff}}} \tag{2.13}$$

is the wall width parameter. This result is shown schematically in figure 2.5(b). Note that, as $\phi(y) = \psi$ is a constant, magnetization rotates as a function of y in a vertical plane defined by ψ. If $\psi = 0$, π, the magnetization profile corresponds to a Bloch domain wall, while $\psi = \pi/2$, $3\pi/2$ corresponds to a Néel domain wall.

The analytical solution for $\theta(y)$ is plotted in figure 2.6(a). The z component of the magnetization, which may be calculated as

$$M_z(y) = M_s \cos\theta(y) , \tag{2.14}$$

is plotted in figure 2.6(b). Note that the actual domain wall width in which most of the magnetization rotation occurs is $\delta = \pi\Delta$. The fact that $\delta \sim \sqrt{A/K_{\text{eff}}}$ is consistent with the observation that exchange favors a gradual turn on magnetization, as it pushes for parallel orientations of adjacent spins, while uniaxial anisotropy favors a rapid turn, as it induces spins to point in the $\hat{z}$ direction.

We finally may obtain the total anisotropy and exchange energy of the domain wall substituting equations (2.11) and (2.12) in equation (2.10) and integrating in all space. The resulting total energy per unit area is [2]

$$\sigma_0 = 4\sqrt{AK_{\text{eff}}} . \tag{2.15}$$

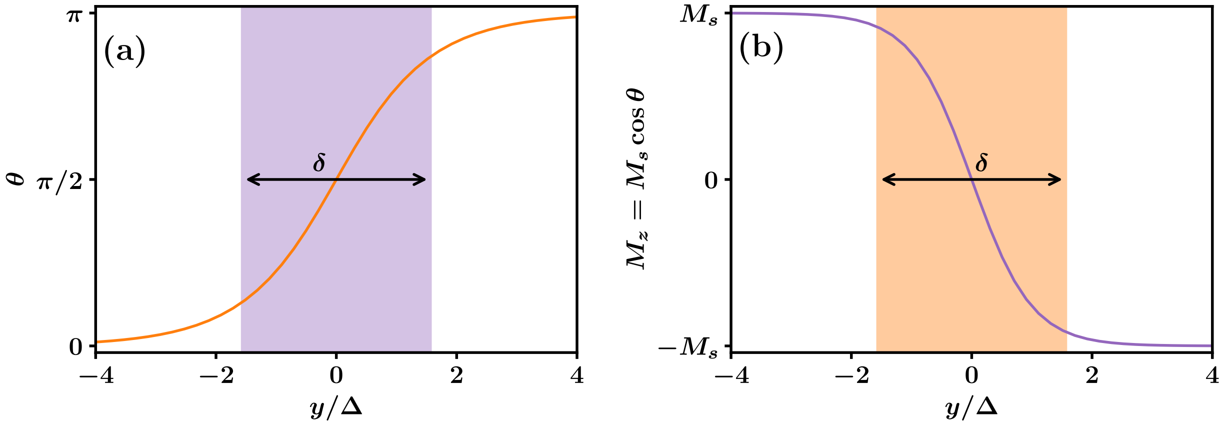

Figure 2.6: **Analytical solution for the static profile of a one-dimensional domain wall.** (a) θ (equation (2.12)) and (b) M_z (equation (2.14)) as a function of y in units of the wall width parameter Δ. The actual domain wall width $\delta = \pi\Delta$ in which most of the magnetization rotation occurs is indicated.

This shows that the existence of domain walls constitutes an energy cost both for the exchange and the anisotropy energies. As mentioned above, this energy cost is usually convenient, as it is compensated by a decrease on the dipolar contribution which may result in a lower total energy. We may alternatively write, using (2.13) and (2.15),

$$\sigma_0 = 4\Delta K_{\text{eff}} \; . \tag{2.16}$$

Equation (2.10) only considers uniaxial anisotropy and exchange energy. In order to account for the magnetostatic energy of the domain wall, which arises from the demagnetizing field generated by the domain wall itself, we shall add a term [2]

$$w_D = \frac{\mu_0}{2} M_s^2 \sin^2\phi \sin^2\theta \; . \tag{2.17}$$

This term evidences that, if no other energy terms are relevant, the equilibrium static domain wall profile corresponds to a Bloch domain wall, in which $\phi(y) = \psi = 0,\ \pi$, resulting on $w_D = 0$. The total domain wall energy σ_0 given by (2.15) is thus the energy per unit area of a one-dimensional Bloch domain wall.

In the following, we will discuss how a magnetic domain wall reacts under an applied magnetic field, in the context of the one-dimensional model. We shall start by presenting the Landau-Lifshitz-Gilbert equation for magnetization dynamics, which is the basis of the micromagnetic approach to domain wall dynamics theory.

2.2.2 Landau-Lifshitz-Gilbert equation

As magnetization is associated to an angular momentum, its dynamics under an applied field may be approached taking as a starting point the fundamental mechanical law for an

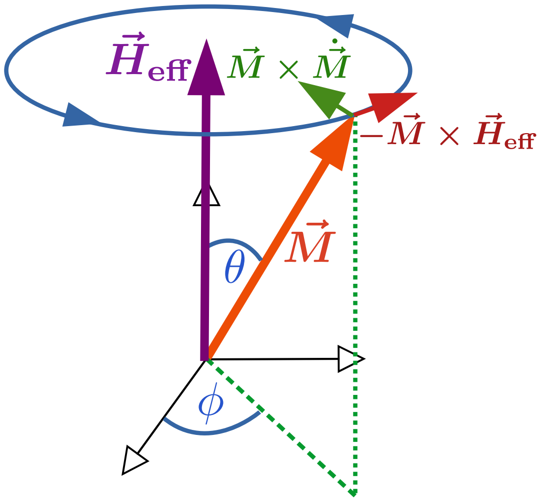

Figure 2.7: **Schematic representation of magnetization dynamics according to the Landau-Lifshitz-Gilbert equation.** Magnetization $\vec{M}$ precesses under an effective field $\vec{H}_{\text{eff}}$ according to the term $-\mu_0\gamma\vec{M} \times \vec{H}_{\text{eff}}$. Meanwhile, dissipative effects given by the term $(\alpha/M_s)\vec{M} \times \dot{\vec{M}}$ induce magnetization to progressively align with $\vec{H}_{\text{eff}}$, approaching a lower energy configuration.

angular momentum $\vec{L}$ under an applied torque $\vec{\tau}$, $\dot{\vec{L}} = \vec{\tau}$. A volume of magnetic moment $\vec{\mu}$ has an associated angular momentum[1] which may be written as $\vec{L} = -\vec{\mu}/\gamma$, where γ is the gyromagnetic ratio [2]. Therefore,

$$-\dot{\vec{\mu}}/\gamma = \vec{\tau}\ . \tag{2.18}$$

The torque $\vec{\tau}$ may be separated on conservative and dissipative terms [2]. The conservative one is $\mu_0\vec{\mu} \times \vec{H}_{\text{eff}}$, where $\vec{H}_{\text{eff}}$ is an effective field resulting from the applied field, magnetic anisotropy, exchange stiffness, demagnetizing field, etc. The dissipative term, the so-called damping torque, may be written as $-\alpha\vec{\mu} \times \dot{\vec{\mu}}/\gamma|\vec{\mu}|$, where α is the Gilbert damping parameter [74]. This term is a phenomelological representation of dissipative effects [2]. As magnetization $\vec{M}$ is the magnetic moment per unit volume, we can re-write these equations in terms of $\vec{M}$. The resulting equation for the dynamics of magnetization $\vec{M}$ is the Landau-Lifshitz-Gilbert equation [74, 75], which may be written as

$$\dot{\vec{M}} = -\mu_0\gamma\vec{M} \times \vec{H}_{\text{eff}} + \frac{\alpha}{M_s}\vec{M} \times \dot{\vec{M}}\ . \tag{2.19}$$

Let us now discuss the physical meaning of this equation. If no effective field $\vec{H}_{\text{eff}}$ exists, or if it is parallel to $\vec{M}$, then $\vec{M} \times \vec{H}_{\text{eff}} = 0$. In this case, the equation is satisfied for

---

[1] This angular momentum of electrons is mainly originated on their spin, with corrections due to orbital motion [2].

$\dot{\vec{M}} = 0$, i.e. no dynamics is induced. On the contrary, if there exists a finite component of $\vec{H}_{\text{eff}}$ perpendicular to $\vec{M}$, the term $-\mu_0\gamma\vec{M} \times \vec{H}_{\text{eff}} \neq 0$ induces a precession of magnetization around $\vec{H}_{\text{eff}}$, as indicated in figure 2.7. This precession corresponds to a component of $\dot{\vec{M}}$ which is perpendicular to $\vec{M}$ and $\vec{H}_{\text{eff}}$. The induced dynamics results in a non-zero dissipative component $(\alpha/M_s)\vec{M} \times \dot{\vec{M}}$ which prompts magnetization to align with $\vec{H}_{\text{eff}}$ while it precesses (see figure 2.7). The resulting trajectory of magnetization is spiral-like, finally arriving to a static situation when $\vec{M}$ aligns with $\vec{H}_{\text{eff}}$. This corresponds to the configuration of lowest energy, as $E_Z \sim -\vec{M} \cdot \vec{H}_{\text{eff}}$ (see equation (2.2)). The magnitude of $\vec{H}_{\text{eff}}$ controls the velocity of precession, while the magnitude of α determines how rapidly dissipation will take place until reaching the lowest energy configuration.

Landau-Lifshitz-Gilbert equation is the basis of magnetization reversal and domain wall dynamics theory. Furthermore, the understanding of mechanisms of precession and damping are crucial both from the fundamental and applied points of view [2, 11, 12, 76]. In the following, we will present the main concepts of the domain wall dynamics theory in the one-dimensional model.

2.2.3 1D model for field-driven domain wall dynamics

In order to start our discussion on the problem of domain wall motion, we present in this section the so-called q-ϕ model. This model takes as starting point the domain wall profile expressed by equations (2.11) and (2.12), now considering that the azimuthal angle is a function of time $\phi(t)$ while

$$\theta(y,t) = 2\arctan\left[\exp\left((y - q(t))/\Delta\right)\right] , \tag{2.20}$$

where $q(t)$ is a displacement parameter indicating the position of the wall center in the y direction, normal to the domain wall. This equation considers that the $\theta(y)$ profile, which is plotted in figure 2.6(a), is static with respect to the position $q(t)$. In other words, domain wall moves with a rigid $\theta(y)$ profile[2]. Assuming this domain wall profile and integrating Landau-Lifshitz-Gilbert equation (2.19) for the coordinates $(\theta(y,t), \phi(t))$ over the wall thickness, it is possible to describe domain wall dynamics in terms of only two parameters, $q(t)$ and $\phi(t)$. Two fundamental differential equations for the partial derivatives of the domain wall energy per unit area σ with respect to q and ϕ are obtained [2]:

$$\frac{\partial\sigma}{\partial q} = -\frac{2M_s}{\gamma}\left(\dot{\phi} + \frac{\alpha}{\Delta}\dot{q}\right) , \tag{2.21}$$

which accounts for the "pressure" over the domain wall that induces its normal displacement given by q, and

$$\frac{\partial\sigma}{\partial\phi} = \frac{2M_s}{\gamma}\left(\dot{q} - \alpha\Delta\dot{\phi}\right) , \tag{2.22}$$

---

[2] This approximation is valid whenever the domain wall structure is primarily determined by anisotropy and exchange forces [2]. A correction to this rigid structure that takes into account domain wall dipolar energy may be made by considering that the domain wall width parameter depends on the wall's internal magnetization and is given by $\Delta(\phi) = \sqrt{A/(K_{\text{eff}} + (\mu_0 M_s^2/2)\sin^2\phi)}$ [77].

which corresponds to the torque over the in-plane domain wall magnetization given by ϕ.

In order to evaluate equation (2.21), we consider that the pressure over the domain wall is given by an applied field of magnitude H_a in the $\hat{z}$ direction. If $H_a > 0$, this field energetically favors the left side domain (see figure 2.5) destabilizing the wall from its static equilibrium. In this context, in accordance with (2.2), the rate of energy change with respect to the domain wall position due to the complete inversion of magnetization is $\partial\sigma/\partial q = -2M_s\mu_0 H_a$ [2], and then

$$\dot{\phi} = \gamma\mu_0 H_a - \frac{\alpha}{\Delta}\dot{q} \ . \tag{2.23}$$

This equation shows that the applied field induces the wall magnetization to precess in its plane at a velocity equal to $\gamma\mu_0 H_a$. The term $(\alpha/\Delta)\dot{q}$ arises due to the damping term of Landau-Lifshitz-Gilbert equation (2.19).

In order to evaluate equation (2.22), we may consider the following expression for the wall energy σ, obtained by integrating the local anisotropy, exchange and dipolar energies given by equations (2.10) and (2.17):

$$\sigma = \sigma_0 + \mu_0 M_s^2 \Delta \sin^2\phi \ , \tag{2.24}$$

where σ_0 is the Bloch domain wall energy given by (2.15). We thus find that $\partial\sigma/\partial\phi = \mu_0 M_s^2 \Delta \sin(2\phi)$, and then

$$\frac{1}{\Delta}\dot{q} = \frac{\gamma}{2}\mu_0 M_s \sin(2\phi) + \alpha\dot{\phi} \ . \tag{2.25}$$

This equation shows that wall motion, given by the velocity $\dot{q}$, is induced by a torque over the wall magnetization. The conservative term, proportional to $M_s \sin(2\phi)$, corresponds to the torque induced by the wall's dipolar field, while the dissipative contribution, proportional to $\alpha\dot{\phi}$, arises from a damping torque [2].

Solving equations (2.23) and (2.25) permits to obtain predictions for the domain wall velocity $\dot{q}$ vs. applied field H_a dependence, in the framework of the micromagnetic one-dimensional model. In the following we will present the solutions of these equations.

Steady regime

Let us first consider solutions of equations (2.23) and (2.25) for $\dot{\phi} = 0$, i.e. for a stationary in-plane magnetization of the domain wall. In this case,

$$\dot{q} = \frac{\gamma\Delta}{\alpha}\mu_0 H_a \tag{2.26}$$

and

$$\sin(2\phi) = \frac{2H_a}{\alpha M_s} \ . \tag{2.27}$$

These two equations correspond to the so-called steady regime of domain wall motion in which, for a fixed applied field H_a, internal magnetization presents a stationary configuration given by (2.27) while domain wall velocity is proportional to $\mu_0 H_a$, as indicated by (2.26). The proportionality factor is the steady state domain wall mobility, given by

$$m_{st} = \frac{\gamma\Delta}{\alpha} \ . \tag{2.28}$$

Walker breakdown

If $2H_a > \alpha M_s$, the solution expressed by equation (2.27) does not stand, meaning that there is no solution for $\dot{\phi} = 0$. The highest stationary ϕ value is $\phi_c = \pi/4$, at a critical field

$$H_w = \frac{\alpha M_s}{2} \tag{2.29}$$

for which the steady motion loses its stability, called the Walker field [78]. The transition from the steady state of $\dot{\phi} = 0$ to the regime of $\dot{\phi} \neq 0$ is the so-called Walker breakdown.

For a domain wall in a system of reduced dimensions like a magnetic thin film, the Walker field needs to be corrected. This is due to its direct relationship with the demagnetizing field of the domain wall, strongly dependent on its dimensions. For a domain wall in a magnetic thin film of thickness t [79],

$$H_w = \frac{\alpha M_s}{2}\frac{t}{t+\Delta} \ . \tag{2.30}$$

This correction to the Walker field is relevant only if t is sufficiently small to be comparable with Δ, and evidences that the Walker breakdown takes place at a lower field for systems of reduced thickness.

Precessional regime

For $H_a > H_w$, solutions of equations (2.23) and (2.25) correspond to $\dot{\phi} \neq 0$. The general solution for ϕ may be obtained by integrating the differential equation

$$\dot{\phi}(t) = \frac{1}{1+\alpha^2}\left[\gamma\mu_0 H_a - \frac{\alpha\gamma}{2}\mu_0 M_s \sin\left(2\phi(t)\right)\right] \ . \tag{2.31}$$

This equation shows that for $H_a > H_w$ the wall's internal magnetization precesses at a non-uniform velocity $\dot{\phi}(t) > 0$. This state is therefore called the precessional regime of domain wall motion.

As for a fixed H_a, $\dot{\phi}(t)$ is not stationary, $\dot{q}(t)$ is not stationary either. The mean domain wall velocity v is obtained by integrating $\dot{q}(t)$ in a period of precession of the wall's internal magnetization,

$$v \equiv \langle \dot{q}(t) \rangle = \frac{\gamma\Delta}{\alpha}\mu_0 H_a - \frac{\Delta}{\alpha}\left\langle \dot{\phi}(t) \right\rangle \ . \tag{2.32}$$

For the limit of a very big driving force, i.e. for $H_a \gg H_w$, we may find an asymptotical solution given by

$$\dot{\phi} = \frac{1}{1+\alpha^2}\gamma\mu_0 H_a \ , \tag{2.33}$$

where we have neglected the term $(\alpha\gamma/2)\mu_0 M_s \sin(2\phi(t))$ with respect to $\gamma\mu_0 H_a$ in equation (2.31). Consequently, we obtain for the domain wall velocity

$$v = \dot{q} = \frac{\alpha^2}{1+\alpha^2}\frac{\gamma\Delta}{\alpha}\mu_0 H_a \ . \tag{2.34}$$

In this asymptotical precessional regime, $\dot{\phi}$ tends to a stationary value and v is proportional to $\mu_0 H_a$, with a proportionality factor

$$m_{asp} = \frac{\alpha^2}{1+\alpha^2} m_{st} \ . \tag{2.35}$$

As $\alpha^2/(1+\alpha^2) < 1$, domain wall mobility is maximum in the steady regime and drops from m_{st} to m_{asp} as the applied field increases above H_w. This fact is very important for technological applications, as it shows that the most efficient domain wall motion is achieved only for $H_a < H_w$.

In figure 2.8(a), we summarize the result for the velocity vs. applied field dependence in the framework of the one-dimensional q-ϕ model. The steady state of highest mobility is evidenced for $H_a < H_w$. Above the Walker breakdown, the mean velocity v drops abruptly due to the precession of domain wall's internal magnetization, tending asymptotically to a new linear dependence of lower mobility. Additionally, units are normalized in terms of γ, Δ and H_w. Therefore, the only variable controlling the curve shape is the Gilbert damping parameter which in this case is $\alpha = 0.4$. As indicated in the figure, α controls the relation between the steady state and the asymptotical precessional state mobilities.

The results that we have just presented are the basis of field-driven domain wall dynamics. As we will see throughout this thesis, behavior changes considerably when disorder and temperature are relevant and therefore, experimental domain wall velocity vs. applied field curves are generally different from the curve shown in figure 2.8(a). However, the Walker breakdown is experimentally observed in a variety of systems. In figure 2.8(b), we show an example of a clear observation of this phenomena in a ferromagnetic nanowire of Ta(3 nm)/Py(20 nm)/Ta(5 nm) with in-plane magnetic anisotropy [80]. The first observation of the Walker breakdown in thin films with perpendicular anisotropy was made by A. Dourlat and collaborators in 2008 [81]. The studied system in that case was the diluted ferromagnetic semiconductor (Ga,Mn)As, very similar to one of the systems studied in this thesis (see section 2.5.2).

In the following, we will discuss how the q-ϕ model is modified when domain wall motion is driven by both an applied field and a spin-polarized current via the spin-transfer torque (STT) mechanism. This is an important issue in the framework of this thesis, as in chapter 6 we present our studies on simultaneous field- and STT-driven domain wall motion in (Ga,Mn)(As,P)/(Ga,Mn)As.

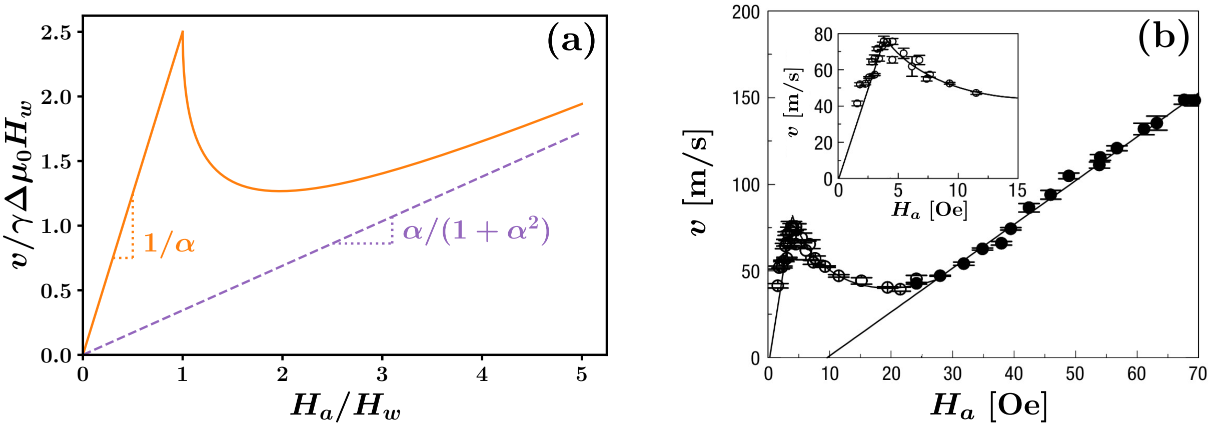

Figure 2.8: **Velocity vs. field dependence and Walker breakdown of a one-dimensional domain wall.** (a) We plot v vs. H_a in normalized units, for $\alpha = 0.4$. Below the Walker breakdown, for $H_a < H_w$, the domain wall moves in the steady state with $v/\gamma\Delta = \mu_0 H_a/\alpha$, reaching a velocity peak for $H_a = H_w$. For $H_a > H_w$, in the precessional regime, mobility drops and velocity tends asymptotically to $v/\gamma\Delta = \mu_0 H_a \alpha/(1+\alpha^2)$. (b) Experimental curve for a field-driven domain wall in a ferromagnetic nanowire of Ta(3 nm)/Py(20 nm)/Ta(5 nm), evidencing the Walker breakdown and the steady and precessional regimes. Adapted from [80].

2.2.4 Domain wall dynamics driven by field and current

An electrical current flowing through a magnetized material transports not only charge but also angular momentum, as the spin of flowing electrons is affected by the magnetized medium in which they move [82]. If these spin-polarized currents traverse a magnetic domain wall, they transfer angular momentum in a way that may be strong enough to produce domain wall motion [19, 20, 22, 23, 83], as confirmed in many laboratories [24–27, 84–86]. Furthermore, the spin-transfer phenomena is the operation basis of several devices as, for example, the spin-transfer torque magnetic random access memories (STT-MRAM) [11]. In the following, we will present how the Landau-Lifshitz-Gilbert equation and the q-ϕ model are modified when the torque on magnetization is generated not only by an applied field but also by spin-polarized currents.

Let us consider a spin-polarized charge current $\vec{J} = -J\hat{y}$ flowing in a one-dimensional domain wall, like the one illustrated in figure 2.5(b), where $J > 0$ and then electrons flow in the $+\hat{y}$ direction. The spin polarization of the current is $P = (n_\uparrow - n_\downarrow)/(n_\uparrow + n_\downarrow)$, where $n_\uparrow$ and $n_\downarrow$ are the number densities of electrons that are polarized in the directions parallel and anti-parallel to $\vec{M}$, respectively. The magnetic moment of each electron is $g\mu_B/2$, where g is the so-called g-factor and μ_B is the Bohr magneton. Consequently, the rate of spin transfer per unit area is $JPg\mu_B/2e$ in the $+\hat{y}$ direction. If we consider that a full and adiabatic transfer of angular momentum occurs, then the rate of change of magnetization due to the spin-transfer torque is [23]

$$\dot{\vec{M}}|_{STT} = -\frac{g\mu_B PJ}{2eM_s}\frac{\partial}{\partial y}\vec{M} \; . \tag{2.36}$$

However, this adiabatic term is not enough to account for experimental results in domain wall motion driven by spin transfer [23]. In 2004, S. Zhang and Z. Li [22] derived a new term for the spin-transfer torque without assuming adiabaticity which permitted to consistently interpret domain wall motion driven by spin-transfer torque. The Landau-Lifshitz-Gilbert equation (2.19) may be modified in order to account for both the adiabatic and the non-adiabatic terms of the spin-transfer torque in the following way [23]:

$$\dot{\vec{M}} = -\mu_0\gamma\vec{M}\times\vec{H}_{\text{eff}} + \frac{\alpha}{M_s}\vec{M}\times\dot{\vec{M}} - \left(\vec{u}\cdot\vec{\nabla}\right)\vec{M} + \frac{\beta_{\text{ST}}}{M_s}\vec{M}\times\left[\left(\vec{u}\cdot\vec{\nabla}\right)\vec{M}\right] \; , \tag{2.37}$$

where

$$\vec{u} = \frac{g\mu_B PJ}{2eM_s}\,\hat{y} \tag{2.38}$$

is the so-called spin-drift velocity. In equation (2.37), on the one hand, the term $-\left(\vec{u}\cdot\vec{\nabla}\right)\vec{M}$ is the generalization of equation (2.36), which corresponds to the adiabatic spin-transfer torque. On the other hand, the term $(\beta_{\text{ST}}/M_s)\,\vec{M}\times\left[\left(\vec{u}\cdot\vec{\nabla}\right)\vec{M}\right]$ corresponds to the non-adiabatic spin-transfer torque. The weight of this term is controlled by the parameter β_{ST}.

Based on equation (2.37) and following the same procedure that we described in 2.2.3, we may obtain equations for the domain wall velocity $\dot{q}$ and the azimuthal angle of the wall's internal magnetization ϕ, in the framework of the one-dimensional model. Then, the generalization of equations (2.23) and (2.25) for field- and STT-driven domain wall motion is [23]

$$\dot{\phi} + \frac{\alpha}{\Delta}\dot{q} = \gamma\mu_0 H_a + \frac{\beta_{\text{ST}}}{\Delta}u \; , \tag{2.39}$$

which is proportional to the pressure on the domain wall, $\partial\sigma/\partial q$, and

$$\frac{1}{\Delta}\dot{q} - \alpha\dot{\phi} = \frac{\gamma}{2}\mu_0 M_s \sin\left(2\phi\right) + \frac{1}{\Delta}u \; , \tag{2.40}$$

which is proportional to the torque on the domain wall magnetization, $\partial\sigma/\partial\phi$. These equations show that the non-adiabatic spin-transfer torque acts only as a pressure over the domain wall, while the adiabatic component acts only as a torque.

Steady regime

In the steady regime of domain wall motion, for $\dot{\phi} = 0$, we find

$$v = \dot{q} = \frac{\gamma\Delta}{\alpha}\mu_0 H_a + \frac{\beta_{\text{ST}}}{\alpha}u \; , \tag{2.41}$$

which may also be written as

$$v = m_{st}\left(\mu_0 H_a + \frac{\beta_{\mathrm{ST}}}{\gamma\Delta} u\right) \ , \tag{2.42}$$

where m_{st} is given by (2.28). This shows that, in the steady regime, the non-adiabatic spin-transfer torque acts as an effective contribution to the applied field of magnitude $(\beta_{\mathrm{ST}}/\gamma\Delta)\, u$. As in the field-driven case, in the steady regime the domain wall velocity is proportional to the driving force.

For the stationary value of the azimuthal angle of internal magnetization ϕ, we find

$$\sin(2\phi) = \frac{2}{\alpha M_s} H_a + \frac{2}{\gamma\Delta\mu_0 M_s}\frac{\beta_{\mathrm{ST}} - \alpha}{\alpha} u \ , \tag{2.43}$$

which shows that the applied current contributes to the tilting of the wall magnetization in the same direction as the applied field if $\beta_{\mathrm{ST}} > \alpha$, while it generates a negative tilting if $\beta_{\mathrm{ST}} < \alpha$. In other words, the non-adiabatic contribution generates a field-like torque over the internal magnetization, while the adiabatic spin-transfer acts over ϕ in the opposite way.

Walker breakdown

The condition for the Walker breakdown for field- and STT-driven domain wall motion corresponds to the limit in which the stationary solution for ϕ loses its stability, i.e. for $\sin(2\phi) = \pm 1$. This condition may then be written as

$$\pm\, \mu_0 H_w = \mu_0 H_a + \frac{\beta_{\mathrm{ST}} - \alpha}{\gamma\Delta} u \ , \tag{2.44}$$

where H_w is given by (2.29) (or (2.30) for a thin film).

Precessional regime

As discussed in 2.2.3, above the Walker breakdown ϕ precesses with a time-dependent velocity $\dot{\phi}(t)$, what results in a time-dependent $\dot{q}(t)$. This precessional regime occurs if

$$\left|\mu_0 H_a + \frac{\beta_{\mathrm{ST}} - \alpha}{\gamma\Delta} u\right| > \mu_0 H_w . \tag{2.45}$$

In this scenario, the mean domain wall velocity may be calculated as

$$v \equiv \langle \dot{q}(t) \rangle = \frac{\Delta}{\alpha}\left(\gamma\mu_0 H_a + \frac{\beta_{\mathrm{ST}}}{\Delta} u - \left\langle \dot{\phi}(t) \right\rangle\right) \ , \tag{2.46}$$

where the time integration is performed over a precession period and

$$\dot{\phi}(t) = \frac{1}{1+\alpha^2}\left[\gamma\mu_0 H_a + \frac{\beta_{\mathrm{ST}}-\alpha}{\Delta}u - \frac{\gamma\alpha}{2}\mu_0 M_s \sin\left(2\phi(t)\right)\right] . \tag{2.47}$$

In the asymptotical precessional limit that corresponds to big driving forces, namely $|\mu_0 H_a + ((\beta_{\mathrm{ST}}-\alpha)/\gamma\Delta)\, u| \gg \mu_0 H_w$, we may write

$$v = \frac{\alpha^2}{1+\alpha^2}\frac{\gamma\Delta}{\alpha}\left[\mu_0 H_a + \frac{1}{\gamma\Delta}\left(\beta_{\mathrm{ST}} + \frac{1}{\alpha}\right)u\right] , \tag{2.48}$$

which is equivalent to

$$v = m_{asp}\left(\mu_0 H_a + \frac{\beta_{\mathrm{ST}}}{\gamma\Delta}u + \frac{1}{\alpha\gamma\Delta}u\right) , \tag{2.49}$$

where m_{asp} is given by (2.35). Interestingly, the adiabatic spin-transfer torque gives rise to an additional term $u/\alpha\gamma\Delta$ on the effective field corresponding to the precessional regime. As discussed above, this is in contrast with its effect in the steady regime, where the adiabatic spin-transfer torque does not contribute to the effective field and, in addition, exerts an opposite torque on the domain wall magnetization.

As evidenced by this one-dimensional model for domain wall motion driven by field and spin-transfer torque, the effect of a spin-polarized current on domain wall dynamics depends strongly on the relation between the β_{ST} and α parameters, corresponding to the non-adiabatic torque and the Gilbert damping parameter, respectively. This relation determines the relative importance of the non-adiabatic vs. the adiabatic spin-transfer torques. Previous works [24, 26] have shown that these two parameters are similar in the diluted ferromagnetic semiconductors $(\mathrm{Ga,Mn})\mathrm{As}$ and $(\mathrm{Ga,Mn})(\mathrm{As,P})$, i.e. $\beta_{\mathrm{ST}} \sim \alpha$, evidencing that in these materials both the adiabatic and the non-adiabatic contributions are of crucial importance. Additionally, these works found that in these systems, $\alpha \simeq 0.25$.

2.2.5 Limitations of micromagnetic theory and alternative approaches

Based on the above discussion, in chapter 6 we shall present our studies on domain wall dynamics driven simultaneously by field and spin-transfer torque in (Ga,Mn)(As,P)/(Ga,Mn)As, while in chapter 4 we will address the field-driven dynamics in GdFeCo. However, we will evidence that the experimentally accessible domain wall motion in thin films with perpendicular anisotropy occurs in a context which is much more complex, where temperature and sample inhomogeneity play a very important role. For this reason, the one-dimensional model that we have presented and discussed in this section does not fully describe the observed domain wall velocity vs. driving force characteristics. In addition, it does not account for the morphological properties of domain walls, namely their roughness, which results from the interplay between domain wall elasticity and sample disorder.

These problems may be treated following diverse approaches with different levels of complexity. The most detailed approach is to numerically apply the micromagnetic theory to a more realistic scenario, in two or three dimensions, and accounting for the presence of inhomogeneities and temperature [87, 88]. However, even if great progress has been made in the last years [89], computational power is a huge limitation for performing simulations that successfully represent the dimensions and time scale of real experiments, specially in the regimes of slow domain wall motion. An alternative approach which is being developed for magnetic domain walls in thin films in the last years is based on the Ginzburg-Landau theory [90–92]. In this approach, the problem is simplified to a two-dimensional scalar field model with a double-well potential. In contrast with the micromagnetic model, which lies in a microscopic scale, the Ginzburg-Landau model permits to address problems in a mesoscopic level, allowing the description of larger spatial and temporal scales while preserving a link with microscopical parameters.

A third approach, which will be thoroughly described in the following section, consists on the effective description of magnetic domain walls in the framework of the theory of elastic interfaces in disordered media [3, 4]. This is the main theoretical framework in which we are based throughout this thesis, and its power is founded on two main factors. One of them is the description of a complex problem as the result of a competition between several key features, which are the elasticity of the domain wall, the medium's disorder, thermal activation and the driving force. This permits to drastically simplify the problem without losing the main ingredients that determine its physics. The second factor is its power for revealing universal features and critical behaviors of domain wall dynamics and morphology. As we will see in the following, this approach permits to successfully describe a wide variety of interface phenomena in nature.

2.3 Elastic interfaces in disordered media

Disorder plays a fundamental role in diverse phenomena and gives rise to complex behaviors whose description is usually challenging. In our work, we valorize the quest for complex and realistic problems and our capability as human beings to appropriately assess them. Therefore, from now on, disorder will be an omnipresent element throughout this manuscript, responsible of much of the inherent complexity of our field of study.

The existence of a huge variety of interfaces, which separate regions of different characteristics, is an evident feature of the natural world. Furthermore, the phenomena that occurs at interfaces is usually very rich and complex, and the understanding of their physics needs to be approached from new points of view, using tools which are different to those that explain the behavior of the extended regions that they separate. The theory of elastic interfaces in disordered media, which is part of the field of Statistical Physics, has permitted to understand the dynamics and morphology of a wide variety of interfaces in nature. Their two main characteristics are the elasticity, which tends to minimize the interface's

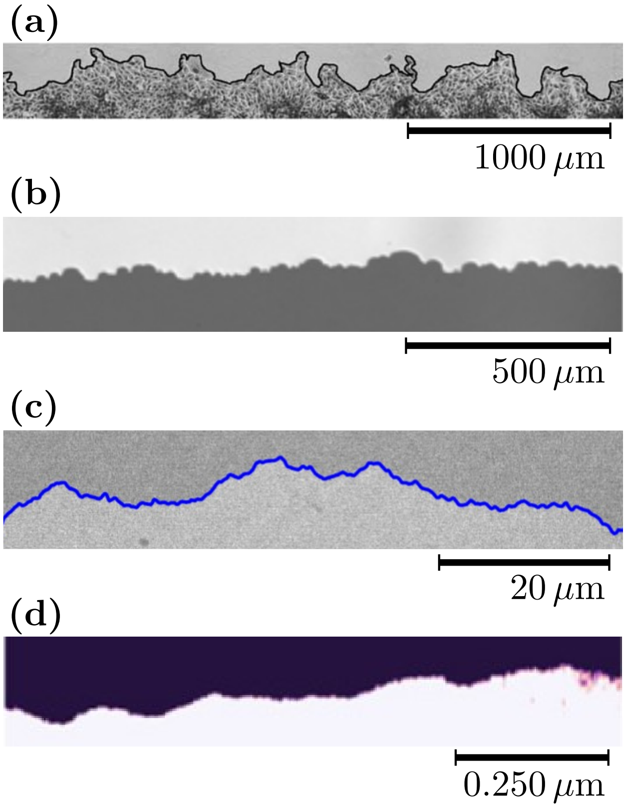

Figure 2.9: **Examples of elastic interfaces in disordered media.** (a) Cell colony front [97], (b) wetting line over a rough surface [95], (c) magnetic domain wall in a thin film of GdFeCo [39], (d) ferroelectric domain wall in $\mathrm{Pb(Zr,Ti)O_3}$ [102].

length or surface, and disorder, which pins the interface inducing it to adopt a rough shape. Some examples of this type of interfaces are firefronts [93], wetting fronts [94, 95], fronts of bacteria or cell colonies [96–98], fractures in solids [99, 100], earthquakes [101], ferroelectric domain walls [102], and magnetic domain walls [103].

In figure 2.9, we show images corresponding to some of these phenomena. This figure puts in evidence the fact that these interfaces have a similar morphology, characterized by their roughness, even if the nature of the microscopic mechanisms that give rise to each of them is completely different. The similarity between these interfaces is a result of the coexistence of disorder and elasticity which, in each case, arise due to its particular microscopic features. Furthermore, the length scale at which this phenomena occurs may be absolutely different for each case, as shown in the figure. In addition, as we will see in the following, these type of interfaces usually have the property of self-affinity, which means that particular scale transformations keep the statistical properties of the interface morphology invariant [3].

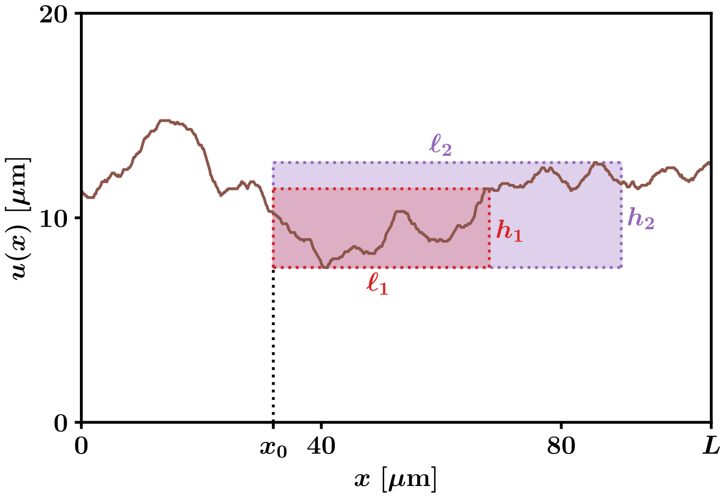

Figure 2.10: **Elastic line in a two-dimensional medium and notion of self-affinity.** The profile corresponds to a magnetic domain wall in a thin film of GdFeCo with perpendicular anisotropy. For a given length ℓ_1 starting from a particular horizontal position x_0, we define $h_1 \equiv h(\ell_1, x_0)$. We do the same for another length ℓ_2, defining $h_2 \equiv h(\ell_2, x_0)$. In order to obtain a function $h(\ell)$, we shall integrate these quantities considering all the possible starting positions x_0 in the horizontal coordinate x. If the interface is self-affine, the resulting $h(\ell)$ follows the relation $h(\ell) \sim \ell^{\zeta}$, where ζ is the roughness exponent.

2.3.1 Roughness characterization

Let us then focus on the morphology of elastic interfaces in disordered media. As we have already noticed (see figure 2.9), they are rough, what arises due to the competition between elasticity and disorder. Interfaces are less rough if the pinning forces induced by disorder are weak with respect to elasticity, and more rough when the opposite occurs. Their morphology may be assessed in the following way, which we exemplify graphically in figure 2.10. The shown profile corresponds to a magnetic domain wall in a thin film of GdFeCo which may be seen as an elastic line (a one-dimensional interface) lying in a two-dimensional disordered medium. We consider that the elastic line, of a total horizontal length L, lies in the horizontal direction $\hat{x}$, with its vertical position described by a continuous, uni-valued function $u(x)$. Taking as a reference an arbitrary coordinate x_0, and given an horizontal length ℓ_1, we look for the minimum vertical height $h_1 \equiv h(\ell_1, x_0)$ necessary to cover a segment of the interface within the rectangle of height h_1 and length ℓ_1. We may repeat this procedure for different lengths ℓ, with $0 < \ell < L - x_0$ and therefore define a continuous function $h(\ell, x_0)$. By integrating over x_0, we may obtain

$$h(\ell) = \frac{1}{L-\ell} \int_0^{L-\ell} h(\ell, x_0)\, dx_0 \ , \tag{2.50}$$

which represents the height of the interface as a function of the segment size.

The function $h(\ell)$ for an elastic line which lies in a two-dimensional disordered medium is usually expected to present particular statistical properties [3]. If it follows the scaling relation $h(\ell) \sim \ell$, then the interface is an isotropic fractal or a self-similar object. If $h(\ell) \sim \ell^{\zeta}$, with $\zeta > 0$, then it is an anisotropic fractal, or a self-affine object. Here, ζ is the so-called roughness exponent. Note that self-similarity is a particular case of self-affinity, corresponding to $\zeta = 1$. As we will further discuss later in this chapter, the ζ value is crucial for the description of elastic interfaces as magnetic domain walls, and it is characteristic of the universality class to which the interface belongs [4]. In the following, we shall formally define several quantities and functions which are closely related to the concept of roughness. Particularly, these definitions will serve us to perform experimental measurements of parameters such as the roughness exponent ζ for magnetic domain walls, which is an important subject of this thesis.

In order to adequately characterize the roughness of an elastic line in a two-dimensional medium, it is important to emphasize that we are interested on making a statistically relevant quantification. This means that the actual quantities and functions that characterize the roughness shall be obtained as a statistical average of multiple realizations of the elastic line, called an average on disorder [104, 105]. Let us take as an example the case of the magnetic domain wall profile shown in figure 2.10. Disorder in the shown region is modeled as an energetic landscape that is statistically uniform and quenched, i.e. it does not change as a function of time. The statistical uniformity of disorder means that there are no preferential regions for the domain wall to lie. Conversely, the wall may adopt many different configurations which result energetically favorable. Thus, the configuration shown in figure 2.10 is only one realization which does not fully describe the statistical properties of the physical problem. Therefore, in order to obtain a statistically relevant measure of domain wall roughness, we shall make an average on disorder in which we consider multiple functions $u(x)$ corresponding to different walls obtained under the same conditions. In the following, we formally define several quantities in which we note this average as an over-line, i.e. $\overline{\cdots}$.

Global width

The roughness of an interface lying over a length L and described by an uni-valued function $u(x)$ may be characterized by its global width, which measures its fluctuations in a given disordered landscape. This quantity is a function $W(L)$ of the interface size L, and it is defined as [104, 105]

$$W(L) = \overline{\left\langle [u(x) - \langle u(x) \rangle_L]^2 \right\rangle_L}^{1/2} , \tag{2.51}$$

where $\overline{\cdots}$ indicates an average on disorder and $\langle \cdots \rangle_L$ denotes a spatial average over the full length L, i.e. $\langle f(x) \rangle_L = L^{-1} \int_0^L f(x)\, dx$.

For a self-affine interface, the global width scales as its size L following the relation

$$W(L) \sim L^{\zeta} , \tag{2.52}$$

where ζ is the roughness exponent. This scaling relation is valid whenever the only relevant characteristic length scale is L. However, for most rough interfaces there exists a characteristic correlation length $\xi < L$, given by the so-called Family-Vicsek scaling form [104–106], above which the relation (2.52) is not valid. In addition, as we will discuss later, other relevant scales may play a role, resulting on more complex scaling relations.

The roughness exponent ζ of a given type of self-affine interface may be measured by calculating the global width as a function of the interface size L and observing the $\ln W(L)$ vs. $\ln L$ dependence in an appropriate range. Then, according to (2.52), the resulting slope corresponds to ζ. This procedure is usual when applied to numerically simulated interfaces, but it requires a control of the interface size over several orders of magnitude. Consequently, its implementation for an experimentally observed interface is generally not possible. This issue may be tackled by defining local quantities as the local width and the displacement-displacement correlation function, which we present in the following. These quantities measure, respectively, interface fluctuations and correlations over a distance r which is smaller than the total size L.

Local width

The local width $w(r)$ is a generalization of the global width, and it is defined as [104, 105]

$$w(r) = \overline{\left\langle \left[u(x) - \langle u(x)\rangle_r\right]^2 \right\rangle_r}^{1/2} , \tag{2.53}$$

where $\langle \cdots \rangle_r$ indicates a spatial average over regions of size r within the interface size L. This function is qualitatively similar to the function $h(\ell)$ that we have graphically defined in figure 2.10. Besides, the limit $r = L$ corresponds to the global width, this is $w(r = L) = W(L)$. Therefore, the function $w(r)$ contains more information about the interface fluctuations than $W(L)$.

It has been found that in many cases, $w(r)$ also exhibits a power-law behavior which is characterized by the same scaling exponents as those that characterize the global width $W(L)$ [104, 105][3]. Consequently, if $W(L)$ satisfies the scaling law (2.52), it is expected that

$$w(r) \sim r^{\zeta} . \tag{2.54}$$

Displacement-displacement correlation function

Another way to assess the roughness of an interface is provided by the displacement-displacement correlation function $B(r)$ of the $u(x)$ profile, which measures the correlation

---

[3] However, there exist cases of anomalous roughness in which the local and global exponents are different [107].

between different points of the interface as a function of the horizontal distance r between them. It is defined, for a given $u(x)$, as

$$B(r) = \frac{1}{L-r}\int_0^{L-r} [u(x+r)-u(x)]^2 dx \ , \tag{2.55}$$

where r belongs to the range $0 < r < L$. The scaling law for $B(r)$ for the case of a self-affine interface, in absence of characteristic lengths other than the system size, is [104, 105]

$$B(r) \sim r^{2\zeta} \ . \tag{2.56}$$

The function $B(r)$ constitutes an appropriate way to experimentally measure the roughness of an elastic line in a two-dimensional disordered medium. In order to obtain a statistically relevant measurement, it is necessary to consider multiple $B(r)$ functions corresponding to different interfaces obtained in the same conditions [39]. In chapter 5, we will present domain wall roughness measurements which are based on the definition (2.55).

Structure factor

Displacement correlation functions may be also computed in the reciprocal space, what often results very useful. The structure factor is the reciprocal-space counterpart of the displacement-displacement correlation function, and it is defined as

$$S(q) = \tilde{u}(q)\tilde{u}(-q) \ , \tag{2.57}$$

where

$$\tilde{u}(q) = \frac{1}{L}\int u(x) e^{-iqx} dx \tag{2.58}$$

is the Fourier transform of $u(x)$. The structure factor and the displacement-displacement correlation function are related through

$$B(r) = \int [1-\cos(qr)]\, S(q) \frac{dq}{\pi} \ . \tag{2.59}$$

For a self-affine interface, $S(q)$ scales as

$$S(q) \sim q^{-(1+2\zeta)} \ . \tag{2.60}$$

The structure factor has been proven to be more appropriate for the roughness characterization than the displacement-displacement correlation function from the theoretical point of view and in cases in which sufficient statistics are obtained. This is particularly relevant when several scaling regimes exist, in which different roughness exponents have to be considered as a function of the observed length scale [40, 104, 105, 108]. As we will further discuss in chapter 5, these different regimes are well separated in the $S(q)$ dependence while they are mixed in $B(r)$. In addition, $B(r)$ cannot account for super-rough interfaces in which $\zeta > 1$ [107]. However, the experimentally obtained $S(q)$ functions are generally too noisy, what prevents the clear observation of the scaling law (2.60) and thus impedes the ζ determination. For this reason, the roughness analysis of experimentally observed domain wall profiles is based on computing the $B(r)$ function. In this context, our discussion on the observed domain wall roughness will be continuously linked to theoretical predictions via the relationship between $B(r)$ and $S(q)$.

We have just presented the main fundamental concepts that permit us to quantitatively analyze the morphology of an elastic line in a two-dimensional medium. Particularly, we have defined the quantities and functions which are closely linked to the concept of roughness and the determination of critical roughness exponents. Later, in 2.4.4, we shall present theoretical predictions on this issue for magnetic domain walls in thin films, which is an important subject for the scope of this thesis: in chapter 5, we will present our studies on domain wall roughness in a thin film of GdFeCo. As domain wall roughness is closely related to its dynamics, we shall first present the main theoretical concepts that constitute the basis for studying the dynamics of driven elastic interfaces. In the following, we will discuss how the main ingredients that we have already mentioned, namely elasticity, quenched disorder, thermal activation and a driving force, may be expressed quantitatively in order to write a stochastic equation of motion for an elastic interface.

2.3.2 Dynamical regimes of driven interfaces

Let us now consider an elastic line which lies in a two-dimensional disordered medium and which is subject to an external, uniform, driving force. The two-dimensional medium corresponds to the xu plane, and the elastic line is now described by a time-dependent uni-valued function $u(x,t)$ of size L in the $\hat{x}$ direction. An instantaneous position may be described by the $u(x)$ function illustrated in figure 2.10, with $\hat{x}$ the horizontal and $\hat{u}$ the vertical direction. The driving force f is applied in the $\hat{u}$ direction.

In this context, the energy of the interface may be written as

$$E[u] = \int_0^L dx \left[\frac{c}{2}(\nabla u(x,t))^2 + U_p(x,u(x,t)) - fu(x,t)\right] , \tag{2.61}$$

where $(c/2)(\nabla u(x,t))^2$ is the elastic energy with a stiffness constant c, $U_p(x,u(x,t))$ is the quenched pinning potential, and $-fu(x,t)$ is the energy associated with the driving force f [5]. This force is uniform and acts in the $\hat{u}$ direction. Then, the equation of motion is obtained as $\gamma_f \partial_t u(x,t) = -\delta E[u]/\delta u(x,t) + \eta(x,t)$, where γ_f is a microscopic friction and $\eta(x,t)$ is an uncorrelated white noise which accounts for the temperature T and satisfies $\overline{\eta(x_1,t_1)\eta(x_2,t_2)} = 2\gamma_f k_B T \delta(x_1-x_2)\delta(t_1-t_2)$. Therefore,

$$\gamma_f \partial_t u(x,t) = c\nabla^2 u(x,t) + F_p(u,x) + \eta(x,t) + f , \tag{2.62}$$

where $F_p(u,x) = -\partial U_p(u,x)/\partial u$ is the pinning force. This is the so-called quenched Edwards-Wilkinson equation [3, 4] and constitutes a paradigmatic model in order to describe a driven elastic interface in a disordered potential. As we will thoroughly discuss throughout this work, the values of the critical exponents that characterize the universal behaviors of an interface phenomena are defined by the used model, what allows for the classification of these phenomena in several universality classes [3].

In equations (2.61) and (2.62), elasticity is considered to be harmonic (i.e. only small deformations are supposed to occur) and short-ranged. Additionally, correlations of the pinning potential $U_p(u, x)$ are considered only in the $\hat{u}$ direction, not in the $\hat{x}$ direction [5]. Two different types of potential are usually considered, each of them giving rise to an universality class [109]. In the so-called random-bond class, the interface moves in a random short-range correlated potential $U_p(u, x)$ which acts locally in a range ξ_p which is the correlation length of disorder. In contrast, in the so-called random-field class, the interface is coupled with the potential $U_p(u, x)$ in an entire region delimited by $u(x, t)$ [41]. Then, in the random-field universality class, $U_p(u, x)$ displays long-range correlations. From now on, we shall consider that the quenched Edwards-Wilkinson (qEW) universality class corresponds to random-bond disorder and short-ranged elasticity.

Another model is usually proposed: the so-called quenched Kardar-Parisi-Zhang (qKPZ) universality class, which is claimed to appropriately describe interface growth processes when lateral displacements are allowed [3, 110–112]. The difference between the qEW and the qKPZ models is the nature of interface elasticity. In the qEW model, as we have just mentioned, harmonic elasticity is considered, corresponding to the linear term $c\nabla^2 u(x, t)$ in equation (2.62). On the other hand, in the qKPZ model an additional nonlinear term $(\lambda/2)\left(\nabla u(x, t)\right)^2$ is considered, where λ is a constant. The quenched Kardar-Parisi-Zhang equation then reads

$$\gamma_f \partial_t u(x, t) = c\nabla^2 u(x, t) + (\lambda/2)\left(\nabla u(x, t)\right)^2 + F_p(u, x) + \eta(x, t) + f \; . \tag{2.63}$$

The qEW and the qKPZ models, equations (2.62) and (2.63), permit to make predictions on the interface velocity as a function of the driving force. The mean velocity v for a given constant force f, which is usually experimentally accessible, corresponds to averaging $\partial u(x, t)/\partial t$ along the whole interface size L within a given time period Δt.

In the following, we shall discuss the predictions that correspond to the qEW universality class. As we will further discuss in chapter 4, the differences between different universality classes lie in the criticality, i.e. in the set of numerical values of critical exponents describing the power-law variation of observable quantities close to the so-called reference states [5]. In figure 2.11(a), we illustrate the predictions of equation (2.62) for the mean velocity v as a function of the force f [4]. Additionally, in figure 2.11(b) we present the force-dependence of characteristic lengths that we will introduce below and are closely related to the interface dynamics.

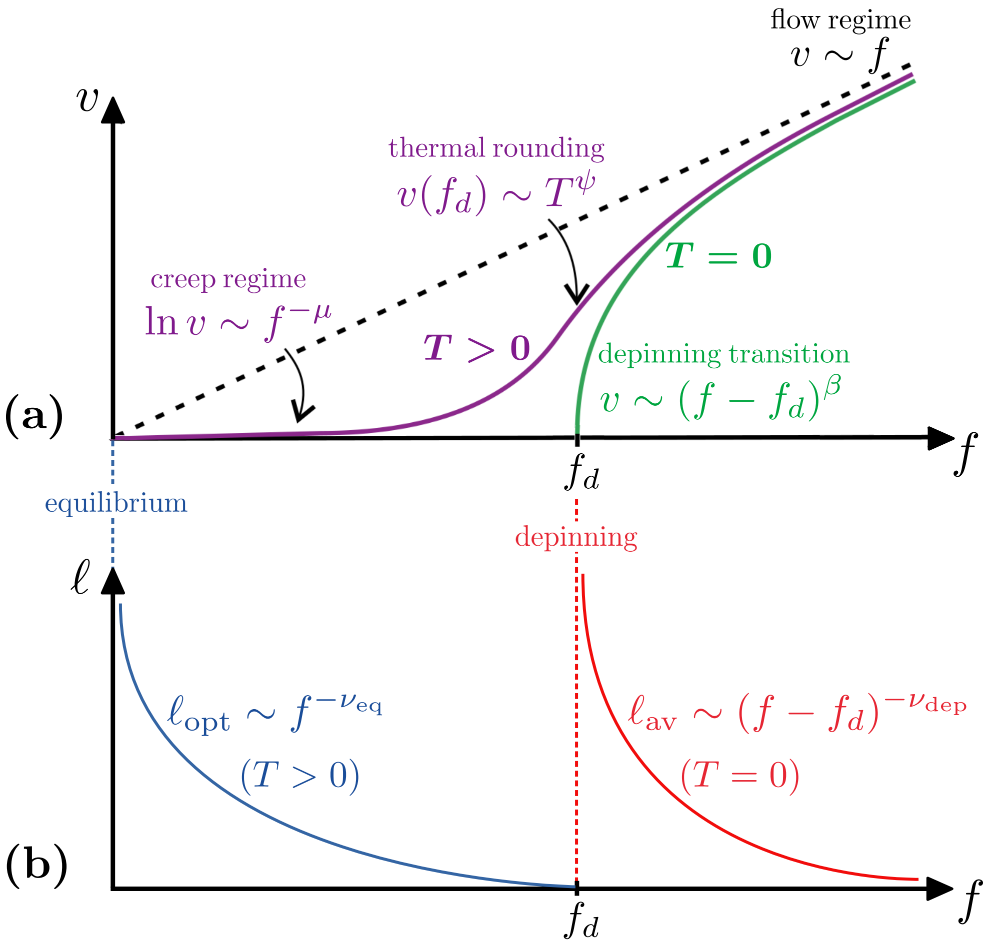

Figure 2.11: **Dynamical regimes and associated critical exponents of an elastic interface in the quenched Edwards-Wilkinson model.** (a) Mean velocity v vs. driving force f. For $T=0$, $v \neq 0$ only if $f > f_d$. In the depinning transition, just above f_d, velocity grows as $v \sim (f-f_d)^{\beta}$. For $f \gg f_d$, $v \sim f$. For $T>0$, thermal activation induces non-zero velocities even for $0 < f < f_d$. In the limit $f \to 0$, which corresponds to the so-called creep regime, $\ln v \sim f^{-\mu}$. For $f = f_d$, velocity grows with temperature as $v(f_d) \sim T^{\psi}$. This is the so-called thermal rounding. For sufficiently high driving forces, in the flow regime, the effects of temperature and disorder become negligible and $v \sim f$. Adapted from [4]. (b) Characteristic lengths ℓ vs. driving force f, corresponding to coherent displacements of interface segments (see figure 2.12). Avalanche size ℓ_{av} diverging as $(f-f_d)^{-\nu_{\mathrm{dep}}}$ when $f \to f_d^{+}$, corresponding to the depinning critical point at $T=0$, and optimal length ℓ_{opt} diverging as $f^{-\nu_{\mathrm{eq}}}$ when $f \to 0$ and $T>0$, corresponding to the equilibrium reference state.

Flow regime

For sufficiently high driving forces velocity tends asymptotically to a proportionality with the driving force which constitutes the so-called flow regime, i.e. $v \sim f$ (see figure 2.11(a)). This limit of very high driving forces, in which disorder becomes negligible, may be modeled as a straight interface lying in an homogeneous medium. Therefore, for the case of a magnetic domain wall, the flow regime is in correspondence with the description of the one-dimensional model that we have discussed in section 2.2.3, in which the driving force is proportional to the applied field H_a. As evidenced in figure 2.8, the flow regime of magnetic domain walls may show a much more complex behavior than the simple proportionality $v \propto f$. This is due to the fact that in the elastic line model, we do not take into account the internal structure of the interface which, in the case of domain walls, gives rise to the Walker breakdown. Simultaneously, as shown by the theoretical prediction of figure 2.11(a), temperature and disorder crucially affect elastic line dynamics for relatively low driving forces. This evidences that both scenarios must be considered in order to fully comprehend magnetic domain wall dynamics in thin films.

Depinning transition at zero temperature

For zero temperature, i.e. if no thermal noise is considered, no net movement of the interface occurs below a critical force f_d which we call the depinning force (see figure 2.11(a)). Above this critical point, velocity is expected to grow following a power-law behavior

$$v \sim (f - f_d)^{\beta} \ , \tag{2.64}$$

where β is a depinning critical exponent. This dynamic transition in which the driving force overcomes the pinning force is the so-called depinning transition. Interestingly, it is analogous to standard second-order transitions as the paramagnetic-ferromagnetic one, with the particularity that in this case v instead of M is the order parameter and f instead of T is the control parameter. Accordingly, β is the depinning order parameter critical exponent.

Slightly above f_d, the motion of a given point in the interface is intermittent: it successively experiences displacements at high velocities which are separated by periods of no motion [5]. As in equilibrium second-order phase transitions, there exists a correlation length that diverges for $f \to f_d^+$. This correlation length is manifested in the collective nature of these displacement events: for f slightly above f_d, large portions of the interface of characteristic size ℓ_{av} successively experience coherent movements at large velocities while most of the interface remains pinned (see figure 2.12). These coherent events are the so-called depinning avalanches. As shown in figure 2.11(b), for $T = 0$, the size ℓ_{av} diverges when $f \to f_d^+$ as

$$\ell_{\text{av}} \sim (f - f_d)^{-\nu_{\text{dep}}} \ , \tag{2.65}$$

where ν_{dep} is the depinning correlation length critical exponent [4, 5].

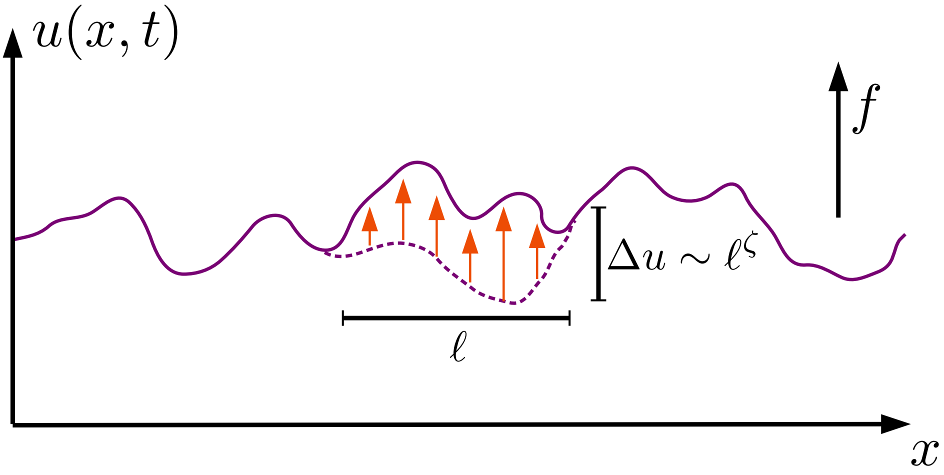

Figure 2.12: **Illustration of the coherent and fast displacement of one segment in a driven elastic line.** The quantity ℓ is the typical size of these events, and Δu is the corresponding displacement which follows the scaling relation $\Delta u \sim \ell^{\zeta}$. In the limit $f \to f_d^{+}$ and for $T = 0$, this coherent movement is a depinning avalanche and then ℓ is ℓ_{av} and ζ is ζ_{dep}. In the limit $f \to 0$ and for $T > 0$, the displacement corresponds to a thermally activated jump over an effective pinning energy barrier, and then ℓ is ℓ_{opt} and ζ is ζ_{eq}.

The quenched Edwards-Wilkinson universality class is characterized by particular values of the depinning critical exponents. These values also depend on the dimension d of the interface, which in the case of a line in a two-dimensional medium is $d = 1$. Additionally, they are dependent on each other: $\beta = \nu_{\text{dep}}(z - \zeta_{\text{dep}})$ and $\nu_{\text{dep}} = 1/(2 - \zeta_{\text{dep}})$, where ζ_{dep} is the roughness exponent corresponding to $T = 0$ and $f = f_d$, and z is the dynamic critical exponent, which corresponds to the scaling law of the relaxation time t_r of an interface segment as a function of its size ℓ, i.e. $t_r(\ell) \sim \ell^{z}$ [3][4]. In this context, $z = 1.43$ and $\zeta_{\text{dep}} = 1.25$ [5] and, therefore, $\nu_{\text{dep}} = 1.33$ and $\beta = 0.24$. Throughout this thesis, we shall thoroughly discuss about the experimental quantification of these depinning critical exponents.

Creep regime

If $T > 0$, thermal activation induces stochastic jumps of the interface over the pinning potential $U_p(u,x)$, thus allowing it to move even for $f < f_d$. In fact, if $T > 0$, $v > 0$ for

---

[4] The scaling relation $\beta = \nu_{\text{dep}}(z - \zeta_{\text{dep}})$ results from considering that, at the depinning transition, $v \sim \Delta u/t_r \sim \ell_{\text{av}}^{\zeta_{\text{dep}}}/\ell_{\text{av}}^{z}$ and, concomitantly, $\ell_{\text{av}} \sim (f - f_d)^{-\nu_{\text{dep}}}$ and $v \sim (f - f_d)^{\beta}$. Thus, $v \sim (f - f_d)^{-\nu_{\text{dep}}(\zeta_{\text{dep}} - z)}$ and consequently $\beta = \nu_{\text{dep}}(z - \zeta_{\text{dep}})$. For its part, the scaling relation $\nu_{\text{dep}} = 1/(2 - \zeta_{\text{dep}})$ is valid if the equation of motion preserves the statistical tilt symmetry [41, 113]. If this condition is satisfied, then $\Delta u/(f - f_d) \sim \ell_{\text{av}}^{2}$ and, as $(f - f_d) \sim \ell_{\text{av}}^{-1/\nu_{\text{dep}}}$ and $\Delta u \sim \ell_{\text{av}}^{\zeta_{\text{dep}}}$, $\nu_{\text{dep}} = 1/(2 - \zeta_{\text{dep}})$. The statistical tilt symmetry is satisfied for the quenched Edwards-Wilkinson model (equation (2.62)) while it is not satisfied for the quenched Kardar-Parisi-Zhang model (equation (2.63)).

any finite force. In this stochastic process, which takes place in the range $0 < f < f_d$, the interface successively visits different metastable states which are characterized by decreasing energies $E[u]$ due to the applied driving force f, as evidenced by equation (2.61). In the limit $f \to 0$, this thermally activated regime of motion is the so-called creep regime. In this scenario, velocity grows with a stretched exponential behavior, namely

$$\ln v \sim f^{-\mu} \, , \tag{2.66}$$

where μ is the so-called creep exponent (see figure 2.11(a)).

Let us now discuss the origin of the creep regime v vs. f dependence, given by (2.66). Thermally activated jumps over pinning energy barriers occur with a time rate which is characterized by an Arrhenius law[5]. Thus we may write

$$v(f) \propto \exp\left(\frac{-E_p(f)}{k_B T}\right) \, , \tag{2.67}$$

where $E_p(f)$ is an effective pinning energy barrier dependent on the driving force and $k_B T$ is the thermal energy. Due to the fact that $E_p(f)$ affects the collective motion of the whole interface, it diverges when $f \to 0$ [5]. The critical exponent accounting for this divergence is the creep exponent μ, i.e. $E_p(f) \sim f^{-\mu}$. Similarly to the case of the depinning transition at $f = f_d$, the equilibrium at $f = 0$ constitutes a reference state characterized by several critical exponents. The particular values of these exponents are defined by the universality class.

In the limit $f \to 0$, the elastic energy term $E_{el}(\ell)$ corresponding to the displacement $\Delta u(\ell)$ of an interface segment of size ℓ (see figure 2.12) grows as

$$E_{el}(\ell) \sim \left(\frac{\Delta u(\ell)}{\ell}\right)^2 \ell^d \sim \ell^{2\zeta_{\text{eq}}+d-2} \tag{2.68}$$

in accordance with equation (2.61). This energy cost is compensated by an energy gain due to the driving force,

$$E_f(\ell) \sim f \Delta u(\ell) \ell^d = f \ell^{\zeta_{\text{eq}}+d} \, . \tag{2.69}$$

The competition between $E_{el}(\ell)$ and $E_f(\ell)$ results in a total energy $E_T(\ell) = E_{el}(\ell) - E_f(\ell)$ which has a maximum at a characteristic length ℓ_{opt} which corresponds to the optimal segment size coherently moving over characteristic pinning energy barriers [5], diverging when $f \to 0$ as

$$\ell_{\text{opt}} \sim f^{-1/(2-\zeta_{\text{eq}})} \, , \tag{2.70}$$

as indicated in figure 2.11(b). This relation is analogous to (2.65), which corresponds to the depinning transition ($f \to f_d^+$ and $T = 0$). Then, for the equilibrium ($f \to 0$ and $T > 0$), we may identify $\nu_{\text{eq}} = 1/(2 - \zeta_{\text{eq}})$. Concomitantly, the characteristic magnitude of pinning energy barriers is $E_T(\ell_{\text{opt}})$, and grows when $f \to 0$ as

$$E_p(f) \sim f^{-\frac{2\zeta_{\text{eq}}+d-2}{2-\zeta_{\text{eq}}}} \tag{2.71}$$

---

[5] The Arrhenius law may be invoked for the time rate of thermally activated events whenever thermal energy is much lower than the energy barrier, i.e. $k_B T \ll E_p(f)$.

where, according to the above discussion, we can identify the creep exponent

$$\mu = \frac{2\zeta_{\text{eq}} + d - 2}{2 - \zeta_{\text{eq}}} \ . \tag{2.72}$$

For the case of a one-dimensional interface, i.e. a line, we have $d = 1$ and $\zeta_{\text{eq}} = 2/3$ [13, 41, 112]. Therefore, for $f \to 0$, ℓ_{opt} diverges as $f^{-\nu_{\text{eq}}}$ with $\nu_{\text{eq}} = 3/4$, and the velocity follows $\ln v \sim f^{-\mu}$ with $\mu = 1/4$. In section 2.4, we shall show that this μ value describes very convincingly the creep regime of magnetic domain walls in thin films.

Thermal rounding

At $f = f_d$, i.e. in the depinning transition, velocity grows with temperature T with a power law given by [114]

$$v(f_d) \sim T^{\psi} \ , \tag{2.73}$$

with the critical exponent ψ being the thermal rounding exponent [115] (see figure 2.11). This effect of temperature in the depinning transition is analogous to the effect of an applied field in the second-order paramagnetic-ferromagnetic phase transition. The thermal rounding for an elastic line in a two-dimensional medium in the quenched Edwards-Wilkinson universality class has been studied numerically resulting on $\psi = 0.15$ [114, 115]. Furthermore, this value has been found to be consistent with experimentally measured values for domain walls in magnetic thin films [15, 116].

We have just presented the main dynamical characteristics of driven elastic interfaces in disordered media. Furthermore, we have established links between the velocity vs. force characteristics, which show different regimes of motion, and the length scales that characterize these dynamics. The characteristic lengths are naturally linked to the interface morphological properties that we have discussed previously. In addition, we have shown that critical behaviors occur both for $f \to f_d^+$ and $f \to 0$. The exponents that characterize these critical points are closely related to the universality class to which the elastic interface belongs. For this reason, we have presented their predicted values for the particular case of the quenched Edwards-Wilkinson universality class, which may be considered as the most simple model capturing the key features that are expected to govern domain wall dynamics and morphology in thin films: short-ranged elasticity, random-bond quenched disorder, thermal noise and a uniform force, as indicated by equation (2.62).

Accordingly, in the following we shall discuss the particular case of magnetic domain walls in thin films with perpendicular anisotropy in the framework of the theory of driven elastic interfaces in disordered media. We shall show that this theory is crucial for the understanding of many experimentally measured velocity vs. force curves and for the study of domain wall morphology and characteristic lengths in the different dynamical regimes. Additionally, we will discuss the experimental access to the theoretically predicted critical exponents, which is a cross-cutting issue of the studies that we present throughout this thesis.

2.4 Magnetic domain walls as driven elastic lines

The different terms which represent key ingredients in the motion of driven interfaces, written in equation (2.62), can be qualitatively linked to the main energy contributions playing a role in magnetic domain wall motion. The elasticity of domain walls is associated with their energy per unit area σ, which arises from the interplay between anisotropy and exchange energies (see equation (2.15)) and induces walls to be as flat as possible. Disorder, whose origin is due to the inhomogeneities in the magnetic sample, is usually modeled as an inhomogeneous anisotropy energy $K_{\text{eff}}(u, x)$ representing the pinning potential $U_p(u, x)$ [90]. Thermal activation is responsible for the spontaneous and stochastic inversion of magnetization which favors domain wall motion over anisotropy energy barriers. Finally, the driving force may be originated by an applied field or current, as we have discussed in sections 2.2.3 and 2.2.4. These elements suggest that the domain wall dynamics and morphology may be assessed in this framework. Accordingly, in this section we will thoroughly discuss this approach and its amazing capability in order to describe domain wall dynamics and morphology in magnetic thin films with perpendicular anisotropy. We will focus on field-driven domain walls; however, as we will further discuss in section 2.5.2 and in chapter 6, the following discussion also applies to current-driven domain walls.

2.4.1 Experimental observation of creep and flow regimes

Let us now discuss experimental measurements of the velocity vs. field dependence for domain walls in thin magnetic films with perpendicular anisotropy. Figure 2.13 shows curves corresponding to thin films of cobalt lying between two films of platinum, i.e. stacks of Pt/Co/Pt [14]. The different shown curves correspond to different thicknesses of cobalt t_{Co}. In these measurements, the different dynamical regimes illustrated in figure 2.11(a) are evidenced.

Figure 2.13(a) shows two velocity v vs. applied field H curves, corresponding to two different values of t_{Co}. In both cases, for sufficiently large fields a proportionality between field and velocity is observed, consistent with predictions for the flow regime. Thus, for sufficiently high fields,

$$v = m\,H \ , \tag{2.74}$$

where the proportionality factor m is the flow-regime mobility. In contrast, for low applied fields, velocity follows a stretched exponential behavior which is consistent with the predicted creep regime, satisfying $\ln v \sim H^{-\mu}$. Two images obtained by Polar Kerr microscopy[6] are shown, each of them corresponding to one of these two dynamical regimes, i.e. creep and flow. They evidence that morphological properties of magnetic domain walls drastically change according to their regime of motion.

---

[6] In chapter 3 we will thoroughly discuss this experimental technique.

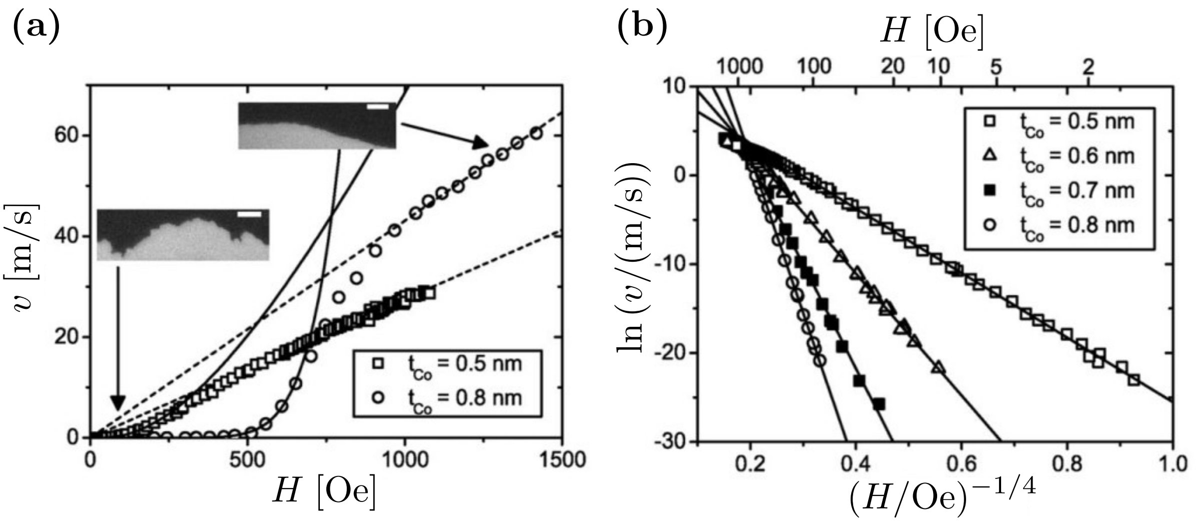

Figure 2.13: **Domain wall velocity versus applied field in Pt/Co/Pt thin films.** (a) Velocity v vs. field H for two magnetic films with different Co thicknesses t_{Co}. Dashed lines correspond to fits of the flow regime, with $v \propto H$. Continuous lines correspond to the creep regime, where $\ln v \sim H^{-\mu}$ with $\mu = 1/4$. The observed domain wall morphology in the different dynamical regimes is illustrated. White scale bars are $5\,\mu$m long. (b) Creep-type plot of $\ln v$ vs. $H^{-\mu}$ with $\mu = 1/4$, for four different values of t_{Co}. Straight lines correspond to the creep regime, which spans over eleven orders of magnitude in measured velocity. Both figures are adapted from [14].

Figure 2.13(b) shows velocity curves for four different t_{Co} values, plotted as $\ln v$ vs. $H^{-1/4}$. As evidenced in the figure, the behavior in all cases is very well described in a wide range of velocities by straight lines which represent the dependence $\ln v \sim H^{-\mu}$ with $\mu = 1/4$, as theoretically predicted for the low velocity creep regime. The wide range of velocities in which this dependence is observed experimentally, which spans from $v \sim 0.1\,\mathrm{nm/s}$ to $v \sim 10\,\mathrm{m/s}$, shows that the predicted behavior is verified in a very robust way. Furthermore, the creep exponent value $\mu = 1/4$ is shown to be consistent with all measurements.

The observation of the creep law with $\mu = 1/4$ for magnetic domain walls in thin films was made for the first time by S. Lemerle and collaborators in 1998 [13]. Nowadays, many experiments in different magnetic thin films have been performed, resulting on similar observations [14–16, 18, 27, 117]. In all cases, the creep exponent value $\mu = 1/4$ is found to be consistent with the observed velocity-field characteristics for low driving forces, what accounts for the universality of the creep dynamical regime.

2.4.2 Universal creep regime

As we have just shown, the creep regime has been observed to span over a wide range of velocities and a relatively wide range of driving forces, beyond the theoretically predicted limit $f \to 0$. Recently, Vincent Jeudy and collaborators [16] proposed an empirical expression for describing the creep law of field-driven magnetic domain walls in the whole range $0 < H < H_d$. This law reads

$$v(H) = v_d \exp\left(-\frac{E_p(H)}{k_B T}\right) , \tag{2.75}$$

where

$$E_p(H) = k_B T_d \left[\left(\frac{H}{H_d}\right)^{-\mu} - 1\right] \tag{2.76}$$

and, consequently, $v_d = v(H_d)$. The particularity of this empirical law is the expression for the effective pinning energy barrier (2.76), which diverges for $H \to 0$ and vanishes linearly for $H \to H_d^-$. The depinning field H_d is material- and temperature-dependent. In addition, a characteristic energy $k_B T_d$ is introduced, with T_d being the so-called depinning temperature. Both T_d and the velocity at depinning v_d are also material- and temperature-dependent. In contrast, the universal creep exponent is $\mu = 1/4$ for any sufficiently thin[7] magnetic film with perpendicular anisotropy at any temperature.

The material- and temperature-dependent quantities H_d, T_d and v_d are determined in the following way. Given a v vs. H curve for a magnetic material at a fixed temperature, the dependence $\ln v$ vs. $H^{-1/4}$ is plotted, as already shown in figure 2.13(b). The range of low fields in which this dependence is linear corresponds to the creep regime, and then a linear fit of the type $y = Sx + I$ may be performed, where $y = \ln v$ and $x = H^{-1/4}$. Then, according to equations (2.75) and (2.76), the fit slope S and intercept I correspond to

$$S = -\frac{T_d}{T} H_d^{1/4} \tag{2.77}$$

and

$$I = \ln v_d + \frac{T_d}{T} . \tag{2.78}$$

In this context, in order to determine H_d, T_d and v_d, it is necessary to independently determine one of them. Considering that the creep law successfully describes the velocity vs. field characteristics in the whole range $0 < H < H_d$, the depinning field H_d may be directly determined as the upper limit of the creep-type behavior. This hypothesis is validated by the existence of an inflection point at H_d that, as we will further discuss in 2.4.3, is an evidence of the depinning transition. The simultaneity of the separation from the creep-law behavior and the inflection point may be clearly observed in figure 2.13(a). Once H_d is determined, both v_d and T_d can be obtained from (2.78) and (2.77).

The determination of material and temperature dependent quantities H_d, T_d and v_d permits to calculate the effective pinning energy barrier $E_p(H)$. The main result of reference [16] is the fact that expressions (2.75) and (2.76) with $\mu = 1/4$ are shown to successfully describe

---

[7] A dimensional crossover is expected to occur in which μ changes from its $d = 1$ value to the $d = 2$ value for sufficiently thick magnetic films [118]. Similarly, a crossover from $d = 1$ to $d = 0$ has been observed for narrow magnetic tracks [117].

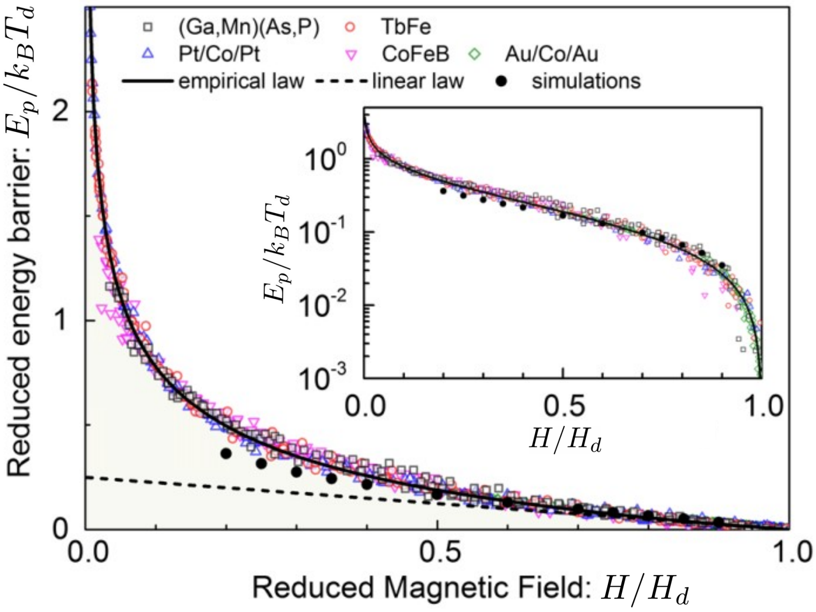

Figure 2.14: **Reduced effective pinning energy barrier as a function of the reduced applied field in the whole creep regime.** Experimental data for several different materials at different temperatures is considered, calculated according to (2.79) showing a very good agreement with the proposed empirical law (2.80). Consistence with numerical simulations for elastic lines in two-dimensional disordered medium [41] is shown. In the limit $H \to H_d^-$, a linear vanishing of $E_p(H)$ is evidenced, which describes very well the dependence over two orders of magnitude, as shown in the inset. Adapted from [16].

the creep regime in the whole range $0 < H < H_d$ for a notoriously wide variety of magnetic materials at different temperatures, what accounts for the universality of the proposed expression for the effective energy barrier. This is evidenced by figure 2.14, where the reduced energy barrier $E_p(H)/k_BT_d$ is plotted as a function of the reduced field H/H_d for many different magnetic thin films with perpendicular anisotropy: the diluted magnetic semiconductor (Ga,Mn)(As,P), the ferrimagnet TbFe, and the ferromagnets Pt/Co/Pt, CoFeB and Au/Co/Au. In addition, for some of these materials, curves at different temperatures are considered.

More specifically, the very good agreement between the experimentally calculated

$$\frac{E_p(H)}{k_BT_d} = -\frac{T}{T_d} \ln\left(\frac{v(H)}{v_d}\right) , \tag{2.79}$$

and the proposed empirical law,

$$\frac{E_p(H)}{k_BT_d} = \left(\frac{H}{H_d}\right)^{-1/4} - 1 , \tag{2.80}$$

is evidenced for different materials and temperatures. Additionally, the consistence with numerical simulations [41] of a one-dimensional elastic line in a two-dimensional disordered medium is shown, what suggests that this empirical law may describe a larger variety of elastic interfaces. In the limit $H \to H_d^-$, a linear vanishing of the effective energy barrier is shown to occur, in agreement with (2.76).

We have just discussed the universality of the velocity vs. field characteristics in the creep regime of magnetic domain walls in thin films. In the following, we shall present the state-of-the-art on the experimental observation of the depinning transition, which is rather elusive, and its universal properties.

2.4.3 Universal depinning transition

Up to now, we have shown that creep and flow regimes of field-driven magnetic domain walls in thin films are rather well understood and observed in a wide variety of materials. However, the experimental study of the velocity-field characteristics in the intermediate depinning regime faces more difficulties. This is due to the relatively narrow field and velocity range in which this regime occurs, and to the thermal effects that hinder the observation of the zero-temperature dependence $v \sim (H - H_d)^\beta$, in accordance with (2.64). Exactly at the depinning field, for $H = H_d$, velocity follows the power law corresponding to the thermal rounding, (2.73). For a magnetic domain wall in a thin film [116],

$$v(H_d) = v_T \left(\frac{T}{T_d}\right)^\psi , \tag{2.81}$$

where v_T is a material and temperature dependent velocity. Concomitantly, in the limit of $T \ll T_d$ and for a limited field range above H_d corresponding to the depinning regime [18],

$$v(H) = v_H \left(\frac{H - H_d}{H_d}\right)^\beta , \tag{2.82}$$

where v_H is another material and temperature dependent velocity. Note that in contrast with the creep law (2.75), which shows a positive concavity[8] of $v(H)$ for $T_d/T \geq (\mu + 1)/\mu$, depinning law (2.82) presents a negative concavity because $\beta < 1$. Therefore, an inflection point should occur close to $H = H_d$.

In 2017, Rebeca Díaz Pardo and collaborators [18] proposed a universal function describing the depinning regime in a range $H_d < H < H_u$, where H_u is a crossover field corresponding to the upper boundary of the depinning regime. This universal function, which reflects the two limit behaviors (2.81) for $H = H_d$ and (2.82) for $T = 0$, is plotted in figure 2.15(a) as a continuous line linking the quantities $(v/v_T)\,(T/T_d)^{-\psi}$ and $[(H - H_d)/H_d]^\beta\,(T/T_d)^{-\psi}$. This function is found to successfully describe experimental data corresponding to three different materials in a very wide temperature range. Furthermore, the relation between the two depinning velocities v_T and v_H is found to be practically independent of the material and the temperature. Specifically, a relation $x_0 \equiv v_T/v_H \simeq 0.65$ has been found for the studied materials and temperatures.

---

[8] The positive concavity of creep law must be satisfied as it has been obtained from the Arrhenius law, which assumes $T_d \gg T$.

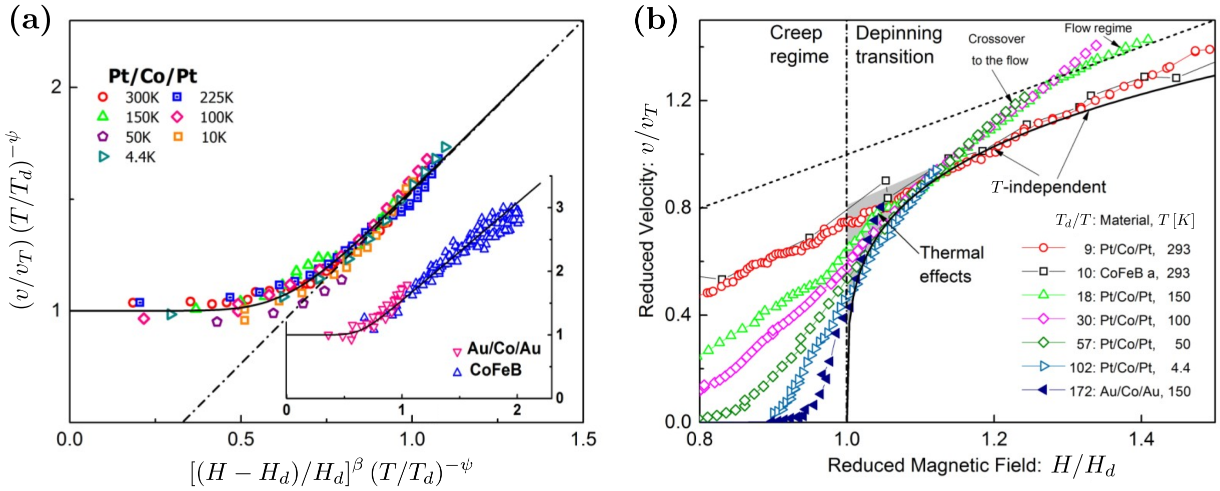

Figure 2.15: **Universality of the depinning transition at finite temperature.** (a) Universal depinning function plotted as a continuous line, and experimental data relating $(v/v_T)\,(T/T_d)^{-\psi}$ vs. $[(H-H_d)/H_d]^{\beta}\,(T/T_d)^{-\psi}$, for Pt/Co/Pt at different temperatures (main panel) and for Au/Co/Au and CoFeB (inset). The dot-dashed straight line corresponds to the zero-temperature depinning law (2.82). (b) Reduced velocity v/v_T vs. reduced field H/H_d for different materials at different temperatures. The continuous line is the zero-temperature depinning law (2.82) with $v_H = v_T/0.65$, and the dashed line corresponds to the flow regime with a mobility $m = v_T/H_d$. The limit at H_d between the universal creep regime and the universal depinning transition is indicated as a dot-dashed line. Thermal effects occur close to H_d due to the thermal rounding. A T-independent behavior is observed in a limited range in which the zero-temperature depinning law successfully describes experimental data. Above this range, a crossover occurs until $v = m\,H$, corresponding to the flow regime, is satisfied for sufficiently high H. Both figures are adapted from [18].

In reference [18], critical exponent values ψ and β are assumed to correspond to the previously accepted ones, $\psi = 0.15$ [114, 115] and $\beta = 0.25$ [119]. However, while ψ was already experimentally determined [15] showing a good agreement with $\psi = 0.15$, β has never been directly measured experimentally.

The material- and temperature-dependent quantities playing a role in the universal depinning function, v_T, T_d and H_d, are determined from the analysis of the creep regime presented in 2.4.2 [16, 18]. Particularly, as the creep law (2.75) is valid up to $H = H_d$, v_d corresponds to $v(H_d)$ in (2.81) and then

$$v_T = v_d \left(\frac{T}{T_d}\right)^{-\psi} . \tag{2.83}$$

This v_T value has a particular physical meaning. In velocity-field curves where the flow regime is observed, as for example the curves shown in figure 2.13, the v_T value was found to systematically coincide with the flow-regime velocity corresponding to H_d [18], this is $v_T = m\,H_d$, where m is the experimentally measured flow-regime mobility. Hence, v_T is the velocity that the domain wall would reach at $H = H_d$ in the absence of pinning.

The above discussion leads to a major conclusion of reference [18]: in a wide range of temperatures and for many different materials, the material- and temperature-dependent values v_d, T_d and H_d determined for the creep regime according to reference [16] can be used in order to successfully describe both the depinning regime in a given range $H_d < H < H_u$ and the flow regime in which $v = m\,H$ for a sufficiently high H. Furthermore, the critical exponents $\beta = 0.25$ and $\psi = 0.15$ are found to be consistent with the velocity-field characteristics in the depinning regime for all studied materials and temperatures. This accounts for the universal nature of the depinning transition.

In figure 2.15(b), the reduced velocity v/v_T is plotted as a function of the reduced field H/H_d for diverse magnetic thin films with perpendicular anisotropy at different temperatures, as indicated. The existence of an inflection point at $H = H_d$, expected according to the above discussion, is evidenced in all cases. The zero-temperature depinning function (2.82) with $v_H = v_T/0.65$ is plotted as a continuous line, and the flow regime $v = m\,H$ with $m = v_T/H_d$ is indicated as a dashed line. For fields slightly above H_d, thermal rounding effects are evidenced and monotonically grow with decreasing T_d/T values, hindering the experimental observation of the power-law $v \sim (H - H_d)^\beta$. However, there exists a limited range in which the zero-temperature law (2.82), which is naturally temperature-independent, describes the velocity vs. field characteristics even for finite temperatures. This corresponds to the dot-dashed straight line plotted in figure 2.15(a). For each curve, there exists an upper boundary of the depinning transition at H_u. Above this value, velocity undergoes a crossover until reaching the flow-regime proportionality $v = m\,H$.

The depinning of field-driven domain walls in the ferrimagnetic GdFeCo, which is one of the major subjects in this thesis, will be thoroughly discussed in chapter 4. One of the main subjects in our study is the depinning transition, which we successfully observe directly in a practically athermal scenario due to the huge value of the ratio T_d/T that we reach at low temperatures. Hence, our studies on the depinning transition in GdFeCo make relevant contributions to the above discussion on the universal depinning transition.

In the following, we will address another important subject of this thesis, related to the morphology of magnetic domain walls. Particularly, we shall present the theoretically predicted field-dependence of the length scales ℓ_{opt} and ℓ_{av} at which different domain wall displacement events occur, already introduced in 2.3.2, now considering the effect of temperature in the vicinity of the depinning transition. Accordingly, we will discuss the role of different roughness exponents in domain wall morphology at the different dynamical regimes.

2.4.4 Length scales and roughness exponents

As we have generally pointed out in section 2.3.2 for elastic interfaces in disordered media, domain wall dynamics close to the depinning transition and in the creep regime occur via the intermittent displacement of segments which have a characteristic size. We have already introduced ℓ_{opt} and ℓ_{av} as diverging characteristic lengths which correspond, respectively, to

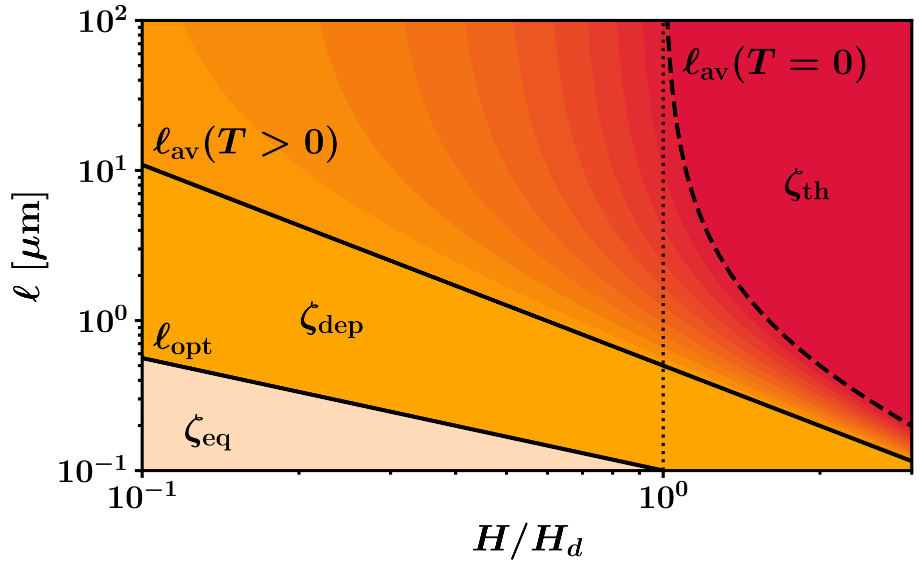

Figure 2.16: **Crossover diagram showing the field-dependence of characteristic length-scales and associated roughness exponents.** Optimal length $\ell_{\rm opt}$ and depinning avalanche length $\ell_{\rm av}$ as a function of the reduced field H/H_d in log-log scale. The expected behavior of $\ell_{\rm av}$ for $T=0$ and for finite temperatures is indicated. A typical Larkin-length value $L_c = 0.1\,\mu$m is considered. Different roughness exponents correspond to different length scale ranges: $\zeta_{\rm eq}$ corresponds to $L_c < \ell < \ell_{\rm opt}$, $\zeta_{\rm dep}$ to $\ell_{\rm opt} < \ell < \ell_{\rm av}$, and $\zeta_{\rm th}$ to $\ell > \ell_{\rm av}$.

the equilibrium reference state and the depinning critical point. For $T>0$ and in the limit $H \to 0$, a domain wall successively jumps over characteristic pinning energy barriers through events of typical length $\ell_{\rm opt} \sim H^{-\nu_{\rm eq}}$. For $T=0$ and in the limit $H \to H_d^+$, the domain wall experiences intermittent depinning avalanches of typical length $\ell_{\rm av} \sim (H-H_d)^{-\nu_{\rm dep}}$.

In figure 2.16, we illustrate the expected field-dependence of $\ell_{\rm opt}$ and $\ell_{\rm av}$ for magnetic domain walls in thin films. We consider that these characteristic sizes are crossover lengths between different interface morphological properties, characterized by different roughness exponents, as theoretically proposed [4, 41]. In the figure, we indicate the three exponents that are expected to govern domain wall morphology at different length scales: $\zeta_{\rm eq}$, $\zeta_{\rm dep}$ and $\zeta_{\rm th}$. In the following, we thoroughly discuss the hypothetical scenario illustrated in this figure.

As we have discussed in 2.4.2 the creep regime, theoretically corresponding to the limit $H \to 0$, stands in all the range $0 < H < H_d$. Accordingly, it is considered that $\ell_{\rm opt}$ has a field-dependence in all this range (see figure 2.16) which may be written as [40]

$$\ell_{\rm opt} = L_c \left(\frac{H}{H_d}\right)^{-\nu_{\rm eq}} . \tag{2.84}$$

The constant L_c is a characteristic material- and temperature-dependent length scale called the Larkin length [120], analogous to the Larkin-Ovchinikov length of vortices in superconductors [121, 122].

For the depinning avalanche characteristic length at zero temperature, we have [40]

$$\ell_{\mathrm{av}}(T=0) = \xi_0 \left(\frac{H - H_d}{H_d} \right)^{-\nu_{\mathrm{dep}}} , \tag{2.85}$$

where ξ_0 is another characteristic length scale of the order of L_c, i.e. $\xi_0 \approx L_c$ [109]. The behavior of ℓ_{av} at finite temperature is yet to be discovered. However, it is expected to be finite for $H \leq H_d$ at $T > 0$ [4, 41]. This hypothesis is illustrated in figure 2.16.

The determination of roughness exponents is crucially affected by the length scale ℓ at which domain wall morphology is observed. Indeed, the measured roughness exponent ζ is expected to change as the length scale of the measurement changes [41]: a particular roughness exponent is expected to be observable for scales below the characteristic size of the events giving rise to that exponent. Above this characteristic size, larger scale events are expected to determine the measured roughness.

In this framework, three different exponents describing domain wall roughness are considered, each of them corresponding to one reference state. The equilibrium roughness exponent ζ_{eq}, which corresponds to $H \to 0$ and $T > 0$, the depinning roughness exponent ζ_{dep}, corresponding to the depinning transition at $H \to H_d^+$ and $T = 0$, and the thermal roughness exponent ζ_{th}, which corresponds to the limit $H \to \infty$. This last exponent describes domain wall roughness in the limit at which pinning force effectively becomes a thermal-like noise [123]. Therefore, in the limit $H \to \infty$, domain wall roughness is induced by thermal-like fluctuations due both to disorder and to the actual thermal noise that is present at finite temperatures. The value of this exponent in the quenched Edwards-Wilkinson universality class is $\zeta_{\mathrm{th}} = 1/2$.

At other field and temperature conditions, each of these three exponents describe domain wall roughness at different length scales. In figure 2.16, we illustrate this scenario [41], considering length scales above the Larkin length[9]. For $L_c < \ell < \ell_{\mathrm{opt}}$, $\zeta = \zeta_{\mathrm{eq}}$. If $\ell_{\mathrm{opt}} < \ell < \ell_{\mathrm{av}}$, $\zeta = \zeta_{\mathrm{dep}}$. Finally, if $\ell > \ell_{\mathrm{av}}$, $\zeta = \zeta_{\mathrm{th}}$. In this context, the roughness of a magnetic domain wall at finite temperature T and for a given driving field $H < H_d$ may be affected by the three different values of ζ, depending on the length scales in which the observation is performed. For $H > H_d$, only depinning and thermal roughness exponents play a role and there exists a unique crossover length ℓ_{av} between the two behaviors.

The displacement-displacement correlation function $B(r)$ and the structure factor $S(q)$ that we have introduced in 2.3.1, equations (2.55) and (2.57), are the functions that we shall consider in order to characterize the roughness of a magnetic domain wall. In chapter 5 we will present our studies on domain wall roughness. There, we will discuss how the scenario illustrated in figure 2.16 affects these functions, what constitutes our framework for the interpretation of domain wall roughness measurements. In order to analyze if this scenario

---

[9] We shall recall the physical meaning of the Larkin length L_c below.

successfully describes domain wall roughness, we shall measure the field- and temperature-dependence of experimentally measured effective roughness exponents.

Some remarks on the Larkin length L_c and the pinning correlation length ξ_p

The Larkin length L_c that appears in (2.84) corresponds to the domain wall segment size at which pinning and elastic energies are equal [13]. Thus, for lengths $\ell > L_c$, a domain wall is affected mostly by disorder resulting in a rough shape, while for $\ell < L_c$ the domain wall elasticity wins over disorder resulting on a segment which is straight for $T = 0$, or which presents a roughness induced by thermal fluctuations for $T > 0$. In this context, a domain wall may be seen as a line formed by successive segments of size L_c, which are the smallest segments that may jump over energy barriers. As we will thoroughly discuss in chapter 5, our experimental observations of domain walls are made well above L_c and, consequently, we shall analyze domain wall roughness according to the scenario illustrated in figure 2.16.

The other fundamental characteristic length of the problem of an elastic line in a two-dimensional disordered potential is the correlation length of the pinning force, ξ_p, already mentioned in section 2.3.2. While L_c is a characteristic length along the domain wall, ξ_p is a characteristic length in the domain wall displacement direction. Therefore, while the typical length of depinning avalanches is given by (2.85), with $\xi_0 \approx L_c$ [109], the corresponding displacement is given by $\Delta u_{\text{av}} \approx \xi_p(\ell_{\text{av}}/\xi_0)^{\zeta_{\text{dep}}}$. Analogously, for the equilibrium critical point ($H \to 0$), the typical length of thermally activated events is ℓ_{opt}, given by (2.84), and the corresponding displacement is $\Delta u_{\text{opt}} \approx \xi_p(\ell_{\text{opt}}/L_c)^{\zeta_{\text{eq}}}$.

The correlation length of disorder ξ_p is rather difficult to quantify, as it is related to the sample heterogeneity responsible for domain wall pinning. Additionally, as a domain wall can only sense spatial variations of the pinning energy larger than its width, ξ_p must satisfy $\xi_p = \max(\delta, r_0)$, where δ is the domain wall width and r_0 is the characteristic length of random sample heterogeneity.

Fortunately, in the framework of collective pinning theory [121, 122], ξ_p is related to the depinning parameters H_d and T_d and to other measurable quantities as the saturation magnetization M_s, the domain wall energy σ and the sample thickness t. This relation may be expressed as [120]

$$\xi_p \approx \left(\frac{(k_B T_d)^2}{2 M_s \mu_0 H_d \sigma t^2} \right)^{1/3} \tag{2.86}$$

and results from the competition between elastic and pinning energy.

An analogous expression can be obtained for the Larkin length, now considering the competition between the Zeeman energy associated to the applied field and the pinning energy, whose effective magnitude is given by $k_B T_d$. The Zeeman energy per unit area associated to the complete inversion of magnetization in a thin film of thickness t is, in accordance with (2.2),

$$\varepsilon_Z(H) = 2\mu_0 H M_s t \; . \tag{2.87}$$

At depinning, characteristic energy barriers of magnitude $k_B T_d$ are overtaken through inversion events of characteristic size $L_c \xi_p$ which is the so-called Larkin surface area [120]. Therefore, we may write

$$2\mu_0 H_d M_s t L_c \xi_p \approx k_B T_d \; . \tag{2.88}$$

Combining relations (2.86) and (2.88), we obtain

$$L_c \approx \left(\frac{\sigma k_B T_d}{4t(\mu_0 H_d M_s)^2} \right)^{1/3} \tag{2.89}$$

for the Larkin length expressed in terms of material and temperature dependent measurable parameters. These expressions will be useful for the study of characteristic length scales which impact on domain wall dynamics and morphology both in chapters 4 and 5.

We have already presented in this chapter the main topics that are addressed by this thesis work and the fundamental concepts constituting their framework. However, we have not presented the particular material systems in which these phenomena are experimentally studied. In the following section, we will describe the main characteristics of the two magnetic thin films that we study in this thesis, namely the ferrimagnetic GdFeCo and the semiconducting (Ga,Mn)(As,P)/(Ga,Mn)As. We shall discuss about their particular properties, which make them suitable in order to study magnetic domain walls and, additionally, have given them a notorious interest in the last decades both from fundamental and applied points of view.

2.5 Studied magnetic thin films

The main scope of this thesis work is the experimental study of the topics we have introduced in this chapter: the dynamics and morphology of domain walls driven by magnetic field and by spin-transfer torque seen with the prism of statistical physics, i.e. focusing on the critical behaviors corresponding to different dynamical regimes. These phenomena occur within magnetic thin films, and even if many of its characteristics are universal and may be observed in a variety of systems, material properties are crucial in order to determine the experimental conditions that permit to observe them.

Furthermore, there exist groups of materials like the rare earth - transition metal ferrimagnetic alloys and the diluted ferromagnetic semiconductors which are of particular interest in the scientific community. The systems that we experimentally study in this thesis belong to these groups. As we will discuss in the following, amorphous rare earth - transition metal (RE-TM) ferrimagnetic alloys like GdFeCo present particular magnetization and domain wall dynamics and highly temperature-dependent properties due to the antiferromagnetic coupling of its two different sub-lattices. We will describe their main characteristics and discuss the field-driven domain wall dynamics in this system in section 2.5.1. On the other hand, the diluted ferromagnetic semiconductors (Ga,Mn)As and (Ga,Mn)(As,P) have a particularly efficient STT-driven domain wall motion, what makes them very suitable in order to study both field- and STT-driven domain wall motion. In section 2.5.2 we shall present their main characteristics and discuss the main features of STT-driven domain wall motion in these systems.

Both studied thin films present perpendicular magnetic anisotropy. This feature is crucial for our experimental studies, and constitutes an important advantage for the development of efficient spintronics devices [11, 12]. The origin of perpendicular anisotropy is manifold. In ultrathin metallic films as Pt/Co/Pt, with $t_{\mathrm{Co}} < 1\,\mathrm{nm}$, perpendicular anisotropy is promoted exclusively by a surface effect due to the hybridization of d orbitals in the interfaces between the ferromagnet (Co) and the heavy metal (Pt) [28, 124]. In amorphous RE-TM ferrimagnetic thin films with a higher thickness $t \sim 10\,\mathrm{nm}$, this surface effect is present but there exists an additional contribution to perpendicular anisotropy due to the anisotropic pairing of rare earth and transition metal atoms [29, 125]. In crystalline diluted magnetic semiconductors as (Ga,Mn)As, perpendicular anisotropy is originated in its interface with the substrate and it is associated to the valence band, which presents an anisotropy that imposes the direction of easy magnetization [126]. This effect can be controlled by deformations of the substrate [30, 127]; consequently, both in-plane or out-of-plane anisotropy can be induced in (Ga,Mn)As.

2.5.1 Rare earth - transition metal ferrimagnetic alloys

Even if many technological advances have been achieved in the field of spintronics, the efficient and fast manipulation of magnetization is still a key challenge in order to develop competitive, low-power devices [128–131]. In order to overcome the difficulties usually encountered in this field with the commonly used ferromagnetic metals, more complex systems are investigated. Particularly, materials in which an anti-ferromagnetic exchange coupling occurs constitute promising systems [132], as this type of interaction results in drastically reduced characteristic times of magnetization dynamics and, therefore, a faster motion of magnetic structures as domain walls [133].

However, if the two anti-ferromagnetically coupled sub-lattices are identical, as occurs in common anti-ferromagnets, sensing of magnetization structure constitutes a huge challenge [43]. This is due to the fact that in these materials, global magnetization is zero and, in addition, both sub-lattices react identically to electric or optical stimulus. This problem is overcome in ferrimagnetic materials like the rare earth - transition metal (RE-TM) alloys, in which the two sub-lattices are different [32]. In these systems, a rare earth as for example gadolinium or terbium provides electronic spins which are anti-ferromagnetically coupled with those provided by a transition metal, like cobalt or iron.

Three main exchange interactions give rise to ferrimagnetism in RE-TM alloys [134,

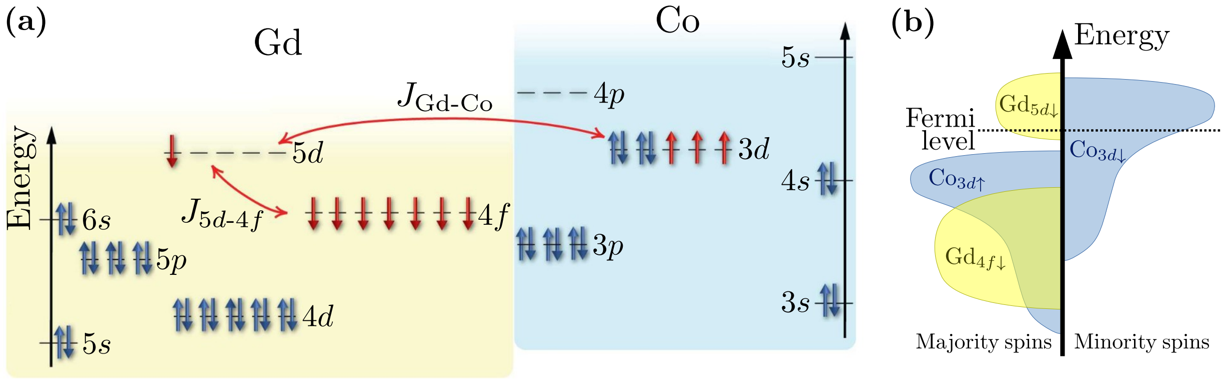

Figure 2.17: **Electronic states and exchange interactions giving rise to ferrimagnetism in a GdCo compound.** (a) Electronic structure. Ferromagnetically coupled $3d$ spins in Co are indirectly coupled anti-ferromagnetically with $4f$ localized spins in Gd via the ferromagnetic coupling between $4f$ and $5d$ spins in Gd, $J_{5d\text{-}4f}$, and the anti-ferromagnetic coupling $J_{\text{Gd-Co}}$ between bands $5d$ in Gd and $3d$ in Co, which are overlapped. Adapted from [137]. (b) Schematic spin-resolved density of electronic states. Yellow and blue regions correspond, respectively, to Gd and Co states.

[135]. Firstly, itinerant $3d$ spins belonging to the transition metal (normally Co and/or Fe) are coupled ferromagnetically, as explained by the Stoner model [136]. Additionally, these spins are anti-ferromagnetically coupled with itinerant $5d$ spins belonging to the rare earth (normally Gd or Tb) due to the overlap between these two bands, namely transition metal $3d$ and rare earth $5d$ bands. Finally, within the rare earth sub-lattice, $5d$ delocalized spins are ferromagnetically coupled with the localized $4f$ spins, giving rise to a big magnetic moment of this sub-lattice. In summary, ferrimagnetism in these RE-TM alloys arises from an indirect exchange interaction between rare earth $4f$ localized electrons and transition metal $3d$ itinerant electrons via the rare earth $5d$ electrons. In figure 2.17(a) we schematize the electronic structure for the case of a GdCo compound and the inter-band exchange interactions that we have just mentioned [137].

The interplay between sub-lattices in a RE-TM alloy results in a band structure in which conduction electrons, close to the Fermi level, mostly belong to transition metal d orbitals [138–140]. This band structure is schematized in figure 2.17(b) for the GdCo alloy [135]. As a major consequence, electric and optical stimulus over a RE-TM compound will affect mostly the transition metal electrons. This is crucial for magneto-optical measurements, which are sensitive to the magnetization of the transition metal sub-lattice rather than to the global magnetization of a RE-TM compound, as we will further discuss in chapter 3. This may be very advantageous for sensing magnetic states in situations in which the global magnetization is tiny, something usual for anti-ferromagnetically coupled sub-lattices.

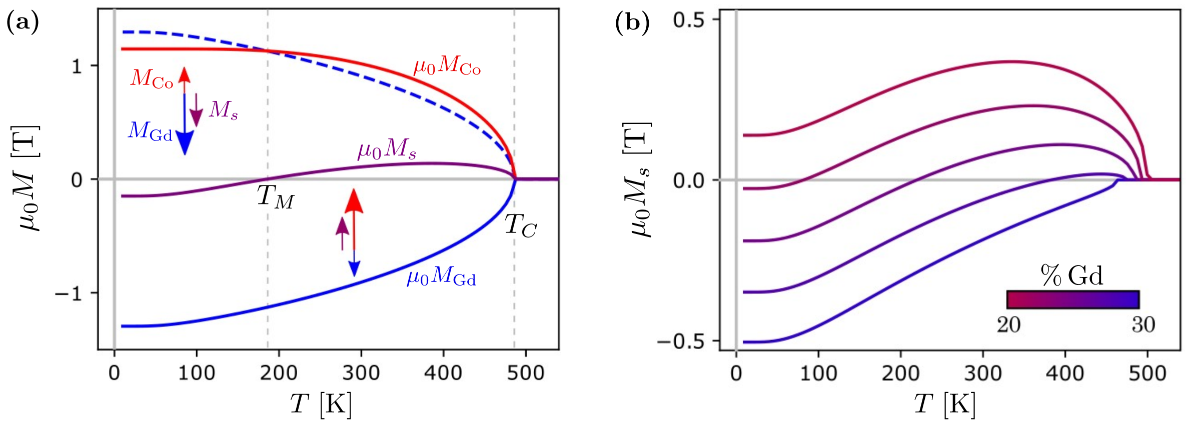

Figure 2.18: **Mean-field calculation of magnetization as a function of temperature in a ferrimagnetic GdCo alloy.** (a) Magnetization versus temperature for $\mathrm{Gd}_{0.25}\mathrm{Co}_{0.75}$, showing the $\mu_0 M$ vs. T dependence for oppositely magnetized Co and Gd sub-lattices, and the resulting saturation magnetization $\mu_0 M_s$, with a compensation temperature T_M where $M_s = 0$. The dashed blue line corresponds to $|\mu_0 M_{\mathrm{Gd}}|$. (b) $\mu_0 M_s$ vs. T for different Gd concentrations. Both figures are adapted from [135].

Temperature dependence of magnetization

A striking property of ferrimagnetic materials is the temperature dependence of their magnetic properties [32]. In a RE-TM alloy, saturation magnetization $M_s(T)$ results from adding the contributions corresponding to the two oppositely magnetized sub-lattices,

$$M_s(T) = M_{\mathrm{TM}}(T) + M_{\mathrm{RE}}(T) \; , \tag{2.90}$$

where $M_{\mathrm{TM}}(T)$ and $M_{\mathrm{RE}}(T)$ have opposite signs and correspond, respectively, to the transition metal and to the rare earth.

Following a mean-field theory approach and the Brillouin formalism [6], it is possible to analytically calculate the temperature dependence of magnetization in a RE-TM alloy [135, 137, 141]. In this model, an effective molecular field [48] resulting from the magnetic states of electrons in all the system is considered to act over each spin. In figure 2.18, the main results of this calculation are illustrated for the archetypal $\mathrm{Gd}_x\mathrm{Co}_{1-x}$ alloy, where x indicates the relative concentration of Gd, belonging to the range $0 < x < 1$ [135]. For this case, $M_{\mathrm{TM}} \equiv M_{\mathrm{Co}}$ and $M_{\mathrm{RE}} \equiv M_{\mathrm{Gd}}$.

In figure 2.18(a), magnetization of both sub-lattices and the resulting saturation magnetization are plotted as a function of temperature for $\mathrm{Gd}_{0.25}\mathrm{Co}_{0.75}$, i.e. $x = 0.25$ or, equivalently, 25 at% of Gd. Spontaneous magnetic order occurs below the Curie temperature T_C [6][10]. Below T_C, the sum of both contributions, M_{Co} and M_{Gd}, results in a particular

---

[10] In most cases, magnetic materials above T_C are paramagnetic.

temperature dependence $M_s(T)$, negative below a characteristic temperature T_M and positive above T_M. This indicates that for $T < T_M$, $|M_{\text{Gd}}(T)| > |M_{\text{Co}}(T)|$, while for $T > T_M$, $|M_{\text{Co}}(T)| > |M_{\text{Gd}}(T)|$. The temperature T_M corresponds to the magnetic compensation, such that $|M_{\text{Co}}(T = T_M)| = |M_{\text{Gd}}(T = T_M)|$ and then $M_s(T = T_M) = 0$. Due to the lower demagnetizing energy associated to low $M_s(T)$ values close to T_M, ferrimagnets close to magnetic compensation are adequate in order to reduce the size of magnetic structures [36, 142], what constitutes an advantage for the miniaturization of spintronics devices.

In figure 2.18(b), the calculated dependence of M_s as a function of T is plotted for $\text{Gd}_x\text{Co}_{1-x}$ with different values of x [135]. As evidenced, the change of Gd concentration in a reduced range ($x = 0.20$ to $x = 0.30$) changes drastically the magnetic properties. For $x = 0.20$, no compensation temperature exists and $|M_{\text{Co}}(T)| > |M_{\text{Gd}}(T)|$ in all the temperature range below T_C. In contrast, for $x = 0.30$ the opposite occurs: $|M_{\text{Gd}}(T)| > |M_{\text{Co}}(T)|$ for any temperature $T < T_C$. In the intermediate range, compensation temperature grows rapidly from 0 to T_C as x grows. Additionally, the Curie temperature T_C slightly decreases as x grows.

Field-driven domain wall dynamics

As we have just shown, ferrimagnetic materials present particularly temperature dependent magnetization properties. This directly affects field-driven domain wall dynamics, as the driving force over walls resulting from an applied field is a consequence of the Zeeman interaction, proportional to the saturation magnetization M_s. Consequently, for a given H, field-driven domain wall velocity v drops close to the magnetic compensation temperature T_M, where $M_s \to 0$. Even if this fact is deduced straightforwardly, the effects of the M_s vs. T dependence on the different dynamical regimes of domain walls are subject of several open questions as, for example, how depinning parameters as H_d, T_d and v_d are affected by magnetic compensation.

In the last years another particular characteristic of ferrimagnets, the compensation of its angular momentum, has given rise to a huge interest due to its direct impact on magnetization dynamics [33–35]. The angular momentum per unit volume $\vec{A}_m$ is related to magnetization as $\vec{A}_m = -\vec{M}/\gamma$, where γ is the gyromagnetic ratio [2]. Therefore, in a RE-TM alloy the angular momenta of both sub-lattices add up and we can write for the temperature-dependent angular momentum of the whole system

$$A_m(T) = -\frac{M_{\text{TM}}(T)}{\gamma_{\text{TM}}} - \frac{M_{\text{RE}}(T)}{\gamma_{\text{RE}}} \,. \tag{2.91}$$

As $M_{\text{TM}}(T)$ and $M_{\text{RE}}(T)$ are opposite, $A_m(T)$ may present a compensation temperature T_A such that $A_m(T = T_A) = 0$. If $\gamma_{\text{TM}} = \gamma_{\text{RE}}$, then the angular compensation coincides with its magnetic counterpart and $T_A = T_M$. However, the gyromagnetic ratios corresponding to both sub-lattices do not coincide in a RE-TM alloy and then $T_A \neq T_M$ [143, 144].

Recently, several experiments [35, 36, 145, 146] have shown impressively fast field-driven

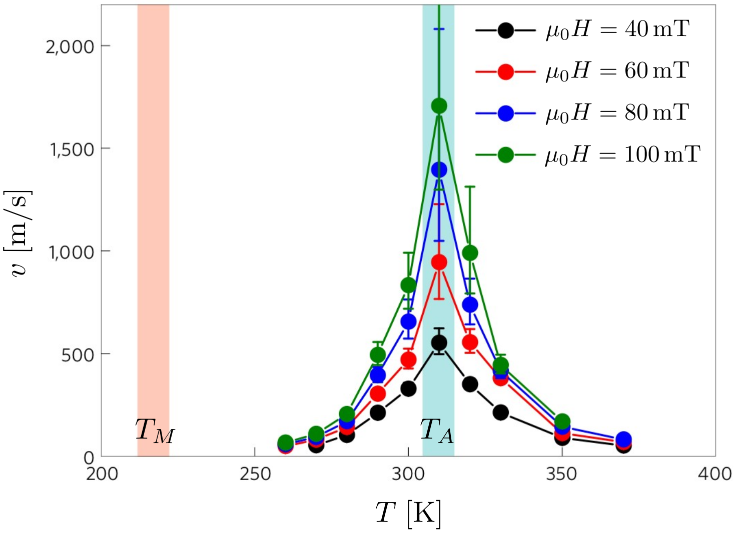

Figure 2.19: **Domain wall velocity peak associated to the angular momentum compensation in GdFeCo.** Domain wall velocity in the flow regime as a function of the temperature for different applied fields. The magnetic and angular compensation temperatures, T_M and T_A, are indicated as shaded vertical areas. Adapted from [35].

domain wall motion close to an angular compensation temperature $T_A \neq T_M$ [144]. This inequality is crucial for observing these high velocities because, as we have discussed above, field-driven domain wall velocity drops at $T = T_M$. In figure 2.19, we show the velocity vs. temperature dependence for different fixed applied fields measured by K.-J. Kim and collaborators in the flow regime of domain wall motion in a thin film of $\mathrm{Gd}_{0.230}\mathrm{Fe}_{0.674}\mathrm{Co}_{0.096}$ with a thickness $t = 30\,\mathrm{nm}$ [35]. Even if the angular compensation temperature has not been directly measured by the authors, they observe a notorious velocity peak which they associate to T_A. The measured magnetic compensation temperature T_M is also shown in the figure, considerably below T_A.

In order to assess if the observed separation between T_M and T_A is reasonable, we shall study the γ values of both sub-lattices. The gyromagnetic ratio of the sub-lattice i is $\gamma_i = g_i \mu_B / \hbar$, where g_i is the corresponding g-factor [6]. The g_i values that correspond to the two sub-lattices in a GdFeCo sample are $g_{\mathrm{FeCo}} \simeq 2.2$ and $g_{\mathrm{Gd}} \simeq 2.0$ [37, 147, 148], what results in $T_A > T_M$, as observed experimentally [35, 36, 144]. The $M_s(T)$ dependence measured by K.-J. Kim and collaborators and corresponding mean-field estimations of $M_{\mathrm{FeCo}}(T)$ and $M_{\mathrm{Gd}}(T)$ show consistency of equations (2.90) and (2.91) with the T_M and T_A values illustrated in figure 2.19 [149].

Even if the static magnetic properties of RE-TM alloys are now quite well understood [32], the dynamic properties are being intensely studied and a thorough comprehension is still lacking. Particularly, the magnetization dynamics close to the magnetic and angular compensation points are nowadays an important subject of study, as it is in these conditions that ferrimagnetic systems fundamentally differentiate from the much well understood ferromagnetic materials. In addition, in this context, adequate characteristics for technological applications arise, as we have already pointed out: close to T_M, magnetic structures are smaller [36], while close to T_A, faster magnetization dynamics occur [35].

Much of the work performed throughout this thesis consists on the study of the temperature dependence of domain wall dynamics in a GdFeCo thin film which, as we have just discussed, is full of rich phenomena. Even if many investigations have been performed on this topic during the last years, most of them have studied the flow regime, where wall velocities are high [35, 36, 145, 146, 150]. In contrast, little efforts have been devoted to studying the lower-velocity dynamical regimes, namely creep and depinning. In chapter 4 we shall thoroughly discuss the experimental studies performed during this thesis on the domain wall dynamics in GdFeCo, with particular focus on the temperature dependence of the key features of creep and depinning regimes. Before, in section 3.3, we shall describe the studied sample and present its magnetic characterization.

2.5.2 Diluted ferromagnetic semiconductors

Ferromagnetic semiconductors possess interesting and useful characteristics due to the combination of spontaneous magnetic order and particular transport properties, both of them being highly tunable by growth conditions, doping, strain, electric field, light, and electric current [42]. One of the most studied ferromagnetic semiconducting materials is the gallium arsenide doped with manganese, (Ga,Mn)As or $\mathrm{Ga_{1-x}Mn_xAs}$, which belongs to the group of the III-V semiconductors [30]. In this compound, the well-known GaAs is doped with a low concentration ($x < 0.10$) of substitutional Mn which occupies Ga sites in the zincblende structure characteristic of GaAs (see figure 2.20(a)) [151].

In $\mathrm{Ga_{1-x}Mn_xAs}$, both the mobility of charge carriers resulting on conducting properties and the ferromagnetic character arise from the incorporation of Mn ions: the onset of ferromagnetic order occurs for $x \approx 0.01$, while the transition from insulating to metallic character occurs for $x \approx 0.02$ [151]. Collective ferromagnetic order arises from the random distribution of spins corresponding to Mn ions which interact via an indirect exchange coupling. Mediators of this interaction are valence-band holes that are anti-ferromagnetically coupled with Mn spins [126]. However, the detailed nature of this interaction is still under debate [42, 151, 152].

The transition to the ferromagnetic phase in (Ga,Mn)As occurs well below room temperature; however, relatively high Curie temperatures have been obtained in this compound compared to other magnetic semiconductors [42, 151], reaching $T_C \simeq 190\,\mathrm{K}$. In figure 2.20(b), magnetization M and inverse susceptibility χ^{-1} are plotted as a function of temperature for a sample with substitutional Mn concentration $x = 0.07$ [151], where $\chi = \partial M/\partial H$ evaluated at $H = 0$. The Curie temperature in this case is $T_C \simeq 184\,\mathrm{K}$. This figure shows a textbook-like second-order paramagnetic-ferromagnetic transition, in which M vanishes with a power-law behavior for $T \to T_C^-$ while $\chi = \partial M/\partial H$ diverges for $T \to T_C^+$. Note the

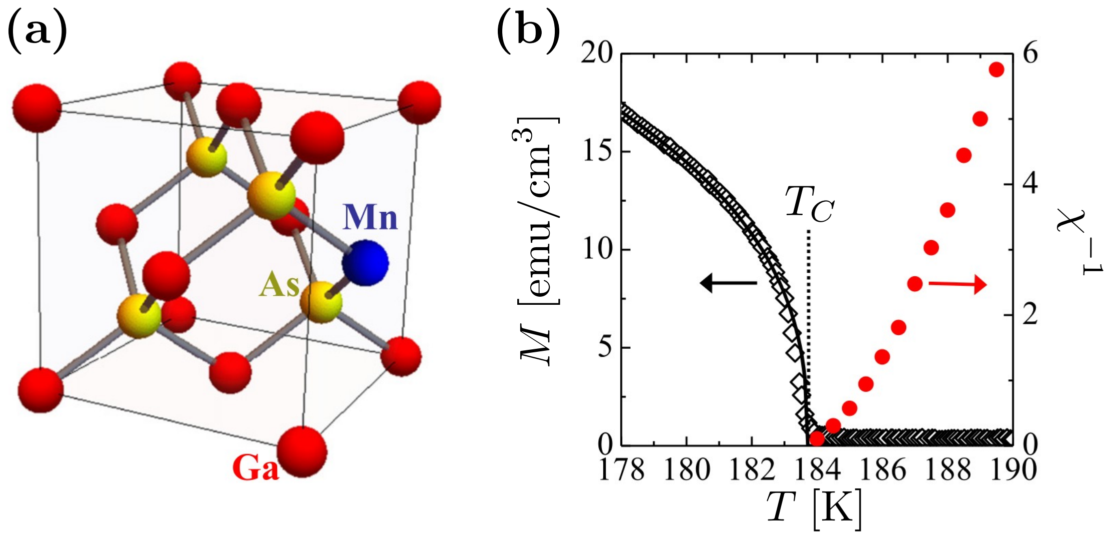

Figure 2.20: **Crystalline structure and temperature dependence of magnetization in (Ga,Mn)As.** (a) Zincblende crystalline structure corresponding to low concentrations of Mn, in which Mn ions substitute a small fraction of Ga ions. (b) M and χ^{-1} vs. T for a sample with substitutional Mn concentration $x = 0.07$, showing the onset of M and the divergence of $\chi = \partial M/\partial H$ characteristic of the paramagnetic-ferromagnetic transition at $T = T_C$. Both figures are adapted from [151].

similarity between this equilibrium second-order transition and the depinning dynamical transition of a driven elastic line illustrated in figure 2.11.

STT-driven domain wall dynamics

In metallic thin films, relatively high current densities are needed in order to generate a domain wall displacement via STT. As a consequence, the Joule heating due to current flow is highly restrictive, not only generating a sensible sample heating but also driving it to a demagnetized state [153]. In this context, most experiments on STT-driven domain wall motion in metallic thin films combine both field and current [154–157]. Domain wall motion driven exclusively by STT has been studied in metallic thin films with perpendicular anisotropy, but only relatively low velocities corresponding to the thermally activated creep regime have been measured for current densities of the order of 10^{10} A/m^2 [156, 158–160].

In contrast, STT in (Ga,Mn)As is particularly efficient, what makes this system paradigmatic for the study of STT-driven domain wall motion. Relatively fast wall dynamics have been observed for current densities as low as 10^8 A/m^2 [24, 26, 27, 161, 162], permitting to successfully observe domain wall motion in the creep, depinning and flow regimes without a problematic Joule heating [163, 164]. In figure 2.21, we show domain wall velocity curves, both field-driven (a) and STT-driven (b), corresponding to a bilayer of (Ga,Mn)(As,P)/(Ga,Mn)As with perpendicular anisotropy [27]. In these measurements,

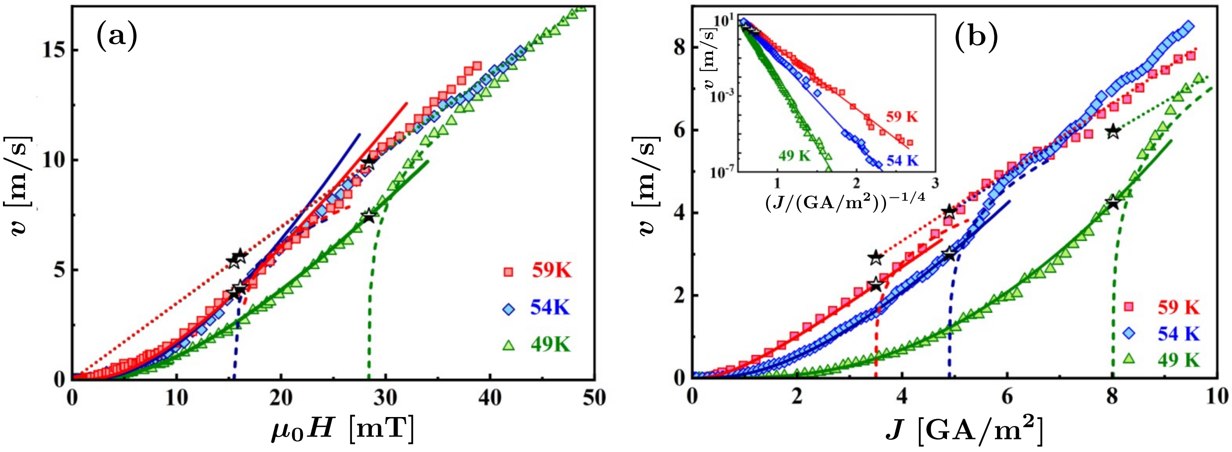

Figure 2.21: **Field- and STT-driven domain wall motion in perpendicularly magnetized (Ga,Mn)(As,P)/(Ga,Mn)As.** (a) Domain wall velocity v as a function of (a) the applied field $\mu_0 H$ and (b) the current density J for different fixed temperatures. Solid lines indicate creep regime fits with a creep exponent $\mu = 1/4$, while dashed lines correspond to the zero-temperature depinning transition and dotted lines to the flow regime. Inset of (b): creep-type plot of v in logarithmic scale vs. $J^{-1/4}$. Both figures are adapted from [27].

both for field- and STT-driven domain wall motion, we may observe the three dynamical regimes introduced in section 2.3.2, namely creep, depinning and flow.

Efficient STT in (Ga,Mn)As is a result of the low saturation magnetization M_s, of the order of 10 kA/m [26], which results in a high spin-drift velocity, equation (2.38). Simultaneously, a low domain wall width parameter $\Delta \sim 5\,\text{nm}$ [81] results in a high effective field corresponding to STT (see equation (2.42)).

In chapter 6, we will present the studies performed throughout this thesis on field- and STT-driven domain wall motion in a bilayer of (Ga,Mn)(As,P)/(Ga,Mn)As with perpendicular anisotropy which is nominally equivalent to the sample studied in reference [27]. We shall focus on the creep regime of motion and compare the driving forces generated by the applied field and current. Furthermore, we will study the effect of the combined application of both stimuli. Before, in section 3.4, we shall describe the main characteristics of the studied sample.

2.6 Chapter summary and thesis overview

In this chapter, we have presented the main topics that constitute the framework of this thesis. As we have evidenced, the experimental work that we will present in the following chapters is linked to a variety of big subjects, from the magnetism of nanostructured thin films to statistical physics and critical phenomena.

We have presented the big area of Magnetism and introduced the concepts of magnetic domains and domain walls in section 2.1. Then, in section 2.2, we have presented the main concepts on the micromagnetic theory of driven domain walls, introducing the applied magnetic field and the spin-transfer torque as possible driving forces. In section 2.3, we discussed the morphological and dynamical properties of elastic interfaces in disordered media, of which one example is magnetic domain walls. Then, in 2.4, we have shown how the theory of elastic interfaces in disordered media applies to the study of driven domain walls, focusing on the universality of the creep and depinning regimes and on the critical behaviors of characteristic length scales, closely related to domain wall roughness. Finally, in section 2.5, we have described the main properties of the studied material systems, which are perpendicularly magnetized thin films belonging to two interesting groups of materials: the rare earth - transition metal ferrimagnetic alloys and the diluted ferromagnetic semiconductors.

In the following, chapter 3, we shall present the main experimental techniques that we used throughout this thesis, focusing on the polar Kerr effect magneto-optical microscopy. In addition, we will describe the particularly studied samples, their growth methods and their magnetic characteristics. Then, chapters 4, 5 and 6 will be devoted to the presentation and discussion of the main experimental results obtained throughout this thesis. We shall cover:

- in chapter 4, the temperature dependence of field-driven domain wall dynamics in GdFeCo, focusing on the characteristics of observed dynamical regimes and the experimental determination of universal depinning critical exponents;
- in chapter 5, the study of domain wall morphology in GdFeCo as a function of temperature in the creep and depinning regimes, focusing on the determination of roughness exponents and associated characteristic length scales;
- in chapter 6, a study of the interplay between magnetic field and STT as domain-wall driving-forces in a bilayer of (Ga,Mn)(As,P)/(Ga,Mn)As, focusing on the creep regime.

Finally, in chapter 7, we will summarize our main conclusions and discuss the perspectives for future work on these subjects.

CHAPTER 3

Experimental techniques and studied samples

“De perto, ninguém é normal.”
Caetano Veloso, ***Vaca profana***

THE studies performed throughout this thesis are based on observations of magnetic domain walls in thin films. Therefore, both the experimental tools that permit these observations and the knowledge of the main characteristics of the studied thin films are fundamental for our research. The domain wall observation technique that we have used is the polar magneto-optical Kerr effect (PMOKE) microscopy, which permits to view magnetic structures in thin films with perpendicular anisotropy with an optical resolution of $\approx 1\,\mu$m. The studied thin films consist, on the one hand, on a ferrimagnetic and metallic thin film of GdFeCo and, on the other hand, on a ferromagnetic and semiconducting bilayer of (Ga,Mn)(As,P)/(Ga,Mn)As which has electrical contacts that permit current injection.

In this chapter, we will thoroughly describe our domain wall observation techniques and the main characteristics of the studied samples. Firstly, in section 3.1, we shall present the principles of magneto-optical Kerr effect imaging, focusing on the polar Kerr effect and the key parameters that permit to perform a good magnetic domain visualization. Secondly, in section 3.2, we will thoroughly describe the PMOKE microscopy setup that we have used: the optical system, the temperature control and magnetic field application setup, and our methods for domain wall dynamics measurements and wall profile detection. Then, in section 3.3, we shall describe the main characteristics of the studied ferrimagnetic GdFeCo sample: its growth methods and composition, and the magnetic characterization that we have performed in order to quantify its main global magnetic properties. Next, in section 3.4 we will describe the characteristics of the studied bilayer of (Ga,Mn)(As,P)/(Ga,Mn)As focusing on its particular shape, which permits to inject electric current in order to move domain walls via the spin-transfer torque mechanism. Finally, in section 3.5 we will conclude and summarize this chapter.

3.1 Magneto-optical Kerr effect imaging

Magneto-optical effects result from the influence of spontaneous magnetization and magnetic fields on the emission or propagation of light in matter [165], and they are the basis for the domain observation in magnetic materials. The transmission of light within a magnetized material results on a rotation of its polarization via the so-called Faraday effect [166]. Additionally, the polarized light which is reflected on a magnetic material's surface may undergo a change of its polarization via the so-called Kerr effect [167]. The first theoretical comprehension of these two effects was proposed by Lorentz [168], based on the idea that left- and right-circularly polarized light couple differently to electrons in the material. For this reason, Faraday and Kerr effects are circular birefringence effects. Other relevant magneto-optical effects are the Voigt [169], Cotton-Mouton [170] and gradient [171] effects. In addition, the Zeeman effect [172] consisting on the splitting of spectral lines of atoms in a magnetic field constitutes another magneto-optical effect of crucial importance in Physics, as it is very valuable for determining the structure of atoms, molecules and crystals.

The use of Kerr effect for the imaging of magnetic domains has become a technique of great importance in the last decades [1, 165]. Even if this effect is rather weak as compared with the Faraday effect[1], most magnetic materials are not transparent and then the transmission of polarized light necessary to exploit the Faraday effect is not possible. A breakthrough in the use of the Kerr effect for domain imaging came in the 1980s with the digital image processing [173], which permitted to get rid of the non-magnetic components of images by simply digitally substracting a background image. This made Kerr microscopy a paradigmatic technique in order to perform real-time observations of magnetic structures and magnetization dynamics. Since light in the visible spectrum is generally used, the optical resolution is typically of $\approx 1\,\mu$m.

---

[1] This difference is due to the fact that Kerr effect results from reflection, i.e. from the coupling of light with electrons in the material's superficial region, while Faraday effect results from transmission, what involves electrons in the whole sample's thickness.

3.1.1 Polar Kerr effect

As we have mentioned above, Kerr effect has its origin in the coupling of light with electrons within the superficial region of a magnetized sample, what impacts on the polarization of the reflected light. Hence, if a polarized light beam is reflected on a magnetized sample, its polarization may change according to the local magnetization in the region of incidence. Kerr effect may be exploited in order to observe domains in samples with in-plane and out-of-plane magnetization. However, different geometries are used in each case.

The so-called longitudinal and transverse geometries [1] permit to observe changes in the reflected polarization associated to the in-plane magnetization of a thin film. On the other hand, the polar configuration is used in order to observe domains in films with perpendicular anisotropy, where magnetization lies out-of-plane. Figure 3.1 shows a schematic representation which illustrates the geometry of the polar Kerr effect.

In this configuration, the incident light beam has a linear polarization and its direction of incidence forms an angle ϑ with the film normal $\hat{z}$. Additionally, the plane of polarization corresponds to the plane of incidence. In this context, the oscillating incident electric field $\vec{E}_{\mathrm{in}}$, with an amplitude A_{in}, generates an oscillation of electrons in the magnetized film's surface in the electric field direction. Then, as electrons are subject to a Lorentz force due to the magnetic field generated by out-of-plane magnetization $\vec{M}$, a component of electron motion arises in the $\hat{x}$ direction (see figure 3.1(a))[2]. Therefore, the reflected beam's electric field $\vec{E}_{\mathrm{re}}$ has two components: a regular component $\vec{E}_{\mathrm{N}}$ which lies in the plane of polarization of the incident beam, and a Kerr component $\vec{E}_{\mathrm{K}}$ which is perpendicular to $\vec{E}_{\mathrm{N}}$. We define the amplitudes of these two components as A_{N} and A_{K}, which satisfy $A_{\mathrm{N}} \gg A_{\mathrm{K}}$. The direction of the Lorentz force over electrons that generates the component $\vec{E}_{\mathrm{K}}$ depends on the direction of the out-of-plane magnetization, and then polarization of the reflected beam's electric field $\vec{E}_{\mathrm{re}}$ will be different for oppositely magnetized domains. The Lorentz force is maximum if $\vec{E}_{\mathrm{in}}$ and $\vec{M}$ are perpendicular and, therefore, the polar Kerr effect amplitude A_{K} is maximum for $\vartheta = 0$, i.e. for perpendicular incidence. If $\vartheta = 0$, by symmetry, the Kerr effect amplitude is equivalent for any polarization plane of the incident light beam.

3.1.2 Magneto-optical contrast

In order to assess the polarization of the reflected light beam, it is necessary to use an analyzer, i.e. a polarizer whose function is to discriminate between different angles of the polarization plane, resulting on different light intensities for differently polarized light beams. Let us consider a perpendicular incidence, i.e. $\vartheta = 0$, and an analyzer whose normal is set with an angle α_{a} with respect to the plane of polarization of the incident light, as indicated

---

[2] This oscillation occurs in a superficial region of several nanometers in metallic samples, corresponding to the so-called skin depth in which the electric field penetrates the sample's surface. Even if samples usually have a non-magnetic capping layer, the stray field due to the magnetic layer impacts on electron dynamics in this capping layer, what permits domain observation via the polar Kerr effect.

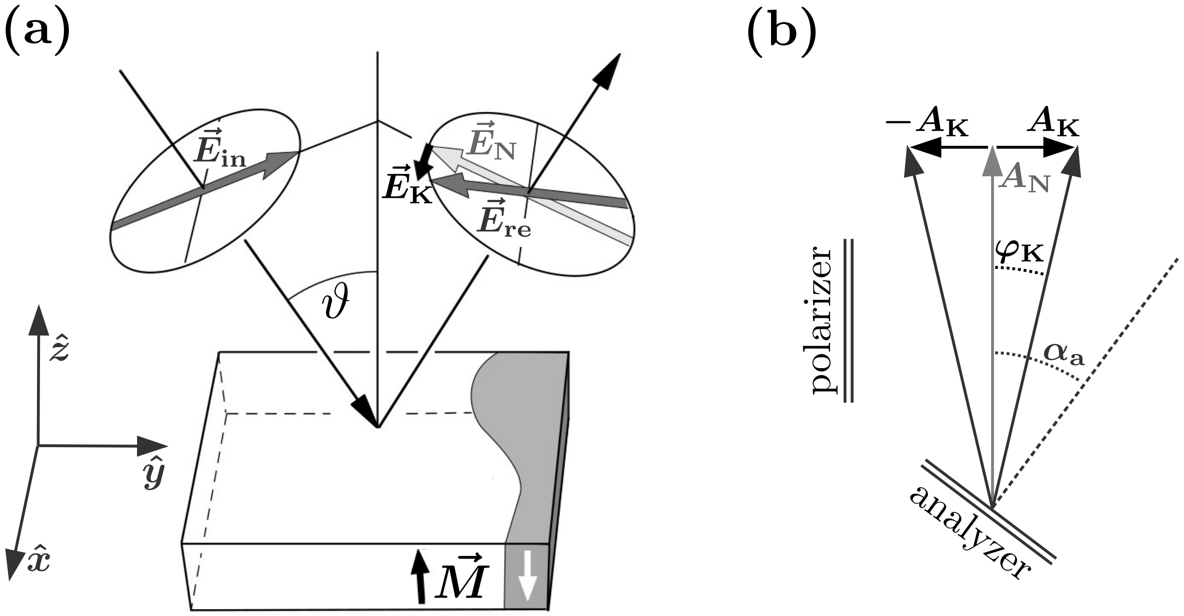

Figure 3.1: **Geometry of the polar Kerr effect.** (a) An incident linearly polarized light beam with its oscillating electric field $\vec{E}_{\mathrm{in}}$ is reflected in the surface of a magnetic thin film with out-of-plane magnetization $\vec{M}$. The angle between the direction of incidence and the film's normal $\hat{z}$ is ϑ, and the plane of polarization corresponds to the plane of incidence. The electric field of the reflected beam $\vec{E}_{\mathrm{re}}$ is the sum of the regular component $\vec{E}_{\mathrm{N}}$, which lies in the plane of polarization of the incident beam, and the Kerr component $\vec{E}_{\mathrm{K}}$, which is normal to $\vec{E}_{\mathrm{N}}$ and results from the contribution to the vibrational motion of electrons in the magnetized material due to the Lorentz force. The direction of the Kerr component depends on the direction of sample magnetization in the position where reflection occurs. Adapted from [1]. (b) Sum of regular and Kerr amplitudes, A_{N} and A_{K}, respectively. The direction of out-of-plane magnetization determines the direction of the Kerr amplitude. The Kerr rotation φ_{K} is defined as $\varphi_{\mathrm{K}} = A_{\mathrm{K}}/A_{\mathrm{N}}$ because $A_{\mathrm{N}} \gg A_{\mathrm{K}}$. The polarizer sets the direction of polarization of the incident light, which determines the direction of the regular component. The analyzer's normal is set with an angle α_{a} with respect to the polarizer in order to assess the polarization of the reflected beam.

in figure 3.1(b). In this context, considering that $A_\mathrm{N} \gg A_\mathrm{K}$, we define the so-called Kerr rotation as $\varphi_\mathrm{K} = A_\mathrm{K}/A_\mathrm{N}$. Accordingly, the signal amplitude transmitted by the analyzer is

$$A_\mathrm{a} \approx A_\mathrm{N} \sin\alpha_\mathrm{a} \pm A_\mathrm{K} \cos\alpha_\mathrm{a} \ , \tag{3.1}$$

where the sign of the Kerr component (i.e. the second term) is given by the direction of out-of-plane magnetization. Therefore, the intensities I_+ and I_- of oppositely magnetized domains may be written as [1]

$$I_+ = (A_\mathrm{N} \sin\alpha_\mathrm{a} + A_\mathrm{K} \cos\alpha_\mathrm{a})^2 + I_0 \tag{3.2}$$

and

$$I_- = (A_\mathrm{N} \sin\alpha_\mathrm{a} - A_\mathrm{K} \cos\alpha_\mathrm{a})^2 + I_0 \ . \tag{3.3}$$

Here, we have introduced a background intensity I_0 which accounts for the residual signal originated in the whole optical system. This component is present in any real magneto-optical imaging setup and should be minimized for better domain observation.

Note that $I_- = I_0$ for $\alpha_\mathrm{a} = \varphi_\mathrm{K} = A_\mathrm{K}/A_\mathrm{N}$. For this analyzer angle setting, if I_0 was negligible, light coming from one of the two types of domains would be completely extinguished. Consequently, one domain would appear completely dark, while the other would appear relatively bright, resulting on a good contrast between them. However, as we will see in the following, the optimization of the magneto-optical contrast is achieved for $\alpha_\mathrm{a} > \varphi_\mathrm{K}$ in real situations where the background intensity I_0 is present[3].

The relative magneto-optical signal s_mo is the difference between the intensities corresponding to the two domains,

$$s_\mathrm{mo} = I_+ - I_- = 2A_\mathrm{K}A_\mathrm{N} \sin(2\alpha_\mathrm{a}) \ , \tag{3.4}$$

and the magneto-optical contrast C_mo is defined as[1]

$$C_\mathrm{mo} = \frac{I_+ - I_-}{I_+ + I_-} \ . \tag{3.5}$$

The optimization of the magneto-optical contrast for visual observation of domains is achieved by maximizing C_mo. This occurs for an optimal analyzer angle $\alpha_\mathrm{a,opt}$ given by

$$\tan\alpha_\mathrm{a,opt} = \sqrt{\frac{A_\mathrm{K}^2 + I_0}{A_\mathrm{N}^2 + I_0}} \ , \tag{3.6}$$

which results in an optimal contrast

$$C_\mathrm{mo,opt} = \frac{A_\mathrm{K}A_\mathrm{N}}{\sqrt{(A_\mathrm{K}^2 + I_0)(A_\mathrm{N}^2 + I_0)}} \approx \frac{A_\mathrm{K}}{\sqrt{A_\mathrm{K}^2 + I_0}} \ , \tag{3.7}$$

---

[3] Another difficulty for the optimization of magneto-optical contrast is that the reflected polarization is usually elliptical. In order to get rid of elliptical polarization, a compensator such as a quarter wave plate is usually used.

where the approximation is valid for $A_\mathrm{N}^2 \gg I_0$. Therefore, if I_0 is sufficiently low, the optimal magneto-optical contrast depends only on the relation between A_K and I_0. Additionally, note that equation (3.6) indicates $\alpha_{\mathrm{a,opt}} > \varphi_\mathrm{K}$ for $I_0 > 0$.

The optimization of magneto-optical contrast according to equations (3.6) and (3.7) is usually not sufficient for obtaining the optimal domain observation. In practice, the signal to noise ratio obtained with a Kerr microscopy setup is usually the most significant parameter that has to be optimized in order to clearly observe magnetic domains. Therefore, the optimal analyzer angle α_a usually needs to be set to a higher angle than that indicated by (3.6).

Three main sources of noise may be identified for a Kerr microscopy setup like the one that we use in this thesis, in which images are digitally obtained by a CCD or a CMOS camera. First, the so-called shot noise, which is due to the quantized nature of light and varies with the square root of the photon number that arrives to the camera. Second, the electronic noise, which depends on the detection electronics and is usually independent of the light intensity. Third, the fluctuations in all the optical setup: the light source, the optical path including all optical elements, and the sample.

In this context, the optimal domain visualization is obtained for a condition of balance in which both a good magneto-optical contrast C_mo and a good signal to noise ratio are achieved. Once a sufficiently good magneto-optical contrast is set by the analyzer angle α_a, the exposure time Δt_exp of the camera may be set to sufficiently high values in order to obtain a signal which is significantly above the noise magnitude. Furthermore, digital contrast settings permit to focus on the intensity range in which the difference between oppositely magnetized domains is observed, therefore obtaining a well-defined domain visualization. This is possible if the intensities of oppositely magnetized domains are sufficiently well separated in the intensity range resolved by the camera. The discrimination of similar intensities is limited by the digital bit depth of the camera, which defines the number of gray levels that can be resolved. An additional way of enhancing domain observation is to digitally substract a background image corresponding to a saturated state of uniform magnetization, what permits to get rid of the backgroud intensity I_0 and highlights changes in magnetization with respect to the saturated state.

As an example of a good domain observation, in figure 3.2 we show a polar magneto-optical Kerr effect (PMOKE) image of a sample of GdFeCo. This image corresponds to one of two pieces of a Ta(5 nm)/$\mathrm{Gd_{32}Fe_{61.2}Co_{6.8}}$(10 nm)/Pt(5 nm) trilayer in which we performed studies on domain wall dynamics and morphology[4], and was obtained by merging 111 individual images that cover all the sample in a static magnetic configuration, at room temperature ($T \simeq 293\,\mathrm{K}$) and with no applied field. The individual images were obtained directly, without background substraction, with an exposure time $\Delta t_\mathrm{exp} = 200\,\mathrm{ms}$. As no background substraction was performed, some dust particles and the sample borders are clearly seen. This GdFeCo sample presents a large Kerr amplitude A_K due to a relatively strong coupling of itinerant $3d$ transition metal electrons with polarized light, as we have

---

[4] For sample details, see section 3.3.

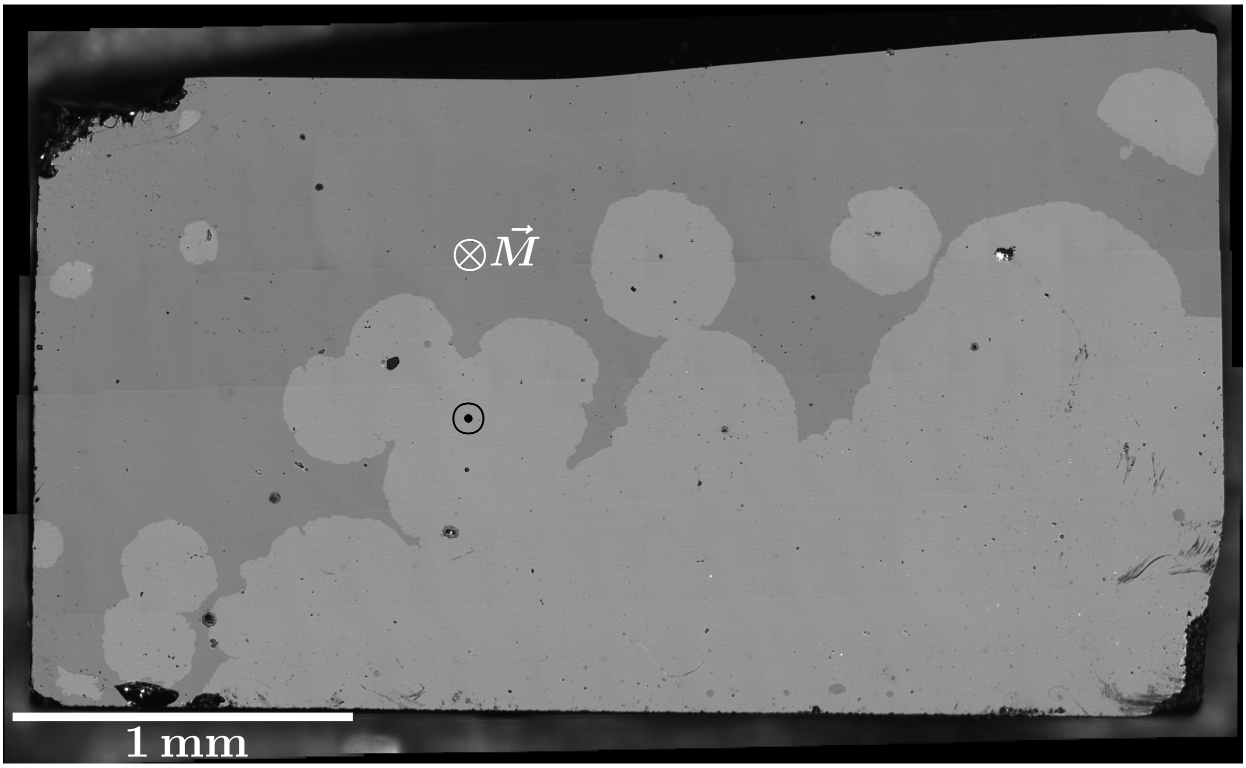

Figure 3.2: **Polar magneto-optical Kerr effect (PMOKE) image of a GdFeCo sample.** Obtained by merging 111 individual images at zero applied field, for a static magnetic configuration, at room temperature ($T \simeq 293\,\mathrm{K}$). The two opposite magnetization directions for the "clear" and the "dark" domains are indicated. The imaged sample is one of two pieces of a Ta(5 nm)/$\mathrm{Gd_{32}Fe_{61.2}Co_{6.8}}$(10 nm)/Pt(5 nm) trilayer studied in this thesis.

pointed out in section 2.5.1.

This PMOKE image satisfies the conditions for domain observation that we have discussed above. Firstly, a good contrast, which permits to clearly observe oppositely magnetized out-of-plane domains and the shape of domain walls separating them. Secondly, a good signal to noise ratio, as the observed domain intensities are very well defined, what evidences that noise is negligible as compared with the signal. Thirdly, a good use of the camera bit depth, as the magnetic signal, corresponding to the intensities of both domains, is within an intermediate intensity range while black and white pixels are found only in dust particles and sample borders.

In the following section, we shall present the PMOKE microscopes that we used in the course of this thesis. We will describe the optical setup, the temperature control setup, and the methods for domain wall velocity measurements and wall profile detection. Additionally, we will describe our methods for the application of magnetic field pulses of diverse durations, which is one of the key characteristics of our experimental setup.

3.2 Polar magneto-optical Kerr effect microscope

Two PMOKE microscopes were used for the studies on domain wall dynamics and morphology performed in the framework of this thesis. One of them is installed at the Magnetic Resonances Laboratory (*Laboratorio de Resonancias Magnéticas*) at *Centro Atómico Bariloche* (CAB), Bariloche, Argentina. The image shown in figure 3.2 was obtained using this setup. The other used microscope is installed at the Solid State Physics Laboratory (*Laboratoire de Physique des Solides*, LPS) in Orsay, France. This setup was used for all studies performed at temperatures $T \leq 275\,\mathrm{K}$.

3.2.1 Optical setup

Both used microscopes permit domain observation in perpendicularly magnetized thin films using an optical system that is schematized in figure 3.3(a). In the laboratory, this setup is assembled on an optical table of approximately $2 \times 1\,\mathrm{m}^2$. The elements L_1, L_2, L_3 and L_4 are optical lenses, while D_1 and D_2 are diaphragms. The diaphragm D_2 and the lens L_3, separated by the lens focal distance f_3, are the two fundamental parts of the objective lens. In order to optimize the polar Kerr contrast, the sample surface is normal to the incidence direction, what results on a common light path of the incident and reflected beams through the objective lens. The incident beam, which is generated at the light source and passes through a polarizer, is then separated in two components by a beam splitter, one of which is then reflected at the sample's surface. The reflected beam also passes through the beam splitter; the transmitted component is analyzed by another polarizer (the analyzer) and is finally collected by a camera. In practice, the light paths of the beams passing through the polarizer and the analyzer are not exactly perpendicular. The beam splitter angle is slightly tilted so that the parasite reflections on its surfaces do not impact on the image formed at the camera sensor.

The used light source is a high radiance red LED with dominant wavelength $\lambda \simeq 630\,\mathrm{nm}$. The camera is based on CCD or CMOS technologies and has a bit depth of 14 bits; this means that $2^{14} = 16384$ intensities may be differentiated by the camera electronics. This bit depth, much higher than the 8 bits of common screens in which only 256 intensities may be differentiated, is crucial for discriminating similar signal intensities by appropriately setting the digital contrast. The polarizer and analyzer qualities are also crucial for domain observation: as the Kerr rotation φ_{K} is generally very small, a very well polarized incident light beam and a good discrimination of different polarization directions by the analyzer are needed in order to observe a measurable Kerr signal. This condition is achieved by using polarizers with a good extintion ratio. This key parameter corresponds to the ratio of transmitted light polarized in the set direction with respect to the transmitted light with perpendicular polarization. Particularly, the polarizers used in the microscope installed at CAB (both the polarizer and the analyzer) are of the type Glan-Thompson, model *Newport 10GT04*, while the ones used in the microscope installed at LPS are of the type Glan-Taylor,

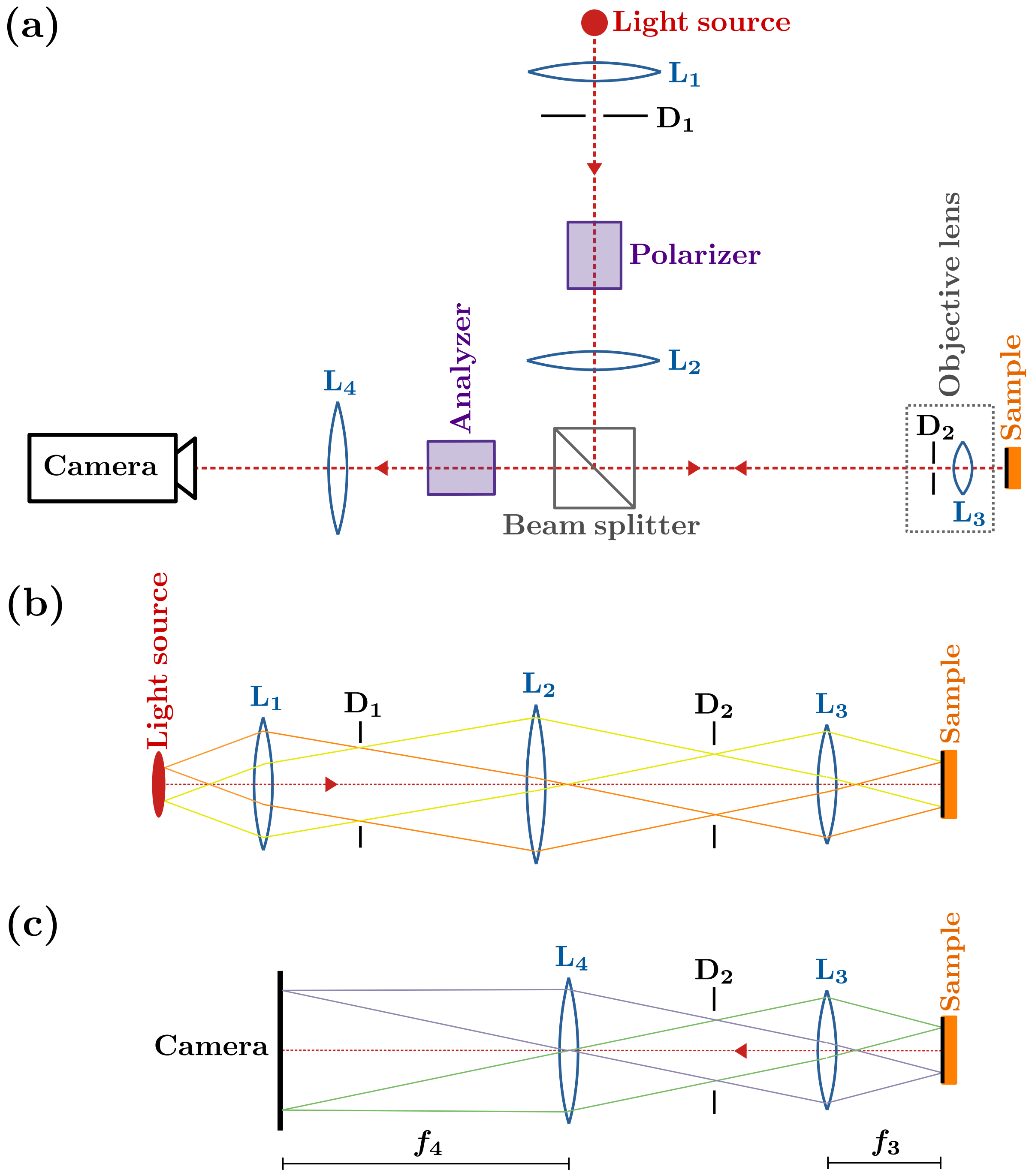

Figure 3.3: **Optical setup of the used PMOKE microscopes.** (a) Schematic representation of the whole optical system indicating all the relevant elements. (b) Illumination path. (c) Imaging path.

model *Casix PGT515*. These polarizers have an extintion ratio $\sim 10^5$.

Let us now describe the optical paths which are illustrated in figures 3.3(b,c). In panel (b), we illustrate the illumination path, i.e. the light path from the light source up to the sample surface. For simplicity, we do not draw the polarizer and the beam splitter. The shown arrangement corresponds to the Köhler illumination [1, 165], which permits to uniformly illuminate the sample surface. This is accomplished by generating an image of the LED light source in the back focal plane of the objective lens, which corresponds to the position of the diaphragm D_2. In this way, each point of the region of interest in the sample receives light from all the punctual sources that compose the LED; therefore, the inhomogeneity of the light source does not impact on the illumination. Additionally, note that D_1, the so-called field diaphragm, is placed in a sample's conjugate plane. Therefore, an image of D_1 is formed on the sample surface. This diaphragm, which has an adjustable aperture, permits to filter diverging rays, hence avoiding unwanted effects such as aberrations and reflections in the borders of the optical elements. The lens L_1 is the so-called collector lens, as it "collects" light coming from the LED source, changing its propagation direction towards the center of the light path.

In figure 3.3(c) we illustrate the imaging path, i.e. the reflected light path from the sample towards the camera. This arrangement permits to form an image of the illuminated region of the sample's surface on the camera sensor. The relation between the illuminated area in the sample and its size in the sensor is given by the relation between the focal distances f_4 and f_3 of the lens L_4 and the objective lens L_3, respectively. In addition, a Bertrand lens may be added between D_2 and L_4 in order to project the image formed at the back focal plane (at D_2) on the camera sensor, what permits to test the correct arrangement of the illumination path [174]. In accordance with the above discussion, a good illumination is obtained if an image of the light source is formed at the camera when using the Bertrand lens.

The camera sensor is an array of individual CCD or CMOS sensors, each of them corresponding to one pixel. The size of the individual sensors and its relation with the ocular magnification given by f_3 and f_4 determine the pixel size of PMOKE images. Additionally, given a pixel size, the number of pixels determines the field of view. In the setup of the microscope installed at CAB, we have used a *QImaging EXi Blue* CCD camera with 1392×1040 pixels. Each individual CCD sensor has a size of $6.45 \times 6.45\,\mu\text{m}^2$. In the microscope installed at LPS, we have used an *ORCA-Flash 4.0 V2* Digital CMOS Camera with 2048×2048 pixels. In this camera, each individual CMOS sensor has a size of $6.5 \times 6.5\,\mu\text{m}^2$. Both cameras have a bit depth of 14 bits, as we have mentioned above.

Both microscopes are equipped with 5× and 20× objective lenses *Olympus LMPLFLN*, with working distances f_3 of 22.5 mm and 12 mm, respectively. In the setup of the microscope installed at CAB, the pixel size is $0.47\,\mu$m if we use the 5× lens, while it is $0.12\,\mu$m if we use the 20× lens. In the microscope installed at LPS, the pixel size for the 5× lens is $0.69\,\mu$m while for the 20× lens it is $0.17\,\mu$m. While a higher pixel size permits to observe a larger area of the sample surface, a lower pixel size permits to observe slow domain wall motion and lower-scale morphological properties. As the optical diffraction limit of red light is $\approx 1\,\mu$m, the resolution cannot be much lower than this value. However, in order to achieve such resolution it is necessary to have a significantly smaller pixel size. This condition is satisfied when we use the 20× lens.

Finally, the focal distances of the other three lenses, namely L_1, L_2 and L_4, are the following. In the microscope installed at CAB, $f_1 = 150\,$mm, $f_2 = 400\,$mm and $f_4 = 500\,$mm. In the microscope installed at LPS, $f_1 = 70\,$mm, $f_2 = 250\,$mm and $f_4 = 300\,$mm. These distances correspond to the light path lengths between the light source and L_1, L_2 and D_2, and L_4 and the camera sensor, respectively, as we have indicated in figure 3.3(b,c).

3.2.2 Temperature control

The studied magnetic samples consist in multilayers deposited on top of a silicon substrate. The bottom side of the substrate is glued to a thermally conducting sample holder. In addition, the sample holder may be precisely positioned by three micrometric positioners in the directions x, y and z, what permits a good focus of the sample image in the focal plane of the objective lens and a precise selection of a region of interest in the sample surface.

The sample holder is thermally connected to a cooling system and a resistive heater. Additionally, a resistive thermometer is fixed close to the sample in order to sense its temperature. The thermometer and the heater are connected to a PID temperature controller system. The correct balance between the cooling and the heater power permits to stabilize the temperature to a desired value. The heater power is set by the PID (proportional-integral-derivative) algorithm according to the target temperature (set-point), the temperature measured by the thermometer, and the P, I and D values. These three parameters need to be tuned depending on the set-point and the system's cooling power in order to achieve a stable temperature at the desired value.

Temperature control close to room temperature

In the setup installed at CAB, we have developed and constructed a sample holder with temperature control which may be used for temperatures $T \gtrsim 280\,$K up to $T \simeq 360\,$K. The lower limit is due to the fact that the sample remains in atmospheric conditions, what according to the ambient temperature and humidity may cause the condensation of water droplets in the sample surface. The upper limit is a security limit below which we are sure that the used sample and other elements of the sample holder are not affected. In this thesis, we used this sample holder for measurements of domain wall dynamics in GdFeCo in the range $283\,\mathrm{K} \leq T \leq 353\,\mathrm{K}$.

The sample holder consists in an metallic piece of aluminium of approximately $5 \times 2 \times 2\,\mathrm{cm}^3$. The sample is glued on one of its ends with *GE 7031* varnish, while the opposite end is attached to a cold finger made of numerous copper wires which are $\sim 30\,\mathrm{cm}$ long. These wires are immersed in liquid nitrogen (LN_2) which is contained in a Dewar flask. The thermal contact of the sample holder with the LN_2 permits its cooling and that of the sample.

Additionally, a resistive heater that consists in a wire winding of manganin is coiled on the metallic sample holder and is therefore in thermal contact with it. A Pt-100 thermometer is placed in a hole of the sample holder, approximately 5 mm away from the sample. Both the heater and the thermometer are connected to a PID temperature controller which, according to a PID algorithm, permits to stabilize the temperature to a chosen set-point value. As all our measurements are made at fixed temperatures, before each measurement we tune the P, I and D parameters in order to obtain a stable fixed temperature with fluctuations below 0.01 K. Note that, for the range $283\,\mathrm{K} \leq T \leq 353\,\mathrm{K}$, this magnitude of the fluctuations represents less than 0.01 %.

Temperature control at low temperatures

In the microscope installed at LPS, we have performed measurements of domain wall dynamics and observations of domain wall morphology in the range $10\,\mathrm{K} \leq T \leq 302\,\mathrm{K}$. The exploration of such a wide temperature range could be performed by using an optical cryostat. Particularly, we have used an open-cycle gas flow optical cryostat *CryoVac KONTI Micro* with nitrogen or helium as circulating gases according to the desired sample temperatures. When using nitrogen, we could explore all the range of temperatures above 77 K, while the use of helium permitted to cool the sample down to 4 K. The used cryogenic gas was pumped through the cryostat using a mechanical pump. Additionally, an insulating vacuum is needed in order to cool the sample well below room temperature[5]. We achieved an insulating vacuum of 10^{-5}-10^{-6} mbar using an *Edwards TIC* pumping station with both a mechanical and a turbomolecular pump.

The fixed metallic sample holder inside the cryostat is in thermal contact both with the flowing gas circuit and with a resistive heater. Additionally, a Cernox thermometer is placed in the interior of the sample holder. Both the heater and the thermometer are connected to a PID temperature controller. The cooling power depends strongly on the insulating vacuum, the rate of gas flow and the actual temperature. Additionally, the sample holder's heat capacity strongly depends on the temperature, and thus the heater power needs to be precisely controlled at very different values according to the desired temperature. Therefore, the P, I and D parameters had to be tuned for obtaining the stability at each studied temperature. The fluctuations were verified to be always below 0.01 K.

---

[5] Such vacuum is crucial both for thermal insulation and for preventing the condensation of water and the formation of ice, what would damage the sample and the whole system installed inside the cryostat.

3.2.3 Domain wall velocity measurement

Let us now describe our methods for measuring the mean magnetic domain wall velocity resulting from the application of an external out-of-plane magnetic field. As we will further discuss in chapter 6, an equivalent method is applied when driving domain walls with current. Figure 3.4(a-b) shows two PMOKE images obtained at CAB which correspond to two successive wall configurations in the GdFeCo sample studied throughout this thesis, at $T = 295\,\mathrm{K}$. Note that, in these PMOKE images, the diaphragm D_1 appears as a focused dark frame due to its correct positioning in a sample's conjugate plane (see figure 3.3(b)). The domain wall displacement occurring between these two configurations was induced by a square-shaped magnetic field pulse generated by a coil.

As shown in figure 3.4(c), after nucleating and positioning a domain wall in the microscope field of view, successive pulses of magnitude H and duration Δt are applied, and PMOKE images are acquired before and after these pulses, when no field is applied. The domain wall displacement may be measured by performing a substraction of two successive wall configurations, as shown in panel (d). For obtaining a representative value for the domain wall displacement Δu, we measure several displacements Δu_i at different wall positions using the *ImageJ* software and we repeat this procedure for different field pulses of the same magnitude and duration. For each H and Δt, we obtain 10-20 individual displacements Δu_i. We then obtain Δu and its uncertainty as the mean value and the standard deviation of Δu_i, respectively.

Assuming that the domain wall moves at a constant mean velocity $v(H, T)$ during all the time Δt in which the pulse is applied, we calculate the mean wall velocity as $v = \Delta u/\Delta t$. For the case illustrated in figure 3.4, i.e. $T = 295\,\mathrm{K}$, $\mu_0 H = 5.57\,\mathrm{mT}$ and $\Delta t = 10\,\mathrm{ms}$, we obtain $v = (3.2 \pm 0.3) \times 10^{-3}\,\mathrm{m/s}$.

The hypothesis that the mean domain wall velocity is stationary for the field magnitudes and pulse times for which we have performed wall velocity measurements has been carefully verified. In figure 3.5 we show the measured domain wall displacements as a function of the pulse duration for two different applied field magnitudes which result in strongly different wall velocities, at $T = 295\,\mathrm{K}$. In panel (a), we plot Δu vs. Δt for $\mu_0 H = 3.82\,\mathrm{mT}$. Note that the application of pulses with durations ranging between 1 and 15 s result on an equivalent domain wall velocity $v = \Delta u/\Delta t$, as indicated by the straight line and the shaded region which correspond to $v = (9.2 \pm 0.4)\,\mu\mathrm{m/s}$. This particular value results from analyzing the wall displacements Δu_i resulting from the application of a 15 s-pulse. This evidences that the mean domain wall velocity is stationary during the field pulse duration and depends only on $\mu_0 H$.

In figure 3.5(b), we show a similar plot for a field magnitude $\mu_0 H = 11.0\,\mathrm{mT}$ which results in a much faster domain wall motion. Two different pulse durations are considered, $\Delta t = 1$ and $5\,\mu\mathrm{s}$. For $\Delta t = 1\,\mu\mathrm{s}$, the mean domain wall velocity results $v = \Delta u/\Delta t = (12 \pm 2)\,\mathrm{m/s}$, while for $\Delta t = 5\,\mu\mathrm{s}$ we obtain $v = \Delta u/\Delta t = (11 \pm 1)\,\mathrm{m/s}$. As both results are equal within their error bars, we may also claim that the domain wall velocity is practi-

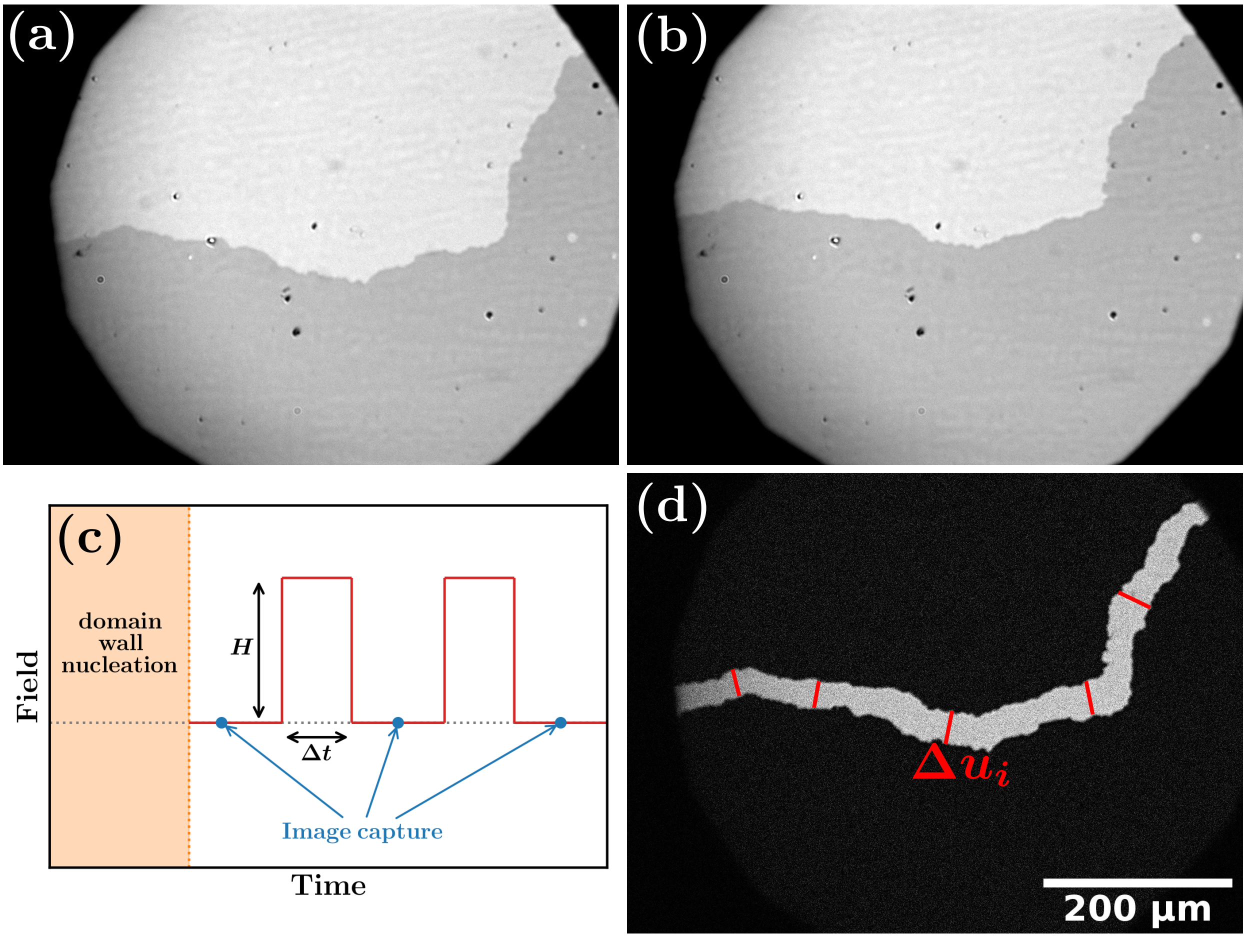

Figure 3.4: **Domain wall velocity measurement.** (a) PMOKE image of a domain wall in the studied GdFeCo sample, nucleated after applying several pulses of $\mu_0 H = 5.57\,\mathrm{mT}$ and $\Delta t = 10\,\mathrm{ms}$ at $T = 295\,\mathrm{K}$. The diaphragm D_1 is observed as a dark frame. (b) Domain wall configuration after applying an additional pulse of the same magnitude and duration. (c) Measurement protocol, indicating that the images showing successive positions of a domain wall are taken at $H = 0$, before and after the application of square-shaped field pulses. (d) Differential image obtained by computing the difference between (a) and (b). The domain wall displacement Δu and its uncertainty are measured by considering displacements Δu_i occurring at different positions and due to equivalent field pulses and computing their mean and standard deviation. For this field magnitude and pulse duration, we obtain $\Delta u = (32{\pm}3)\,\mu\mathrm{m}$; thus, the domain wall velocity results $v = \Delta u/\Delta t = (3.2{\pm}0.3){\times}10^{-3}\,\mathrm{m/s}$.

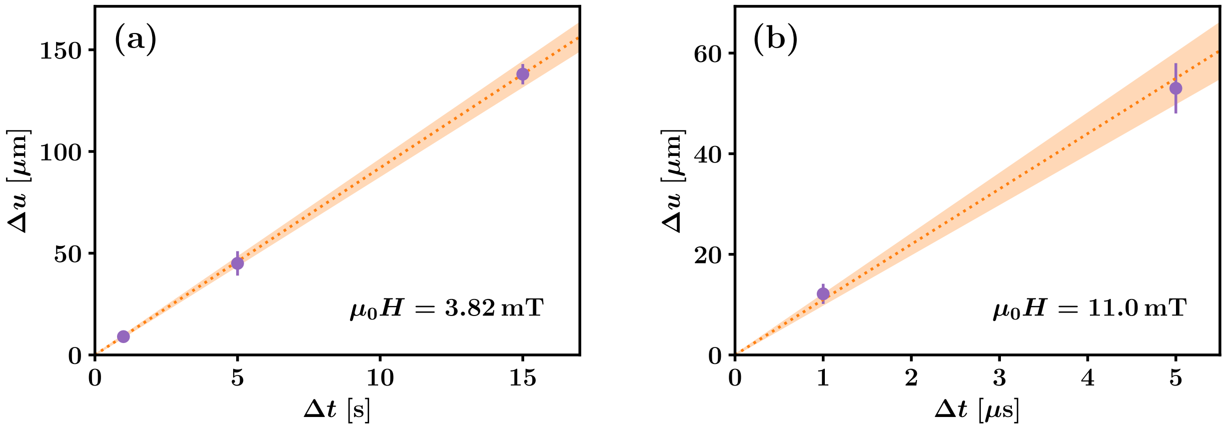

Figure 3.5: **Domain wall displacement as a function of the pulse time.** (a) Wall displacements Δu resulting from the application of pulses with a magnitude $\mu_0 H = 3.82\,\mathrm{mT}$ in the studied GdFeCo sample at $T = 295\,\mathrm{K}$. The pulse durations Δt are 1, 5 and 15 s. All measured displacements are consistent with a domain wall velocity $v = \Delta u/\Delta t = (9.2 \pm 0.4)\,\mu\mathrm{m/s}$, represented by the dotted line and the shaded region. (b) Fast wall displacements Δu resulting from the application of short pulses with a magnitude $\mu_0 H = 11.0\,\mathrm{mT}$ in the same sample, at the same temperature. The pulse durations are $\Delta t = 1$ and $5\,\mu\mathrm{s}$. Both measured displacements are consistent with a wall velocity $v = \Delta u/\Delta t = (11 \pm 1)\,\mathrm{m/s}$ which is represented by the dotted line and the shaded region.

cally stationary within the pulse duration even for this relatively fast domain wall motion. This analysis has been repeated in all the range of studied velocities and for each studied temperature. Due to the limited field of view of the PMOKE microscope, the comparison between pulse times which differ in more than an order of magnitude was not possible.

Let us finally make a remark regarding the initial domain wall state, i.e. the procedure for nucleating a domain wall before measuring its velocity (see figure 3.4(c)). When possible, we have nucleated this domain wall with the same field magnitude for which we would then perform velocity measurements. This prevents any dependence of the wall velocity on its initial state, as we are interested on the stationary domain wall velocity. In the range of low fields, which do not permit domain nucleation, we have applied a higher magnitude pulse in order to nucleate a domain wall, and then applied several pulses of the desired field magnitude in order to generate a proper initial state. We then measured wall velocities starting from this state in order to get rid of any impact of the nucleation field magnitude.

3.2.4 Magnetic field pulses

The above discussion evidences that a good control of the applied field magnitude, the pulse duration and the pulse shape is crucial for an adequate domain wall dynamics measurement. Particularly, our method requires the field pulses to be square-shaped. In addition, several orders of magnitude in the wall velocity are explored: we have measured velocities ranging from 10^{-9} to 10^{2} m/s. While the measurement of the lowest velocities require the application of a magnetic field during times of the order of an hour, the measurement of the highest velocities require the application of field pulses of $\sim 1\,\mu$s.

As we have studied mainly the thermally activated creep regime and the depinning regime (see section 2.4), several orders of magnitude in the velocity are covered with relatively narrow field ranges. For this reason, in most of our measurements, the main limitations for measuring high velocities is the need of a too short pulse duration rather than a too high field. Regarding the lowest velocities, the main difficulties arise from the fact that the stability of the sample position and the optical system may be lost during a long measurement, what may result on a lost of the sample focus and/or a difficult comparison between images before and after the field application. Additionally, the current that is applied in a coil in order to generate a magnetic field produces its heating, what prevents the field application during long times in conditions for which the necessary field magnitude is relatively high.

We have used three types of coils in order to cover a wide domain wall velocity range. Firstly, a "large coil" which has a bore diameter of $\simeq 3$ cm is fixed to the optical table and is placed in the same position as the objective lens, i.e. the objective lens is placed in its interior. It consists in a wire winding of copper coiled on an aluminium piece. The copper wire has a diameter of $\simeq 1.8$ mm. The same type of large coil is used both in the microscope installed at CAB and at LPS. As it is big with respect to the sample size, the field generated by this coil is uniform in all the sample, and thus the calibration of the out-of-plane field magnitude as a function of the applied current is easy to perform. For the microscope installed at CAB, the field vs. current factor is 3.48 mT/A, while for the microscope installed at LPS it is 2.62 mT/A. We have used these coils for driving domain walls with pulses of durations $\Delta t \geq 1$ s, what corresponds to wall velocities up to 10^{-4} m/s.

Secondly, we used a medium sized coil which has a bore diameter of ~ 0.5 cm and is made of a copper wire which has a diameter of ≈ 0.3 mm. In order to make measurements with this coil, we place it on the sample holder, above the sample, allowing the light path to enter through its bore. For the field to be uniform in the microscope's field of view, we observe a sample region which is centered with respect to the coil. As this coil is relatively small, the generated field $\mu_0 H$ when applying a given current I depends on the position of the observed region. Additionally, as the domain wall velocity depends strongly on the field, the most precise way to calibrate the field $\mu_0 H$ vs. applied current I dependence of this coil consists in comparing velocities measured with this coil and with the large coil. This is, after having measured several velocities with the large coil, we measure similar velocities as a function of I using the smaller coil and tune the calibration factor $\mu_0 H/I$ so that both measurements are consistent between each other. For the measurements made with the medium sized coil that are presented in this thesis, the used field vs. current factor is 26.5 mT/A. We have used a unique calibration factor because all the domain wall velocity measurements performed with this coil correspond to the same sample region, with a fixed position of the coil.

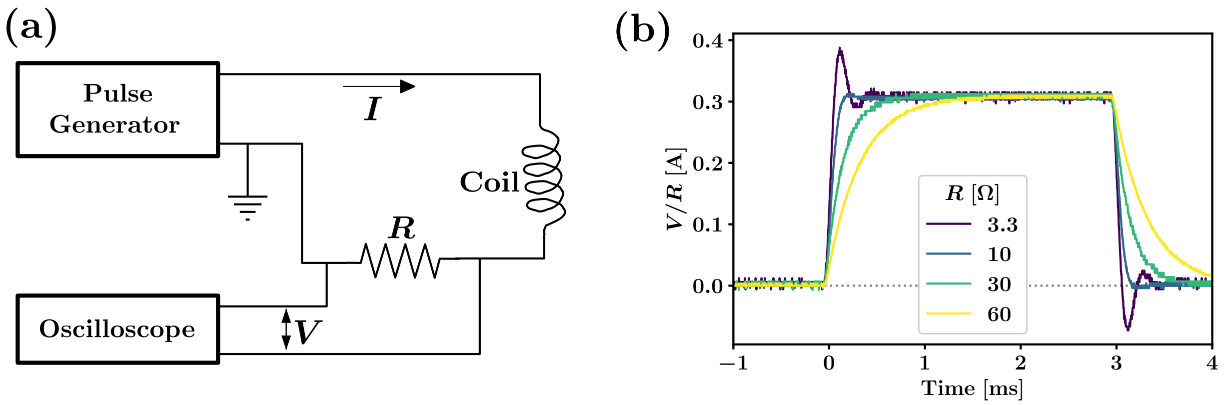

Figure 3.6: **Application of field pulses and measurement of their shape when using the medium sized coil.** (a) Schematic representation of the circuit. A pulse generator applies a current pulse through a circuit formed by a coil and a resistance R, connected in series. The voltage V measured by the oscilloscope is proportional to the current I flowing through the circuit. (b) Observed pulse shapes detected by the oscilloscope for a current $I = 300\,\mathrm{mA}$ and an applied pulse duration $\Delta t_{ap} = 3\,\mathrm{ms}$, for different magnitudes R of the resistance connected in series with the coil.

We have used the medium sized coil for field pulses of durations ranging between 1 ms and 500 ms. We therefore have access to velocities ranging between 10^{-5} and 10^{-1} m/s using this coil. The lower limit for the pulse time is due to the rise time of the circuit used for applying pulses, and the upper limit is due to excessive coil heating. In figure 3.6(a), we show a schematic representation of the circuit used for applying field pulses with the medium sized coil. The use of a resistance in series with the coil is important both for obtaining square-shaped pulses and for sensing the pulse shape with an oscilloscope. In figure 3.6(b), we show the observed pulse shapes for a current $I = 300\,\mathrm{mA}$ and an applied pulse duration $\Delta t_{ap} = 3\,\mathrm{ms}$. As evidenced, changing the magnitude R of the resistance connected in series results in different pulse shapes. For the shown case, the optimal pulse shape is obtained for $R = 10\,\Omega$ and we therefore use this resistance value for domain wall velocity measurements. However, different field amplitudes and pulse durations may require a change on the used resistance due to changes in the internal configuration of the pulse generator. The rise time t_{rise} (equal to $\simeq 0.2\,\mathrm{ms}$ for the case shown in the figure for $R = 10\,\Omega$) is considered for computing domain wall velocities, i.e. $v = \Delta u/\Delta t$ with $\Delta t = \Delta t_{ap} - t_{rise}$. The used equipment when applying field pulses with the medium sized coil are an *Agilent B2902A* pulse generator and a *Tektronix TDS 2024B* oscilloscope.

Finally, the measurement of velocities ranging between 10^{-1} and 10^{2} m/s was made using tiny coils made with ~ 50 turns of a copper wire of $\simeq 100\,\mu$m in diameter. We made these coils by rolling the copper wire on a toothpick, gluing it externally to a teflon piece, and finally taking away the toothpick. We then attached the teflon piece on the sample holder, above the sample, so as to see the sample surface through the coil center, which has a diameter of 0.5-1 mm. The limited number of turns of these coils permits to obtain a rise time well below the microsecond. Concomitantly, a relatively high current needs to be

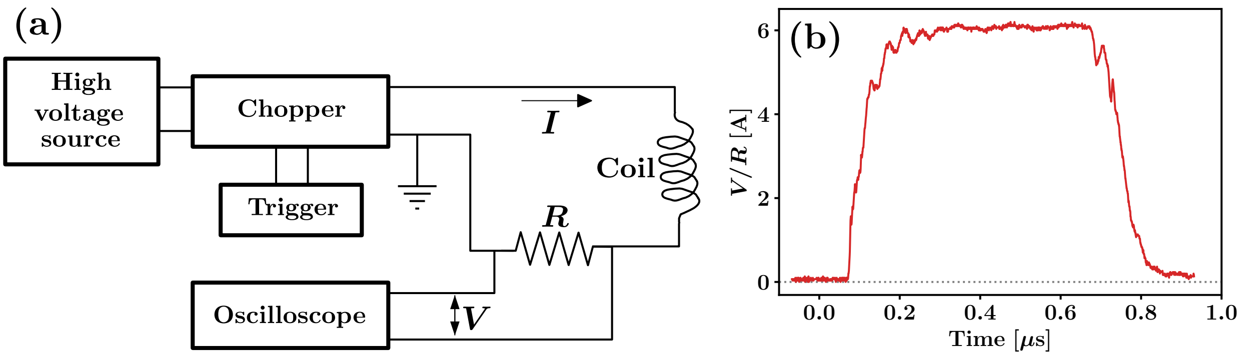

Figure 3.7: **Application of short field pulses and measurement of their shape.** (a) Schematic representation of the circuit. The trigger is a pulse generator which applies a 5 V pulse of a duration Δt_{ap} on the chopper, which releases the voltage generated by the high voltage source during Δt_{ap} in the circuit formed by a tiny coil and a $50\,\Omega$ resistance R connected in series. The oscilloscope detects the voltage on the resistance, which is proportional to the current I flowing through the circuit. (b) Typical pulse shape measured with the oscilloscope, for the shortest applied field pulses, corresponding to $\Delta t = \Delta t_{ap} - t_{rise} = 0.5\,\mu$s.

applied in order to generate the magnetic field necessary to measure domain wall velocities above ~ 1 m/s. For this reason, we have used a high-voltage source connected to a chopper that, when triggered by a 5 V pulse during a desired time Δt_{ap}, discharges during this time the voltage set by the source. The high voltage pulse is applied on a circuit in which the tiny coil is connected in series with a $50\,\Omega$ resistance in order to adapt the impedance of the circuit with that of the chopper. This resistance is required for optimizing the pulse shape and also for observing it with an oscilloscope. In figure 3.7(a) we show a schematic representation of the setup.

The drawback of this short pulse application setup is that it does not support pulse times well above $10\,\mu$s. This is due to the fact that the high voltage discharged by the chopper is stable during a limited time. For higher pulse times, their application should be made with a pulse generator using the circuit shown in figure 3.6(a), with the difficulty that pulses applied in this way using a tiny coil are more limited on its magnitude. Some of the measurements at intermediate domain wall velocities were made in this way, using a pulse generator *HP 8114A*.

In figure 3.7(b) we show a typical short pulse, applied with a tiny coil used for the highest velocity measurements presented in this thesis. The observed rise time t_{rise} of the circuit is $\approx 0.1\,\mu$s. As when using the medium sized coil, the pulse shape was monitored in all our measurements and the rise time was considered and substracted from the applied pulse time for measuring wall velocities; this is, we assume the effective application of a square-shaped pulse with a duration $\Delta t = \Delta t_{ap} - t_{rise}$. The validity of this approximation was verified by the independence of the wall displacement with Δt, as we have shown in figure 3.5. In other words, for the velocity measurements that we present in this thesis, the domain wall displacement during the rise time is negligible with respect to the displacement during the time Δt in which the current through the coil is maximum. This verification also permits to discard other transient effects that could affect the applied field control as, for example, the induction of eddy currents in the sample holder.

The pulse shown in figure 3.7(b) corresponds to $\Delta t = 0.5\,\mu$s, which is the lowest pulse time used in our measurements, and a field magnitude $\mu_0 H = 19.6\,$mT. As this coil is extremely small and thus the field is not uniform, the dependence of the effective field magnitude with the current in the coil is calibrated in terms of the domain wall velocity, by the overlap of equal velocity measurements made with different coils. Particularly, the applied field when using the medium sized coil is obtained in terms of the measurements made with the large coil as we have explained above and, in turn, the applied field when using a tiny coil is obtained in terms of the measurements made with the medium sized coil. In some particular cases, measurements made with a tiny coil could be directly compared with those made with the large coil. Once the calibration factor $\mu_0 H/I$ is well established for a particular coil and sample region, velocities are measured always in the same region, what allows us to use the obtained factor.

3.2.5 Domain wall profile detection

In order to study domain wall morphology, it is important to develop tools that permit to obtain the function $u(x)$ describing a wall profile (see section 2.3.1). In the following, we briefly describe the method we have applied for detecting wall profiles, which was developed by Daniel Jordán and Sebastian Bustingorry [175].

The description of one-dimensional elastic interfaces in a two-dimensional disordered medium that we have presented in section 2.3 assumes that the interface lies in a given direction $\hat{x}$ and, thus, the movement occurs in the perpendicular direction, $\hat{y}$. Therefore, an imaged domain wall must lie, on average, in a given direction in order to describe it in this framework. Figure 3.8(a) shows a PMOKE image of an horizontally lying domain wall. This image was obtained by substracting a background image for contrast enhancement and then applying a gaussian blur for noise reduction. Additionally, in order to obtain an horizontal wall, we have selected a wall segment which is straight on average and, then, we have adequately rotated the image.

Once we have obtained an image as the one shown in figure 3.8, panel (a), we proceed to the domain wall profile detection. In panel (b), we show the intensity profile corresponding to an arbitrary position $x = x_0$. The domain wall position at $x = x_0$, $u(x_0)$, is determined as the middle of the range $[y_1, y_2]$ in which the derivative of the signal intensity vs. y dependence overcomes an appropriately defined threshold. The used threshold corresponds to 0.9 times the maximum value of the intensity vs. y derivative. This procedure is repeated for all x positions, what permits to define the univalued function $u(x)$ shown in panel (a). Note that the analyzed domain wall segment must not have overhangs in order to define a

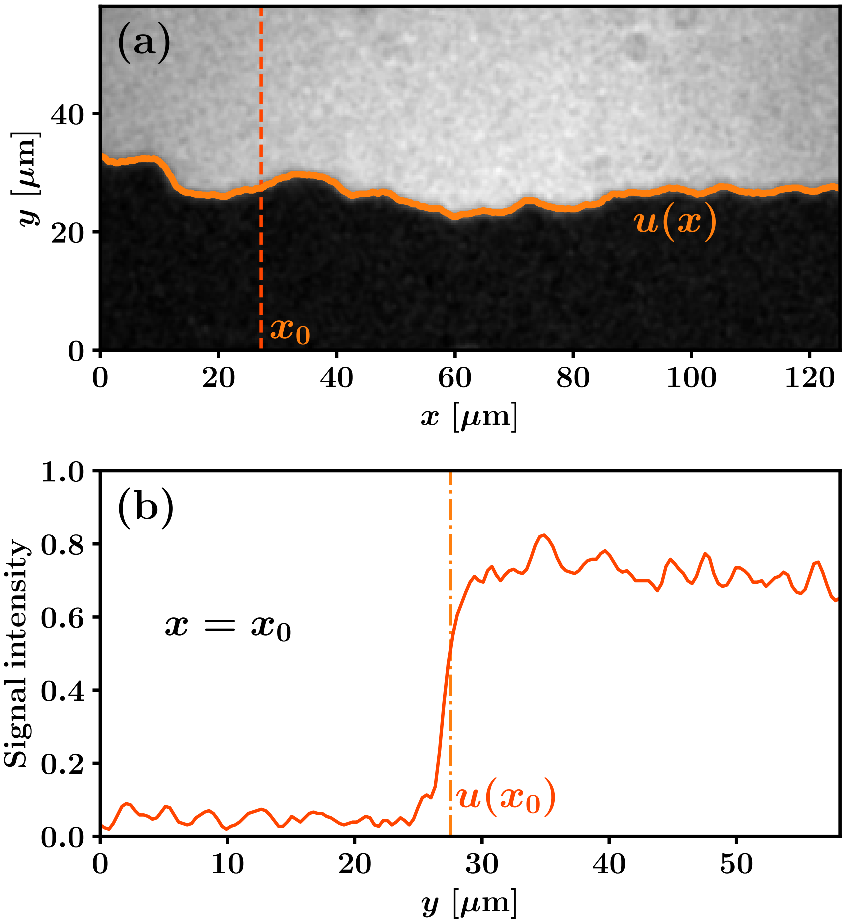

Figure 3.8: **Domain wall profile detection.** (a) PMOKE image of an horizontally lying domain wall whose profile is described by the function $u(x)$. A background substraction and a gaussian blur filter has been applied to the original image. The domain wall was imaged after several pulses of $\mu_0 H = 5.71\,\mathrm{mT}$ and $\Delta t = 2\,\mathrm{s}$ at $T = 275\,\mathrm{K}$. (b) Signal intensity vs. y corresponding to an arbitrary position $x = x_0$, indicated in (a). The determined domain wall position at $x = x_0$, $u(x_0)$, is indicated.

$u(x)$ function that correctly describes it. For more details on the algorithm for domain wall profile detection, see reference [175].

The detection of domain wall profiles has been used throughout this thesis for the analysis of wall roughness (presented in chapter 5) and for the study of domain wall velocity correlations (presented in section 4.3.4). The obtained wall profiles were analyzed at different temperatures and with no applied magnetic field, i.e. in a static configuration, after the application of field pulses. For example, the domain wall shown in figure 3.8(a) was obtained after applying several pulses of $\mu_0 H = 5.71\,\mathrm{mT}$ and $\Delta t = 2\,\mathrm{s}$, at $T = 275\,\mathrm{K}$, what corresponds to a domain wall velocity $v = 2.7\,\mu\mathrm{m/s}$. As the exposure time used for obtaining images, $\Delta t_{\mathrm{exp}} = 200\,\mathrm{ms}$, is relatively long, it is not possible to image well defined domain wall profiles with applied field for most of the studied velocities. Even if this is a limitation for optimally describing the morphology of moving domain walls, in chapter 5 we will see that the domain wall morphological properties are dependent on the state of motion just before turning off the applied field, what allows for a study of domain wall morphology as a function of field and temperature in our experimental conditions. This can be explained by considering that domain walls are quenched to a metastable state associated to the applied field value just before this field is turned off. Their relaxation to an equilibrium state occurs in a timescale which is considerably longer than any experimental timescale [176].

3.3 Thin film of GdFeCo

One of the two types of magnetic thin films that we have studied in this thesis is a rare earth - transition metal ferrimagnetic alloy, the GdFeCo[6]. The particular studied sample is a trilayer of Ta(5 nm)/$Gd_{32}Fe_{61.2}Co_{6.8}$(10 nm)/Pt(5 nm) deposited by radio-frequency (RF) sputtering on a silicon substrate with a thermally oxidized upper layer SiO_2(100 nm). The sub-indexes are nominal concentrations and the thicknesses of each of the three layers are indicated in parentheses. This sample was grown at the Lawrence Berkeley National Laboratory in United States by the group of J. Gorchon, C.-H. Lambert, S. Salahuddin and J. Bokor.

The buffer and capping layers of Ta and Pt are crucial for the surface properties of the ferrimagnetic GdFeCo layer, and they therefore strongly affect the magnetic properties of the whole sample and impact on domain wall motion. First, they prevent the formation of oxide. Second, they enhance the perpendicular magnetic anisotropy [28, 124], even if in GdFeCo this anisotropy is mainly due to the anisotropic pairing of Gd and FeCo atoms [29, 125]. Third, the buffer Ta layer reduces inhomogeneity of the bottom GdFeCo surface. Additionally, these heavy metals enhance other effects related to the spin-orbit coupling like the Dzyaloshinskii-Moriya interaction [55–57, 177]. However, studying the influence of these effects on domain wall motion is beyond the scope of this thesis.

The grown sample was divided in two pieces of similar size; one of them, whose complete PMOKE image is shown in figure 3.2, was studied at CAB, the other one was studied at LPS. The studies on domain wall dynamics and morphology performed in both sample pieces, which are presented in chapters 4 and 5, are consistent between each other.

3.3.1 Magnetic characterization

In order to characterize the global static magnetic properties of the studied sample, we have performed several magnetometry measurements. These studies permitted us to obtain relevant quantities as the saturation magnetization M_s, the coercive field H_c and the anisotropy energy K_{eff} as a function of temperature. In the following, we present and discuss these

---

[6] For a description of the general properties of this type of systems, see section 2.5.1.

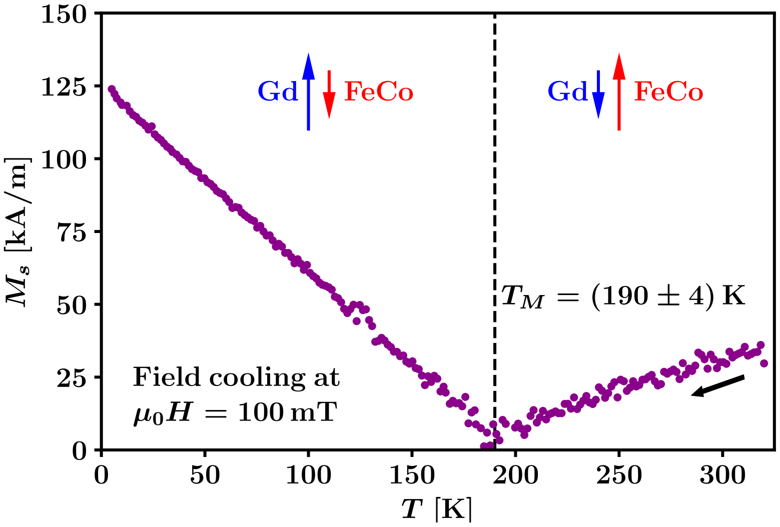

Figure 3.9: **Saturation magnetization as a function of temperature in GdFeCo.** SQUID magnetometry measurement made by cooling from $T = 320$ K to $T = 5$ K with a fixed applied field of 100 mT. The obtained magnetic compensation temperature, indicated as a vertical dashed line, is $T_M = (190 \pm 4)$ K. Below T_M, the Gd sub-lattice magnetization dominates over the FeCo magnetization. Above T_M, the FeCo magnetization dominates.

measurements.

Figure 3.9 shows a measurement of the saturation magnetization M_s as a function of the temperature T, carried out with a SQUID magnetometer *Quantum Design MPMS* which is placed at the Low Temperatures Laboratory at CAB. This measurement was made by cooling from $T = 320$ K to $T = 5$ K with a fixed applied field $\mu_0 H = 100$ mT so as to assure that the sample magnetization corresponds to the saturated state. Note that, in the studied range, the magnetization decreases with decreasing temperature from $M_s \simeq 30$ kA/m at $T = 320$ K to $M_s \approx 0$ at $T = 190$ K. This particular temperature corresponds to the magnetic compensation temperature, which we may quantify from this measurement as $T_M = (190 \pm 4)$ K. Below T_M, M_s grows linearly with decreasing temperature until $M_s \simeq 120$ kA/m for $T = 5$ K.

Note the similarity between the measured M_s vs. T dependence and the general expected behavior that is illustrated in figure 2.18. The fact that in our measurement M_s is always positive is due to the orientation of the global magnetization in the direction of the applied field. As we have discussed in section 2.5.1, the Gd sub-lattice magnetization is larger than the FeCo magnetization below T_M while the opposite occurs above T_M. Exactly at T_M, both sub-lattices are compensated.

A further characterization of the sample's magnetic properties can be made by performing hysteresis cycles as a function of the applied field at fixed temperatures. We have made this type of studies by applying both out-of-plane and in-plane field, what gives us information about the coercivity and the anisotropy energy, respectively.

In figure 3.10 we show hysteresis cycles for out-of-plane field application, obtained using the PMOKE microscope installed at LPS. Firstly, for each fixed temperature, we obtained PMOKE images as a function of a DC field applied with the large coil, starting from $\mu_0 H = 21\,\mathrm{mT}$, going down to $-21\,\mathrm{mT}$ and back to $21\,\mathrm{mT}$. For the studied temperatures, these limits correspond to a saturated state of the sample's magnetization. Then, we simply computed the total signal intensity in a given region of the sample as a function of the out-of-plane field applied with the large coil. In order to highlight the signal associated to the polar Kerr effect in the sample surface, we substracted a constant mean value and a linearly varying component which is associated to the Faraday effect in the glass of the objective lens. The resulting cycles, presented in the figure, clearly show the coercive field $\mu_0 H_c$ at which the sample magnetization experiences an inversion from a saturated state to the oppositely saturated state. Additionally, they clearly evidence that the Kerr signal is associated to the magnetization orientation of the transition metal (FeCo) sub-lattice, as we have discussed in section 2.5.1: for $T > T_M$ (panels (a) and (b)), where the FeCo magnetization dominates and it is thus oriented in the same direction as the global magnetization, sufficiently large fields in the positive direction (defined arbitrarily) result on a positive Kerr signal; in contrast, Kerr cycles are inverted for $T < T_M$ (panels (c) and (d)), indicating that the sensed magnetization is opposite to the global magnetization.

As magnetization inversion is achieved by domain nucleation and the subsequent domain wall propagation, the coercive field measured from hysteresis cycles as the ones shown in figure 3.10 is dependent on the field scanning velocity. It is convenient to perform coercive field measurements with slow scanning velocities so as to reveal the domain nucleation threshold and neglect the dependence of the coercive field on domain wall velocity. These particular cycles were made with a relatively slow scanning velocity, ranging from 0.1 to $0.9\,\mathrm{mT/s}$. The lowest scanning velocities correspond to the vicinity of the coercive field, while the highest velocities correspond to $|\mu_0 H| > \mu_0 H_c$. The obtained coercive field values for these temperatures, corresponding to a scanning velocity $\simeq 0.1\,\mathrm{mT/s}$, are $\mu_0 H_c = (3.5 \pm 0.2)\,\mathrm{mT}$ for $T = 302\,\mathrm{K}$, $\mu_0 H_c = (13.9 \pm 0.3)\,\mathrm{mT}$ for $T = 242\,\mathrm{K}$, $\mu_0 H_c = (16.0 \pm 0.4)\,\mathrm{mT}$ for $T = 102\,\mathrm{K}$, and $\mu_0 H_c = (11.9 \pm 0.2)\,\mathrm{mT}$ for $T = 20\,\mathrm{K}$.

Furthermore, we have measured hysteresis cycles with in-plane applied field, what allows for a characterization of the uniaxial anisotropy energy K_{eff}. This quantity may be estimated by considering that, in a ferromagnetic film with out-of-plane anisotropy, the in-plane applied field which is needed in order to induce the magnetization to point in-plane is the so-called anisotropy field $H_K = 2K_{\text{eff}}/M_s$ [6]. In a ferrimagnetic film, this is true whenever the applied field does not affect the anti-parallel orientation of the two sub-lattices.

In figure 3.11, we show hysteresis cycles which were obtained with an applied in-plane field $\mu_0 H_{ip}$ at fixed temperatures. The measured signal is the Hall voltage that results from applying a current through the sample in an arbitrary direction and measuring a voltage generated in the perpendicular direction in the sample's plane. In the figure, this signal is normalized with respect to its value for $\mu_0 H_{ip} = 0$. In order to perform these measurements,

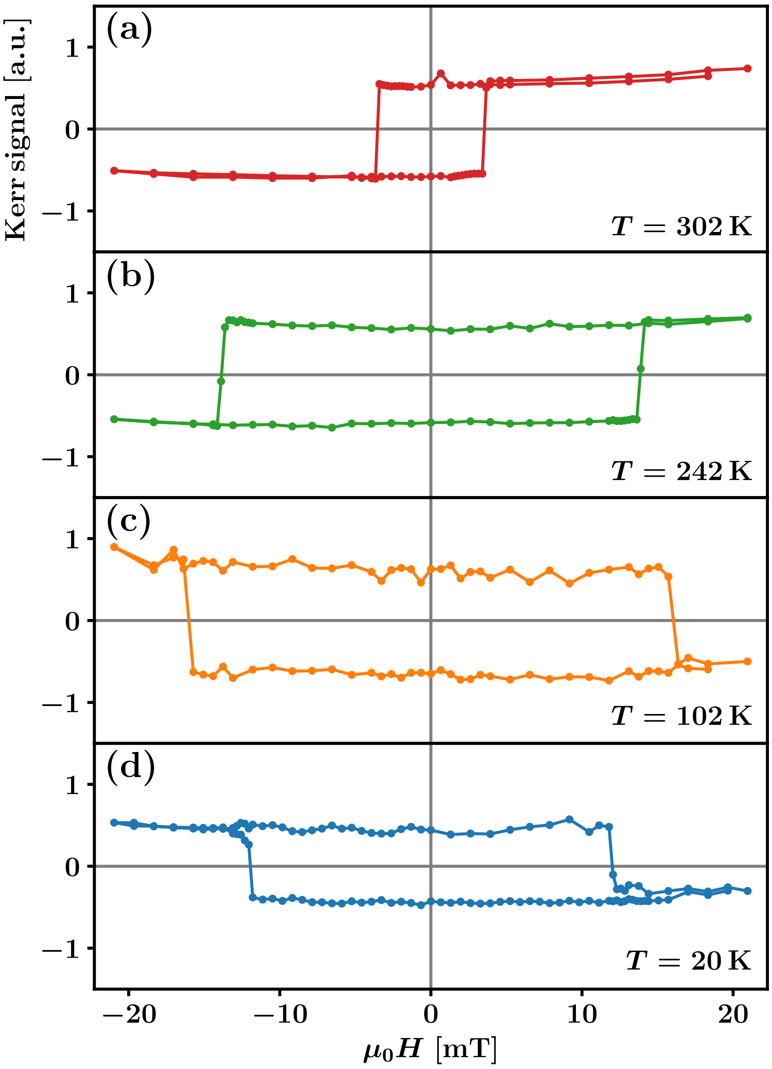

Figure 3.10: **Polar Kerr effect hysteresis cycles as a function of the field for different temperatures.** The time between successive points is $\simeq$ 3 s; consequently, the scanning velocity ranges from 0.1 to 0.9 mT/s according to the distance between successive points. The lowest scanning velocities correspond to the vicinity of the coercive field.

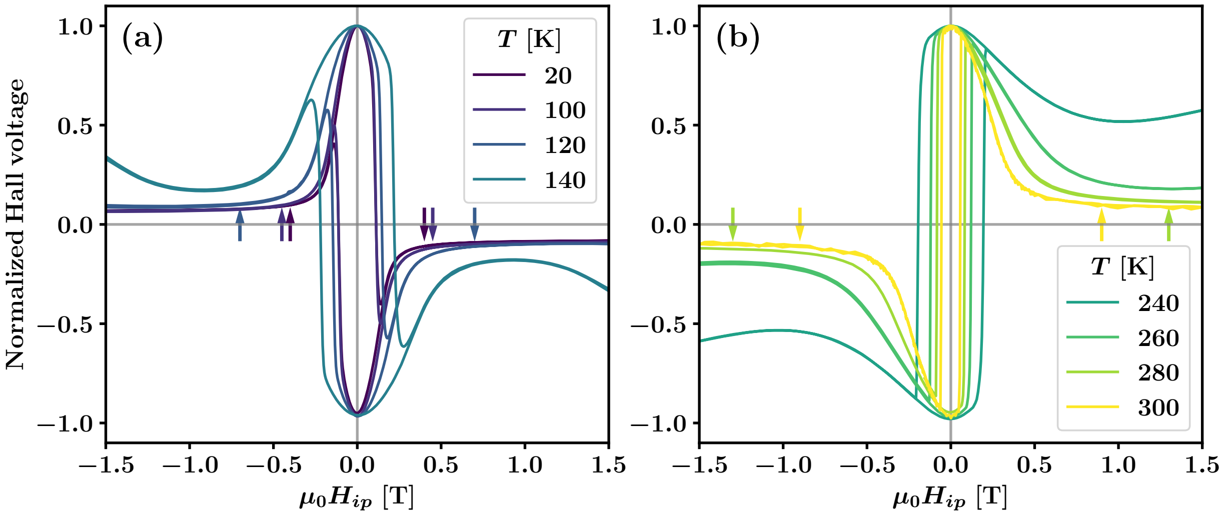

Figure 3.11: **Anomalous Hall effect measurement of hysteresis cycles with in-plane applied field at different fixed temperatures.** Panel (a) corresponds to $T < T_M$, and panel (b) to $T > T_M$. The observed signal is proportional to the out-of-plane magnetization of the FeCo sub-lattice. The anisotropy field H_K may be estimated if the signal saturates to a value that corresponds to the saturation magnetization M_s pointing in the field direction. This is achieved for the temperatures and fields indicated by arrows, i.e. for $T = 20$, 100, 120, 280 and 300 K.

thin gold wires were bonded in four extremes adequately positioned so as to apply a current and measure a voltage in the perpendicular direction. The obtained Hall signal has its origin in the so-called anomalous Hall effect (AHE) and is proportional to the out-of-plane magnetization of the FeCo sub-lattice [178]. The field scanning velocity is, on average, $\simeq 8\,\mathrm{mT/s}$. These measurements were made in a Physical Property Measurement System (PPMS) *Quantum Design Model 6000* installed at LPS. Note that the $\mu_0 H_{ip}$ magnitudes involved in these measurements are much higher than the out-of-plane field magnitudes used in PMOKE microscopy experiments.

In order to interpret the hysteresis cycles shown in figure 3.11, let us consider that the sample's plane is slightly tilted with an angle α_t with respect to the applied field $\mu_0 H_{ip}$. For $\mu_0 H_{ip} = 0$, the sample is saturated in the out-of-plane direction and then, a value equal to 1 for the normalized Hall voltage corresponds to an out-of-plane magnetization equal to M_s. If we assume that the anti-parallel coupling of the Gd and the FeCo sub-lattices is not affected by the field, a sufficiently high $\mu_0 H_{ip}$ will induce the magnetization, with magnitude M_s, to point in the applied field direction. Therefore, the saturation value of the normalized Hall voltage will be $\sin \alpha_t$. The plotted curves for $T = 20$, 100, 120, 280 and 300 K show a saturation at a unique value which is consistent with $\sin \alpha_t \simeq 0.1$. Furthermore, the observed coercivity is consistent with an inversion of the out-of-plane component of magnetization at a field $\mu_0 H_{ip} = \mu_0 H_c / \sin \alpha_t$ with $\sin \alpha_t \simeq 0.1$ and $\mu_0 H_c$ determined from hysteresis cycles obtained with out-of-plane field. For intermediate temperatures, closer to T_M, the saturation at this value is not verified; this is an evidence that for these cases, the anti-parallel coupling

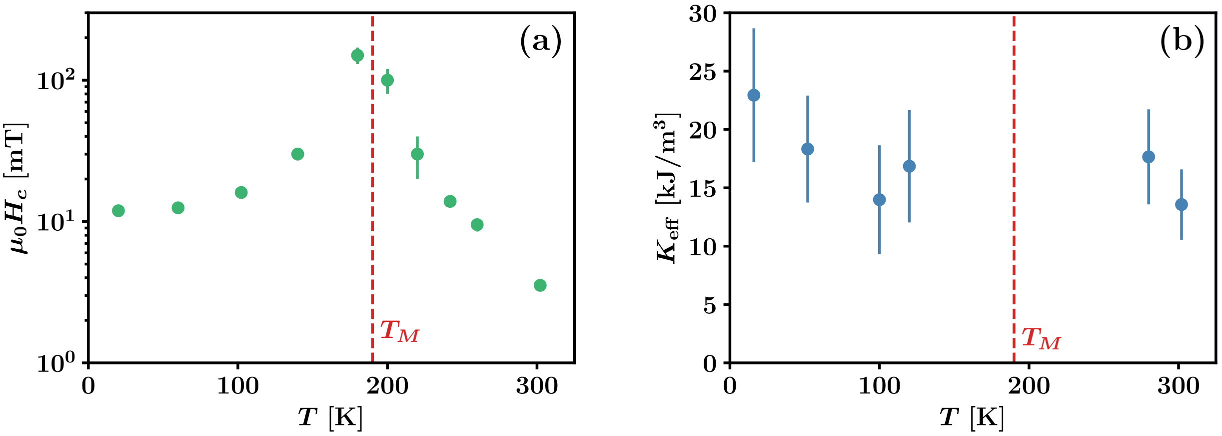

Figure 3.12: **Coercive field and anisotropy energy as a function of the temperature.** (a) Coercive field $\mu_0 H_c$ obtained from hysteresis cycles measured with an applied out-of-plane field. (b) Anisotropy energy per unit volume K_{eff} calculated as $M_s H_K/2$ from the measured saturation magnetization M_s and the estimated anisotropy field H_K.

between the two sub-lattices breaks before the expected saturation occurs, what impedes the estimation of the effective anisotropy field H_K.

The anisotropy field H_K was thus estimated from the cycles shown in figure 3.11 as the in-plane field at which the out-of-plane magnetization saturates to ≈ 0.1, as indicated by the arrows. The uncertainties for these estimations range from $\pm 0.1\,\mathrm{T}$ for $T = 20\,\mathrm{K}$ to $\pm 0.3\,\mathrm{T}$ for $T = 280\,\mathrm{K}$. Then, the anisotropy energy K_{eff} was calculated as $K_{\mathrm{eff}} = M_s H_K/2$, where the M_s values correspond to the measurement shown in figure 3.9.

In figure 3.12 we show the obtained values of the coercive field $\mu_0 H_c$ and the anisotropy energy K_{eff} as a function of the temperature. The temperature dependence of $\mu_0 H_c$, shown in panel (a), was obtained by combining both the polar Kerr effect measurements shown in figure 3.10 and anomalous Hall effect measurements with out-of-plane field (not shown). The observed divergence when approaching T_M is consistent with the fact that $M_s \to 0$ for $T \to T_M$, what reduces the Zeeman energy (2.2) that induces magnetization inversion for a given applied field. The obtained K_{eff} vs. T values, shown in panel (b), do not show a clear temperature dependence and, as explained above, its estimation for temperatures close to T_M was not possible. However, our results permit us to estimate that K_{eff} ranges between 10 and $25\,\mathrm{kJ/m^3}$ in the whole studied temperature range.

The obtained $\mu_0 H_c$ and K_{eff} values together with the saturation magnetization M_s, whose temperature dependence was shown in figure 3.9, are the main results regarding the global magnetic characterization of our studied GdFeCo sample. As we will discuss in chapters 4 and 5, the determination of these physical quantities is useful for the analysis and interpretation of our experimental studies on the domain wall dynamics and morphology in this sample.

3.4 (Ga,Mn)(As,P)/(Ga,Mn)As bilayer

While the experimental studies that will be presented in chapters 4 and 5 were performed in the ferrimagnetic GdFeCo sample that we have described above, the studies on field- and current-driven domain wall dynamics that will be presented in chapter 6 were performed in a diluted ferromagnetic semiconductor. The magnetic part of the particularly studied sample is a bilayer of (Ga,Mn)(As,P)(3 nm)/(Ga,Mn)As(1 nm) with perpendicular magnetic anisotropy. As we have discussed in section 2.5.2, the ferromagnetic nature of this sample arises due to the incorporation of a low concentration of manganese. Additionally, the incorporation of phosphorus in the (Ga,Mn)(As,P) layer is done in order to control the magnetic anisotropy [179].

The studied sample was grown by Aristide Lemaître using molecular beam epitaxy (MBE) and lithography at the C2N (Orsay, France). It is patterned so as to permit the application of an electrical current, what induces domain wall motion via the spin-transfer torque (STT) mechanism. In figure 3.13(a), we show a microscopy image that displays this pattern. The two electrodes for injecting a current density J in the magnetic bilayer are indicated as I_- and I_+. This current density is uniform in the area of interest indicated in the figure, where we observe domain wall motion with the PMOKE microscope. We have systematically verified this uniformity when performing domain wall velocity measurements by simply comparing wall velocities in different regions of this area.

Figure 3.13(b) shows a schematic representation of the stack of thin layers forming the whole sample, corresponding to a cut through the dotted line shown in panel (a). The buffer layers of AlAs and GaAs were grown at $T \simeq 550\,°\mathrm{C}$, resulting on a epitaxial (001) GaAs buffer layer for the (Ga,Mn)(As,P)(3 nm), (Ga,Mn)As(1 nm) and GaAs(2 nm) layers, which were grown at $T \simeq 220\,°\mathrm{C}$ [180–182]. These three layers were patterned as a rectangle of $133 \times 210\,\mu\mathrm{m}^2$, as shown by the darker area in panel (a). Additionally, a post growth annealing at $T \simeq 200\,°\mathrm{C}$ was performed in order to remove interstitial Mn ions. The effective Mn concentration after this process is $\sim 5\,\%$ [180]. The two electrode bars used for current injection are bilayers of of Ti(20 nm)/Au(200 nm) and were deposited on the GaAs capping layer at both sides of the stack. Additionally, above the capping layer of GaAs, an insulating 55 nm thick SiO_2 layer (clearer region in panel (a)) was deposited by plasma-enhanced chemical vapor deposition at $T \simeq 200\,°\mathrm{C}$. Then, it was covered by an evaporated film of Ti/Au which serves as a gate for applying an electrical field and tuning the effective magnetic anisotropy [181]. This gate was disconnected in the experiments presented in this thesis.

In order to apply current pulses for generating domain wall displacement via STT, we have applied voltages V_j between the two electrodes I_+ and I_- which range from 2 to 98 V, with pulse times ranging from 900 ms to 1.4 μs. The sample resistance, measured between these two electrodes, has a magnitude of 22.14 kΩ. As the resistivity of the (Ga,Mn)(As,P)/(Ga,Mn)As magnetic layer is much lower than that of the GaAs buffer and capping layers, the relation between the applied voltage and the resulting current density is

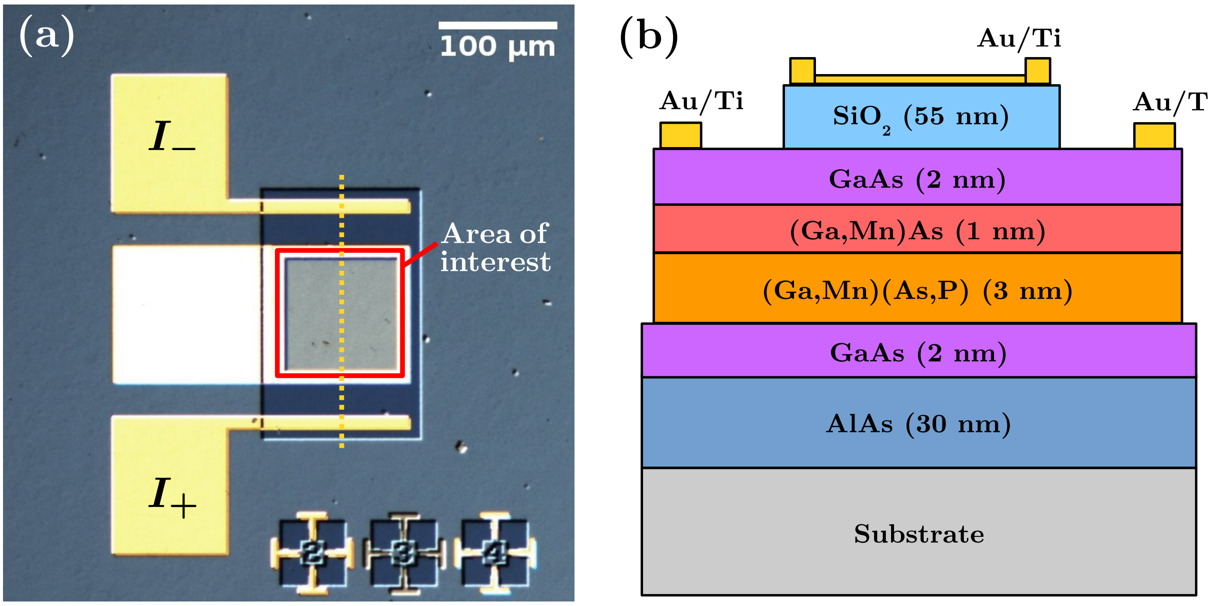

Figure 3.13: **Studied (Ga,Mn)(As,P)/(Ga,Mn)As sample.** (a) Optical microscopy image of the sample, which was patterned by lithography. We indicate the two Au/Ti electrodes I_+ and I_- used for current injection and highlight the area of interest in which we observe domain wall motion with PMOKE microscopy. (b) Schematic representation of the stack forming the sample corresponding to a cut through the dotted line drawn in (a). The ferromagnetic components are the (Ga,Mn)(As,P)(3 nm) and the (Ga,Mn)As(1 nm) layers. The Au/Ti electrodes at the two sides are used for current injection, while the superior Au/Ti pad serves as a gate for generating an electric field.

$$J/V_j = (4\,\mathrm{nm} \times 133\,\mu\mathrm{m} \times 22.14\,\mathrm{k}\Omega)^{-1} \approx 0.1\,(\mathrm{GA/m^2})/\mathrm{V}.$$

The flow of a current through the (Ga,Mn)(As,P)/(Ga,Mn)As sample generates a power dissipation that results in Joule heating. The subsequent sample's temperature rise may affect domain wall dynamics. Rebeca Díaz Pardo and Vincent Jeudy have studied the Joule heating in the same sample that we have studied in this thesis [182] following a procedure proposed by Javier Curiale and collaborators [163]. They have verified that the temperature rise in this sample due to Joule heating can be quantified and established the conditions of current injection for which the temperature remains practically unchanged. For the current density magnitudes J and the pulse times Δt that we have explored in this thesis, the temperature rise due to Joule heating is lower than 0.3 K, what results in a domain wall velocity variation which is not higher than 3 % for the studied conditions. As this percentage is lower than the uncertainties with which we determine domain wall velocities, the Joule heating is negligible in our experimental studies.

The Curie temperature of this sample, below which spontaneous ferromagnetic order arises, is $T = 65\,\mathrm{K}$. This temperature was determined simply by observing the vanishing of magneto-optical contrast for $T \to 65\,\mathrm{K}$. Therefore, all our studies on domain wall dynamics in this sample are performed for $T < 65\,\mathrm{K}$. These studies will be presented in chapter 6.

3.5 Chapter summary

In this chapter, we have thoroughly described our main measurement technique, the polar magneto-optical Kerr effect (PMOKE) microscopy. We have started by describing the principles of magneto-optical imaging based on the polar Kerr effect and we have discussed on the main parameters that affect the magneto-optical contrast, which needs to be optimized in order to distinguish between oppositely magnetized domains in a PMOKE microscope. Then, we have described in detail the main features of the used PMOKE microscopes and the techniques we implemented in order to study magnetic domain walls in thin films with perpendicular anisotropy: we have described the optical arrangement, the temperature control setup, the technique for domain wall velocity measurements, the particularities of the magnetic field pulse application setup, and the protocol for domain wall profile detection that permits to study wall morphology.

Furthermore, we have presented the main features of the two magnetic thin films that are studied throughout this thesis. Firstly, we have described the ferrimagnetic thin film of Ta/$Gd_{32}Fe_{61.2}Co_{6.8}$/Pt and presented a detailed characterization of its main global magnetic properties through magnetometry measurements. Secondly, we have described the diluted ferromagnetic and semiconducting bilayer of (Ga,Mn)(As,P)/(Ga,Mn)As, which has the particularity that a uniform current density can be injected in it so as to study current-driven domain wall motion.

In the following three chapters, we will present and discuss our studies on the domain wall dynamics and morphology in these two samples, what constitutes the main research performed throughout this thesis. In chapter 4, we shall discuss on the domain wall dynamics in the GdFeCo sample, focusing on its behavior as a function of temperature in a wide temperature range and on the experimental determination of universal critical exponents characterizing the depinning transition. In chapter 5, we will study the domain wall morphology as a function of field and temperature in GdFeCo, focusing on the obtained roughness exponents and proposing a plausible theoretical interpretation of our results. In chapter 6, we shall present our studies on the field- and current-driven domain wall motion in (Ga,Mn)(As,P)/(Ga,Mn)As, which are focused on establishing a comparison between these two different driving forces and analyzing the effects of their simultaneous action on the creep regime of wall motion.

CHAPTER 4

Field-driven domain wall dynamics in a ferrimagnetic GdFeCo thin film

"Lo mismo con las canciones,
los pájaros, los alfabetos:
Si quieres que algo se muera,
déjalo quieto."
Jorge Drexler, *Movimiento*

THE natural world's richness is result of its changes and movements, and motion phenomena possess themselves plenty of complex features which are worth studying. In this context, Dynamics, i.e. the study of movement and the forces that produce it, is a crosscutting issue in all areas of Physics. During this thesis, we have performed a deep study of the field-driven domain wall dynamics in a ferrimagnetic GdFeCo thin film with perpendicular anisotropy. All these studies, to which this chapter is devoted, were performed by observing domain walls and measuring their velocities with a polar magneto-optical Kerr effect (PMOKE) microscope[1]. The main particularities of our study are the careful observation of the velocity vs. field characteristics, which permits us to analyze the three dynamical regimes, i.e. creep, depinning and flow, and the exploration of a very wide range of temperatures. Particularly, we measured velocity vs. field curves for 25 different temperature values, ranging from 10 to 353 K.

---

[1] We have presented and discussed in detail the characteristics of this imaging technique in 3.1, and we have described our experimental setup in section 3.2.

The main goals of our research on the domain wall dynamics in GdFeCo are the study of how the different dynamical regimes are affected by the material's temperature dependence of magnetic properties and the characterization of the depinning transition and associated critical exponents. Throughout this chapter, we will present our results on domain wall dynamics and thoroughly discuss these issues. We shall carefully characterize for each temperature the creep and depinning regimes, what will give us access to the temperature dependence of a variety of physical quantities. Remarkably, this characterization will permit us to experimentally determine the complete set of critical exponents that define the universality class to which domain walls in this thin film belong.

The particularly studied sample consists in a Ta(5 nm)/$Gd_{32}Fe_{61.2}Co_{6.8}$(10 nm)/Pt(5 nm) trilayer deposited on a thermally oxidized silicon SiO_2(100 nm) substrate by RF sputtering[2]. One of its main features is the existence of a magnetic compensation temperature at $T_M = (190 \pm 4)\,\mathrm{K}$. We could not determine experimentally the angular compensation temperature T_A; however, we have estimated it as $T_A \sim 270\,\mathrm{K}$ according to previous investigations which establish a correlation between T_M and T_A [144]. In this chapter, among other topics, we will discuss which are the effects of the magnetic compensation on the physical quantities characterizing the dynamical regimes of domain walls, and we will comment on the possibility of observing signatures of the angular compensation in our measurements.

In the following section we will overview previous investigations that give us a framework and motivate our studies on domain wall dynamics in GdFeCo. Firstly, in 4.1.1, we will discuss some investigations on the thermally activated regimes in GdFeCo and the depinning transition. We will see that these studies do not deepen on the universal nature of creep and depinning and, in addition, they do not cover a wide range of temperatures, what calls for further investigations. Secondly, in 4.1.2, we shall briefly review previous theoretical studies on the critical exponents characterizing the universal depinning transition. These investigations constitute the basis for our experimental studies on the depinning transition, as one of our main interests in this thesis is the experimental characterization of universal critical exponents.

The presentation and discussion of our experimental results in this chapter is separated in two main sections. On the one hand, in section 4.2, we shall present the study of domain wall velocity vs. applied field curves in a wide temperature range, from $T = 10\,\mathrm{K}$ to $T = 353\,\mathrm{K}$. These studies will give us insight on the particularities of creep, depinning and flow regimes in different temperature ranges, both above and below the magnetic compensation temperature T_M, and will permit us to analyze the temperature dependence of depinning parameters such as H_d, T_d, v_d and related quantities which are linked to the characteristics of the disordered landscape in which domain walls move. On the other hand, section 4.3 will be devoted to the study of the depinning transition in the range of low temperatures, for $T < 100\,\mathrm{K}$. These results are the most relevant findings of our study, as we show a direct experimental measurement of the universal depinning critical exponents β and ν_{dep}. This result, which is possible due to the clear observation of the zero-temperature-like depinning

---

[2] See section 3.3 for sample details and magnetic characterization.

transition, permits us to experimentally quantify for the first time the full set of critical exponents characterizing the depinning transition. Finally, we end this chapter in section 4.4 by summarizing our main findings on domain wall dynamics in GdFeCo.

4.1 Motivation, framework and previous investigations

Our study of domain wall dynamics in GdFeCo is motivated mainly by the particular temperature dependence of magnetic properties, both static and dynamic, that this type of materials present, already discussed in section 2.5.1. As we have pointed out, this results on interesting dynamical features of domain walls. Additionally, variable magnetic properties permit us to study domain wall dynamics in diverse conditions using a single sample. Specifically, domain wall velocity vs. applied field curves at different fixed temperatures present distinctive features, as we will discuss throughout this chapter. Remarkably, however, all these curves are expected to show universal features that characterize the dynamics of elastic interfaces in disordered media. Therefore, we shall study a wide variety of velocity vs. field curves within a unique theoretical framework. As we will see, studies at different temperature ranges shed light over diverse particularities of creep and depinning dynamical regimes.

In the following, we shall briefly review previous investigations on two subjects that we will thoroughly study in this chapter through experimental measurements of domain wall dynamics. On the one hand, the effect of magnetic and angular compensation temperatures on wall dynamics in the creep and depinning regimes. On the other hand, the characterization of universal depinning critical exponents.

4.1.1 Thermally activated dynamics and depinning transition

In figure 2.19, we have shown that domain wall velocity in the flow regime shows a maximum at the angular compensation temperature T_A. However, below the depinning field domain walls show intermittent, thermally activated dynamics in which the angular compensation may not play any notorious role [36, 145].

In figure 4.1(a), we show velocity vs. temperature curves corresponding to different fixed applied fields in a sample of SiN(100 nm)/$\mathrm{Gd}_{23.5}\mathrm{Fe}_{66.9}\mathrm{Co}_{9.6}$(30 nm)/SiN(5 nm) with perpendicular magnetic anisotropy, measured by Y. Hirata and collaborators [145]. For $\mu_0 H = 68\,\mathrm{mT}$, a sharp peak on domain wall velocity is evidenced. This peak is shown to correspond to an angular compensation temperature $T_A \simeq 236\,\mathrm{K}$. However, for lower applied fields, the velocity peak moves to higher T values and finally vanishes. This is due to the fact that below the depinning field, domain wall velocity is dominated by thermal activation and therefore grows for increasing temperature even above T_A. The lower peaks observed for $\mu_0 H = 44$ and $36\,\mathrm{mT}$ at $T > T_A$ correspond to the temperatures at which domain

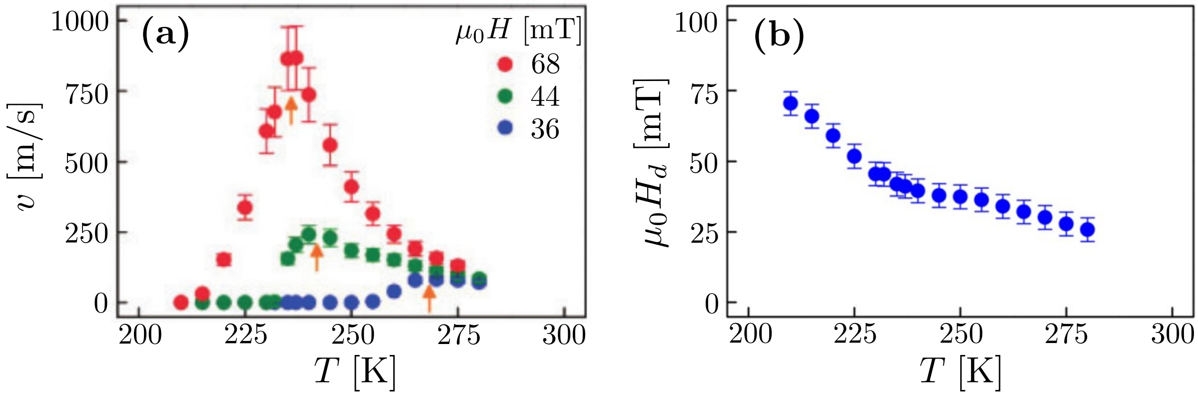

Figure 4.1: **Effect of the depinning field on domain wall velocity in GdFeCo close to the angular compensation.** (a) Wall velocity v vs. temperature T for different applied fields $\mu_0 H$. The velocity peak associated to angular compensation is indicated. Adapted from [145]. (b) Depinning field $\mu_0 H_d$ vs. temperature T. Adapted from [150].

walls reach the flow regime for each applied field, what evidences that the depinning field $\mu_0 H_d$ depends on temperature. Specifically, figure 4.1(a) suggests that for $T = T_A \simeq 236\,\mathrm{K}$, $44\,\mathrm{mT} \lesssim \mu_0 H_d(T) < 68\,\mathrm{mT}$, while for $T \simeq 240\,\mathrm{K}$, $36\,\mathrm{mT} < \mu_0 H_d(T) < 44\,\mathrm{mT}$ and finally, for $T \simeq 270\,\mathrm{K}$, $\mu_0 H_d(T) < 36\,\mathrm{mT}$.

Figure 4.1(b) shows the depinning field vs. temperature dependence obtained by T. Nishimura and collaborators in a sample of identical characteristics [150]. Decreasing $\mu_0 H_d$ values with increasing T results consistent with the fact that in this sample, $T_M < 200\,\mathrm{K}$ and, therefore, the saturation magnetization M_s grows with temperature for a certain range above 200 K [3]. As the driving force f over domain walls arises from Zeeman energy, which is proportional to $\mu_0 H M_s$, the depinning field $\mu_0 H_d$ that has to be applied in order to overcome effective energy barriers is expected to be inversely proportional to M_s [120]. Close to T_M, therefore, Zeeman interaction vanishes and a divergence of $\mu_0 H_d$ for $T \to T_M$ is expected. However, this divergence has not yet been reported in the literature.

These investigations, which to our knowledge constitute the most recent studies on depinning phenomena close to compensation temperatures, show that a detailed study of creep and depinning regimes in ferrimagnets and corresponding parameters as the depinning field and temperature is still lacking. In this chapter, we shall present a thorough study of these issues, analyzing in detail velocity vs. field curves in a wide temperature range and the corresponding dependence of parameters as $\mu_0 H_d$ and T_d.

---

[3] Note that M_s is expected to decrease for sufficiently high temperatures, close to the Curie temperature T_C.

4.1.2 Universal depinning critical exponents

The experimental measurement of critical exponents is one of the main subjects of this thesis. In particular, as we will discuss in section 4.3, the study of domain wall dynamics in GdFeCo at low temperatures permits us to experimentally determine the full set of critical exponents corresponding to the depinning transition. This set of exponents characterizes the universality class to which domain walls belong.

As we have discussed in section 2.3.2, driven elastic lines in disordered media as domain walls in magnetic thin films are usually described in the framework of one of two possible universality classes, which are the quenched Edwards-Wilkinson (qEW) and the quenched Kardar-Parisi-Zhang (qKPZ) universality classes. Each universality class is characterized by two sets of critical exponents, associated to the equilibrium ($f \to 0$) reference state and to the depinning ($f \to f_d^+$ and $T \to 0$) critical point. Interestingly, the equilibrium critical exponents, corresponding to the limit $f \to 0$, are equivalent for both qEW and qKPZ universality classes and thus the creep exponent μ, easily accessible experimentally, is equal to 1/4 in both cases. However, the depinning critical exponents differ but their experimental distinction for magnetic domain walls in thin films with perpendicular anisotropy still constitutes a challenge.

Table 4.1 shows the complete set of depinning critical exponents, the observable quantities to which they are related and corresponding scaling laws, and their numerical calculations reported in the literature for the qEW and the qKPZ universality classes. These values are independently determined; however, for the qEW class, the five exponents are related through the relations $\nu_{\text{dep}} = 1/(2 - \zeta_{\text{dep}})$, $\beta = \nu_{\text{dep}}(z - \zeta_{\text{dep}})$ and $\tau_{\text{dep}} = 2 - 2/(d + \zeta_{\text{dep}})$ [5], which result from scaling laws. The dimension for the case of an elastic line in a bi-dimensional medium is $d = 1$. Therefore, the determination of two of them is sufficient in order to calculate the full set of exponents. In the qKPZ class, two relations exist, $\beta = \nu_{\text{dep}}(z - \zeta_{\text{dep}})$ and $\tau_{\text{dep}} = 2 - (\zeta_{\text{dep}} + 1/\nu_{\text{dep}})/(d + \zeta_{\text{dep}})$ and therefore, the independent determination of three exponents is needed for calculating the full set.

We have already introduced, in section 2.3, the exponents β for the power-law variation of velocity $v \sim (f - f_d)^\beta$, ν_{dep} for the divergence of the depinning avalanche size $\ell_{\text{av}} \sim (f - f_d)^{-\nu_{\text{dep}}}$, ζ_{dep} for the scaling law of the interface profile, $u(x) \sim x^{\zeta_{\text{dep}}}$, and z for the relaxation time of the interface as a function of its size, $t_r(\ell) \sim \ell^z$ [3]. The exponent τ_{dep} is the so-called Gutenberg-Richter exponent, corresponding to the distribution of depinning avalanche areas S_{av}, which scales as $P(S_{\text{av}}) \sim S_{\text{av}}^{-\tau_{\text{dep}}}$ [185]. The qualitative relationship between the observable quantities to which critical exponents are related is confirmed by the relationships written above, which show that only two (for qEW) or three (for qKPZ) of these exponents are independent.

In this thesis work, as we will discuss in section 4.3, we succeeded to experimentally determine β and ν_{dep} from domain wall velocity measurements. This constitutes the first direct and independent experimental determinations of each of these critical exponents. As we will see, the found values are consistent with the qEW universality class while they are

	Observable	**qEW**	**qKPZ**
$\boldsymbol{\beta}$	$v(f) \sim (f - f_d)^{\beta}$	0.245 ± 0.006 [119] 0.33 ± 0.02 [184]	$\simeq 0.64$ [5, 112, 183]
$\boldsymbol{\nu}_{\mathbf{dep}}$	$\ell_{\text{av}}(f) \sim (f - f_d)^{-\nu_{\text{dep}}}$	1.333 ± 0.007 [119]	$\simeq 1.73$ [183]
$\boldsymbol{\zeta}_{\mathbf{dep}}$	$u(x) \sim x^{\zeta_{\text{dep}}}$	1.250 ± 0.005 [119]	$\simeq 0.63$ [112]
$\boldsymbol{z}$	$t_r(\ell) \sim \ell^{z}$	1.433 ± 0.007 [119]	1 [183]
$\boldsymbol{\tau}_{\mathbf{dep}}$	$P(S_{\text{av}}) \sim S_{\text{av}}^{-\tau_{\text{dep}}}$	1.11 ± 0.04 [185]	$\simeq 1.26$ [5, 112, 183]

Table 4.1: **Universal depinning critical exponents.** We indicate the observables to which each exponent is linked and the corresponding scaling relations, which are valid in the limit $T \to 0$ and $f \to f_d^+$. Numerical values correspond to computational calculations reported in the literature for the quenched Edwards-Wilkinson (qEW) and for the quenched Kardar-Parisi-Zhang (qKPZ) universality classes.

inconsistent with the qKPZ class, what has allowed us to calculate the full set of depinning critical exponents in accordance with the qEW class.

In the following, we will present our experimental results on domain wall dynamics in a GdFeCo thin film with perpendicular anisotropy. Firstly, we will present our deep study of creep and depinning regimes in a wide temperature range and secondly, the determination of depinning critical exponents which, as we will see, is accessible experimentally in the range of low temperatures.

4.2 Domain wall dynamics in a wide temperature range

In this section, we present and discuss our results on domain wall dynamics performed in a ferrimagnetic thin film of GdFeCo, in the temperature range $10\,\mathrm{K} \leq T \leq 353\,\mathrm{K}$. The distinctive features of our experimental study consist on the measurement of velocity vs. field curves in a wide range of velocities and, more importantly, in a wide range of temperatures. As we will see, the velocity-field characteristics that we measure experimentally strongly depend on temperature. For the creep regime, we can separate the nature of this dependence in two groups. One of them is the intrinsic variation with temperature of the physical parameters $H_d(T)$, $T_d(T)$ and $v_d(T)$. On the other hand, there is an explicit temperature dependence arising from the thermally activated nature of creep regime, as indicated by equation (2.75). As we have discussed in section 2.4.3, the depinning and flow regimes may be assessed through these three temperature-dependent parameters.

Physical parameters vary in a particular way due to the intrinsic temperature variation of the saturation magnetization $M_s(T)$. The existence of a magnetic compensation temperature T_M such that $M_s(T \to T_M) = 0$ induces particular features in the velocity-field characteristics. For example, as we have already pointed out, a divergence of $H_d(T)$ is expected to occur at $T \to T_M$. In addition, as we will discuss later, distinctive properties are observed when comparing temperature ranges below and above T_M.

The explicit role of temperature in equations describing the creep regime (equation (2.75)) and the thermal rounding at the depinning transition (equation (2.81)) is directly related to thermal activation, what evidences its crucial role in domain wall motion at relatively low drives. A thorough discussion of how thermal activation evolves as a function of the reduced temperature T/T_d will be presented in the following, focusing on the consequences of decreasing thermal energy as T decreases in the velocity-field characteristics.

The presentation and discussion of results in this section is organized in four parts. First, in 4.2.1, we will present the general protocol used in order to analyze velocity vs. field curves, which are measured as explained in 3.2.3. Secondly, in 4.2.2, we shall discuss the domain wall dynamics for temperatures above T_M. In third place, in 4.2.3, we will present and discuss the results on domain wall dynamics below T_M. The distinction between temperature ranges above and below magnetic compensation is justified by the particularities of velocity curves in these two ranges, which compels us to perform slightly different analysis of velocity curves. Furthermore, the lowest temperature range, $T < 100\,\mathrm{K}$, is left for a thorough discussion in section 4.3 due to its striking particularities. In the fourth part of this section, 4.2.4, we summarize the temperature dependence of physical parameters related to creep and depinning regimes in the whole temperature range. This gives us insight on the nature of disorder and its influence on domain wall dynamics as a function of temperature.

4.2.1 General analysis of domain wall velocity curves

Let us first present the main features that we have observed in the measurement of v vs. $\mu_0 H$ curves. This discussion will guide us in the analysis of these curves in all the studied temperature range. Figure 4.2 shows the v vs. $\mu_0 H$ characteristics for $T = 353\,\mathrm{K}$. Domain wall velocities are measured for fields ranging between 0.76 and 15 mT. In the linear plot, we observe that the onset on velocity appears at $\mu_0 H \simeq 4\,\mathrm{mT}$, and the highest measured values correspond to $v \simeq 260\,\mathrm{m/s}$ at $\mu_0 H \simeq 15\,\mathrm{mT}$. As we have discussed in section 3.2.4, these high values are close to the experimental limits of the Kerr microscopy technique.

Even if the onset on velocity appears to occur at 4 mT, when v approaches values of the order of 1 m/s, our Kerr microscopy technique and the possibility of applying low-field and high duration pulses allows the measurement of velocities in a very wide range below 1 m/s. In the inset of figure 4.2, we plot the DW velocity in logarithmic scale as a function of $(\mu_0 H/\mathrm{mT})^{-1/4}$, in order to evidence the creep regime of domain wall motion. As we can observe, the creep relation $\ln v \sim H^{-\mu}$, with the creep exponent $\mu = 1/4$, satisfactorily describes the velocity-field characteristics in a range of 8 orders of magnitude in the velocity, from $v \sim 10^{-7}\,\mathrm{m/s}$ at $\mu_0 H = 0.76\,\mathrm{mT}$ to $10\,\mathrm{m/s}$ at $\mu_0 H \simeq 6\,\mathrm{mT}$. In this range, we may perform a linear fit of the type $y = Sx + I$ with $y = \ln(v/(\mathrm{m/s}))$ and $x = (\mu_0 H/\mathrm{mT})^{-1/4}$.

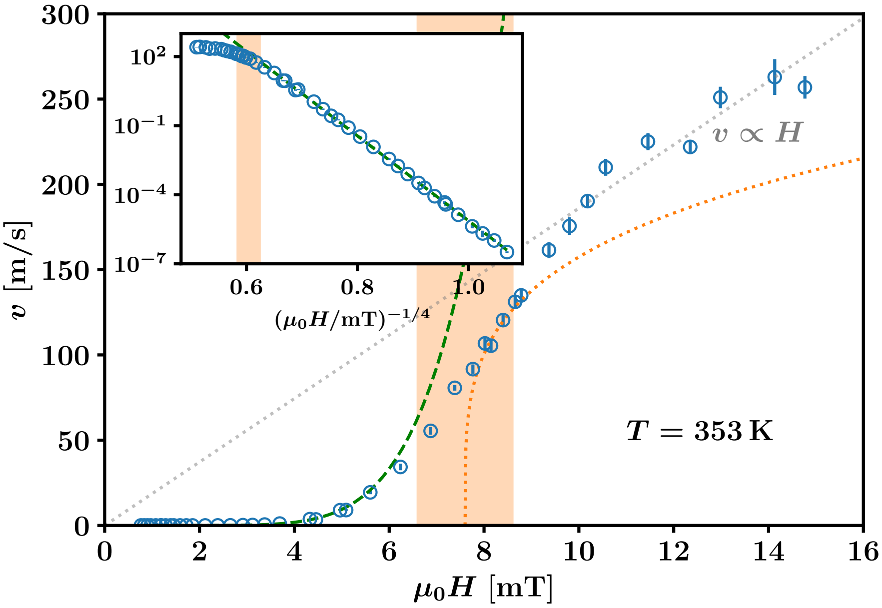

Figure 4.2: **Domain wall velocity as a function of the applied field for $T = 353\,\mathrm{K}$.** Main panel: linear scale, showing the creep dependence which describes low-velocity measurements as a dashed line, an estimation of the corresponding athermal depinning regime as a dotted curve, and an estimated proportionality of velocity and field corresponding to flow regime as a dotted straight line. For the depinning field, we estimate $\mu_0 H_d = (7.6 \pm 1.0)\,\mathrm{mT}$. This range is indicated as a vertical shaded area. Inset: creep plot, with a logarithmic scale for the velocity as a function of $(\mu_0 H/\mathrm{mT})^{-1/4}$, showing that creep law with $\mu = 1/4$ describes the observed dependence in a range of 8 orders of magnitude in the velocity. Creep fit is shown as a dashed line, with resulting slope $S = (T_d/T)(H_d/\mathrm{mT})^{1/4} = 42.4 \pm 0.2$ and intercept $I = \ln{(v_d/(\mathrm{m/s}))} + T_d/T = 30.6 \pm 0.1$.

This fit, which is shown in the figure as a dashed line, allows to obtain the following values according to equations (2.75) and (2.76): $S = (T_d/T)(\mu_0 H_d/\mathrm{mT})^{1/4} = 42.4 \pm 0.2$ and $I = \ln{(v_d/(\mathrm{m/s}))} + T_d/T = 30.6 \pm 0.1$.

From a velocity-field curve like the one presented in figure 4.2, we can infer the corresponding value of the depinning field $\mu_0 H_d$. The depinning transition is evidenced by a range in which $v(H)$ separates from the stretched exponential behavior characteristic of creep with increasing field, presenting lower velocities, and by an inflection point above which concavity becomes negative, as we have pointed out in section 2.4.3. These two features usually occur simultaneously, permitting a relatively precise determination of the depinning field: in this scenario, $\mu_0 H_d$ is the field at which the inflection point *and* the separation between the creep fit and the velocity curve occur. Furthermore, the coincidence of these two features permits the realization of the self-consistent analysis proposed by Rebeca Díaz Pardo and collaborators [18]. From the creep fit parameters and the determination of the depinning field value, this method permits to calculate the depinning velocity v_H and the mobility m

which determine, respectively, the depinning and flow functions for $v(H)$, equations (2.82) and (2.74).

For $T = 353\,\mathrm{K}$, however, the separation from creep behavior occurs between 6 and 7 mT, while an inflection is observed in the range $7\,\mathrm{mT} < \mu_0 H < 9\,\mathrm{mT}$ (see figure 4.2). This slight mismatch is sufficient to prevent the realization of the auto-consistent analysis: if we consider that depinning field occurs between 6 and 7 mT, we would then obtain a flow prediction which falls well below the highest velocity points. If, conversely, we consider that the depinning field is above 7 mT, the velocity at depinning $v_d = v(H_d)$ given by the creep fit for $H = H_d$ would be too large and then, the athermal depinning transition curve would fall above measured velocities in a considerable range for $H > H_d$. As theoretically predicted and evidenced by figure 2.15(b), equations (2.74) and (2.82) are upper and lower boundaries of DW velocity for $H \geq H_d$ and, consequently, these results are not compatible with the analysis proposed in reference [18].

Even if the hypothesis of simultaneity of the inflection and the separation from creep behavior is not verified in many of our measurements, these two signatures of depinning transition may be observed in a given field range in most of the velocity-field curves. As we have discussed, this is the case for the data presented in figure 4.2. Thus, for this case we estimate $\mu_0 H_d = (7.6 \pm 1.0)\,\mathrm{mT}$. In addition, using this value, we may plot an estimation of the corresponding athermal depinning transition which, as discussed in section 2.4.3, is expected to coincide with velocity measurements in a reduced range for $\mu_0 H > \mu_0 H_d$. In the figure we plot this dependence as a dotted curve, following equation (2.82) with $\beta = 0.25$ (in accordance with [119] and [18]) and an estimated value $v_H = 210\,\mathrm{m/s}$.

In figure 4.2 we can also observe that at higher fields, above $\mu_0 H_d \simeq 8\,\mathrm{mT}$, the velocity-field characteristics progressively transform into a linear variation, $v \propto H$, in accordance with the flow regime of domain wall motion. In the figure, we plot a dotted straight line corresponding to a mobility $m = 18.6\,(\mathrm{m/s})/\mathrm{mT}$, which constitutes an estimation of the velocity-field proportionality for higher fields. As we will see below, this condition of proportional variation corresponding to the flow regime is not reached for most of our velocity-field curves.

In the following section, we will present and discuss all the measurements of velocity-field curves above the compensation temperature at $T_M = (190 \pm 4)\,\mathrm{K}$, i.e. for $T > T_M$. We shall analyze the measurement of a creep-type dependence and its characterization for each of the different temperatures, the evidences of the depinning transition, and the determination of quantities like the depinning field and temperature. Then, in section 4.2.3 we will present our measurements below the compensation temperature, i.e. for $T < T_M$. As we will see, this range presents some particularities which are induced mainly by two factors: on the one hand, the decreasing M_s vs. T dependence (in contrast with the increasing M_s vs. T for $T > T_M$); on the other hand, the progressive vanishing of thermal effects with decreasing temperature.

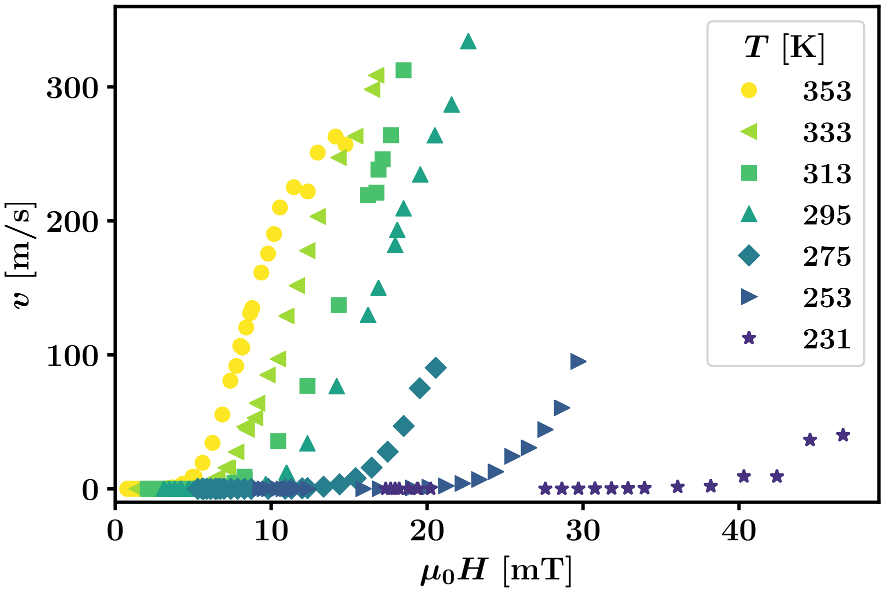

Figure 4.3: **Domain wall velocity as a function of the applied field above the magnetic compensation temperature.** Set of velocity-field curves plotted in linear scale which represent the observed behavior above T_M.

4.2.2 Domain wall dynamics above magnetic compensation

Let us now discuss the main features that we observe in the curves corresponding to $T > T_M$; particularly, in the range $209\,\mathrm{K} \leq T \leq 353\,\mathrm{K}$, in which we measured 13 velocity-field curves. In figure 4.3 we present a set of curves which are representative of this range.

Some features are remarkable of the set of curves plotted in figure 4.3. First of all, we observe that measured velocities shift to higher magnetic fields as temperature decreases. In other words, it is necessary to apply a higher field at lower temperatures in order to obtain the same domain wall velocity. This monotonous shifting to higher field with decreasing temperatures is the expected behavior, as saturation magnetization M_s decreases when approaching T_M, resulting on lower forces over domain walls for a given applied field.

Another remarkable observation is the measurement of velocities of $\simeq 300\,\mathrm{m/s}$ in the range of highest temperatures. Even if we succeed to reach these relatively high velocities, in most of the cases we are not able to clearly reach the flow regime, characterized by a proportionality between field and velocity, $v \propto \mu_0 H$. Nevertheless, as we will see in the following, there are signatures of the depinning transition in every measured v vs. $\mu_0 H$ curve.

The highest measured velocities decrease to $\sim 100\,\mathrm{m/s}$ as temperature decreases below $T \simeq 280\,\mathrm{K}$. This is mainly due to the appearance of a higher density of nucleation centers

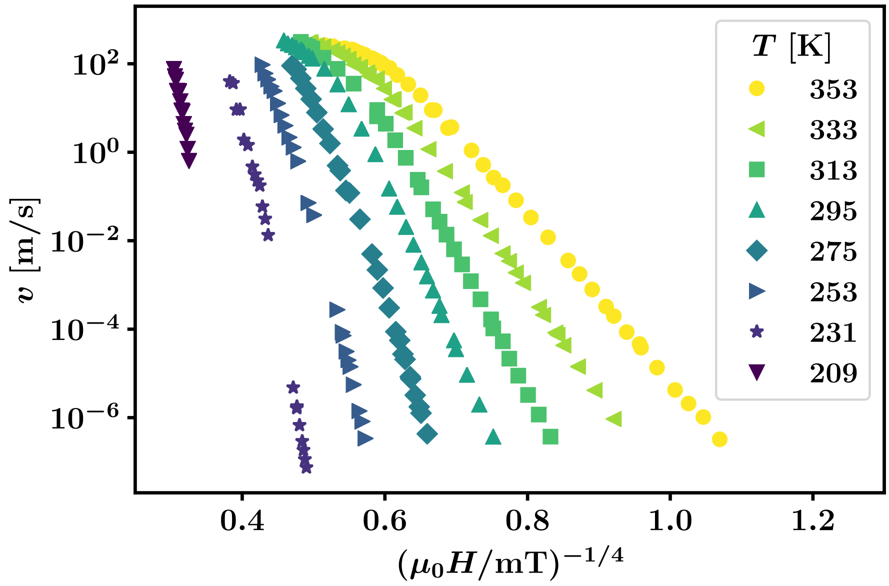

Figure 4.4: **Creep-type plot of domain wall velocity curves above the magnetic compensation temperature.** Set of representative curves of the velocity v in logarithmic scale as a function of $(\mu_0 H)^{-1/4}$ above T_M, showing the good agreement with creep formula for velocities below 10 m/s.

for the conditions of field and temperature at which we reach the highest velocities. This prevents the observation of long domain wall displacements, as walls nucleated in different points merge with other walls in their way. While measurements above 280 K have been performed in the microscope installed at CAB, those below 280 K were performed in the microscope installed at LPS, in a different region of the sample. Therefore, the appearance of a higher density of nucleation centers might be due to inhomogeneities of the sample that result on different domain nucleation conditions in different regions. However, as we will see below, the domain wall dynamics do not show any particular change at $T \simeq 280$ k that we could associate to this fact.

Let us take a look at the creep regime in this range of temperatures. Figure 4.4 shows representative curves corresponding to $T > T_M$ in a creep plot, i.e. v in logarithmic scale vs. $(\mu_0 H)^{-1/4}$. We may observe that the slope of the linear relation $\log v \sim H^{-1/4}$ grows as the temperature decreases, while the curves move to lower values of $(\mu_0 H)^{-1/4}$, i.e. to higher field values. For $T = 209$ K, the high fields necessary to move domain walls make it impossible to measure in the region of low velocities, as low-velocity measurements are performed by applying field pulses of relatively long duration. We observe for all curves that there exists a well-defined low-velocity region, for v lower than ~ 10 m/s, where a creep-type dependence with $\mu = 1/4$ is observed. The lower limit if this low-velocity region spans from $\sim 10^{-7}$ m/s for $T \geq 231$ K to ~ 1 m/s for $T = 209$ K. For higher velocities, data points separate from this creep dependence, what constitutes an evidence of the depinning transition's proximity.

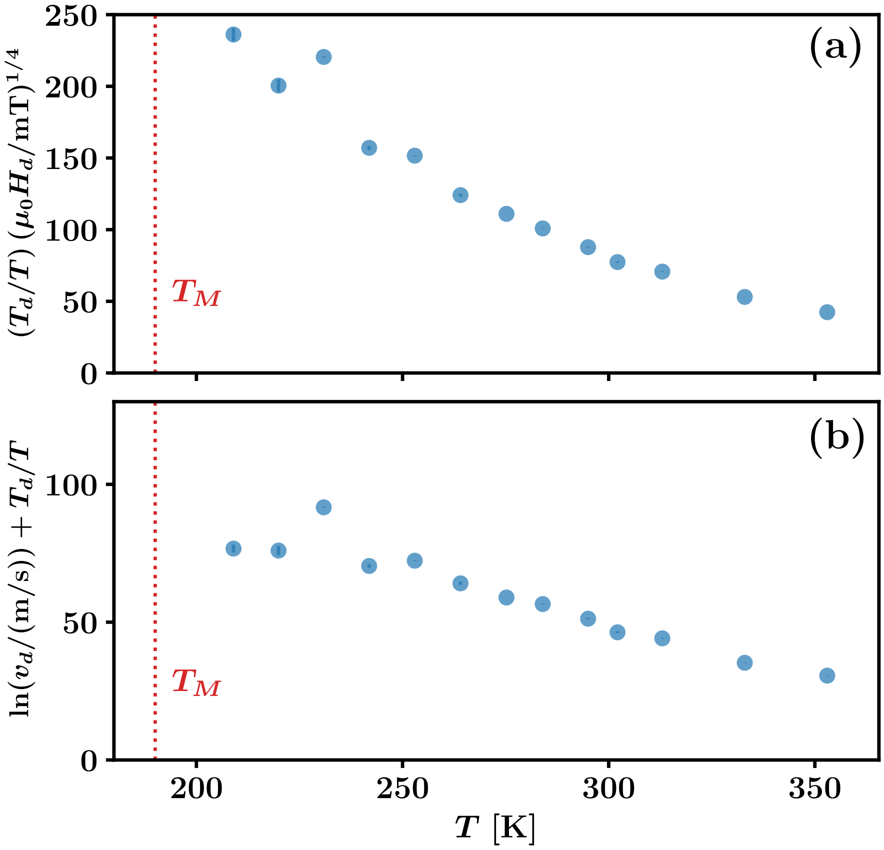

Figure 4.5: **Creep fit parameters above T_M as a function of the temperature.** (a) Slope $S = (T_d/T)(\mu_0 H_d/\mathrm{mT})^{1/4}$ and (b) intercept $I = \ln(v_d/(\mathrm{m/s})) + T_d/T$ resulting from the linear fits of the type $y = Sx + I$ with $y = \ln(v/(\mathrm{m/s}))$ and $x = (\mu_0 H/\mathrm{mT})^{-1/4}$. We indicate the position of magnetic compensation at $T = 190\,\mathrm{K}$ as a vertical dotted line.

Fitting the creep regime

Let us now present our quantitative analysis of the observed creep regime. We perform linear fits of the type $y = Sx + I$, with $y = \ln(v/(\mathrm{m/s}))$ and $x = (\mu_0 H/\mathrm{mT})^{-1/4}$, for the different temperatures, in the ranges in which we observe the characteristic dependence $\ln v \sim H^{-1/4}$. In this way, we obtain the temperature dependence of the slope

$$S(T) = \frac{T_d(T)}{T}\left(\frac{\mu_0 H_d(T)}{\mathrm{mT}}\right)^{1/4} \tag{4.1}$$

and the intercept

$$I(T) = \ln\left(\frac{v_d(T)}{\mathrm{m/s}}\right) + \frac{T_d(T)}{T} \tag{4.2}$$

according to equations (2.75) and (2.76). In figure 4.5 we present the fit results for these quantities, taking into account all the measured velocity-field curves above the magnetic compensation temperature T_M.

Creep fit slopes S increase notoriously when decreasing temperature in the range $209\,\mathrm{K} \leq T \leq 353\,\mathrm{K}$. This fact was already noticed by observing figure 4.4, and it is explicitly shown in figure 4.5(a). As we mentioned previously, the two points of lowest temperatures correspond to creep fits performed in a reduced range of velocities, and they are shown to be consistent with the observed tendency. This supports the idea that these fits are a good estimation of the creep regime corresponding to these temperatures.

The values presented in figure 4.5(a) constitute a first quantitative approach to the determination of the temperature dependence of the depinning field and temperature, H_d and T_d respectively, as these parameters are related through the relationship (4.1). In the following we will discuss how we determine these two parameters for $T > T_M$. Moreover, depinning field and temperature will give us insight on microscopic physical quantities that are derived from them.

The temperature dependence of the intercept I resulting from the creep fits, which is related to T_d and v_d as indicated by (4.2), is presented in figure 4.5(b). It also grows when decreasing temperature, but in a less notorious way. The main interest for the determination of this quantity is the possibility of obtaining v_d, which is a crucial parameter in order to predict the mobility m corresponding to the flow regime, as we have discussed in 2.4.3. However, its precise determination is elusive because a relatively small uncertainty in the depinning field generates a relatively large uncertainty in v_d, obtained as $v(H_d)$.

The temperature dependence of S and I discussed above is consistent with recent studies [186] in which the field-driven creep regime is observed for several temperatures well above T_M in ferrimagnetic TbFe wires. In those studies, however, the temperature and velocity ranges in which the creep regime is observed are much smaller.

Determining the depinning field and temperature

We have already discussed, following figure 4.2, the determination of the position of the depinning transition, i.e. the depinning field $\mu_0 H_d$, in the velocity-field curve corresponding to $T = 353\,\mathrm{K}$. In the following, we will present the determination of the depinning field values as a function of the temperature for $T > T_M$. Then, resulting from the combination of the $\mu_0 H_d$ values and the creep fit slopes S, we shall find the depinning temperature T_d also as a function of T.

In figure 4.6 we present three representative curves for the range $209\,\mathrm{K} \leq T \leq 353\,\mathrm{K}$, both in linear scale (a) and in creep-type scale (b), i.e. v in logarithmic scale vs. $(\mu_0 H)^{-1/4}$. Presented curves correspond to 333, 295 and 253 K. We also plot as dashed lines the creep regime fits corresponding to each temperature, and we indicate as shaded vertical regions the ranges of field in which we estimate the depinning field occurs, as described before.

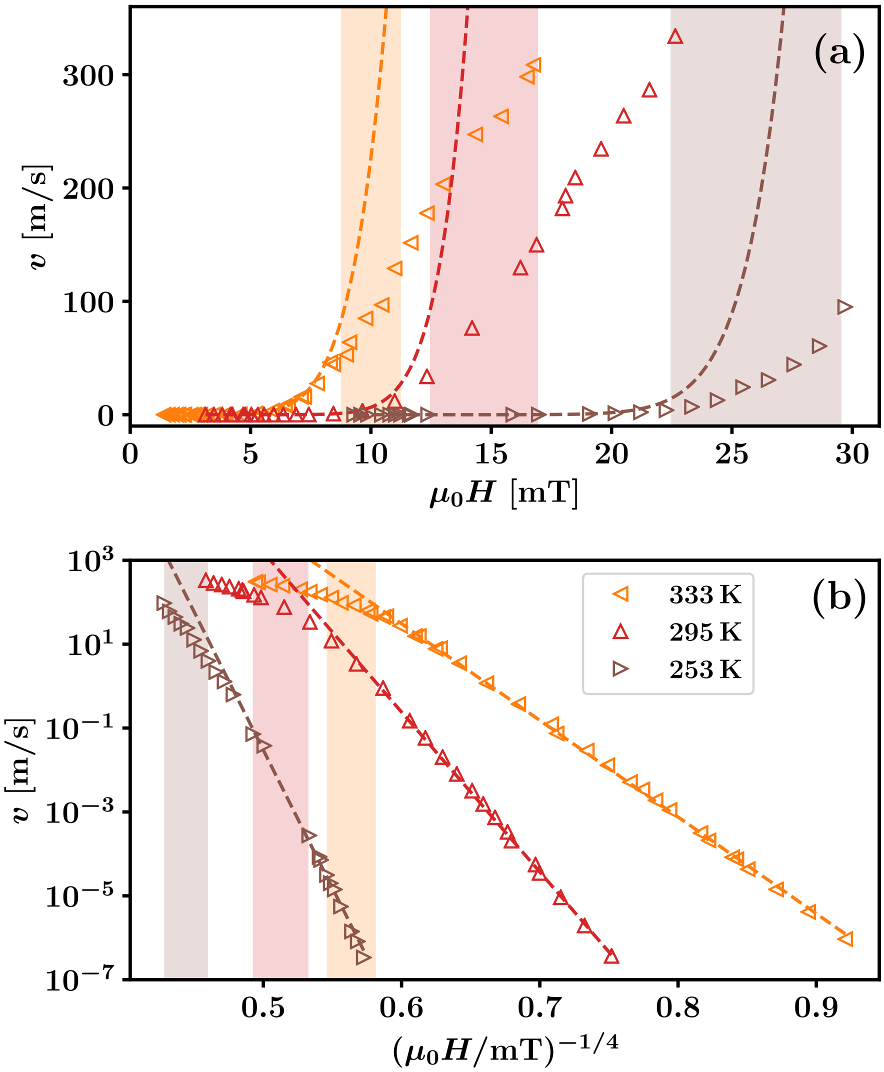

Figure 4.6: **Depinning field determination for velocity curves above T_M.** v vs. $\mu_0 H$ curves for $T = 333$, 295 and 253 K, in (a) linear scale and (b) creep scale. We plot as dashed lines the curves corresponding to the creep fits at each temperature, and we indicate as vertical shaded areas the ranges $[\mu_0 H_{d,\min}, \mu_0 H_{d,\max}]$ in which we determine the depinning field occurs. For $T = 333\,\mathrm{K}$, we estimate $\mu_0 H_d = (10 \pm 1)\,\mathrm{mT}$; for $T = 295\,\mathrm{K}$, $\mu_0 H_d = (15 \pm 2)\,\mathrm{mT}$; and for $T = 253\,\mathrm{K}$, $\mu_0 H_d = (26 \pm 4)\,\mathrm{mT}$.

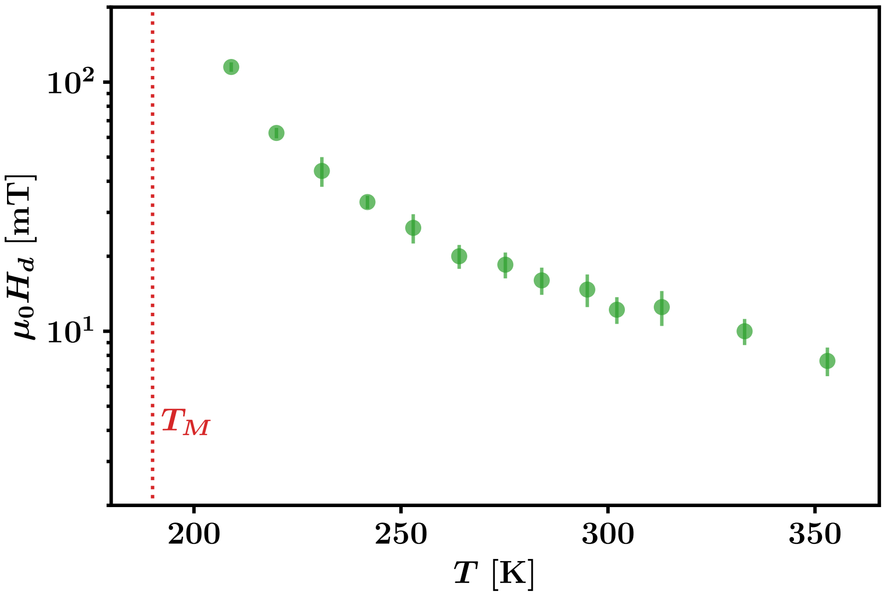

Figure 4.7: **Depinning field vs. temperature for $T > T_M$.** We indicate the position of magnetic compensation at $T = 190\,\mathrm{K}$ as a vertical dotted line.

As we explore a rather wide range of temperatures and all curves do not share the same characteristics, we are not able to use a unique protocol in order to determine the depinning field. As described before, its estimation is performed taking into account the separation of the velocity curve from the creep fit, which evidences the proximity of the depinning transition, and the existence of an inflection point[4] which is characteristic of the depinning transition as it indicates the crossover between creep, of positive concavity, and depinning regime, of negative concavity. These two signatures are systematically observed at velocities which range approximately between 50 and 150 m/s, without any clear temperature dependence. In other words, $v(H_d)$ roughly belongs to this range for all the studied curves. The observation of these elements in a quite well defined range of fields for each temperature permits us to make an estimation of $\mu_0 H_d$ and its uncertainty with a good degree of confidence.

As indicated in figure 4.6, the depinning field values for these three temperatures are estimated as $\mu_0 H_d = (10 \pm 1)\,\mathrm{mT}$ for $T = 333\,\mathrm{K}$, $\mu_0 H_d = (15 \pm 2)\,\mathrm{mT}$ for $T = 295\,\mathrm{K}$, and $\mu_0 H_d = (26 \pm 4)\,\mathrm{mT}$ for $T = 253\,\mathrm{K}$. In figure 4.7 we present the full set of depinning field values obtained in all the range of studied temperatures above the magnetic compensation temperature. Note the similarity between this dependence and that shown in figure 4.1(b). This finding extends the studies performed by T. Nishimura and collaborators [150] to a wider temperature range. In the following section we shall broaden this range by including temperatures $T < T_M$ and then, in 4.2.4 we will discuss in more detail the whole depinning

---

[4] In many cases, we do not observe a clear inflection point but do identify a region of linear dependence, i.e. an “inflection region” of zero concavity.

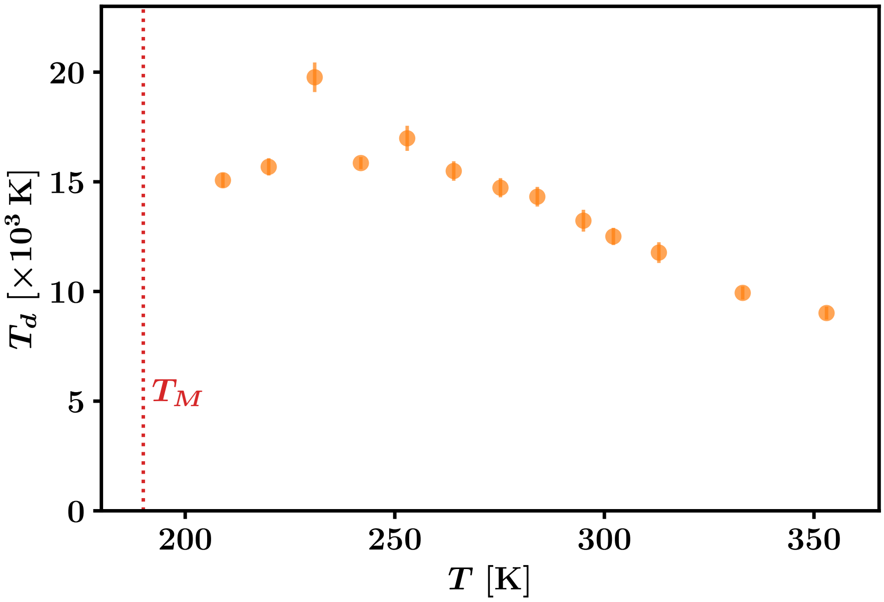

Figure 4.8: **Depinning temperature vs. temperature for $T > T_M$.** We indicate the position of magnetic compensation at $T = 190\,\mathrm{K}$ as a vertical dotted line.

field vs. temperature dependence. Additionally, we will compare it with the coercive field vs. temperature dependence that we have shown in figure 3.12(a).

The depinning field values illustrated in figure 4.7 are plotted in logarithmic scale, showing that $\mu_0 H_d$ grows dramatically when approaching the magnetic compensation temperature, ranging from $\sim 10\,\mathrm{mT}$ at $T = 353\,\mathrm{K}$ to $\sim 100\,\mathrm{mT}$ at $T = 209\,\mathrm{K}$. This behavior is expected, as discussed in section 4.1.1: the saturation magnetization M_s goes to zero when approaching T_M, resulting on higher fields needed to generate a given force over domain walls.

The depinning field determination for a given temperature permits us to obtain the corresponding depinning temperature T_d via the already determined slope S of the creep fit, which is given by equation (4.1) and is plotted in figure 4.5(a) as a function of T. Following this procedure, in figure 4.8 we present the T_d vs. T dependence for the same temperature range, calculated as $T_d = ST(\mu_0 H_d/\mathrm{mT})^{-1/4}$. We may observe that T_d gradually grows when decreasing temperature, following an apparently linear dependence. For $T < 250\,\mathrm{K}$, a less clear $T_d(T)$ dependence is observed, probably associated to the proximity of T_M and the difficulty for the measurement of low velocities.

The depinning temperature corresponds to a characteristic scale $k_B T_d$ for the effective creep energy barrier, as indicated by equation (2.76). The origin of this effective energy is the collective effect of the disordered landscape over the whole domain wall. Its increase with decreasing temperature may thus be linked to an effective enhancement of pinning forces. Note that thermal activation, quantified by the reduced temperature T/T_d, naturally decreases for decreasing temperature resulting on less frequent jumps over energy barriers, even if effective barriers remained of the same magnitude. However, not only thermal activation decreases, but also k_BT_d increases with decreasing temperature, enhancing the reduction of domain wall velocity for a given applied driving field. We shall extend this discussion later, when analyzing the temperature dependence of μ_0H_d, k_BT_d and other parameters in the whole studied range.

A last remark that we can make about the analysis of domain wall dynamics for $T > T_M$ presented above is that no effect of the angular compensation T_A is observed. This characteristic temperature, estimated as $T_A \sim 270\,\mathrm{K}$ as mentioned previously, does not appear to make any notorious effect on the intermittent domain wall dynamics characteristic of creep and depinning regimes. No clear change on the temperature dependence of velocity nor on the depinning field and temperature is observed at any point of the studied temperature range above T_M. This is consistent with the results of Y. Hirata and collaborators [145] shown in figure 4.1(a), where they observe a maximum on the $v(T)$ dependence at $T = T_A$ only for H well above H_d. The comprehension of the lacking influence of angular compensation on thermally activated dynamics is still subject of present discussions.

4.2.3 Domain wall dynamics below magnetic compensation

Let us now discuss the domain wall velocity curves obtained for temperatures below the magnetic compensation at $T_M = (190 \pm 4)\,\mathrm{K}$. In this section, we will present and discuss these results similarly to how we did in section 4.2.2 on domain wall dynamics above T_M. As we will see, the already discussed methods permit us to analyze this lower temperature range, while we find several new ingredients and characteristics that lead us to new discussions. We will find that the depinning transition becomes more abrupt and notorious as temperature decreases while the creep regime is reduced to more restricted velocity and field ranges. This results on the possibility of a direct analysis of the depinning regime below 100 K and, concomitantly, the impossibility of observing the creep regime. This phenomenology is due to the vanishing thermal activation occurring as temperature decreases, quantified by the relation T/T_d.

In figure 4.9 we present, in linear scale, a set of velocity-field curves which are characteristic of the studied temperature range below T_M, i.e. $10\,\mathrm{K} \leq T \leq 177\,\mathrm{K}$. The first notorious observation is the displacement of velocity curves to lower fields as temperature decreases. This is opposite to the behavior observed above T_M and is also an expected phenomena: as saturation magnetization increases when decreasing temperature below T_M, the field necessary to generate a given force over domain walls decreases.

Another feature of velocity curves below T_M, which is well observed in linear scale plots (figure 4.9) is that the onset on velocity is more abrupt: the field range in which experimental data grow from $\sim 10\,\mathrm{m/s}$ to $\sim 200\,\mathrm{m/s}$ is relatively narrow. As we will discuss rigorously in the following, this is the result of a much lower effective thermal activation, given by

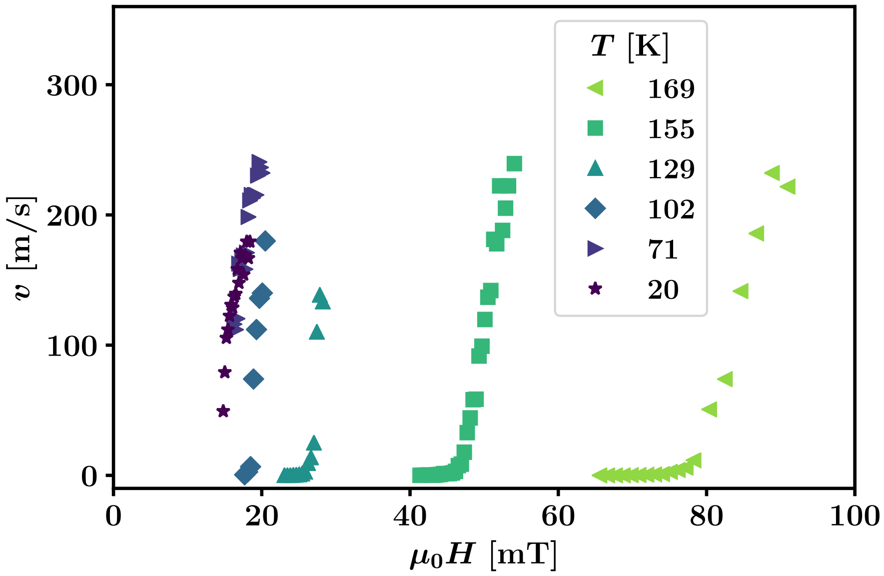

Figure 4.9: **Domain wall velocity as a function of the applied field below the magnetic compensation temperature.** Set of velocity-field curves plotted in linear scale which represent the observed behavior below T_M.

the combination of a lower temperature and a higher T_d. The observable consequences in velocity curves are a higher slope for the creep regime, and a more notorious inflection point corresponding to depinning transition, given by a weaker thermal rounding.

Similarly to what we observe above magnetic compensation temperature, below T_M we observe very high velocities, reaching values between 200 and 300 m/s, but in none of the cases we reach an evident flow regime with the characteristic proportionality between velocity and field. This is a rare circumstance of which we don't know the origin: in most domain wall velocity vs. field curves previously reported, the flow regime is well established for velocities of the order of 100 m/s.

In figure 4.10, we present representative velocity curves below T_M in a creep-type plot, showing that creep law with $\mu = 1/4$ satisfactorily describes most of them for velocities below $\sim$ 100 m/s. However, clear differences are observed when comparing these results with those corresponding to $T > T_M$ (figure 4.4), which we will discuss in the following.

Response to low fields in the low temperature range

One particularity of the velocity-field curves corresponding to $T < T_M$ is that measured velocities are always above 10^{-2} m/s. For $129\,\mathrm{K} \leq T < T_M$, lower velocity measurements were not possible due to the experimental impossibility of applying field pulses of duration longer than 50 μs with magnitudes higher than 21 mT. However, below 129 K we were not

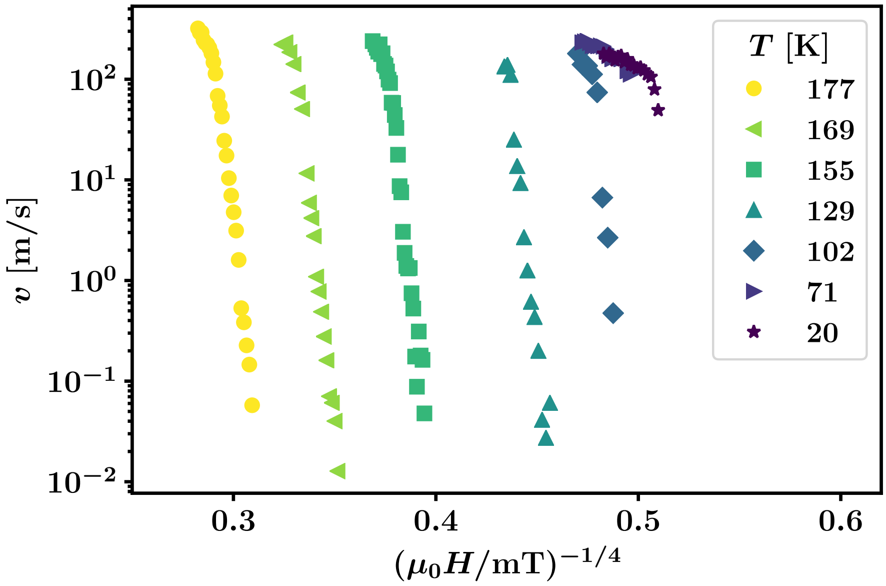

Figure 4.10: **Creep-type plot of domain wall velocity curves below the magnetic compensation temperature.** Set of representative curves of the velocity v in logarithmic scale as a function of $(\mu_0 H)^{-1/4}$ below T_M. A good agreement with creep formula for velocities below 100 m/s is observed for temperatures above 100 K. Below this temperature, creep regime is not observed.

able to measure low velocities either. The observed magnetization dynamics resulting from the application of low fields has shown a high complexity which prevents the observation of a rather uniform domain wall motion and, consequently, the measurement of wall velocity.

Figure 4.11 shows PMOKE images for $T = 102\,\mathrm{K}$. There, we exemplify the behavior of magnetic domain walls under the application of three different field magnitudes between 16.2 and 19.3 mT, showing diverse behaviors which allow or not the measurement of domain wall velocities. Images (a), (d) and (g) (left column) correspond to three different initial states. They were obtained after the application of several field pulses of 16.2 mT and 2 s (a), 17.3 mT and 40 μs (d), and 19.3 mT and 0.5 μs (g). Images (b), (e) and (h) (middle column) are the obtained images after applying one field pulse, starting from the corresponding initial state shown in the left column. Applied field pulses are, respectively, of 16.2 mT and 2 s, 17.3 mT and 40 μs, and 19.3 mT and 0.5 μs. Images (c), (f) and (i) (third column) are the differential images obtained from performing a substraction of first and second column images. This allows to clearly observe the shape and size of the inverted regions due to the application of one field pulse for each of the three cases.

The field pulse corresponding to figures (a), (b) and (c) was applied using a big coil, appropriate for low fields (lower than 21 mT) applied during a relatively long time, $\Delta t \geq 1\,\mathrm{s}$. In this case, we observe that the field pulse causes the inversion of an important region, but with the particularity that there remain many uninverted areas within this inverted region.

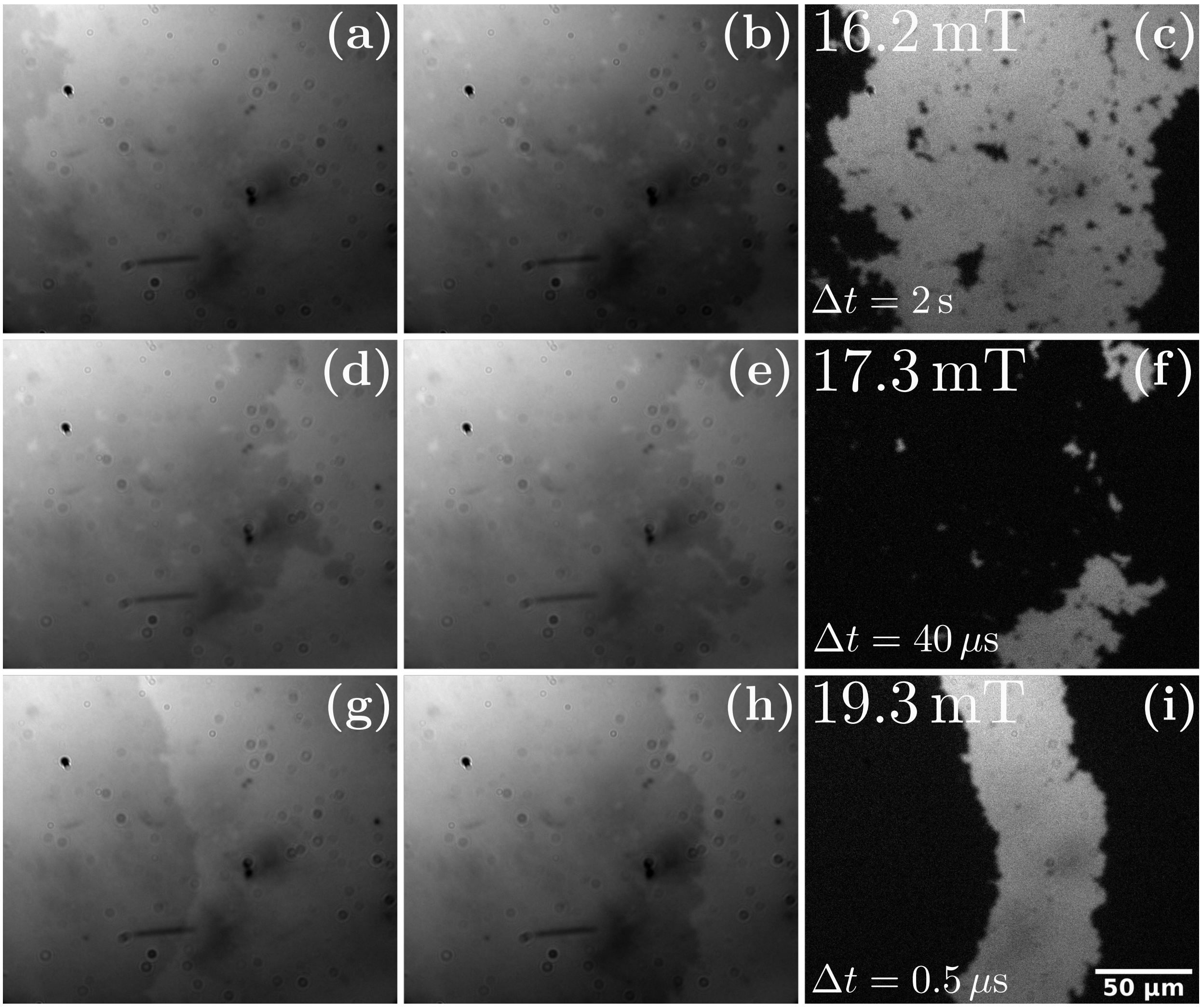

Figure 4.11: **Effect of different magnetic field amplitudes on domain walls at $T = 102\,\mathrm{K}$.** Each row of PMOKE images corresponds to two successive states between which a single field pulse of different amplitudes and durations was applied. (a), (d) and (g) correspond to initial states obtained after applying several field pulses of 16.2 mT and 2 s, 17.3 mT and 40 μs, and 19.3 mT and 0.5 μs, respectively. (b), (e) and (g) are the final states after applying one more pulse of the same amplitude and duration over the initial states. (c), (f) and (i) are differential images obtained by substracting the initial and final states.

These images illustrate that in this case, the inversion mechanism cannot be associated uniquely to the displacement of one continuous domain wall. There exist other relevant mechanisms, which could be the nucleation of multiple domains within the inverted area and the existence of strong pinning regions where domain walls do not move appreciably under this relatively low magnetic field. The existence of these rather strong pinning sites could cause domain walls to "break" in the course of their displacement, leaving "islands" along its path. Given this scenario, for this field magnitude we consider that the measurement of domain wall velocity is not possible.

Slightly higher magnetic fields applied at $T = 102\,\mathrm{K}$ during timescales of the order of the second generate a complete inversion of the observed area. As it is illustrated in figures (d), (e) and (f), for $\mu_0 H = 17.3\,\mathrm{mT}$ pulse time has to be dramatically reduced to the tens of microseconds in order to generate the observable inversion of only one part of the sample in the microscope's field of view. In this case, after a pulse time of $40\,\mu\mathrm{s}$ between figures (d) and (e), the inversion of a finite area which could be associated to domain wall motion occurs. Nevertheless, this apparent movement is very irregular, and there exist segments of the initial domain wall that do not move at all. In addition, some small regions remain uninverted within the newly inverted area, similarly to what we observed for $\mu_0 H = 16.2\,\mathrm{mT}$. In this context, a mean velocity which is representative of the global domain wall movement cannot be defined. In summary, we are not able to determine the domain wall velocity for this magnitude of the magnetic field either, even if this field is high enough to generate magnetization inversion with a microseconds-time pulse. This highlights the fact that, at this temperature, mean domain wall velocities below $\sim 0.5\,\mathrm{m/s}$ cannot be measured in our sample.

For slightly higher fields, domain walls move in a more regular way and we are able to infer a domain wall velocity which is representative of the whole wall. Images (g), (h) and (i) (figure 4.11) show the effect of applying $\mu_0 H = 19.3\,\mathrm{mT}$ during $\Delta t = 0.5\,\mu\mathrm{s}$. As it is evident, in this case the observed domain wall is displaced by the applied field pulse in a uniform way, with the characteristic fluctuations resulting from disorder. The determined domain wall velocity for this field magnitude at $T = 102\,\mathrm{K}$ is $v = (110 \pm 10)\,\mathrm{m/s}$.

The difficulty of measuring low domain wall velocities that we have just discussed becomes more crucial when decreasing temperature below $100\,\mathrm{K}$. For this range of lowest temperatures, it is even impossible to measure domain wall velocities below $10\,\mathrm{m/s}$, leading to the absence of an observable creep dependence in the velocity-field curves. However, as we will see in section 4.3, for $T < 100\,\mathrm{K}$ we are able to directly perform fits of the depinning regime, which is clearly observed due to the vanishing relevance of thermal activation as temperature decreases.

Fitting the creep regime

Let us now put our focus in the performed creep fits and obtained parameters. As we have noticed when discussing figure 4.10, the creep regime in the range of $T < T_M$ corresponds

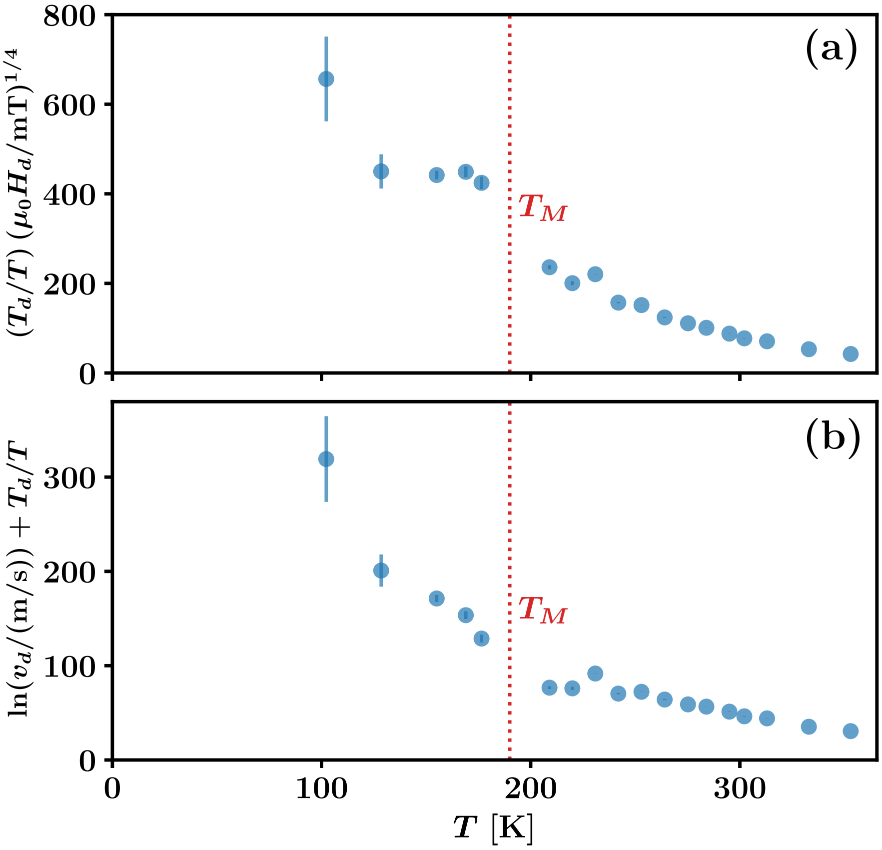

Figure 4.12: **Creep fit parameters as a function of the temperature in the whole temperature range.** (a) Slope $S = (T_d/T)(\mu_0 H_d/\mathrm{mT})^{1/4}$ and (b) intercept $I = \ln(v_d/(\mathrm{m/s})) + T_d/T$ resulting from the linear fits of the type $y = Sx + I$ with $y = \ln(v/(\mathrm{m/s}))$ and $x = (\mu_0 H/\mathrm{mT})^{-1/4}$. We indicate the position of magnetic compensation at $T = 190\,\mathrm{K}$ as a vertical dotted line.

to velocities in the range $0.01\,\mathrm{m/s} < v < 100\,\mathrm{m/s}$. In figure 4.12, we plot all the slopes S (a) and intercepts I (b) we obtained in all the temperature range, i.e. including the data already shown in figure 4.5, which corresponds to $T > T_M$. These quantities are related with depinning parameters $\mu_0 H_d$, T_d and v_d through relations (4.1) and (4.2).

Below T_M, the obtained creep slopes S are practically constant between 129 and 177 K. This feature is in contrast with the clear change on creep slope observed for $T > T_M$. Note that the $\mu_0 H_d(T)$ dependence plays a crucial role on the $S(T)$ dependence, as it is given by the combination $(T_d(T)/T)(\mu_0 H_d(T)/\mathrm{mT})^{1/4}$, equation (4.1). Above T_M, $\mu_0 H_d$ increases with decreasing temperature due to its divergence at $T = T_M$ (see figure 4.7) and (T_d/T) also increases with decreasing temperature (see figure 4.8). Consequently, both $\mu_0 H_d$ and (T_d/T) collaborate on the increase of S with decreasing T. Conversely, and also due to the divergence at $T = T_M$, $\mu_0 H_d$ decreases with decreasing temperature for $T < T_M$, as we will explicitly show below. This explains the fact that a different $S(T)$ dependence is observed above and below T_M. For $T = 102\,\mathrm{K}$, the creep slope is notoriously higher, but with a considerable uncertainty as the fit range is much smaller due to the reduced range of measurable velocities.

Another notorious feature of the temperature dependence of the creep slope S, plotted in figure 4.12(a), is the jump of almost a factor two between $T = 209\,\mathrm{K}$, above $T_M = 190\,\mathrm{K}$, and $T = 177\,\mathrm{K}$, below T_M. The precise determination of $\mu_0 H_d$ and T_d for these temperatures, which we will present and discuss in the following, will shed light on this feature.

Creep fit intercepts I, related to T_d and v_d according to equation (4.2) and plotted in figure 4.12(b), show a monotonous decrease when increasing temperature. As we will show below, this dependence is associated fundamentally to $T_d(T)/T$. Depinning velocities v_d, which may be obtained as $v(H_d) = \exp(IT/T_d)$, are determined with a rather big uncertainty; however, they do not change significantly in the studied range. As we have pointed out before, they are systematically of the order $v_d \sim 100\,\mathrm{m/s}$.

Determining the depinning field and temperature

We shall now present our determination of the depinning field below the compensation temperature. We will discuss the temperature dependence of $\mu_0 H_d$ and, then, the temperature dependence of T_d which arises from the combination of $\mu_0 H_d$ values and creep slopes A. Furthermore, we will discuss how thermal activation, represented by the reduced temperature T/T_d, decreases notoriously with decreasing temperature, leading to the practical disappearance of observable thermal effects below 100 K.

Figure 4.13 illustrates the depinning field determination for three different temperatures, which are representative of the range $102\,\mathrm{K} \leq T \leq 177\,\mathrm{K}$. We consider the ingredients already discussed for the determination of $\mu_0 H_d$ from the velocity-field curves: the separation from creep fit, and the inflection point.

In velocity curves measured between 100 K and T_M, we observe the coincidence of the inflection point and the separation from the fitted creep law. This is the hypothesis that needs to be fulfilled for the application of the self-consistent method presented by Rebeca Díaz Pardo and collaborators [18] and discussed in section 2.4.3. In this context, we are able to perform a prediction on the mobility corresponding to the flow regime. This fact and the high values of creep slopes, which generate a more abrupt separation from creep behavior at $\mu_0 H_d$, make the determination of the depinning field much more precise in the range $102\,\mathrm{K} \leq T \leq 177\,\mathrm{K}$; in other words, we are able to determine $\mu_0 H_d$ with a much smaller relative uncertainty. Figure 4.13 shows the velocity curves corresponding to $T = 177$, 169 and 155 K, their creep laws as dashed lines, the estimations of $\mu_0 H_d$ with their uncertainties as vertical shaded areas, the corresponding zero-temperature depinning regime curves which follow equation (2.82), and the corresponding predictions for the flow regime proportionality $v \propto \mu_0 H$.

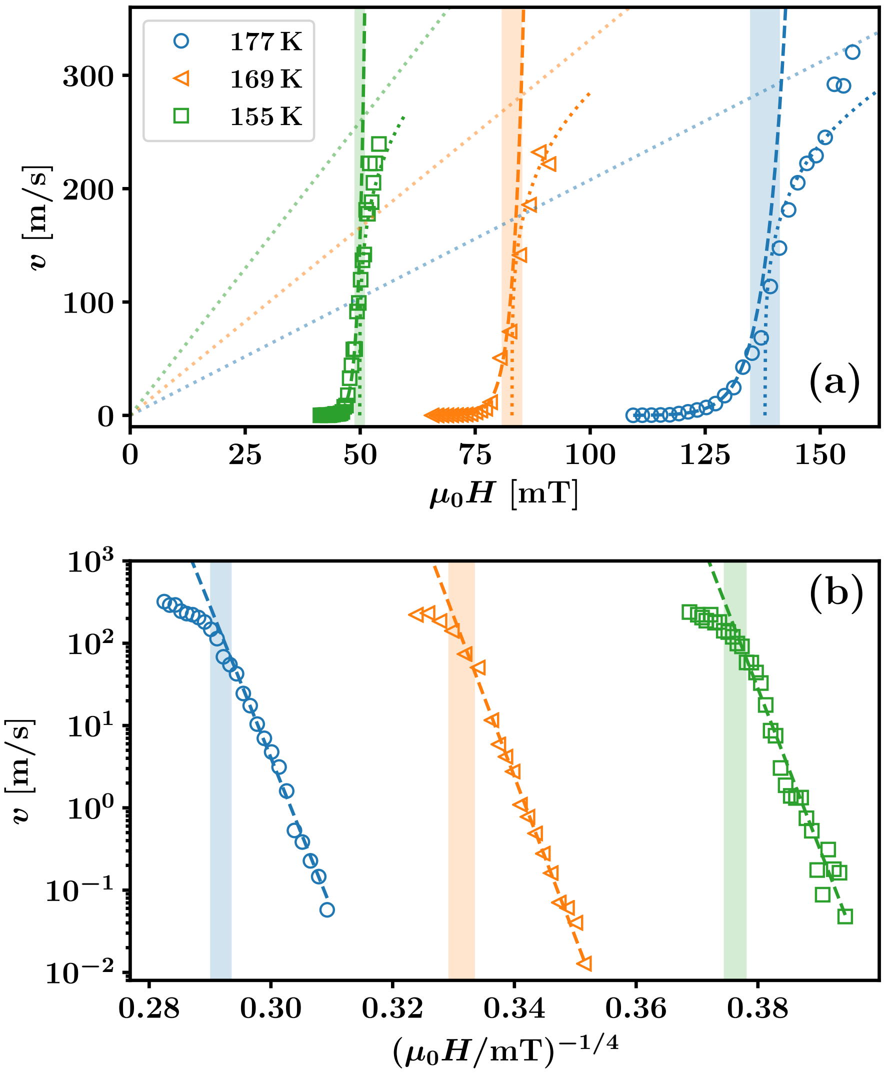

Figure 4.13: **Depinning field determination for velocity curves below T_M and above 100 K.** Velocity v vs. field $\mu_0 H$ curves for $T = 177$, 169 and 155 K, in (a) linear scale and (b) creep scale. We plot the creep fits at each temperature as dashed curves, and we indicate as vertical shaded areas the ranges in which we determine the depinning field occurs. For $T = 177\,\mathrm{K}$, we estimate $\mu_0 H_d = (138 \pm 3)\,\mathrm{mT}$; for $T = 169\,\mathrm{K}$, $\mu_0 H_d = (83 \pm 2)\,\mathrm{mT}$; and for $T = 155\,\mathrm{K}$, $\mu_0 H_d = (49.9 \pm 0.9)\,\mathrm{mT}$. In the linear scale plot, zero-temperature depinning regime (equation (2.82)) with $\beta = 0.25$ corresponding to each of the temperatures are plotted as dotted curves. Resulting v_H values are $v_H = 440\,\mathrm{m/s}$ for $T = 177\,\mathrm{K}$, $v_H = 420\,\mathrm{m/s}$ for $T = 169\,\mathrm{K}$, and $v_H = 400\,\mathrm{m/s}$ for $T = 155\,\mathrm{K}$. Calculations of flow regime mobilities permit us to indicate as dotted straight lines the predictions for the flow regime. Obtained mobilities are $m = 2.1$, 3.3 and 5.2 (m/s)/mT for $T = 177$, 169 and 155 K respectively.

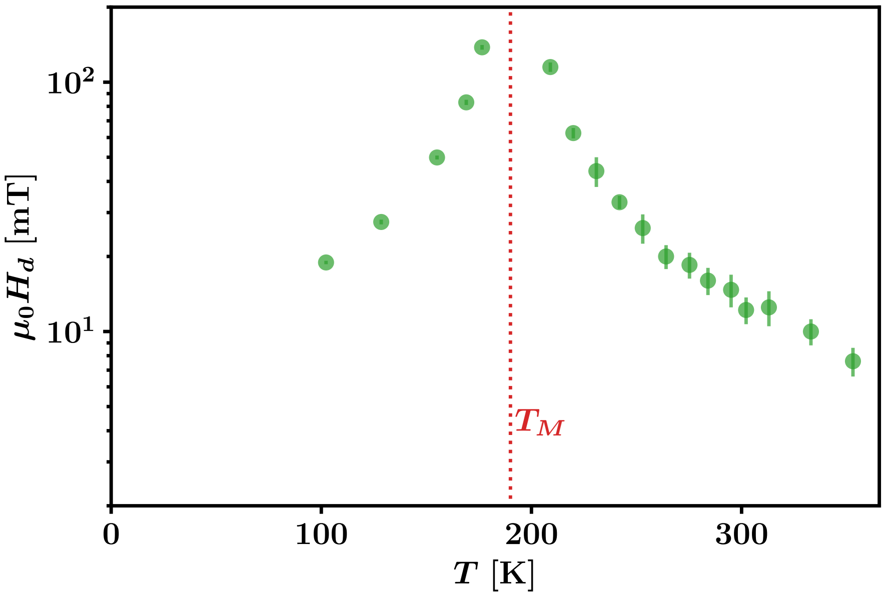

Figure 4.14: **Depinning field as a function of T for $T > 100\,\mathrm{K}$.** We indicate as a vertical dotted line the position of the magnetic compensation temperature at 190 K.

The obtained depinning field values for the three represented temperatures are $\mu_0 H_d = (138 \pm 3)\,\mathrm{mT}$ for $T = 177\,\mathrm{K}$, $\mu_0 H_d = (83 \pm 2)\,\mathrm{mT}$ for $T = 169\,\mathrm{K}$, and $\mu_0 H_d = (49.9 \pm 0.9)\,\mathrm{mT}$ for $T = 155\,\mathrm{K}$. Note that, as we mentioned above, in this temperature range uncertainties in $\mu_0 H_d$ correspond to $\sim 2\,\%$ of the determined value, while for $T > T_M$ they were generally above 10 %. Zero-temperature depinning curves were plotted using the determined $\mu_0 H_d$ values and the velocities v_H calculated as $v_H = v_T / x_0$, with $x_0 = 0.65$ [18] and $v_T = v_d\,(T/T_d)^{-\psi}$, according to equation (2.81). In this last expression, we used $\psi = 0.15$, $T_d = ST(\mu_0 H_d/\mathrm{mT})^{-1/4}$, and $v_d = \exp{(IT/T_d)}$, in accordance with (4.1) and (4.2).

Figure 4.14 presents all the determined depinning fields for $T \geq 102\,\mathrm{K}$, plotted as a function of temperature. The divergence of the depinning field when approaching the compensation temperature T_M becomes evident, both above and below T_M. As we have already discussed, this is an expected behavior because $M_s \to 0$ when $T \to T_M$. Note that the coercive field follows a similar divergence, as evidenced in figure 3.12(a). In the following section we will discuss this issue more deeply.

In figure 4.15(a) we present T_d values plotted as a function of temperature, obtained from the combination of $\mu_0 H_d$ values and creep slopes A according to (4.1). We may observe that the depinning temperature $T_d(T)$ follows a monotonous decreasing behavior with increasing temperature which is not affected significantly close to the compensation temperature T_M. A remarkable finding is that the obtained T_d values are considerably higher than most previously reported results [120]. In particular, the T_d values of 20000-30000 K that correspond to the range $102\,\mathrm{K} \leq T \leq 177\,\mathrm{K}$ are among the highest reported

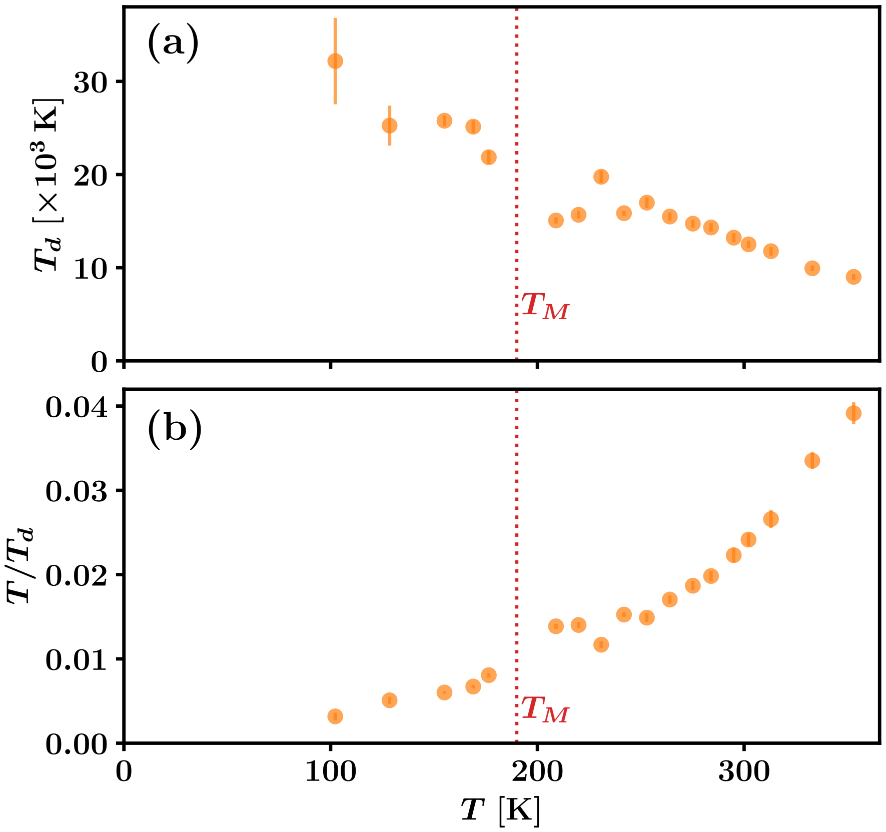

Figure 4.15: **Depinning temperature T_d and reduced temperature T/T_d as a function of T.** (a) T_d vs. T and (b) T/T_d vs. T. We indicate in both cases as a vertical dotted line the position of the magnetic compensation temperature at 190 K.

values [187–189]. This indicates that effective creep energy barriers in the studied sample are relatively large and, besides, their magnitude is enhanced as temperature decreases.

Once we have determined the T_d vs. T dependence, we may compute the reduced temperature T/T_d and plot it as a function of temperature; we present this result in figure 4.15(b). The reduced temperature is directly related to the effective thermal activation energy, which as we have repeatedly claimed plays a crucial role in domain wall dynamics, particularly in the creep regime and the thermal rounding of the depinning transition.

As it is illustrated in figure 4.15(b), effective thermal activation drops continuously when cooling, from a reduced temperature $T/T_d = 0.04$ at $T = 353$ K to $T/T_d = 0.003$ at $T = 102$ K. Such extremely low values, corresponding to the proximity of $T = 100$ K, had never been observed experimentally [120]. The value $T/T_d = 0.003$ constitutes a lower limit for our experimental access to the measurement of a creep-type dependence below the depinning transition: very low T/T_d values imply huge slopes S, what reduces the field range in which creep occurs and necessitates a very precise field control. This difficulty aggregates to the fact that, as we have shown previously, domain wall displacements at relatively low velocities cannot be measured with our experimental setup in the low temperature range.

As we have already noted in the previous discussion, for temperatures below 100 K we are only able to measure velocities for values of field $\mu_0 H \gtrsim \mu_0 H_d$. In this context, we are only able to observe and analyze the depinning regime. However, as we will discuss in detail in section 4.3, our observation of the depinning regime in velocity curves corresponding to $T < 100\,\mathrm{K}$ is particularly clear, what permits an unprecedented direct characterization of this regime.

4.2.4 Temperature dependence of depinning parameters

After having discussed the domain wall dynamics in a wide temperature range, let us now analyze the complete dependence of physical quantities which characterize the pinning of field-driven magnetic domain walls in our GdFeCo sample. These quantities are plotted as a function of temperature in figure 4.16.

In panel (a), we plot the SQUID measurement of the saturation magnetization M_s, already presented in figure 3.9. As we have pointed out, this global magnetic quantity impacts on the depinning field $\mu_0 H_d$ and the coercive field $\mu_0 H_c$, plotted in panel (b). Note that, while both $\mu_0 H_d$ and $\mu_0 H_c$ show a similar behavior, they are close to each other for $T < T_M$ and they are well separated for $T > T_M$, with $\mu_0 H_c < \mu_0 H_d$. This evidences that the nucleation of magnetic domains and subsequent domain wall displacement occurs well below the depinning of domain walls for $T > T_M$, while it occurs close to the depinning for $T < T_M$. This may be qualitatively linked to the fact that domain wall motion in the creep regime, i.e. below $\mu_0 H_d$, spans over a rather wide range of fields for $T > T_M$ (see section 4.2.2) while it spans over a narrow range for $T < T_M$ (see section 4.2.3).

The close relation between $\mu_0 H_d$ and M_s, which is predicted to be an inverse proportionality [120], is evidenced, particularly in the limit $T \to T_M$, where $M_s \to 0$ and $\mu_0 H_d$ diverges. In the plot of $\mu_0 H_d$ vs. T shown in panel (b), we also consider the depinning field determination in the lowest temperature range, $T < 100\,\mathrm{K}$, of which we have not yet presented the detailed analysis but will be described in section 4.3. The $\mu_0 H_d(T)$ dependence obtained for $10\,\mathrm{K} \leq T \leq 353\,\mathrm{K}$ constitutes to the best of our knowledge the first measurement of the depinning field temperature dependence in such a wide range.

In order to quantitatively analyze the relationship between M_s and $\mu_0 H_d$ and to obtain an insight on the nature of characteristic intermittent domain wall displacement events, we may assess the Zeeman energy per unit area $\varepsilon_Z(H_d)$ resulting from the inversion of magnetization at the depinning transition and given by

$$\varepsilon_Z(H_d) = 2\mu_0 H_d M_s t \tag{4.3}$$

in accordance with (2.87), where $t = 10\,\mathrm{nm}$ is the film thickness. As discussed in 2.4.4, this characteristic quantity is related to the effective pinning energy barrier, whose magnitude is $\sim k_B T_d$, through relation (2.88).

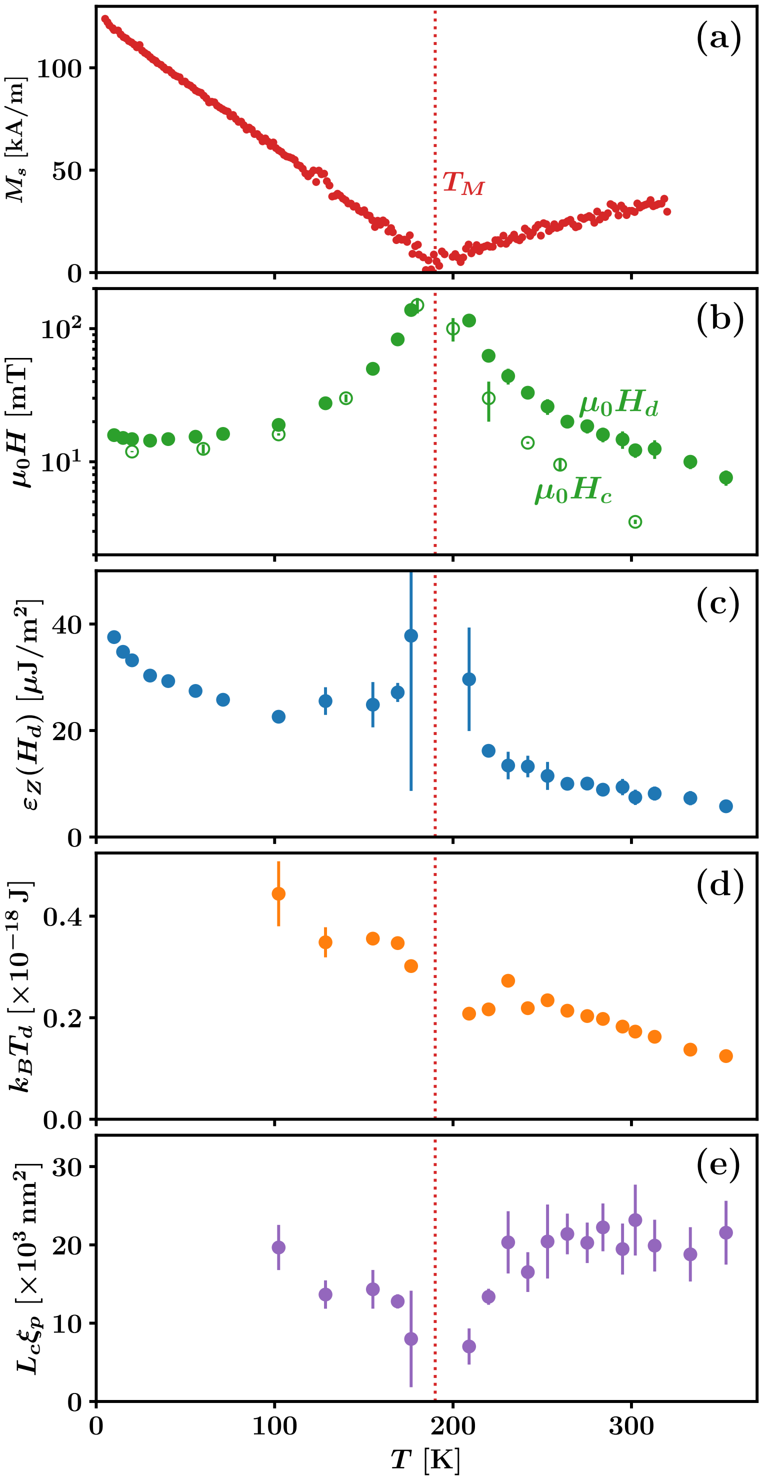

Figure 4.16: **Temperature dependence of obtained physical quantities characterizing the pinning of magnetic domain walls.** (a) Saturation magnetization M_s. (b) Depinning field $\mu_0 H_d$ (full symbols) and coercive field $\mu_0 H_c$ (empty symbols). (c) Zeeman energy per unit area $\varepsilon_Z(H_d)$ corresponding to a domain wall displacement at depinning. (d) Characteristic magnitude $k_B T_d$ of the effective pinning energy barrier. (e) Estimated characteristic Larkin surface area $L_c \xi_p$.

In figure 4.16(c), we plot the Zeeman energy per unit area at depinning. Close to $T = T_M$, obtained values have big error bars due to a big relative uncertainty of vanishing M_s values. The observed increase of $\varepsilon_Z(H_d)$ for decreasing temperatures independently confirms a fact previously evidenced by the observed $T_d(T)$ dependence, this is, the increasing magnitude of the effective pinning energy barrier as temperature decreases.

Figure 4.16(d) shows the characteristic pinning energy $k_B T_d$, calculated as described previously from the analysis of domain wall velocity curves. The fact that $\varepsilon_Z(H_d)$ and $k_B T_d$ follow similar behaviors support the relation (2.88) between independently calculated characteristic energies. This is assessed in figure 4.16(e), where we plot the estimated characteristic area $L_c \xi_p$, the so-called Larkin surface area, estimated as $L_c \xi_p = k_B T_d / \varepsilon_Z(H_d)$. As evidenced in the figure, this quantity belongs to the range 10000-20000 nm^2 in all the temperature range, suggesting that the characteristic length scales of disorder do not change considerably even if the magnitude of energy barriers change as evidenced by the dependence of $k_B T_d$ with temperature. This aspect, namely the magnitudes of characteristic lengths playing a role in domain wall motion and morphology, will be further addressed in section 4.3.4 and in chapter 5.

We have already discussed various aspects of the phenomenology encountered when analyzing domain wall velocity curves in a wide range of temperatures. Furthermore, we have studied the temperature variation of several physical parameters which play a role on domain wall dynamics in the creep and depinning regimes and, additionally, shed light on the properties of effective disorder playing a leading role in these phenomena. However, the observed behaviors still keep several open questions which call for further research. For example, the microscopic origin of the effective increase of the pinning magnitude when temperature decreases is still unclear.

The discussion made above has been focused on temperature- and material-dependent physical parameters, without talking deeply about universal aspects. In the following section, which constitutes the second and final part of the presentation of results corresponding to this chapter, we will present the measurements of domain wall dynamics which have driven us to the most relevant result of this chapter; namely, the direct experimental determination of the complete set of universal critical exponents corresponding to the depinning transition.

4.3 Athermal depinning transition at low temperatures

In our discussion about the temperature dependence of relative thermal activation, quantified by the reduced temperature T/T_d, we have pointed out that for temperatures close to 100 K we reach extremely low values $T/T_d \simeq 0.003$ (see figure 4.15). To the best of our knowledge, such low experimentally measured values had never been reported [120]. In this conditions, and also due to the difficulty of measuring relatively low velocities (see figure 4.11), the observation of the creep regime below $T = 100$ K was not possible. However, the extremely low thermal activation gives rise to an unprecedentedly clear observation of the

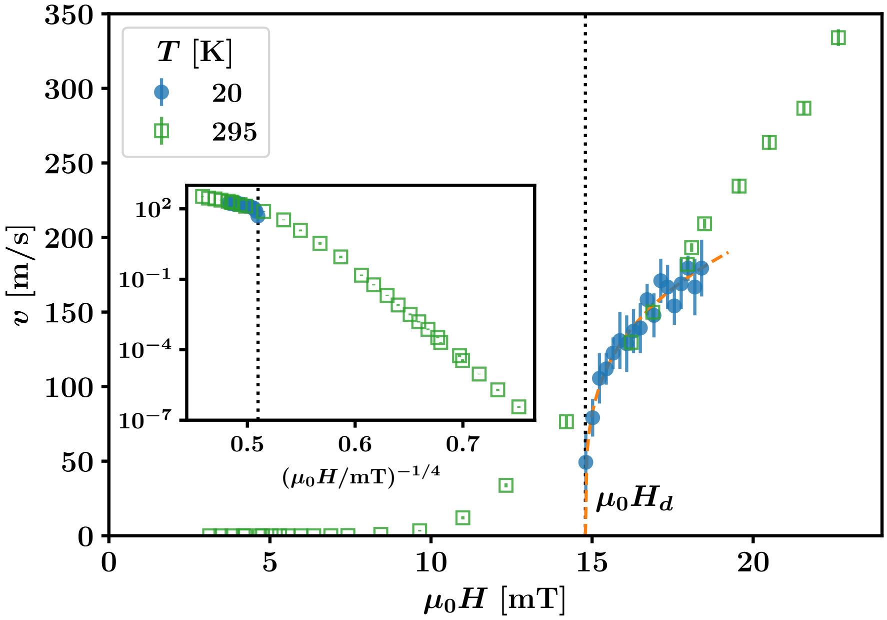

Figure 4.17: **Thermally activated v vs. $\mu_0 H$ curve at $T = 295\,\mathrm{K}$ and athermal curve at $T = 20\,\mathrm{K}$.** Main panel: plot in linear scale. A zero-temperature depinning curve, equation (2.82), is plotted as a dashed line. The corresponding depinning field is $\mu_0 H_d = 14.8\,\mathrm{mT}$, which is indicated as a vertical dotted line. Velocity vs. field dependence is practically the same for both curves in a range of 3 to 4 mT above this value. Inset: Creep type plot where thermally activated creep regime is appreciated for $T = 295\,\mathrm{K}$, while it cannot be observed for $T = 20\,\mathrm{K}$.

depinning transition, with practically athermal, i.e. zero-temperature-like, characteristics.

4.3.1 Zero-temperature-like characteristics

Let us now discuss the observed phenomenology for domain wall velocity curves in the low temperature range, comparing it to the thermally activated behavior that we have analyzed for higher temperatures in section 4.2. In figure 4.17, we plot two representative v vs. $\mu_0 H$ curves: one of them corresponds to $T = 20\,\mathrm{K}$, and the other one to ambient temperature, i.e. $T = 295\,\mathrm{K}$. A particularity of these two curves is that the determined depinning field is practically equivalent: for $T = 20\,\mathrm{K}$, $\mu_0 H_d = (14.8 \pm 0.2)\,\mathrm{mT}$, while for $T = 295\,\mathrm{K}$, $\mu_0 H_d = (15 \pm 2)\,\mathrm{mT}$. This, and the fact that they coincide in a finite range of $\mu_0 H$, permits to perform a direct comparison of the two curves, one of them showing a zero-temperature-like behavior while the other presents evident thermally activated dynamics.

In the main panel, we plot the velocity vs. field characteristics in linear scale. For $T = 20\,\mathrm{K}$, depinning transition is clearly observed with its characteristic curvature, as theoretically predicted for $T = 0$ (note the similarity with figure 2.11(a)). This permits to describe the whole $v(H)$ dependence via the zero-temperature depinning regime, equation (2.82). The best obtained fit[5] of this relation is drawn as a dashed curve. We indicate the corresponding depinning field at $\mu_0 H_d = 14.8\,\mathrm{mT}$ as a vertical dotted line. Furthermore, due the practical absence of thermal effects, at $T = 20\,\mathrm{K}$ no domain wall velocities could be measured for $\mu_0 H < \mu_0 H_d$. For $T = 295\,\mathrm{K}$, in contrast, the typical thermally activated behavior is evidenced, with domain wall velocities measured in a relatively wide range below $\mu_0 H_d$. The inset evidences the very well defined creep regime dependence, which is not observed at all for $T = 20\,\mathrm{K}$. Conversely, for $\mu_0 H > \mu_0 H_d$, the curves corresponding to both temperatures coincide in a finite range, from $\mu_0 H \simeq 15.5\,\mathrm{mT}$ to $\mu_0 H \simeq 18.5\,\mathrm{mT}$, what evidences that thermal effects are substantially less relevant above depinning. These two curves constitute an experimental realization of the theoretically predicted velocity-force characteristics corresponding to a driven elastic line in a bi-dimensional disordered medium with and without thermal activation that we have presented in figure 2.11(a).

4.3.2 General procedure for fitting the athermal depinning transition

Let us now describe the analysis method that we implement in order to fit the athermal depinning law, equation (2.82), what permits us to obtain the parameters $\mu_0 H_d$, v_H and β. We may write that equation taking the logarithm at both sides, as

$$\ln v = \ln v_H + \beta \, \ln \left(\frac{H - H_d}{H_d} \right) . \tag{4.4}$$

Consequently, we can perform a linear fit of the type $y = I + Sx$ with $y = \ln(v/(\mathrm{m/s}))$ and $x = \ln((H - H_d)/H_d)$ in order to obtain β as the slope S and $\ln(v_H/(\mathrm{m/s}))$ as the intercept I.

Precise determination of the depinning field $\mu_0 H_d$

Before performing such fitting procedure, it is necessary to find a value for $\mu_0 H_d$. In the following, we present the protocol for the determination of $\mu_0 H_d$ that we implement for all the velocity curves corresponding to the range of temperatures below $100\,\mathrm{K}$. A first approximation can be directly made by looking at each velocity curve in linear scale. For example, for $T = 20\,\mathrm{K}$ (see figure 4.17), depinning field is clearly close to $15\,\mathrm{mT}$, with an uncertainty which is below $0.5\,\mathrm{mT}$.

In order to have a better insight, we look at the phenomenology of domain wall motion observed with the PMOKE microscope. In figure 4.18 we present a set of images for three different applied fields in the range $14.6\,\mathrm{mT} \leq \mu_0 H_d \leq 15.4\,\mathrm{mT}$. For these three values of the applied field, a sequence of two images and the corresponding differential image is

---

[5] In 4.3.2 we will describe the fitting methods.

presented, similarly to what we have shown in figure 4.11, in order to illustrate the type of magnetization inversion that we may appreciate via the PMOKE microscope in these experimental conditions.

As we can appreciate in figure 4.18, images (a), (b) and (c), at 14.6 mT magnetization reversal is not due to an homogeneous drive over continuous domain walls. They apparently move in some areas while they don't move in other areas. Additionally, they present overhangs and, within the regions which are inverted by the applied pulse, there exist small "islands" remaining uninverted. This may be caused by the occurrence of plastic events that occur at relatively strong pinning sites and "break" domain walls, or may be the result of a magnetization process dominated by the nucleation of many small domains. These observations evidence that domain walls are not under the hypothesis of a continuous elastic line subject to an homogeneous drive; consequently, we cannot measure a representative mean domain wall velocity that could be interpreted in the framework of the elastic line model. As we do not observe a clear global domain wall displacement, we assume that the depinning transition occurs at higher fields; then, for this case, $\mu_0 H_d > 14.6\,\mathrm{mT}$.

In contrast, at 15.4 mT (see figure 4.18 (g-i)), we observe a clear and uniform domain wall motion which corresponds to $v \simeq 100\,\mathrm{m/s}$. In addition, domain walls do not have overhangs, and there is no evidence of plastic events breaking them. In this case, we have a good velocity measurement with a relatively high value, of the order of typical v_d values[6], and then we consider that the applied field is above the depinning transition, i.e. $\mu_0 H_d < 15.4\,\mathrm{mT}$ for this case.

There exists an intermediate field range $(\mu_0 H_{d,\mathrm{min}}, \mu_0 H_{d,\mathrm{max}})$ where behavior shares some features of these two extreme cases. For $T = 20\,\mathrm{K}$, this range corresponds to $14.6\,\mathrm{mT} < \mu_0 H < 15.2\,\mathrm{mT}$. In figure 4.18 (d-f) we may appreciate the effect of an applied field pulse within this range, in this case $\mu_0 H = 15.0\,\mathrm{mT}$. Domain wall motion is relatively uniform, but there exists evidence of plastic events generating islands and overhangs. We then assume that $\mu_0 H_d$ belongs to this crossover range in which domain wall motion passes from being unidentifiable to uniform, thus permitting to define a representative mean velocity which may be analyzed in the framework of a continuous elastic line moving due to an uniform drive.

In figure 4.19 we plot the velocity vs. field measurements for $T = 20\,\mathrm{K}$, indicating with vertical dotted lines the range $(\mu_0 H_{d,\mathrm{min}}, \mu_0 H_{d,\mathrm{max}})$ in which we consider depinning transition occurs. In order to evaluate more precisely the field at which depinning transition occurs, we perform fits of equation 4.4 using $\mu_0 H_d$ values in all the range $(\mu_0 H_{d,\mathrm{min}}, \mu_0 H_{d,\mathrm{max}})$. All these fits shall be performed considering the same number of data points, and then we do not take into account velocity measurements within this range (empty circles in the figure). In other words, we consider data points of v vs. $\mu_0 H$ corresponding to $\mu_0 H \geq \mu_0 H_{d,\mathrm{max}}$ (full circles in the figure). The final step for the determination of the $\mu_0 H_d$ value and its uncertainty, indicated in the figure as a vertical dashed line and a shaded region respectively, consists on a maximization of the $\ln(v/(\mathrm{m/s}))$ vs. $\ln((H - H_d)/H_d)$ fit quality that we will

---

[6] See section 4.2 for a discussion on $v_d = v(H_d)$ values.

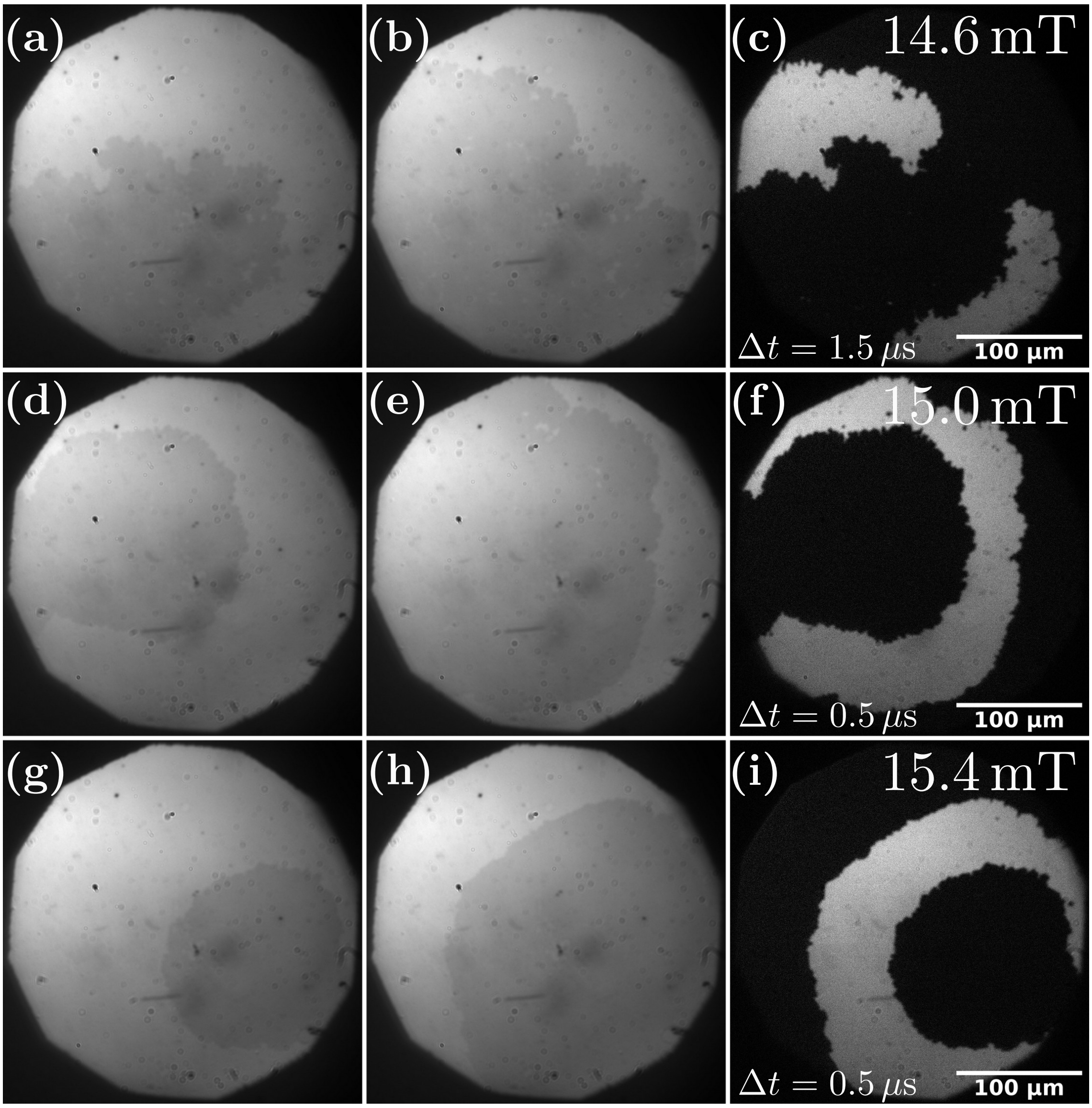

Figure 4.18: **PMOKE microscopy images in the vicinity of the depinning transition at $T = 20\,\mathrm{K}$.** Each row corresponds to two successive states obtained for different field pulse amplitudes and durations. (a), (d) and (g) are initial states obtained after the application of several pulses of 14.6 mT and 1.5 μs, 15.0 mT and 0.5 μs, and 15.4 mT and 0.5 μs, respectively. (b), (e) and (h) are final states after applying one more pulse of the same amplitude and duration. (c), (f) and (i) are differential images obtained from substracting initial and final states.

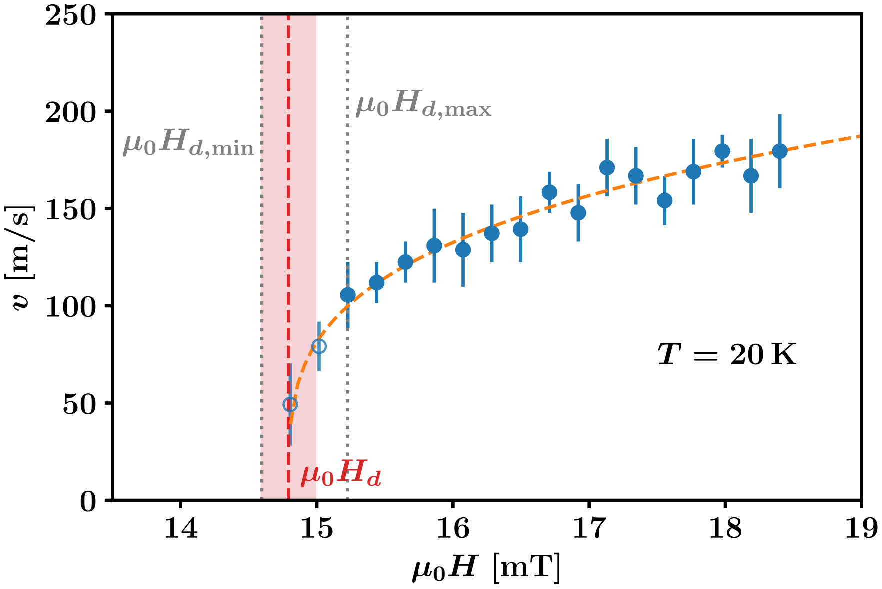

Figure 4.19: **Depinning transition in the velocity vs. field curve for $T = 20\,\mathrm{K}$.** We indicate with vertical dotted lines the range $(\mu_0 H_{d,\mathrm{min}}, H_{d,\mathrm{max}})$ in which we consider depinning transition occurs according to PMOKE microscopy observations. Full symbols indicate $v(H)$ which are considered for the fitting procedure, while empty symbols, corresponding to the range $(\mu_0 H_{d,\mathrm{min}}, H_{d,\mathrm{max}})$, are not considered. The finally determined depinning field and its uncertainty are indicated with a vertical dashed line and a vertical shaded area, respectively. The zero-temperature depinning regime law (2.82) is plotted as a dashed curve, with parameters $\mu_0 H_d = 14.8\,\mathrm{mT}$, $\beta = 0.28$ and $v_H = 270\,\mathrm{m/s}$.

describe in the following.

First, we calculate the χ^2 parameter of the fit,

$$\chi^2(H_d) = \frac{1}{N}\sum \sigma_i^2(H_d) = \frac{1}{N}\sum\left(\frac{y_i - (I(H_d) + S(H_d)x_i)}{\delta y_i}\right)^2 , \tag{4.5}$$

as a function of $\mu_0 H_d$, where N is the number of considered data points, and x_i, y_i and δy_i are, respectively, their x and y coordinates and y uncertainties. The intercept I and slope S of a given fit depend on the chosen $\mu_0 H_d$ value.

Next, we look for the minimum value χ^2_{min} in the range $(\mu_0 H_{d,\mathrm{min}}, \mu_0 H_{d,\mathrm{max}})$, and take into account all the $\mu_0 H_d$ values resulting on $\chi^2 < 1.1\,\chi^2_{\mathrm{min}}$. This defines a new, reduced range which determines the depinning field value and its uncertainty: $\mu_0 H_d$ is the central value in this range, and its uncertainty $\mu_0 \delta H_d$ is half of its width.

Figure 4.20(a) presents the χ^2 vs. $\mu_0 H_d$ dependence for $T = 20\,\mathrm{K}$ in the field range $(\mu_0 H_{d,\mathrm{min}}, \mu_0 H_{d,\mathrm{max}})$. In this case, the minimum value χ^2_{min} corresponds to the lower limit of this range, but we consider that the depinning field cannot be lower because the mean domain wall velocity is not well defined for $\mu_0 H \leq \mu_0 H_{d,\mathrm{min}}$. The figure shows as a dotted horizontal line the limiting value $1.1\,\chi^2_{\mathrm{min}}$, which permits to define the range corresponding to our determination of $\mu_0 H_d$ and its uncertainty $\mu_0 \delta H_d$ in which the fit quality is sufficiently good. The range $[\mu_0 H_d - \mu_0 \delta H_d, \mu_0 H_d + \mu_0 \delta H_d]$ is indicated as a vertical shaded area, which corresponds in this case to $\mu_0 H_d = (14.8 \pm 0.2)\,\mathrm{mT}$.

Determination of the critical exponent β and the depinning velocity v_H

In figure 4.20(b) we plot, for $T = 20\,\mathrm{K}$, the β values obtained from fitting equation (4.4), as a function of the chosen $\mu_0 H_d$ value corresponding to the range $(\mu_0 H_{d,\mathrm{min}}, H_{d,\mathrm{max}})$. These values, corresponding to the fit slopes, are determined with a given uncertainty for each $\mu_0 H_d$. The uncertainties are indicated as a shaded region around the "best" β vs. $\mu_0 H_d$ dependence, and is taken into account in order to obtain a representative β value for each temperature. As shown in the figure, we consider all β values and their uncertainties in the range $[\mu_0 H_d - \mu_0 \delta H_d, \mu_0 H_d + \mu_0 \delta H_d]$ in order to finally obtain, for $T = 20\,\mathrm{K}$, $\beta = 0.28 \pm 0.08$. As indicated in figure 4.20(c), exactly the same process is performed for the fit intercepts $\ln(v_H/(\mathrm{m/s}))$ in order to finally obtain $\ln(v_H/(\mathrm{m/s})) = 5.6 \pm 0.1$. This results on $v_H = (270 \pm 40)\,\mathrm{m/s}$.

In figure 4.21, we present the $\ln(v/(\mathrm{m/s}))$ vs. $\ln((H - H_d)/H_d)$ dependence which results from our best estimation of the depinning field, $\mu_0 H_d = 14.8\,\mathrm{mT}$, for $T = 20\,\mathrm{K}$. Only data points corresponding to $\mu_0 H \geq \mu_0 H_{d,\mathrm{max}}$ are represented because these are the considered data for the depinning regime fit. As evidenced in the figure, a straight line describes very well the observed dependence, what validates the realization of a fit following equation 4.4. The dashed straight line corresponds to this relation, with the best values of β and v_H determined following the previously described protocol: $\beta = 0.28$ and $v_H = 270\,\mathrm{m/s}$.

4.3.3 Universal and non-universal depinning parameters

The same protocol that we have just described for the analysis of the depinning transition has been applied to all the studied temperatures below $100\,\mathrm{K}$. Accordingly, the experimentally measured v vs. $\mu_0 H$ curves in this temperature range were analyzed in terms of the theoretically predicted equation (4.4). In order to evidence the good agreement of experimental data with this relation, we plot in figure 4.22 the v/v_H vs. $((H - H_d)/H_d)^\beta$ dependence obtained for all temperatures, using the best $\mu_0 H_d$, β and v_H values for each temperature. This observed collapse of all experimentally measured velocity vs. field curves on a single dependence clearly highlights the fact that the seven measured curves in the range $10\,\mathrm{K} \leq T \leq 71\,\mathrm{K}$ share a common behavior which is well described by the theoretically predicted zero-temperature depinning, illustrated in figure 2.11(a) for an elastic line in a disordered bi-dimensional medium, and expressed by equation (2.82). Concomitantly, it validates the description of the observed behavior in terms of the obtained values of depinning parameters $\mu_0 H_d$, β, and v_H.

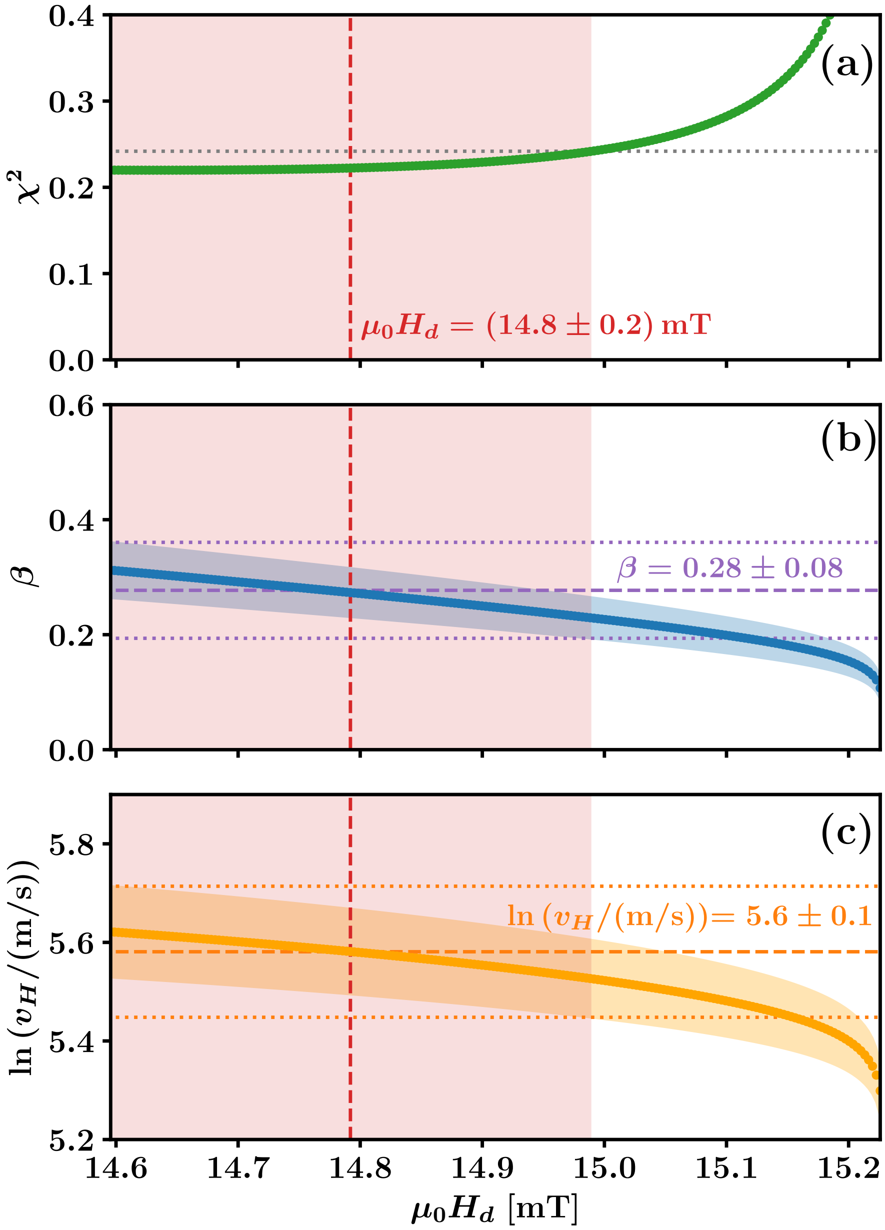

Figure 4.20: **Depinning fit parameters as a function of $\mu_0 H_d$ in the range $(\mu_0 H_{d,\mathrm{min}}, H_{d,\mathrm{max}})$ for $T = 20\,\mathrm{K}$.** (a) χ^2 vs. $\mu_0 H_d$. We indicate as an horizontal dotted line the limiting value $1.1\,\chi^2_{\mathrm{min}}$, which permits to define the range $[\mu_0 H_d - \mu_0 \delta H_d, \mu_0 H_d + \mu_0 \delta H_d]$ in which $\chi^2 < 1.1\,\chi^2_{\mathrm{min}}$. The depinning field is determined as $\mu_0 H_d = (14.8 \pm 0.2)\,\mathrm{mT}$ and indicated as a vertical dashed line and a shaded area. (b) Slope β vs. $\mu_0 H_d$, indicating the uncertainty in its determination in all the range as a shaded region around the mean value dependence. The final determination $\beta = 0.28 \pm 0.08$ is made taking into account this uncertainty, as indicated by the horizontal lines. (c) Intercept $\ln(v_H/(\mathrm{m/s}))$ vs. $\mu_0 H_d$, indicating the uncertainty in its determination in all the range as a shaded region around the mean value dependence. The final determination $\ln(v_H/(\mathrm{m/s})) = 5.6 \pm 0.1$ is made taking into account this uncertainty, as indicated by the horizontal lines.

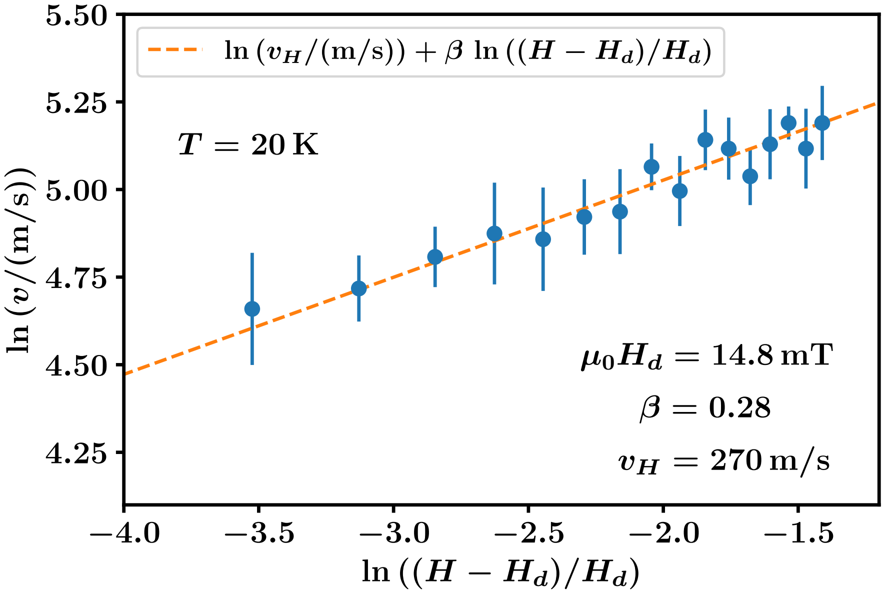

Figure 4.21: **Log-log velocity vs. reduced field dependence corresponding to the athermal depinning transition for $T = 20\,\mathrm{K}$.** $\ln(v/(\mathrm{m/s}))$ vs. $\ln((H - H_d)/H_d)$, considering $\mu_0 H_d = 14.8\,\mathrm{mT}$. We plot only the data points taken into account for the linear fits of the depinning law, i.e. those corresponding to $\mu_0 H \geq \mu_0 H_{d,\mathrm{max}}$. The straight dashed line corresponds to the depinning law with our best determined parameters, $\beta = 0.28$ and $v_H = 270\,\mathrm{m/s}$.

The obtained values of these three depinning parameters for all the studied temperatures below $T = 100\,\mathrm{K}$ are plotted as a function of T in figure 4.23. As we have described, the precisely determined $\mu_0 H_d$ values, which are plotted in (a), permit to obtain β and v_H with a good degree of confidence. These two parameters are plotted as a function of T in (b) and (c), respectively.

Both $\mu_0 H_d$ and v_H are non-universal, and they are therefore material and temperature dependent parameters. For this reason, they are expected to vary as a function of temperature. As it can be observed in figure 4.23, $\mu_0 H_d$ shows a smooth non-monotonous temperature-dependent behavior, with a minimum at $T \sim 30\,\mathrm{K}$, while v_H seems to be constant or slightly grow with temperature. Conversely, β is a universal critical exponent in the framework of statistical physics and then, it is temperature and material independent for any phenomena which can be allocated into a given universality class. The uniqueness of β is verified in the figure, as it is shown to fluctuate over a mean value, without any noticeable temperature dependence. We have calculated a mean value $\overline{\beta} = 0.30 \pm 0.03$ which is representative of the whole set of β values.

The determination of the depinning velocity critical exponent β performed for several temperatures and described above constitutes, to the best of our knowledge, the first direct experimental determination of this critical exponent. Furthermore, the mean value $\overline{\beta} =$

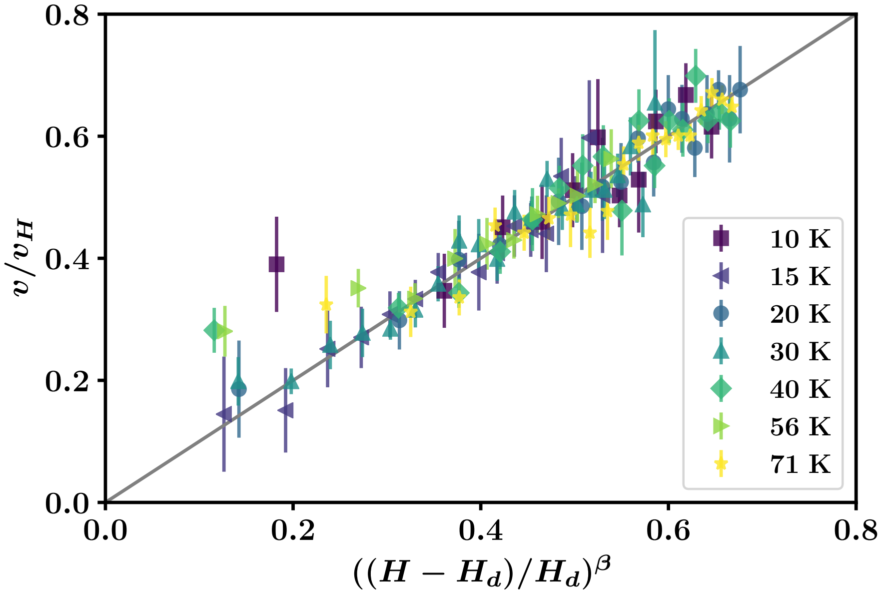

Figure 4.22: **Master curve showing the good agreement of velocity-field curves below $T = 100\,\mathrm{K}$ with the theoretically predicted zero-temperature depinning transition.** Reduced velocity v/v_H as a function of $((H - H_d)/H_d)^\beta$ for $H > H_d$, using as parameters $\mu_0 H_d$, β and v_H the best obtained values for each case.

0.30 ± 0.03, which is representative of all the values that we have plotted in figure 4.23(b), is consistent with theoretically predictions corresponding to the quenched Edwards-Wilkinson universality class. Conversely, our result is not consistent with the predicted β for the quenched Kardar-Parisi-Zhang class (see table 4.1).

Let us briefly review the theoretically predicted β values for the qEW class, which are presented in table 4.1. In 2005, O. Duemmer and W. Krauth computationally calculated $\beta = 0.33 \pm 0.02$ [184], consistent with our result $\overline{\beta} = 0.30 \pm 0.03$. In 2013, E. Ferrero and collaborators calculated the asymptotic value $\beta = 0.245 \pm 0.006$ [119]. This value is expected to be reached only for driving fields sufficiently close to the depinning field, in the limit $\ell_{\mathrm{av}} \gg L_c$, i.e. for a typical depinning avalanche size much larger than the Larkin length. Otherwise, a larger effective β is expected and, therefore, our result may be also consistent with this reference.

As we have pointed out in 4.1.2, in the qEW universality class the five critical exponents corresponding to the depinning transition may be obtained if two of them are independently calculated. In the following, we will show that the correlation length critical exponent ν_{dep} may also be assessed experimentally at low temperatures. The experimental determination of both β and ν_{dep} will permit us to determine the full set of critical exponents in agreement with the qEW universality class.

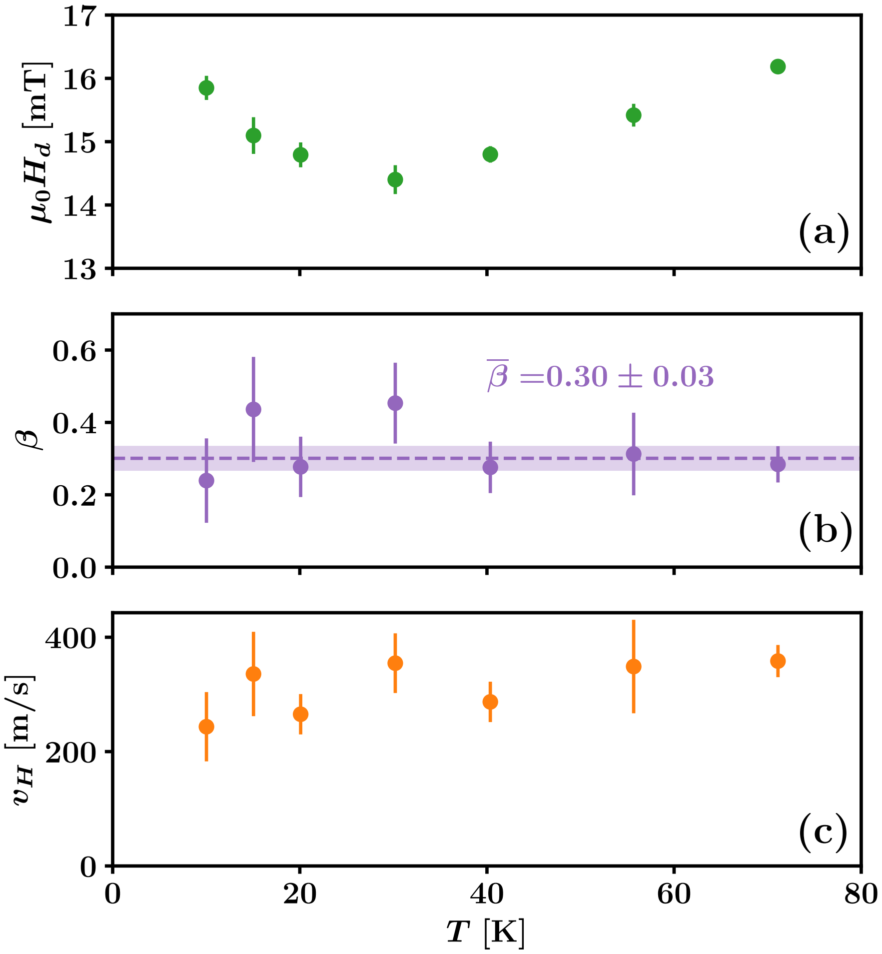

Figure 4.23: **Depinning parameters $\mu_0 H_d$, β and v_H as a function of T, obtained for all studied temperatures below $T = 100\,\mathrm{K}$.** (a) $\mu_0 H_d$ vs. T. (b) β vs. T. We show as an horizontal dotted line and a shaded area the mean value $\overline{\beta}$ and its uncertainty. (c) v_H vs. T.

4.3.4 Critical behavior of the depinning correlation length

In section 2.4.4, we have introduced the divergence of the characteristic size of depinning avalanches ℓ_{av} in the limit of $T = 0$ and $H \to H_d^+$, as $\ell_{\mathrm{av}} \sim (H - H_d)^{-\nu_{\mathrm{dep}}}$ (see equation (2.85)) [4]. In the following we will see that, through the measurement of the local velocity at low temperatures, we are able to quantify ℓ_{av}. This allows for the experimental access to the critical exponent ν_{dep}.

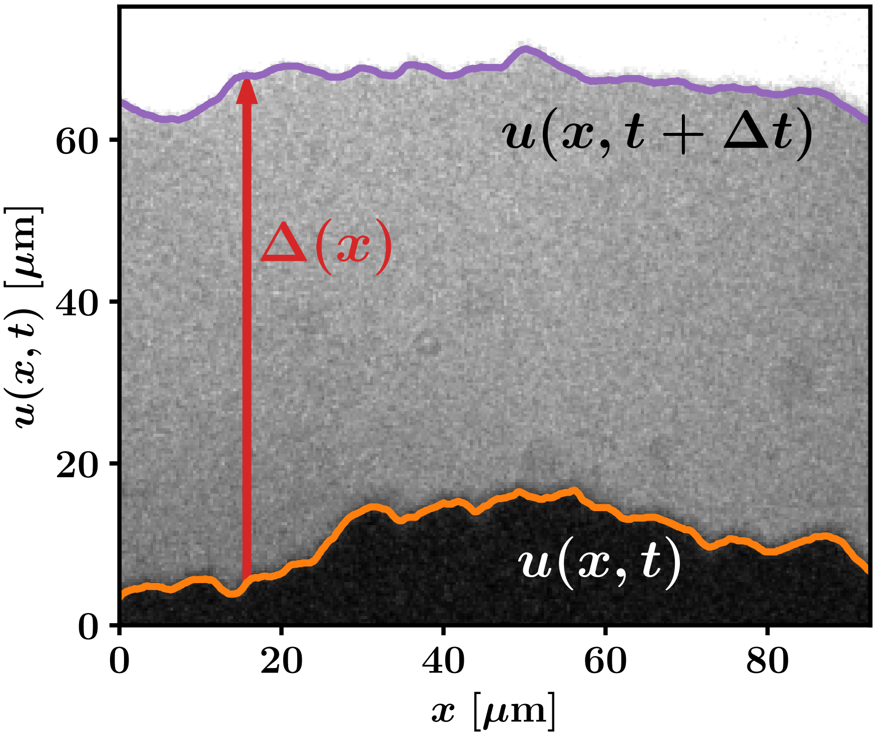

Figure 4.24: **Successive domain wall profiles considered for calculating the depinning correlation length at $T = 20\,\mathrm{K}$.** Between both configurations, a magnetic field pulse of $\mu_0 H = 15.44\,\mathrm{mT}$ and $\Delta t = 0.5\,\mu\mathrm{s}$ was applied. We indicate the distance corresponding to the local domain wall displacement $\Delta(x)$ at a position x. The corresponding mean velocity for this case is $v = \overline{\Delta}/\Delta t = (112.3 \pm 0.3)\,\mathrm{m/s}$. Gray levels result from the superposition of corresponding successive PMOKE images.

Domain wall velocity correlation function $C_v(x)$

As in the depinning transition domain wall motion occurs through the intermittent displacement of segments with characteristic size ℓ_{av}, the local velocity $v_{\mathrm{loc}}(x_0)$ at a position x_0 of the wall is strongly correlated with $v_{\mathrm{loc}}(x_0 + x)$ if depinning avalanches affect simultaneously the displacement at both considered positions, i.e. if $x \lesssim \ell_{\mathrm{av}}$. Consequently, in the following we consider that ℓ_{av} is the correlation length along the domain wall at the depinning transition.

In figure 4.24, we show two successive domain wall profiles obtained at $T = 20\,\mathrm{K}$. Between the initial state $u(x, t)$ and the final state $u(x, t + \Delta t)$, a magnetic field pulse of $\mu_0 H = 15.44\,\mathrm{mT}$ and $\Delta t = 0.5\,\mu\mathrm{s}$ was applied. The corresponding local displacement at a position x is $\Delta(x) = u(x, t + \Delta t) - u(x, t)$, and the local velocity is $v_{\mathrm{loc}}(x) = \Delta(x)/\Delta t$.

In order to quantify the correlation length ℓ_{av}, we first compute the velocity correlation function $C_v(x)$, which may be calculated as [184]

$$C_v(x) = \sum_{i=1}^{N} \left(v_{\mathrm{loc}}(i\delta_r + x) - v \right) \left(v_{\mathrm{loc}}(i\delta_r) - v \right) \ , \tag{4.6}$$

where the sum is performed over all the reference points $x_0 = i\delta_r$ and $\delta_r = 0.171\,\mu$m is the pixel size (see section 3.2 for details). The wall size, which is unique for each considered pair of domain walls, is $L = N\delta_r$.

The mean velocity v is calculated as $v = \overline{\Delta}/\Delta t$, where

$$\overline{\Delta} = \frac{1}{N} \sum_{i=1}^{N} \Delta(i\delta_r) \tag{4.7}$$

and its uncertainty is

$$\sigma_{\overline{\Delta}} = \frac{1}{\sqrt{N}} \left[\frac{1}{N} \sum_{i=1}^{N} \left(\Delta(i\delta_r) - \overline{\Delta} \right)^2 \right]^{1/2} \ . \tag{4.8}$$

For the example shown in figure 4.24, $v = (112.3 \pm 0.3)\,\mathrm{m/s}$. Note that this uncertainty is much smaller than the usual considered uncertainties for the mean velocity, obtained as explained in section 3.2.3 and indicated for $T = 20\,\mathrm{K}$ as error bars in figure 4.19. While larger uncertainties are representative of the observable effect of different field pulses of a given magnitude in the whole field of view of the microscope, which generates fluctuating mean displacements, the much smaller error corresponding to the mean value $\overline{\Delta}/\Delta t$ is associated to a particular pair of successive walls as the ones shown in figure 4.24, which may not be representative of the fluctuating effects of a given applied field. For this reason, in the analysis that we describe in the following, for some of the applied fields we consider several pairs of domain walls which may result not only on different velocity correlation functions $C_v(x)$ but also on different mean velocities $v = \overline{\Delta}/\Delta t$.

The velocity correlation function is thus calculated as

$$C_v(x) = \frac{1}{\Delta t^2} \sum_{i=1}^{N} \left(\Delta(i\delta_r + x) - \overline{\Delta} \right) \left(\Delta(i\delta_r) - \overline{\Delta} \right) \tag{4.9}$$

for several different pairs of successive domain walls at each temperature. In figure 4.25, we show normalized velocity correlation functions $C_v(x)/C_0$ for several different pairs of walls, indicating the applied field corresponding to each of them. The normalization is made in terms of the value corresponding to $x = 0$ for each case, i.e. $C_0 \equiv C_v(x = 0)$.

An exponential decay is expected for the velocity correlation function, $C_v(x) \sim e^{-x/\ell_{\mathrm{av}}}$ [184]. However, the obtained functions plotted in figure 4.25 show fluctuations which difficult the analysis through fits following the expected relation. We therefore estimate the depinning correlation length as the distance x at which $C_v(x)$ falls considerably with respect to C_0. Specifically, we calculate ℓ_{av} according to

$$C_v(x = \ell_{\mathrm{av}}) = c\, C_0 \ , \tag{4.10}$$

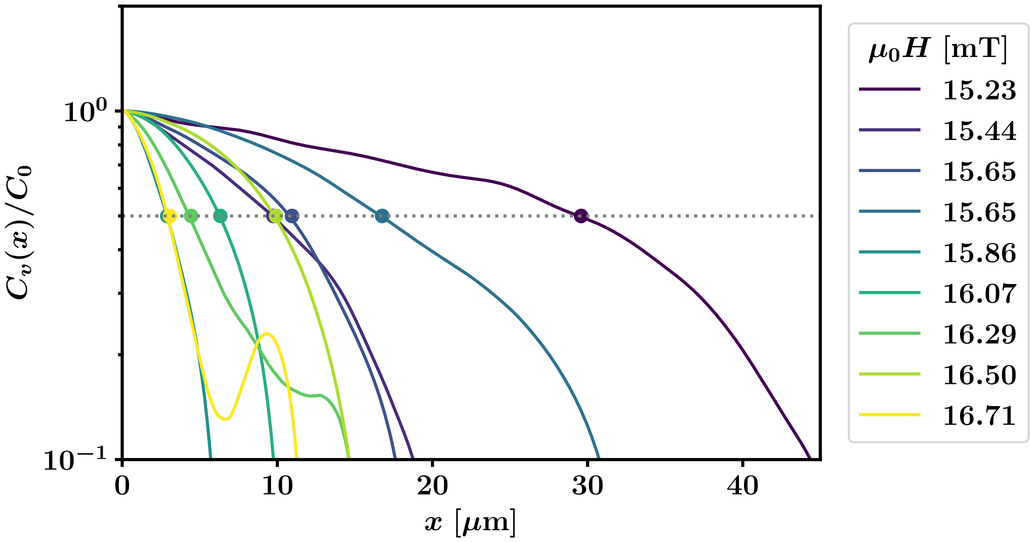

Figure 4.25: **Normalized velocity correlation functions for different applied fields at $T = 20\,\mathrm{K}$.** Each normalized function $C_v(x)/C_0$ corresponds to a pair of successive domain walls resulting from applying the indicated field magnitudes during $\Delta t = 0.5\,\mu$s. The horizontal dotted line at $C_v(x)/C_0 = 0.5$ indicates the criteria used to compute the correlation length ℓ_{av}: $C_v(x = \ell_{\mathrm{av}})/C_0 = 0.5$.

where we consider $c = 0.5$. Even if this c value is arbitrary, we have verified that results do not change significantly for the range $0.2 < c < 0.7$.

In figure 4.25, we indicate as a dotted horizontal line the value $C_v(x)/C_0 = 0.5$ which is crossed at $x = \ell_{\mathrm{av}}$ for each velocity correlation function. We thus obtain a ℓ_{av} value for each pair of successive domain walls, each of them corresponding to a particular mean velocity $v = \overline{\Delta}/\Delta t$.

Determination of the critical exponent ν_{dep} and the characteristic length ξ_0

The combination of equations (2.82) for the mean velocity v at the depinning transition and (2.85) for the depinning avalanche size ℓ_{av} permits to write the following relation between these two quantities:

$$v = v_H \left(\frac{\ell_{\mathrm{av}}}{\xi_0}\right)^{-\beta/\nu_{\mathrm{dep}}} . \tag{4.11}$$

Therefore,

$$\ln v = \ln v_H + \frac{\beta}{\nu_{\mathrm{dep}}} \ln \xi_0 - \frac{\beta}{\nu_{\mathrm{dep}}} \ln \ell_{\mathrm{av}} . \tag{4.12}$$

In figure 4.26, we plot the v vs. ℓ_{av} results in logarithmic scale, obtained for $T = 20\,\mathrm{K}$, corresponding to the pairs of successive walls whose velocity correlation functions are plotted

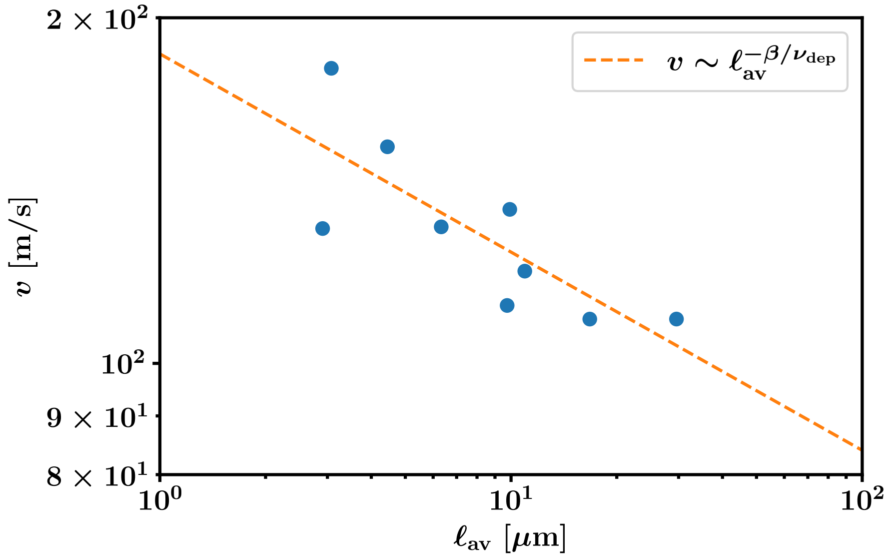

Figure 4.26: **Mean domain wall velocity vs. depinning avalanche size for $T = 20$ K.** Each point corresponds to a pair of successive domain walls. The best fit of $\ln(v/(\text{m/s}))$ vs. $\ln(\ell_{av}/\mu\text{m})$, shown as a dashed line, has a slope $-\beta/\nu_{dep} = -0.17$.

in figure 4.25.

A linear fit of these data points of the type $y = Sx + I$, with $y = \ln(v/(\text{m/s}))$ and $x = \ln(\ell_{av}/\mu\text{m})$, permits to obtain $I = \ln(v_H/(\text{m/s})) + \dfrac{\beta}{\nu_{dep}} \ln(\xi_0/\mu\text{m})$ and $S = -\beta/\nu_{dep}$, in accordance with (4.12). The obtained slope corresponding to the data of figure 4.26, for $T = 20$ K, is $S = -0.17 \pm 0.05$ and $I = 5.2 \pm 0.2$.

We are particularly interested in the slope S, as it permits to quantify a new depinning critical exponent, ν_{dep}. For $T = 20$ K, the obtained correlation length critical exponent, calculated as $-\beta/S$ using the β value previously obtained for this temperature, is $\nu_{dep} = 1.6 \pm 0.7$. This value is consistent both with the qEW and the qKPZ universality classes due to the large uncertainty resulting from the poor fit quality. In order to perform a more precise determination, we have repeated an analogous analysis for several different temperatures that we will present below.

Additionally, once ν_{dep} is determined for a given temperature, we may calculate the characteristic length ξ_0 from the intercept I and the already determined v_H and β for the corresponding temperature. For $T = 20$ K, this analysis results on $\xi_0 = (0.1 \pm 0.2)\,\mu$m. As the uncertainty is bigger than the obtained value, this determination is not significant; however, its order of magnitude $\sim 0.1\,\mu$m is consistent with the prediction $\xi_0 \approx L_c$, as we will further discuss later.

The depinning correlation length critical exponent ν_{dep} and the characteristic length ξ_0

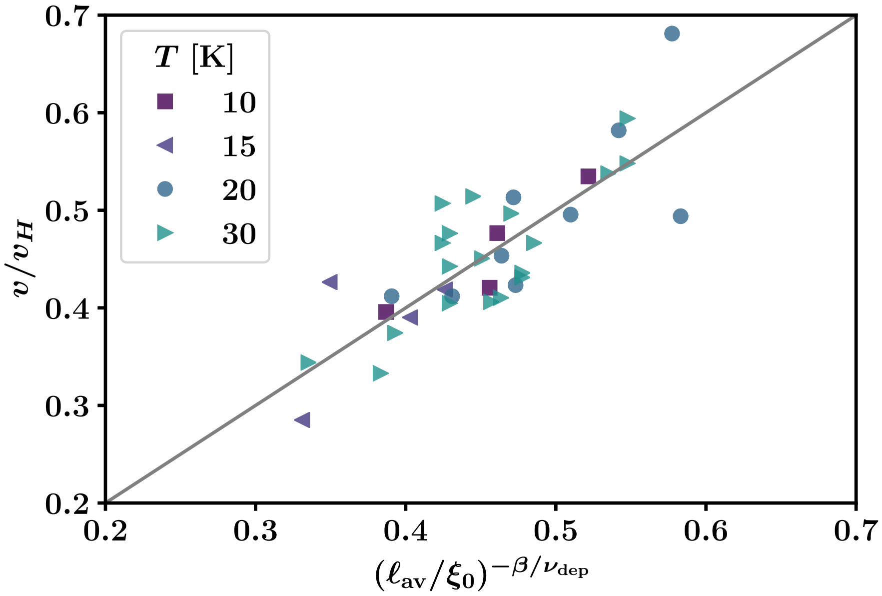

Figure 4.27: **Common dependence of reduced parameters relating the mean domain wall velocity and the depinning avalanche length for different temperatures.** We plot v/v_H vs. $(\ell_{\rm av}/\xi_0)^{-\beta/\nu_{\rm dep}}$, using the best values of v_H, ξ_0, β and $\nu_{\rm dep}$ obtained for each temperature. Despite considerable fluctuations, the observed common dependence validates the relation given by (4.11).

were determined as explained above for $T = 10$, 15, 20 and 30 K. At higher temperatures, the obtained plots of v vs. $\ell_{\rm av}$ did not yield any meaningful result, as no tendency was observed relating these observables. A possible explanation of this fact is that thermal effects may result on a loss of validity of equation (2.85) and, therefore, of (4.11). This might occur at lower temperatures than the appearance of considerable thermal rounding effects impeding the observation of the zero-temperature-like $v(H)$ dependence, which as we have shown occurs above $T = 100$ K.

In figure 4.27, we plot the relation v/v_H vs. $(\ell_{\rm av}/\xi_0)^{-\beta/\nu_{\rm dep}}$ for the considered temperatures, using the best values of the parameters v_H, ξ_0, β and $\nu_{\rm dep}$ that we have obtained for each temperature (these values are plotted in figures 4.23 and 4.28). Even if rather large fluctuations are observed, as already shown for $T = 20$ K in figure 4.25, a common behavior with a clear tendency is observed, what validates the use of equation (4.11) for the analysis of these data.

In figure 4.28, we plot as a function of the temperature the obtained values of $\nu_{\rm dep}$ and ξ_0. As predicted for a universal critical exponent, no noticeable tendency with temperature exists for $\nu_{\rm dep}$ and, therefore, we calculate its mean value which results on $\overline{\nu}_{\rm dep} = 1.3 \pm 0.3$. This result is fully consistent with the qEW universality class, while it permits to discard the qKPZ class (see table 4.1).

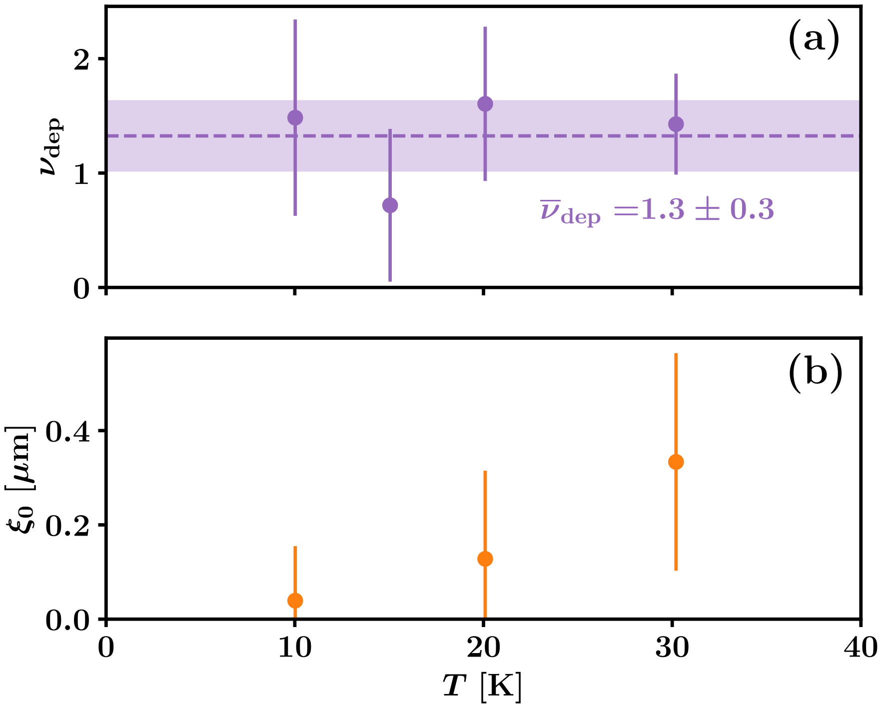

Figure 4.28: **Depinning correlation length parameters ν_{dep} and ξ_0 as a function of T for the lowest temperatures.** (a) ν_{dep} vs. T, indicating the mean obtained value $\overline{\nu}_{\text{dep}} = 1.3 \pm 0.3$ as a dashed horizontal line and a shaded area illustrating the uncertainty. (b) ξ_0 vs. T, where the value $\xi_0 = (1 \pm 2)\,\mu$m corresponding to $T = 15\,$K has been omitted due to its out of scale value and uncertainty.

As we have shown above for $T = 20\,$K, the ξ_0 values are determined with huge error bars. This makes the tendency with temperature observed in figure 4.28(b) weakly representative. However, its values of the order of $0.1\,\mu$m are consistent with the theoretical prediction that $\xi_0 \approx L_c$, as we will briefly discuss in the following.

Larkin length L_c and pinning correlation length ξ_p

In section 2.4.4, we have pointed out that L_c and ξ_p are the fundamental characteristic lengths in the theoretical framework corresponding to a one-dimensional domain wall driven in a bi-dimensional disordered medium. These quantities may be estimated using expressions (2.86) and (2.89), in terms of H_d, T_d, the domain wall energy σ, the saturation magnetization M_s, and the film thickness $t = 10\,$nm.

In order to estimate these characteristic lengths, we make the following considerations. We use $T_d = (30000 \pm 5000)\,$K, which corresponds to the lowest temperature for which we could measure T_d, $T = 102\,$K. The domain wall energy σ is estimated according to equation (2.16), with $\Delta = (15 \pm 5)\,\mathrm{nm}$ [135, 146, 190] and an effective uniaxial anisotropy $K_{\mathrm{eff}} = (22 \pm 6)\,\mathrm{kJ/m^3}$ estimated for the range $10\,\mathrm{K} \leq T \leq 30\,\mathrm{K}$ (see figure 3.12(b)). The saturation magnetization M_s has been measured, as plotted in figure 3.9, and the depinning field values are plotted in figure 4.23(a). This analysis yields, in the range $10\,\mathrm{K} \leq T \leq 30\,\mathrm{K}$,

$$\xi_p = (70 \pm 20)\,\mathrm{nm} \tag{4.13}$$

for the pinning correlation length, and

$$L_c = (170 \pm 30)\,\mathrm{nm} \tag{4.14}$$

for the Larkin length.

Interestingly, the correlation length of disorder ξ_p is slightly larger than the domain wall width $\delta \simeq \pi\Delta$ and, thus, ξ_p can be associated to the characteristic length of the random heterogeneity in the sample r_0 [109], i.e. $\xi_p \simeq r_0 \simeq 70\,\mathrm{nm}$. This constitutes an insight on the microscopic origin of disorder, which is generally of difficult experimental access.

On the other hand, the obtained L_c value results of the same order of magnitude as ξ_0 (see figure 4.28(b)). Hence, in the whole range $10\,\mathrm{K} \leq T \leq 30\,\mathrm{K}$ we have $\xi_0 \sim L_c$, as theoretically expected for the critical regime at depinning [109], while ℓ_{av} is one or two orders of magnitude larger. Furthermore, note that the obtained ξ_p and L_c values are consistent with those estimated for the Larkin surface area $L_c\xi_p$ for $T \geq 100\,\mathrm{K}$ (see figure 4.16(e)). The found consistences between experimentally obtained quantities and theoretical predictions validate the use of the elastic line model, giving robustness to our results and, particularly, to our insight on domain wall's critical behaviors.

4.3.5 Universality class of magnetic domain wall depinning

The independent determination of the depinning critical exponents β and ν_{dep}, which to the best of our knowledge had not been experimentally determined before for driven magnetic domain walls, is the most significant result of this chapter. As we have discussed in 4.1.2, two universality classes are generally considered as candidates in order to describe field-driven domain wall dynamics in thin films with perpendicular anisotropy. These universality classes are the quenched Edwards-Wilkinson (qEW) and the quenched Kardar-Parisi-Zhang (qKPZ) classes, which share the same critical behavior in the limit $H \to 0$, making it impossible to distinguish between them by measuring the equilibrium critical exponents. An example of a widely studied equilibrium exponent is the creep exponent μ, equal to $1/4$ for both universality classes in agreement with experimental studies (see section 2.4.2).

As we have shown above, our results for the depinning exponents $\overline{\beta} = 0.30 \pm 0.03$ and $\overline{\nu}_{\mathrm{dep}} = 1.3 \pm 0.3$ are both consistent with the qEW class while they are significantly smaller than those predicted for the qKPZ class. A comparison with the values written in table 4.1 clearly shows this finding. The slight inconsistence between the obtained $\overline{\beta}$ and one of the theoretical predictions for the qEW class, $\beta = 0.245 \pm 0.006$, can be explained considering

	Experimental	**qEW class**
$\boldsymbol{\beta}$	0.30 ± 0.03	0.245 ± 0.006 [119] 0.33 ± 0.02 [184]
$\boldsymbol{\nu_{\mathrm{dep}}}$	1.3 ± 0.3	1.333 ± 0.007 [119]
$\boldsymbol{\zeta_{\mathrm{dep}}}$	1.2 ± 0.2	1.250 ± 0.005 [119]
$\boldsymbol{z}$	1.5 ± 0.2	1.433 ± 0.007 [119]
$\boldsymbol{\tau_{\mathrm{dep}}}$	1.11 ± 0.07	1.11 ± 0.04 [185]

Table 4.2: **Experimentally determined depinning critical exponents.** β and ν_{dep} were independently measured, while ζ_{dep}, z and τ_{dep} result from them by using scaling laws (4.15), (4.16) and (4.17). Our results are fully compatible with the qEW universality class.

that our measurements are not sufficiently close to H_d, since this computationally calculated value is an asymptotical result valid in the limit of $H \to H_d^+$ and $\ell_{\mathrm{av}} \gg L_c$. In our case, $\ell_{\mathrm{av}} \sim$ 10-100 L_c while the considered field ranges roughly correspond to $H_d < H < 1.3\, H_d$. In this context, the effective observed β value is expected to be larger than $\beta = 0.245 \pm 0.006$ [119], in accordance with our $\overline{\beta} = 0.30 \pm 0.03$ and with the other computationally calculated $\beta = 0.33 \pm 0.02$ [184].

Now that we have shown that both independently obtained exponents are consistent only with the qEW universality class, we may calculate all the depinning critical exponents by using the following scaling relations, valid in the context of the qEW universality class [5]:

$$\zeta_{\mathrm{dep}} = 2 - \frac{1}{\nu_{\mathrm{dep}}} \,, \tag{4.15}$$

$$z = \frac{\beta}{\nu_{\mathrm{dep}}} + \zeta_{\mathrm{dep}} \,, \tag{4.16}$$

$$\tau_{\mathrm{dep}} = 2 - \frac{2}{d + \zeta_{\mathrm{dep}}} \,, \tag{4.17}$$

where the interface dimension for an elastic line in a bi-dimensional medium is $d = 1$.

In table 4.2, we show the complete set of experimentally determined depinning critical exponents, including the resulting ζ_{dep}, z and τ_{dep}, calculated using scaling relations (4.15), (4.16) and (4.17) with $\beta = \overline{\beta} = 0.30 \pm 0.03$ and $\nu_{\mathrm{dep}} = \overline{\nu}_{\mathrm{dep}} = 1.3 \pm 0.3$. These results confirm the full agreement between our experimentally determined depinning critical exponents and predictions for the qEW universality class. Furthermore, as a universality class is completely characterized by its critical exponents, they constitute an evidence that the depinning transition of magnetic domain walls in perpendicularly magnetized thin films belongs to the qEW universality class.

4.4 Chapter summary and conclusions

Throughout this chapter, we have presented our studies on field-driven domain wall dynamics in a ferrimagnetic sample of GdFeCo and discussed our main findings. We have addressed two main subjects of interest. On the one hand, the relationship between the rich temperature dependence of magnetic properties that occurs in this type of materials and the dynamical regimes of domain wall motion, fundamentally the creep and depinning regimes. On the other hand, the direct characterization of the depinning transition in practically athermal conditions, which is possible due to the extremely low values of T/T_d.

The analysis of velocity vs. applied field curves of varying properties in a unique framework corresponding to the theory of elastic interfaces in disordered media has shed light on the universal and non-universal properties of domain wall creep and depinning regimes. Particularly, we have noted and discussed different properties of velocity-field characteristics found above and below the magnetic compensation temperature $T_M = (190 \pm 4)\,\mathrm{K}$. In contrast, we have not observed any impact of the angular compensation at $T = T_A$, estimated as $T_A \sim 270\,\mathrm{K}$, on the creep and depinning regimes.

Additionally, these studies have permitted us to analyze the temperature dependence of the depinning field H_d. We have experimentally confirmed the theoretically predicted divergence of the depinning field at the magnetic compensation temperature $T = T_M$ due to the corresponding vanishing of the saturation magnetization M_s.

Furthermore, we have analyzed the temperature dependence of the depinning temperature T_d, which characterizes the magnitude of collective pinning energy barriers. We have shown that T_d grows with decreasing temperature, what boosts the categorical decrease of thermal effects when decreasing temperature.

The joint analysis of the H_d, T_d and M_s temperature dependence has allowed us to study fundamental properties linked to domain wall pinning, shedding light over characteristic parameters as the Larkin length L_c and the pinning correlation length ξ_p. The found quantities are consistent with their theoretically expected magnitudes, what validates our approach for the interpretation and analysis of domain wall dynamics.

Below $T = 100\,\mathrm{K}$, we have shown that practically athermal characteristics can be observed in velocity vs. field curves, allowing for the direct analysis of the depinning transition. We have thus experimentally measured the critical exponent β of domain wall velocity at the depinning transition, obtaining a mean value $\overline{\beta} = 0.30 \pm 0.03$ which successfully describes our experimental data and is in good agreement with theoretical predictions for the quenched Edwards-Wilkinson universality class.

Not only that, but we also succeeded to experimentally quantify the characteristic length of depinning avalanches for different applied fields at several temperatures in the low temperature range. This characteristic length, which constitutes a diverging correlation length in the context of the depinning transition, has permitted us to experimentally assess the critical exponent ν_{dep}. We obtained, for four different temperatures in the range $10\,\text{K} \leq T \leq 30\,\text{K}$, a representative value $\overline{\nu}_{\text{dep}} = 1.3 \pm 0.3$ which also agrees with theoretical predictions for the quenched Edwards-Wilkinson universality class.

These findings permit to allocate the observed phenomena of domain wall motion in perpendicularly magnetized thin films in the framework of the quenched Edwards-Wilkinson universality class, discarding the quenched Kardar-Parisi-Zhang model. Additionally, using the scaling laws which are valid in this context, we have calculated the full set of depinning critical exponents which characterize the universality class of domain wall depinning in agreement with theoretical predictions. Our findings constitute a robust experimental demonstration of the predictive power of the theory of elastic interfaces in disordered media.

CHAPTER 5

Domain wall roughness in a ferrimagnetic GdFeCo thin film

"Le dessin n'est pas la forme,
il est la manière de voir la forme."
Edgar Degas

THE present chapter is devoted to the study of domain wall morphological properties. Particularly, we shall analyze walls observed by polar magneto-optical Kerr effect microscopy[1] in a GdFeCo thin film with perpendicular anisotropy[2] at different driving field and temperature conditions. The domain wall dynamics are thoroughly studied in the same sample as a function of the driving field and in a wide range of temperatures in chapter 4. Those studies on domain wall dynamics are closely related to the morphological properties that we shall study in this chapter; indeed, domain wall motion in the creep and depinning regimes is achieved through events of characteristic sizes, what impacts directly on its roughness properties, as we have discussed in sections 2.3 and 2.4.4.

We have extensively addressed the importance of experimentally measuring universal critical exponents, what constitutes one of our main motivations in this thesis. Indeed, in chapter 4 we have shown that our most relevant result obtained from the measurement of domain wall dynamics is the independent experimental determination of two depinning

---

[1] See section 3.1 for details on this technique and section 3.2 for a description of our experimental setup.
[2] See section 3.3 for sample details.

critical exponents, β and ν_{dep}. This result permitted us to claim that the domain wall depinning in magnetic thin films with perpendicular anisotropy belongs to the quenched Edwards-Wilkinson universality class with random-bond disorder and short-range elasticity. In this chapter, our attention will be also focused on critical exponents (particularly, on the roughness exponents), considering as starting point that domain walls belong to the quenched Edwards-Wilkinson universality class. In this context, we will study the impact of the different involved roughness exponents on domain wall morphology in order to calculate, as a function of T and H, characteristic length scales as L_c, ℓ_{opt} and ℓ_{av}, what will permit us to test theoretical predictions.

In the following section, we shall motivate the studies presented in this chapter by summarizing the state-of-the-art on experimental measurements of the roughness exponent ζ for magnetic domain walls. Then, in section 5.2 we will present our methods for performing meaningful roughness measurements and the resulting parameters obtained for different fields and temperatures. The methods we implement, which were developed by Daniel Jordán and collaborators [39], introduce a careful analysis of uncertainties and take into account the intrinsic statistical dispersion of roughness exponents [104, 105]. In section 5.3 we will present our analysis and interpretation of roughness measurements in the framework of the quenched Edwards-Wilkinson universality class, what allows for quantifying relevant characteristic lengths and testing the theoretical scenario that we have introduced in 2.4.4. Finally, in section 5.4 we will present a chapter summary and review our main conclusions.

5.1 Previous experimental roughness measurements

Since the first observation of the creep regime by S. Lemerle and collaborators in 1998 [13], magnetic domain walls in thin films with perpendicular anisotropy have become a prototypical example of elastic lines in a disordered bi-dimensional medium. In that work, and using a PMOKE microscope, the authors not only observed a creep exponent $\mu = 1/4$ characterizing the velocity vs. field dependence, but they also measured the roughness exponent ζ. In order to obtain ζ, they calculated the displacement-displacement correlation function $B(r)$ for multiple observed domain wall profiles, equation (2.55), and used the scaling relation $B(r) \sim r^{2\zeta}$. From the analysis of 36 domain wall profiles, they obtained an average value $\overline{\zeta} = 0.69 \pm 0.07$, consistent with the equilibrium roughness exponent $\zeta_{\text{eq}} = 2/3$. These results were considered as a double-proof that the observed domain wall creep corresponds to the quenched Edwards-Wilkinson universality class, with the theoretically calculated exponents $\zeta_{\text{eq}} = 2/3$ and $\mu = (2\zeta_{\text{eq}} - 1)/(2 - \zeta_{\text{eq}}) = 1/4$ for a one-dimensional wall (see equation (2.72)).

However, further investigations, both theoretical and experimental, have shown that the real scenario is much more complex. Firstly, because the characteristic length of optimal avalanches in the creep regime ℓ_{opt} is small compared to the typical length scale of magneto-optical microscopy images (see equation (2.84) and references [40, 108, 120, 195]),

Sample type	ζ	**Reference**	**Observation**
Pt/Co/Pt	0.69 ± 0.07	[13]	
	0.60 ± 0.05	[191]	
	0.71	[192]	
	0.83	[192]	
	0.68 ± 0.04	[160]	
	0.73 ± 0.04	[193]	
	0.79 ± 0.04	[193]	ac field
(Ga,Mn)(As,P)	0.62 ± 0.02	[118]	
	0.61 ± 0.04	[27]	
Pt/CoFe/Pt	0.66 ± 0.02	[194]	
CoFe/Pt	0.98 ± 0.03	[194]	multilayer
Pt/CoNi/Al	0.64 ± 0.05	[193]	
GdFeCo	0.759 ± 0.008	[39]	
	0.747 ± 0.009	[39]	
	0.716 ± 0.007	[39]	in-plane field

Table 5.1: **Experimentally determined roughness exponents reported in the literature, corresponding to field-driven domain walls.** All these measurements were performed via the analysis of wall profiles observed by magneto-optical microscopy. We indicate the type of magnetic thin film studied in each case and observations regarding sample or applied field particularities when applicable.

what suggests that other exponents as ζ_{dep} and ζ_{th} should play a role even for $H < H_d$ [4, 41]. In this context, the measured ζ exponent does not correspond uniquely to ζ_{eq} even if it is compatible with its value. Secondly, because several roughness exponent determinations have resulted on higher values. Table 5.1 shows the reported results of multiple ζ determinations for field-driven domain walls, some of them being different from all the theoretically predicted exponents, $\zeta_{\text{eq}} = 2/3$, $\zeta_{\text{dep}} = 1.25$ and $\zeta_{\text{th}} = 1/2$. Additionally, their values are rather disperse, what could be an evidence of its non-universality, in contrast with all the theoretical framework and dynamics measurements supporting the universality of field-driven domain wall motion. These results call for further investigations in order to find an appropriate interpretation.

The existence of crossover lengths ℓ_{opt} and ℓ_{av} separating scales in which different roughness exponents characterize domain wall morphology, illustrated in figure 2.16, may constitute the scenario that correctly explains the measured values. In this context, experimentally obtained roughness exponents may be *effective* values ζ_{eff} which result from the joint action of ζ_{eq}, ζ_{dep} and ζ_{th}. In this chapter, particularly in section 5.3, we shall analyze our roughness measurements within this framework in order to provide a successful interpretation not only for our results but also for the previous measurements written in table 5.1.

In order to test this theoretical scenario, we have carefully measured the field- and temperature-dependence of effective roughness exponents. In the following, we will thoroughly describe the methods that we use in order to experimentally obtain $B(r)$ functions and the corresponding roughness parameters, and we will present the results for different fields and temperatures.

5.2 Statistically meaningful roughness measurement

An adequate roughness exponent determination, with a representative resulting value and uncertainty, is crucial for its contrast with theoretical predictions. Recently, J. Guyonnet, S. Bustingorry and collaborators [104, 105] have shown that the distribution of roughness exponents calculated for individual interfaces under equivalent experimental conditions are inherently wide, and thus pointed out that a representative determination needs the analysis of at least ~ 40 independent interfaces under the same conditions. This fact was not taken into account in most of the investigations cited in table 5.1; therefore, the reported values and uncertainties should be considered with some reservations. Additionally, $B(r)$ fitting procedures should be as well defined as possible in order to tackle the impact of observer criteria on obtained results. The work by Daniel Jordán and colleagues [39, 175], which constitutes a collaboration in the framework of this thesis, permitted to systematize a method for roughness parameter determinations which takes into account their statistical dispersion and provides well defined fitting procedures.

As we use this method for the roughness characterization presented in this chapter, we shall thoroughly describe it in the following. First, we will discuss our procedure for calculating the displacement-displacement correlation function $B(r)$ of a domain wall profile. Second, we shall present its fitting methods and the careful quantification of roughness parameters and their uncertainties. Then, we will discuss the statistics resulting from repeating this procedure for multiple domain walls in a particular condition of field and temperature, what permits to obtain representative and meaningful values. Finally, we shall present the results we have obtained for different fields and temperatures.

5.2.1 Computing the displacement-displacement correlation function of a domain wall profile

Given a domain wall, obtained with the PMOKE microscope at a particular temperature T and after applying a given field H, its profile $u(x)$ is determined as described in 3.2.5. The x direction is formed by a discrete and evenly spaced set of points $x_j = j\delta_r$ with $j = 0, \ldots, N$, where δ_r is the pixel size, equal to $0.171\,\mu$m for the measurements presented in this section. At each point x_j, the position of the domain wall, of length $L = N\delta_r$, is $u(x_j)$.

In figure 5.1(a) we show a domain wall profile $u(x)$ obtained at $T = 275\,$K, after applying

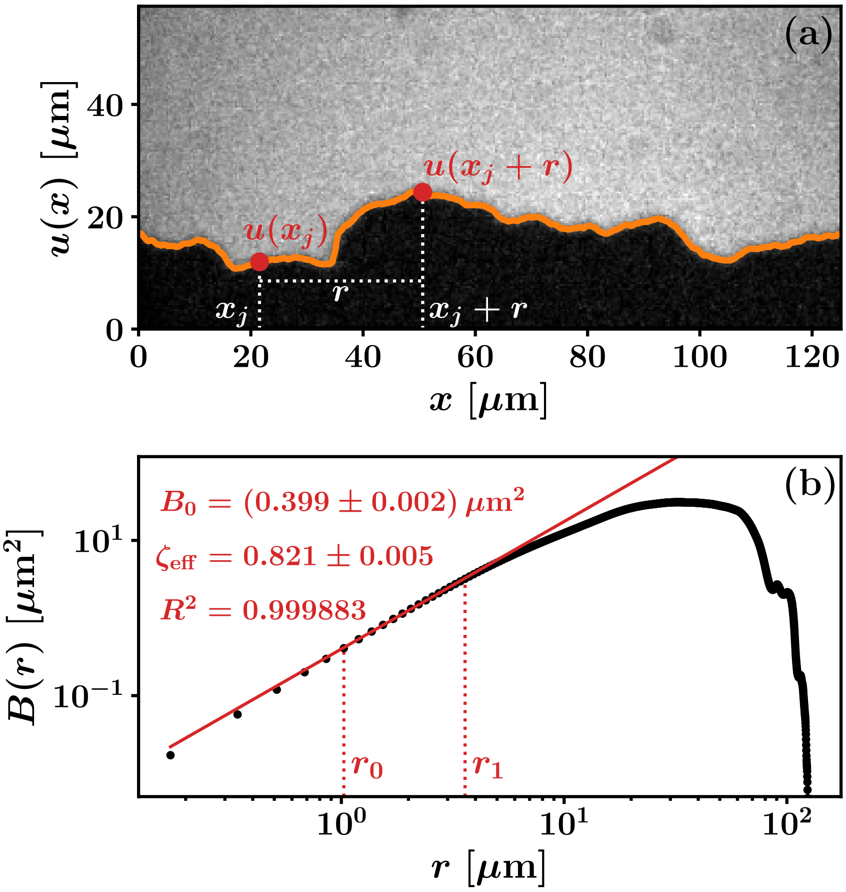

Figure 5.1: **Displacement-displacement correlation function for a single domain wall profile.** (a) PMOKE image where we highlight a wall profile $u(x)$ corresponding to $T = 275\,\mathrm{K}$ and $\mu_0 H = 5.71\,\mathrm{mT}$. We indicate a particular value $u(x_j)$ separated by an horizontal distance r from another value $u(x_j + r)$. The integration through all x_j values permits to obtain $B(r)$ according to (5.1). (b) Corresponding $B(r)$ function and resulting fit following equation (5.2) in the range $r_0 \leq r \leq r_1$.

pulses of $\mu_0 H = 5.71\,\mathrm{mT}$ and $\Delta t = 2\,\mathrm{s}$. Arbitrary positions $(x_j, u(x_j))$ and $(x_j + r, u(x_j + r))$ are indicated, horizontally separated by a distance $r = k\delta_r$, where k is an integer value, $k = 1$, ..., N.

The displacement-displacement correlation function $B(r)$ of a domain wall profile $u(x)$ is calculated for this discrete case as

$$B(r) = \frac{1}{N - k + 1} \sum_{j=0}^{N-k} \left[u(x_j + r) - u(x_j)\right]^2 \ . \tag{5.1}$$

Accordingly, $B(r)$ is obtained for each distance r by integrating over all the possible reference positions x_j. The $B(r)$ function resulting from the particular domain wall profile shown in figure 5.1(a) is plotted in (b).

As expressed by the scaling relation (2.56), $B(r)$ is expected to follow

$$B(r) = B_0 \left(\frac{r}{\mu\mathrm{m}}\right)^{2\zeta_{\mathrm{eff}}} , \tag{5.2}$$

where B_0 is the so-called roughness amplitude and the length unit is specified for B_0 to have the same units as $B(r)$. The $B(r)$ function computed for a given domain wall may thus be fitted using the relation

$$\log\left(B(r)/\mu\mathrm{m}^2\right) = \log\left(B_0/\mu\mathrm{m}^2\right) + 2\zeta_{\mathrm{eff}} \log\left(r/\mu\mathrm{m}\right) ; \tag{5.3}$$

this is, fitting $y = \log\left(B(r)/\mu\mathrm{m}^2\right)$ vs. $x = \log\left(r/\mu\mathrm{m}\right)$ as $y = I + Sx$, with resulting intercept $I = \log\left(B_0/\mu\mathrm{m}^2\right)$ and slope $S = 2\zeta_{\mathrm{eff}}$. It is worth noting that by definition of $B(r)$, $\zeta_{\mathrm{eff}} \leq 1$ and then, a roughness exponent $\zeta > 1$ cannot be revealed by $B(r)$ [107].

As evidenced in figure 5.1(b), the linear dependence characteristic of a self-affine domain wall is not verified at large length scales. Several factors may induce this behavior: the action of strong pinning sites, finite-size effects, and the coexistence of different roughness exponents. Additionally, at very low scales the correct determination of domain wall profiles is affected by the discrete nature of PMOKE images, with a pixel size δ_r, and by the optical resolution of $\approx 1\,\mu$m. Consequently, the fit of relation (5.3) must be performed within an appropriate range with lower and upper limits.

In figure 5.1(b), we show the results of performing this fit in the range $r_0 \leq r \leq r_1$, with $r_0 = 6\delta_r = 1.026\,\mu$m (i.e. discarding distances lower than 6 pixels) and $r_1 = 21\delta_r = 3.591\,\mu$m. The obtained roughness parameters for this case are $B_0 = (0.399 \pm 0.002)\,\mu\mathrm{m}^2$ and $\zeta_{\mathrm{eff}} = 0.821 \pm 0.005$. The fit goodness is quantified by the coefficient of determination $R^2 = 0.999883$, which would be equal to 1 if all the considered points were perfectly aligned[3]. The indicated uncertainties for B_0 and ζ_{eff} correspond to the statistical error of the fit and are relatively low due to the high fit goodness. However, the variations in B_0 and ζ_{eff} due to slight changes on the arbitrarily selected limits r_0 and r_1 are relatively large. In the following, we present the method we apply in order to appropriately determine the roughness parameters and their uncertainties, taking into account the fact that the fitting range significantly affects the results.

5.2.2 Determining the roughness parameters and their uncertainties

In order to make a representative determination of B_0 and ζ_{eff}, we consider the results obtained from fitting equation (5.3) in a range in which the coefficient R^2 is sufficiently high. This range is determined as follows.

---

[3] The coefficient of determination for two variables X and Y is defined as $R^2 = \sigma_{XY}^2/\sigma_X^2\sigma_Y^2$, where σ_{XY}^2 is the covariance of (X, Y) and σ_X^2 and σ_Y^2 are the variances of X and Y, respectively. In our case, X corresponds to $\log\left(r/\mu\mathrm{m}\right)$ and Y to $\log\left(B(r)/\mu\mathrm{m}^2\right)$.

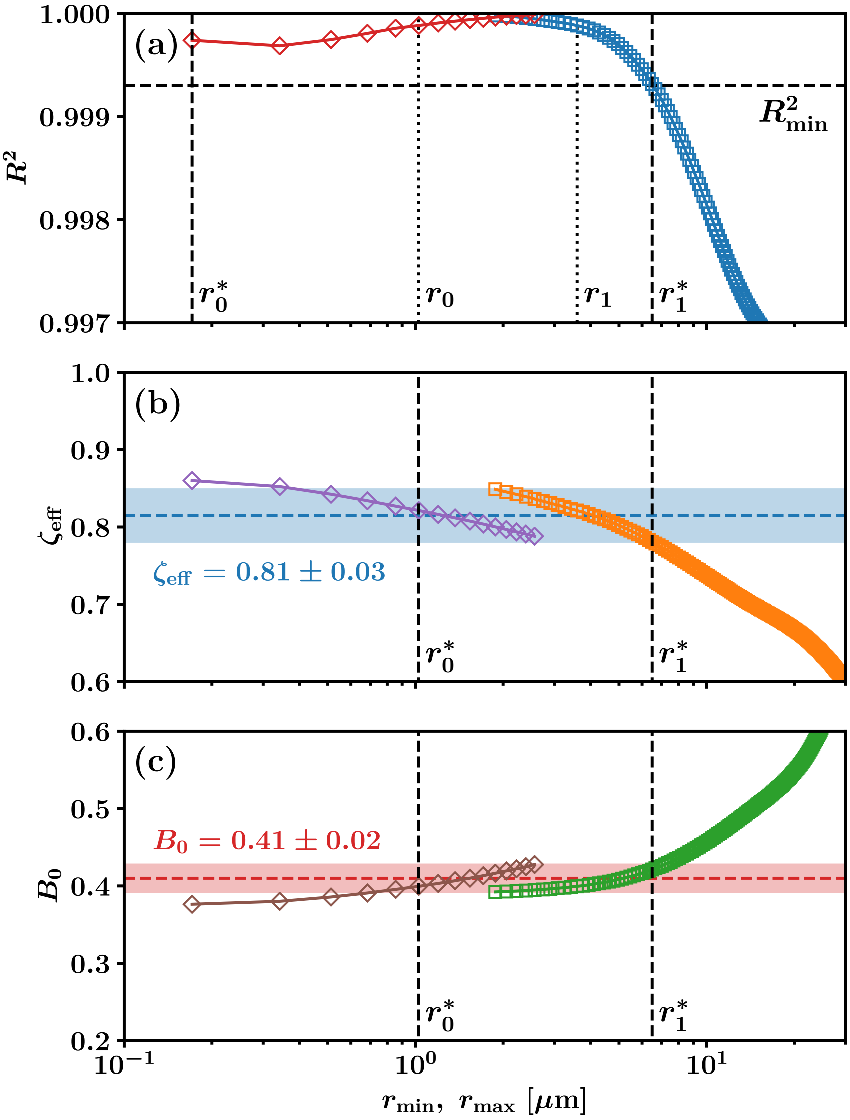

Figure 5.2: **Protocol for determining roughness parameters and their uncertainties for a single domain wall profile.** (a) Coefficient of determination R^2 resulting from fits performed in ranges $[r_0, r_{\mathrm{max}}]$ (blue squares) and $[r_{\mathrm{min}}, r_1]$ (red diamonds) as a function of r_{max} and r_{min}, respectively, for the $B(r)$ of a single domain wall profile. We indicate the lower bound R^2_{min} considered for defining r_0^* and r_1^*. r_0^* is then redefined as $r_0^* = \max(r_0, r_0^*)$. (b) Roughness exponent ζ_{eff} and (c) roughness amplitude B_0 resulting from the same fits. We consider all the values obtained for $[r_{\mathrm{min}}, r_1]$ with $r_{\mathrm{min}} \geq r_0^*$ and for $[r_0, r_{\mathrm{max}}]$ with $r_{\mathrm{max}} \leq r_1^*$ in order to determine ζ_{eff} and B_0 and their uncertainties, as indicated by the shaded areas.

Figure 5.2(a) shows the R^2 values resulting from fits performed in ranges $[r_0, r_{\max}]$ (blue squares) and $[r_{\min}, r_1]$ (red diamonds) as a function of the upper and lower range limits $r_{\max}$ and $r_{\min}$, respectively, for the $B(r)$ plotted in figure 5.1(b). All fits consider at least 6 points, hence $\delta_r \leq r_{\min} \leq r_1 - 5\delta_r$ and $r_0 + 5\delta_r \leq r_{\max} \leq L$. The figure evidences that, for sufficiently high $r_{\max}$, the linear $\log B(r)$ vs. $\log r$ dependence is lost, what may be identified as a sharp decrease of R^2. In contrast, linearity is verified for lower range limits as low as $r_{\min} = \delta_r$, as no considerable decrease of R^2 occurs at low $r_{\min}$ values. This characteristic is verified for most of our roughness measurements.

In order to define the ranges in which the fit quality is sufficiently good, it is necessary to choose a minimum R^2 value. We have chosen $R^2_{\text{min}} = 0.9993$ for all the results shown in this chapter. We thus define r_0^* and r_1^* as the values such that fits performed in ranges $[r_0, r_{\max}]$ with $r_{\max} \leq r_1^*$ and $[r_{\min}, r_1]$ with $r_{\min} \geq r_0^*$ have a coefficient $R^2 \geq 0.9993$. Then, we redefine $r_0^* = \max(r_0, r_0^*)$ because we consider that distances within the first 5 pixels (below $1\,\mu$m) may comprise errors due to the discrete nature of $u(x)$ and the microscope's optical resolution. In a small fraction of our roughness measurements, we have observed a loss of linearity at low r values resulting on $r_0^* > r_0$.

We thus obtain ζ_{eff} and B_0 and their uncertainties considering all the fits performed in the defined ranges, i.e. $[r_{\min}, r_1]$ with $r_{\min} \geq r_0^*$ and $[r_0, r_{\max}]$ with $r_{\max} \leq r_1^*$, as indicated in figures 5.2(b) and (c). Note that the obtained uncertainties are considerably larger than the uncertainty of an individual fit, exemplified in figure 5.1(b). The described protocol results on representative values and uncertainties for the roughness parameters ζ_{eff} and B_0 of a single domain wall. The arbitrary elections of r_0, r_1 and R^2_{min} do not affect significantly these final results, and they could be changed according to the particular characteristics of the considered $B(r)$ functions. All the measurements presented in this chapter were obtained using $r_0 = 1.026\,\mu$m, $r_1 = 3.591\,\mu$m and $R^2_{\text{min}} = 0.9993$.

5.2.3 Statistics of roughness parameters

As we have mentioned before, the roughness parameters determined for a single domain wall may be not representative of the field and temperature conditions at which that wall was imaged. Due to the intrinsic dispersion of roughness parameters [104, 105], the analysis described above for one domain wall has to be repeated for multiple walls in order to obtain a statistically meaningful measure which may be associated to a particular position in the H - T diagram.

In figure 5.3, we show the results of analyzing $\mathcal{N} = 63$ domain wall profiles for $T = 275\,$K and $\mu_0 H = 5.71\,$mT. In panel (a), all the obtained ζ_{eff} are plotted, each of them being determined as presented above. Panel (b) shows the corresponding histogram of ζ_{eff} values. The mean value $\overline{\zeta}_{\text{eff}} = 0.823 \pm 0.007$ is obtained considering both the dispersion of ζ_{eff} values and their individual uncertainties, and is thus representative of the domain walls observed in our sample for this particular driving field and temperature. In panels (c) and (d), the

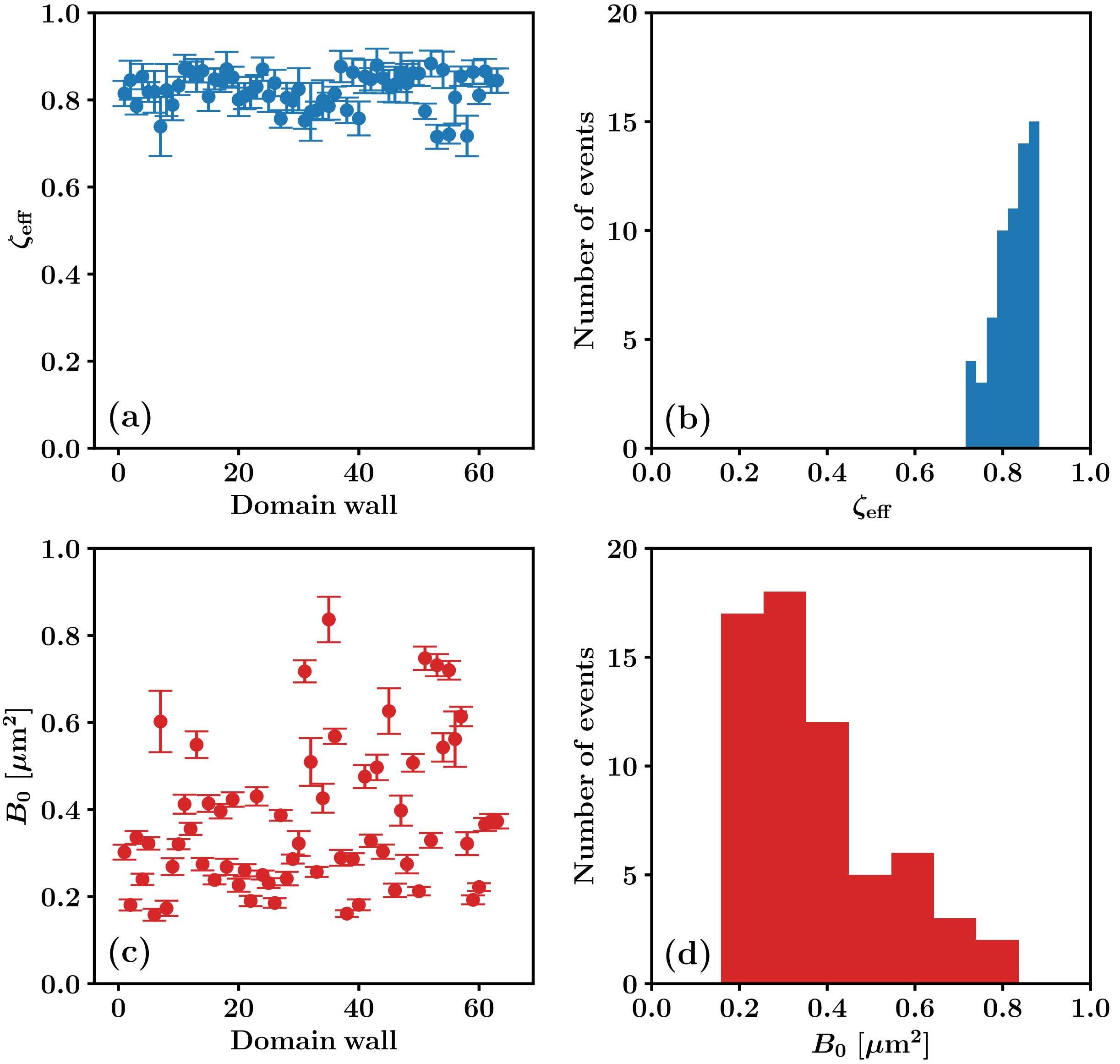

Figure 5.3: **Statistics of roughness parameters for a particular field and temperature condition.** (a) Obtained values of the exponent ζ_{eff} for the $\mathcal{N} = 63$ considered domain wall profiles at $T = 275\,\mathrm{K}$ and $\mu_0 H = 5.71\,\mathrm{mT}$. (b) Histogram of roughness exponents. The resulting mean value is $\overline{\zeta}_{\mathrm{eff}} = 0.823 \pm 0.007$. (c) Obtained values of the amplitude B_0 for the same domain walls. (d) Histogram of roughness amplitudes. The resulting mean value is $\overline{B}_0 = (0.37 \pm 0.02)\,\mu\mathrm{m}^2$.

analogous results are shown for B_0, resulting on a mean value $\overline{B}_0 = (0.37 \pm 0.02)\,\mu\text{m}^2$.

Several features may be observed in figure 5.3. First, the asymmetric nature of the resulting histograms, which results from the fact that both ζ_{eff} and B_0 are bounded. While $\zeta_{\text{eff}} \leq 1$, B_0 cannot be negative. Second, the rather wide dispersion of both parameters, which is in accordance with predictions [104, 105] and previous experimental measurements [39]. However, as we have just mentioned, their mean values may be determined with a rather small uncertainty due to the multiplicity of considered domain wall profiles.

In the following, we will show the results of applying this procedure for multiple domain walls at different field and temperature conditions. By doing so, we obtain representative values of ζ_{eff} and B_0 corresponding to different places in the H - T diagram. These results will be our starting point in order to test the theoretical predictions described in 2.4.4 and quantify relevant characteristic lengths.

5.2.4 Roughness parameters in the field-temperature diagram

Let us now present the mean roughness parameters $\overline{\zeta}_{\text{eff}}$ and $\overline{B}_0$ obtained at different fields and temperatures. Multiple magnetic domain wall profiles were analyzed at several fixed temperatures ranging from $T = 20\,\text{K}$ to $T = 295\,\text{K}$, and after applying field pulses of diverse magnitudes which generate domain wall motion in the creep and depinning regimes covering up to 8 orders of magnitude in the velocity. Thereby, we have covered most of the experimentally accessible space in the H - T diagram.

Figure 5.4 shows the velocity vs. field curves[4] corresponding to the set of temperatures for which we performed these careful roughness measurements. For each temperature, several fixed applied magnetic fields, corresponding to different domain wall velocities, were considered for roughness measurements. Thus, we highlight their positions in the velocity-field curves. Slight mismatches between these points and the velocity curves may be due to the fact that images for roughness measurements and for velocity vs. field curves were obtained on different days, what could imply that slightly different temperatures were reached and/or different sample regions were analyzed. In addition, we indicate as vertical dotted lines the depinning field $\mu_0 H_d$ corresponding to each temperature[5].

As we have discussed in section 4.2.3, below $T_M = (190 \pm 4)\,\text{K}$ the observable velocity range is less wide and, additionally, observed domain walls at low velocities present overhangs. Consequently, for $T < T_M$ the range in which domain wall roughness is measurable following our protocols is reduced. For this reason, roughness measurements for $T = 155$ and $20\,\text{K}$ could be made only close to the depinning field. The two points at $T = 295\,\text{K}$, well in the creep regime, correspond to previous measurements performed by Daniel Jordán

---

[4] See chapter 4 for a thorough study on the temperature dependence of domain wall dynamics in the same sample.

[5] See chapter 4 for details on the depinning field determination.

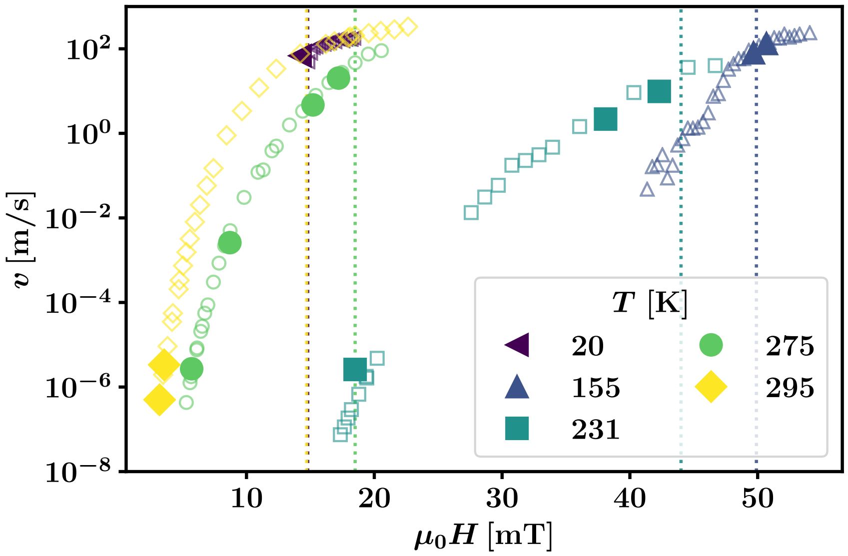

Figure 5.4: **Velocity vs. field curves corresponding to temperatures for which we performed domain wall roughness measurements.** We indicate with filled symbols the particular points $(\mu_0 H, v)$ which correspond to measurements of wall roughness. Vertical dotted lines indicate the depinning field $\mu_0 H_d$ corresponding to each temperature.

[39].

In figure 5.5 we present the obtained mean roughness parameters, $\overline{\zeta}_{\text{eff}}$ and $\overline{B}_0$, plotted as a function of the reduced field H/H_d for the selected temperatures. Remarkably, the roughness exponent $\overline{\zeta}_{\text{eff}}$ does not coincide for any temperature and field with any of the reference values that correspond to theoretical predictions. These values, which are indicated in figure 5.5(a), are $\zeta_{\text{eq}} = 2/3$, $\zeta_{\text{eff,max}} = 1$ and $\zeta_{\text{th}} = 0.5$. The value $\zeta_{\text{eff,max}} = 1$ corresponds to the upper limit of ζ_{eff} that can be obtained from a $B(r)$ function; this is the expected ζ_{eff} value if $\zeta > 1$ and, particularly, if $\zeta = \zeta_{\text{dep}} = 1.25$.

Let us briefly describe the field- and temperature-dependence of $\overline{\zeta}_{\text{eff}}$ and $\overline{B}_0$ that is shown in figure 5.5. The roughness exponent appears to slightly decrease with increasing field for each temperature, with the exception of $T = 231\,\text{K}$, where $\overline{\zeta}_{\text{eff}}$ is rather constant. However, we do not appreciate a clear tendency with changing temperature: all the obtained mean roughness exponents roughly belong to a range spanning between $\simeq 0.7$ and $\simeq 0.8$.

The mean roughness amplitude $\overline{B}_0$, however, shows a more clear field dependence: it decreases with increasing field. This is consistent with the qualitative observation that domain walls seem to become less rough with increasing velocity, as pinning force becomes less relevant with respect to the increasing driving force induced by the applied field [39, 108]. The temperature dependence of $\overline{B}_0$ is less clear in figure 5.5(b) due to a lack of experimental data for different temperatures at a given reduced field H/H_d. However, for a fixed H/H_d value, roughness amplitude seems to decrease with increasing temperature for $T > T_M$, what could be qualitatively interpreted as due to thermal activation reducing the roughening effect

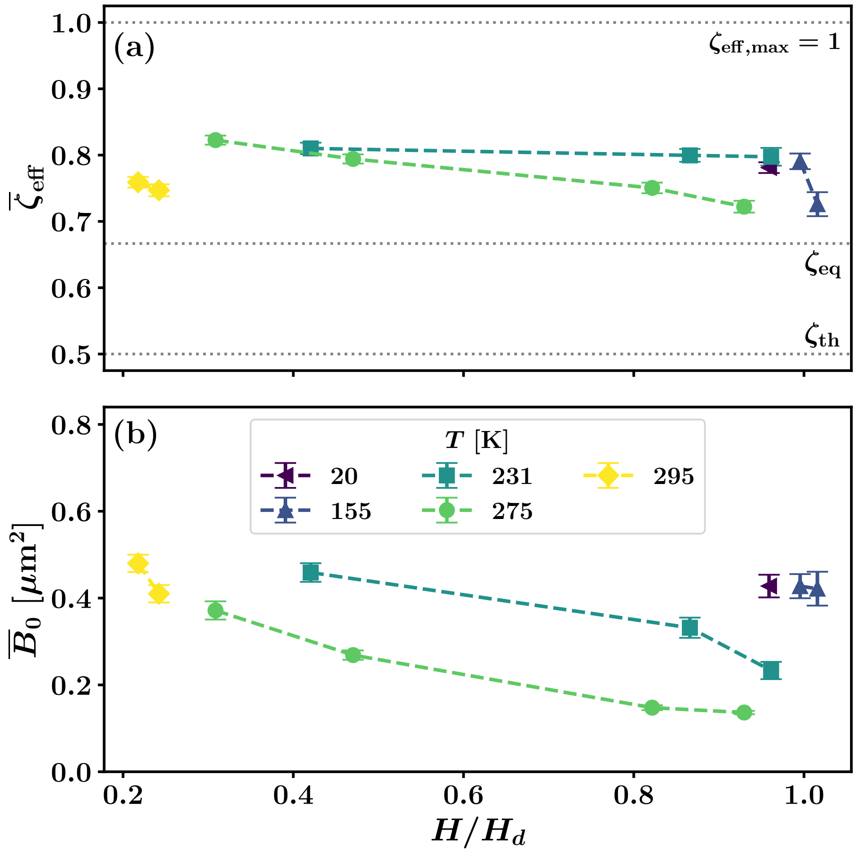

Figure 5.5: **Mean roughness parameters as a function of the reduced field for different temperatures.** (a) $\overline{\zeta}_{\mathrm{eff}}$ vs. H/H_d indicating the reference values, $\zeta_{\mathrm{th}} = 0.5$, $\zeta_{\mathrm{eq}} = 2/3$, and $\zeta_{\mathrm{eff,max}} = 1$ corresponding to the upper limit of ζ_{eff} that can be obtained from $B(r)$ functions. (b) $\overline{B}_0$ vs. H/H_d.

of pinning potential.

In the following section, we will present the analysis we have performed in order to successfully interpret these results in the framework of the quenched Edwards-Wilkinson universality class. For doing so, we shall establish a relationship between the obtained roughness parameters and the structure factor $S(q)$.

5.3 Analysis in terms of crossover lengths

Let us now present the interpretation of our roughness measurements in the framework of the theoretical scenario we have discussed in 2.4.4. We shall formally propose an expression for the structure factor $S(q)$ which considers the existence of two crossover lengths ℓ_{opt} and ℓ_{av} separating length scales at which ζ_{eq}, ζ_{dep} or ζ_{th} govern domain wall roughness. This description will permit us to relate the $S(q)$ that is predicted in this framework with the measured roughness parameters B_0 and $\zeta_{\rm eff}$, directly related to the displacement-displacement correlation function $B(r)$. Once this link is established, we shall determine the $S(q)$ parameters, closely related to $\ell_{\rm opt}$ and $\ell_{\rm av}$. Combining the results shown in figure 5.5 with dynamics and magnetometry measurements, we will show a method for the determination of these two crossover lengths. Finally, we shall present and discuss an experimentally obtained H - T diagram of crossover lengths, which may be directly compared with the theoretical picture illustrated in figure 2.16. This interpretation provides a framework for understanding both our roughness measurements and those reported in previous works, written in table 5.1.

5.3.1 Structure factor with two crossovers

The structure factor $S(q)$, given by equations (2.57) and (2.58), is the function that best captures roughness properties from the theoretical point of view [41]. For this reason, it is extensively used for precisely determining roughness exponents in numerical calculations [41, 104, 105, 119, 185].

In the following, we propose an expression for $S(q)$ that considers the existence of two crossovers between different length scales. Such a structure factor may be written as [40]

$$S(q) = \left(\frac{1}{S_{\rm th}(q)} + \frac{1}{S_{\rm dep}(q) + S_{\rm eq}(q)} \right)^{-1} , \tag{5.4}$$

with

$$S_{\rm eq}(q) = S_0 \left(\frac{q}{q_{\rm opt}} \right)^{-(1+2\zeta_{\rm eq})} , \tag{5.5}$$

$$S_{\rm dep}(q) = S_0 \left(\frac{q}{q_{\rm opt}} \right)^{-(1+2\zeta_{\rm dep})} , \tag{5.6}$$

$$S_{\rm th}(q) = S_0 \left(\frac{q_{\rm av}}{q_{\rm opt}} \right)^{-(1+2\zeta_{\rm dep})} \left(\frac{q}{q_{\rm av}} \right)^{-(1+2\zeta_{\rm th})} . \tag{5.7}$$

The characteristic crossover values are $q_{\rm opt} = 2\pi/\ell_{\rm opt}$ and $q_{\rm av} = 2\pi/\ell_{\rm av}$. The expression (5.4) for $S(q)$ satisfies the desired limits:

$$S(q) = \begin{cases} S_{\rm th}(q) \sim q^{-(1+2\zeta_{\rm th})} & \text{for } q \ll q_{\rm av} \\ S_{\rm dep}(q) \sim q^{-(1+2\zeta_{\rm dep})} & \text{for } q_{\rm av} \ll q \ll q_{\rm opt} \\ S_{\rm eq}(q) \sim q^{-(1+2\zeta_{\rm eq})} & \text{for } q_{\rm opt} \ll q \end{cases} \tag{5.8}$$

In figure 5.6(a), we plot the $S(q)$ function given by the above equations, what evidences three q regions in which each of the limits written in (5.8) prevail. The log-log scale plot shows the corresponding slopes $-(1+2\zeta)$, with the appropriate ζ value at each range. The parameters for calculating the plotted $S(q)$ function are $L = 100\,\mu$m, $\ell_{\rm opt} = 0.67\,\mu$m, $\ell_{\rm av} = 23.0\,\mu$m, and $S_0 = 1.33 \times 10^{-6}\,\mu$m^2.

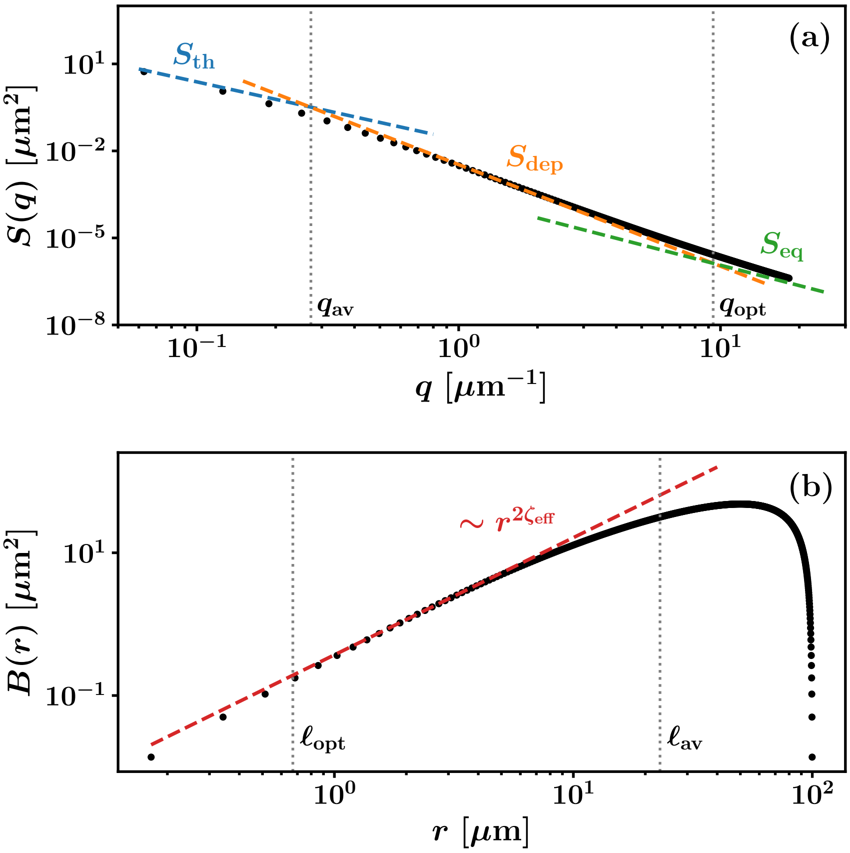

Figure 5.6: **Structure factor and displacement-displacement correlation function of an elastic line with two crossovers between different roughness exponents.** (a) Structure factor $S(q)$ in log-log scale. The reference S_{eq}, S_{dep} and S_{th} are indicated as dashed lines with slopes equal to $-(1+2\zeta)$ with $\zeta = \zeta_{\mathrm{eq}} = 2/3$ for $q \gg q_{\mathrm{opt}}$, $\zeta = \zeta_{\mathrm{dep}} = 1.25$ for $q_{\mathrm{av}} \ll q \ll q_{\mathrm{opt}}$, and $\zeta = \zeta_{\mathrm{th}} = 1/2$ for $q \ll q_{\mathrm{av}}$. The crossover q values are $q_{\mathrm{av}} = 2\pi/\ell_{\mathrm{av}}$ and $q_{\mathrm{opt}} = 2\pi/\ell_{\mathrm{opt}}$, with $\ell_{\mathrm{opt}} = 0.67\,\mu$m and $\ell_{\mathrm{av}} = 23.0\,\mu$m. The interface size is $L = 100\,\mu$m, and the structure factor amplitude is $S_0 = 1.33 \times 10^{-6}\,\mu\mathrm{m}^2$. (b) Associated $B(r)$ function in log-log scale. The corresponding roughness parameters are $\zeta_{\mathrm{eff}} = 0.82 \pm 0.04$ and $B_0 = (0.37 \pm 0.02)\,\mu\mathrm{m}^2$.

In practice, as domain wall profiles $u(x)$ are discretized, $S(q)$ shall be treated as a discrete function. Accordingly, we define

$$S(q_n) = \tilde{u}(q_n)\,\tilde{u}(-q_n) \tag{5.9}$$

in terms of the Fourier transform of the domain wall profile

$$\tilde{u}(q_n) = \frac{1}{N}\sum_{j=1}^{N} u(x_j)\,\exp\left(-iq_n x_j\right)\,, \tag{5.10}$$

where $q_n = 2\pi n/L$, with $L = N\delta_r$ being the wall size and $n = 1, ..., N$. The discrete displacement-displacement correlation function $B(r)$ may be calculated for $r \ll L$ in terms of the structure factor as [40]

$$B(r) = 4\sum_{n=1}^{(N-1)/2} S(q_n)\left[1 - \cos\left(q_n r\right)\right]\,, \tag{5.11}$$

where $r = k\delta_r$ with $k = 1, ..., N$. Here, we have chosen the symmetric basis for the Fourier modes q_n. Particularly, for computing the $S(q)$ function, we consider an odd N value so that $n = -(N-1)/2, -(N-1)/2+1, ..., (N-1)/2$ and take into account the periodicity of $S(q)$ and the fact that $S(q_n) = S(-q_n)$ [40]. The $B(r)$ function corresponding to the $S(q)$ shown in figure 5.6(a) is plotted in (b), in log-log scale. Note the similarity with the experimental $B(r)$ that we have presented in figure 5.1(b).

In contrast with $S(q)$, which shows three rather well defined slopes, $B(r)$ does not show well defined slopes in the different ranges of r. The implementation of the protocol described in 5.2.2 for the computed $B(r)$ shown in figure 5.6(b) shields an effective roughness exponent $\zeta_{\text{eff}} = 0.82 \pm 0.04$ and an amplitude $B_0 = (0.37 \pm 0.02)\,\mu\text{m}^2$.

The ζ_{eff} value evidences that the three roughness exponents are mixed in the $B(r)$ function resulting from a $S(q)$ with two crossovers. In addition, the drop of $B(r)$ at high r values, which also reduces its effective slope, is due to finite-size effects: $B(r)$ has a maximum at $r \simeq L/2$, where L is the interface size. Furthermore, as we have already pointed out, $\zeta_{\text{eff}} \leq 1$ by definition of $B(r)$ and then, the depinning roughness exponent $\zeta_{\text{dep}} = 1.25$ cannot be reflected only by $B(r)$ [107]. These three factors difficult the discrimination of interplaying roughness exponents by means of the displacement-displacement correlation function $B(r)$.

However, as we have extensively discussed, our experimental studies have permitted us to obtain, from the analyzed domain wall profiles and their $B(r)$ functions, representative roughness parameters $\overline{\zeta}_{\text{eff}}$ and $\overline{B}_0$ for different fields and temperatures. The computations of $S(q)$ from experimental wall profiles are very noisy, resulting on highly inaccurate definitions of the slopes [175], hence impeding the observation of the crossovers illustrated in 5.6(a). Consequently, the challenge we have to handle consists on relating the experimentally obtained parameters with the structure factor parameters S_0, q_{opt} and q_{av}; the last two being directly related to ℓ_{opt} and ℓ_{av}.

T [K]	M_s [kA/m]	K_{eff} [kJ/m^3]	$\mu_0 H_d$ [mT]	T_d [K]	σ [μJ/m^2]	L_c [nm]
20	112(2)	22(6)	14.8(0.2)	30000(5000)*	1300(600)	170(30)
155	25(5)	15(5)	49.9(0.9)	25800(600)	900(500)	170(40)
231	15(2)	15(5)	44(6)	19800(700)	900(500)	240(50)
275	27(1)	18(5)	19(3)	14700(500)	1000(500)	280(50)
295	32(2)	14(5)	15(3)	13200(500)	900(400)	260(50)

Table 5.2: **Relevant material- and temperature-dependent parameters at selected temperatures.** M_s and K_{eff} were obtained from magnetometry measurements, while $\mu_0 H_d$ and T_d result from the analysis of domain wall velocity vs. field curves. σ values were obtained from equation (2.16), with $\Delta = (15 \pm 5)$ nm. L_c is obtained following equation (2.89), with $t = 10$ nm. Uncertainties are indicated in brackets. * The T_d value for $T = 20$ K was estimated as an extrapolation from higher temperature values.

In the following, we will describe the procedure that we have implemented in order to obtain the parameters that define the structure factor $S(q)$ for each temperature and field. First, we shall describe the independent determination of the Larkin length L_c and the equilibrium correlation length ℓ_{opt}, which will then be combined with the data shown in figure 5.5.

5.3.2 Larkin length and equilibrium correlation length

As we have three unknown parameters, S_0, q_{opt} and q_{av}, and only two measured ones, $\overline{\zeta}_{\text{eff}}$ and $\overline{B}_0$, we shall use additional independent information in order to determine the unknown quantities. Hence, we independently calculate $q_{\text{opt}} = 2\pi/\ell_{\text{opt}}$ using equation (2.84) for ℓ_{opt}, with the characteristic Larkin length L_c being calculated by using equation (2.89). In order to obtain L_c, domain wall energy σ, depinning temperature T_d, depinning field H_d, saturation magnetization M_s and sample thickness t shall be considered. All these quantities, except $t = 10$ nm, are temperature-dependent. The values of the relevant parameters for the studied temperatures and corresponding results for L_c are written in table 5.2. They were obtained from magnetometry experiments (see section 3.3.1) and from velocity vs. field measurements (see chapter 4). The domain wall energy σ is estimated following the expression for a Bloch wall, equation (2.16), with a typical width parameter $\Delta = (15 \pm 5)$ nm [135, 146, 190] and the K_{eff} values indicated in the table.

The calculated values of L_c, written in table 5.2, are plotted in figure 5.7(a) as a function of T. These values permit us to obtain the optimal size ℓ_{opt} corresponding to thermally activated jumps over characteristic energy barriers as a function of the reduced field H/H_d for each temperature using equation (2.84). Resulting curves are shown in figure 5.7(b) for the different temperatures, highlighting points corresponding to the H/H_d values for which we have performed roughness measurements. These ℓ_{opt} vs. H/H_d curves are only differentiated by the factor $L_c(T)$. Specifically, according to (2.84), for any temperature we

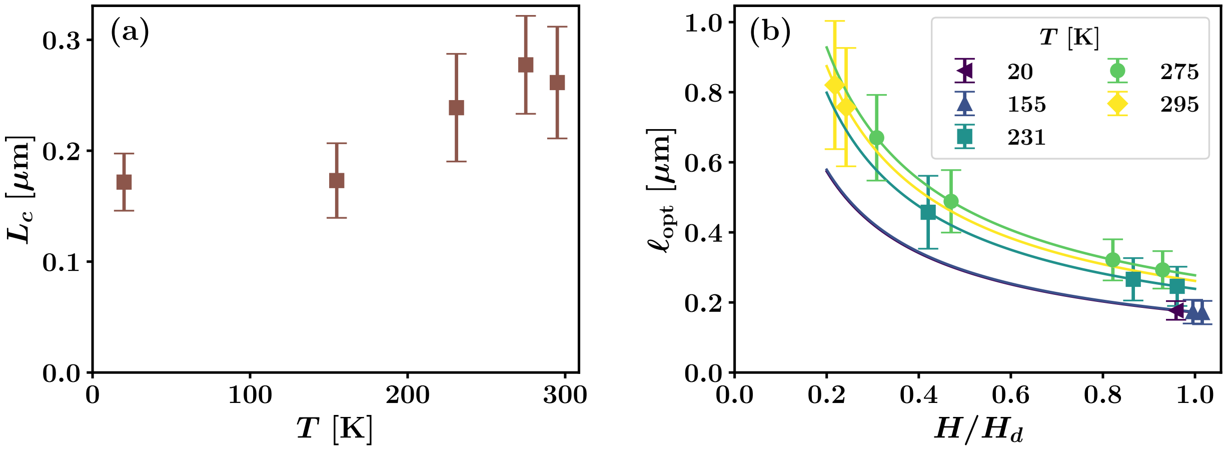

Figure 5.7: **Calculated Larkin length L_c and optimal event size ℓ_{opt}.** (a) L_c vs. T for the considered set of temperatures. (b) ℓ_{opt} vs. the reduced field H/H_d for the different temperatures, indicating the full dependence (5.12) and values corresponding to the analyzed domain walls.

may write

$$\ell_{\mathrm{opt}}(H,T) = L_c(T)\left(\frac{H}{H_d(T)}\right)^{-\nu_{\mathrm{eq}}}, \tag{5.12}$$

where $\nu_{\mathrm{eq}} = 1/(2-\zeta_{\mathrm{eq}}) = 3/4$.

The fact that ℓ_{opt} is larger than the pixel size $\delta_r = 0.171\,\mu\mathrm{m}$ for all the considered temperatures and applied fields suggests that the domain wall morphology below ℓ_{opt} may affect the experimentally observed wall profiles. As for the optical resolution $\approx 1\,\mu\mathrm{m}$, it is above ℓ_{opt} in less than one order of magnitude. Particularly, the lowest distance that we have considered for the fits of $\log B(r)$ vs. $\log r$ is $r_0 = 1.026\,\mu\mathrm{m}$ (see section 5.2.2). As we have discussed above, the three roughness exponents may impact on ζ_{eff} even outside their corresponding length scale range. Consequently, the equilibrium roughness exponent $\zeta_{\mathrm{eq}} = 2/3$ that characterizes domain wall morphology below ℓ_{opt} should be taken into account. Therefore, at least one crossover between S_{eq} and S_{dep} at $q_{\mathrm{opt}} = 2\pi/\ell_{\mathrm{opt}}$ should be considered for the structure factors characterizing domain wall roughness. In the following, we will see that the second crossover between S_{dep} and S_{th} at $q_{\mathrm{av}} = 2\pi/\ell_{\mathrm{av}}$ should also be considered in order to comprehend the roughness exponents plotted in figure 5.5(a).

5.3.3 Depinning correlation length and structure factor amplitude

In order to determine q_{av} and S_0 for each temperature and field, we shall find the structure factor $S(q)$ which is in best accordance with the obtained ℓ_{opt}, $\overline{\zeta}_{\mathrm{eff}}$ and $\overline{B}_0$. As we have presented above, there is an independently calculated ℓ_{opt} value for each combination of T and H/H_d. We therefore calculate $S(q)$, equation (5.4), fixing $q_{\mathrm{opt}} = 2\pi/\ell_{\mathrm{opt}}$ and varying

$q_{\rm av}$ and S_0. This calculation is performed for a domain wall of size $L = 100\,\mu$m and pixel size $\delta_r = 0.171\,\mu$m, what defines the q range $q_{\rm min} \leq q \leq q_{\rm max}$ with $q_{\rm min} = 2\pi/L$ and $q_{\rm max} = 2\pi(N-1)/2L = \pi/\delta_r - \pi/L$.

For each $q_{\rm av}$ and S_0, we then compute the associated $B(r)$ function following equation (5.11). Using exactly the same protocol that we have described in 5.2.2 for $B(r)$ functions computed from experimental domain wall profiles, we obtain the corresponding $\zeta_{\rm eff}$ and B_0 values with their uncertainties. The pursued $S(q)$ is the structure factor with $q_{\rm av}$ and S_0 such that $\zeta_{\rm eff}$ and B_0 are in accordance with the experimentally measured $\overline{\zeta}_{\rm eff}$ and $\overline{B}_0$.

In figure 5.8(a) we plot, as a function of $q_{\rm av}$ and for a fixed $q_{\rm opt}$, the $\zeta_{\rm eff}$ values corresponding to the $B(r)$ function obtained from the calculated $S(q)$. This $\zeta_{\rm eff}$ vs. $q_{\rm av}$ dependence is independent of S_0. We consider $\ell_{\rm opt} = 2\pi/q_{\rm opt} = 0.67\,\mu$m, corresponding to $T = 275\,$K and $H/H_d = 0.31$ ($\mu_0 H = 5.71\,$mT and $\mu_0 H_d \simeq 18.5\,$mT).

As illustrated in the figure, $\zeta_{\rm eff}$ follows a smooth and monotonous decay for increasing $q_{\rm av}$, with two asymptotical values corresponding to $q_{\rm av} < q_{\rm min}$ and $q_{\rm av} > q_{\rm max}$. The low $q_{\rm av}$ (high $\ell_{\rm av}$) limit, with $\zeta_{\rm eff} \simeq 0.9$, corresponds to $\ell_{\rm av} > L$, resulting on only one crossover between $\zeta_{\rm eq} = 2/3$ and $\zeta_{\rm dep} = 1.25$ at $q = q_{\rm opt}$. Therefore, this $\zeta_{\rm eff}$ value results from the interplay of $\zeta_{\rm eq} = 2/3$, $\zeta_{\rm eff,max} = 1$, and finite-size effects which reduce the $\log B(r)$ vs. $\log r$ slope for distances r approaching $L/2$. This particular $\zeta_{\rm eff}$ value depends on $q_{\rm opt}$ and L. However, we have verified that the maximum distance r_1^* that we consider in order to obtain $\zeta_{\rm eff}$, which is always close to or below $10\,\mu$m (see section 5.2.2), is sufficiently below $L/2$ so that this result does not depend on L for $L \geq 100\,\mu$m. In other words, this result is not significantly affected by finite-size effects. Remarkably, for all the considered fields and temperatures $\zeta_{\rm eff} \simeq 0.9$ for $\ell_{\rm av} > L$ and, for their part, all the measured $\overline{\zeta}_{\rm eff}$ values (see figure 5.5(a)) are below 0.9. Consequently, a finite $\ell_{\rm av}$ must be considered in order to interpret our results.

On the other hand, the high $q_{\rm av}$ (low $\ell_{\rm av}$) limit corresponds to $\zeta_{\rm eff} = \zeta_{\rm th} = 0.5$. In this limit, $\ell_{\rm av} < \delta_r$, meaning that the observed domain wall fluctuations occur above the characteristic length $\ell_{\rm av}$ and then the decisive roughness exponent is the thermal exponent $\zeta_{\rm th}$. Note that, as $q_{\rm opt} < q_{\rm max}$ (i.e. $\ell_{\rm opt} > \delta_r$), this limit is unphysical because $\ell_{\rm av}$ must be larger than $\ell_{\rm opt}$.

The experimentally determined $\overline{\zeta}_{\rm eff} = 0.823 \pm 0.007$ for $T = 275\,$K and $H/H_d = 0.31$ is indicated in figure 5.8(a) as an horizontal line with a shaded area accounting for the uncertainty. This value is consistent with the $\zeta_{\rm eff}$ values obtained from the calculated structure factor $S(q)$ for $q_{\rm av} = q_{\rm av}^\star = (0.27 \pm 0.02)\,\mu\text{m}^{-1}$, as indicated by a vertical line and shaded area given by the intersection between the calculated $\zeta_{\rm eff}(q_{\rm av})$ dependence and the experimentally determined $\overline{\zeta}_{\rm eff}$. We thus calculate $\ell_{\rm av} = 2\pi/q_{\rm av}^\star = (23 \pm 2)\,\mu$m.

A noteworthy result is that this $\ell_{\rm av}$ value is higher than the r_1^* limit below which we consider $\log B(r)$ vs. $\log r$ linear fits in order to obtain $\zeta_{\rm eff}$ (see for example figure 5.6(b), where the fit satisfactorily describes the $\log B(r)$ vs. $\log r$ slope for $r < 7\,\mu$m).

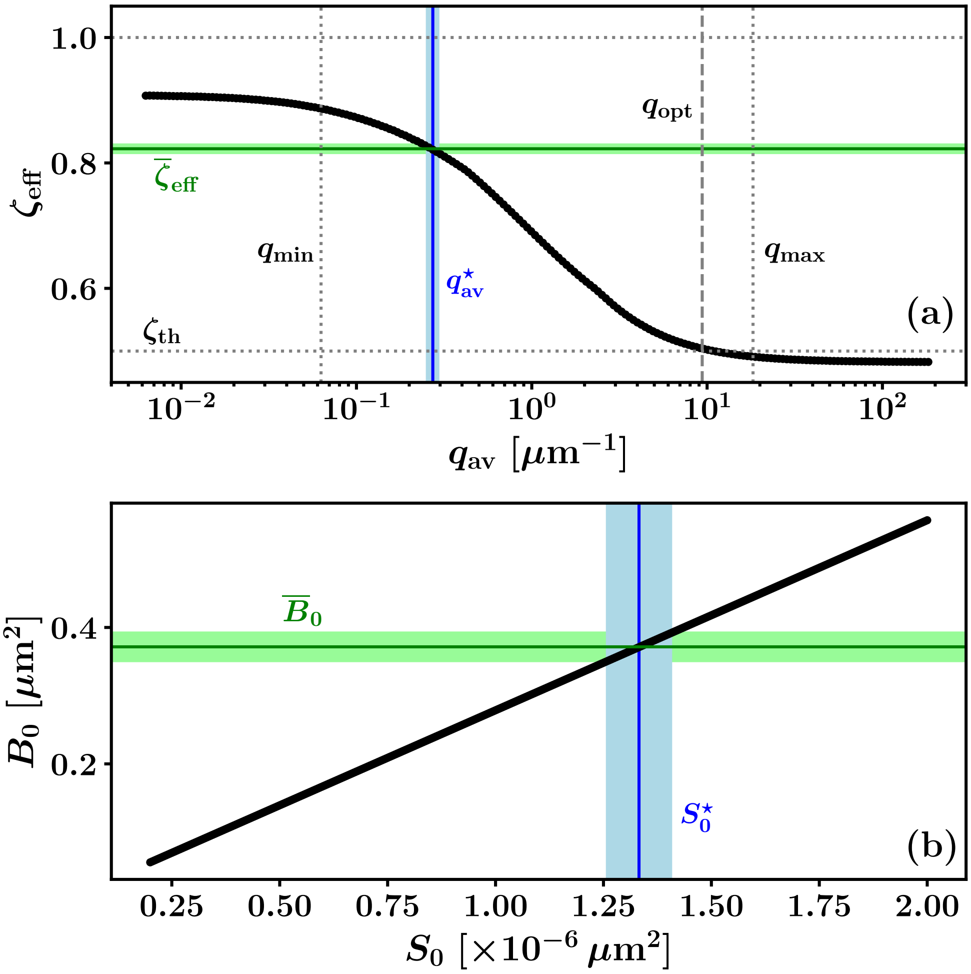

Figure 5.8: **Determination of structure factor parameters $q_{\rm av}$ and S_0 in accordance with measured roughness parameters $\overline{\zeta}_{\rm eff}$ and $\overline{B}_0$.** (a) $\zeta_{\rm eff}$ as a function of $q_{\rm av}$ for the $B(r)$ obtained from a $S(q)$ with $\ell_{\rm opt} = 0.67\,\mu$m, corresponding to $T = 275$ K and $H/H_d = 0.31$ ($\mu_0 H = 5.71$ mT and $\mu_0 H_d \simeq 18.5$ mT). The shown curve is independent of S_0. $q_{\rm opt} = 2\pi/\ell_{\rm opt}$ is indicated. $q_{\min}$ and $q_{\max}$ correspond to the window used for calculating $S(q)$: $q_{\max} = 2\pi/\delta_r$ and $q_{\min} = 2\pi/L$. $\overline{\zeta}_{\rm eff} = 0.823 \pm 0.007$, experimentally obtained for this particular T and H, is indicated as an horizontal shaded region. We determine $q_{\rm av}$ as the value $q^\star_{\rm av}$ that satisfies $\zeta_{\rm eff}(q^\star_{\rm av}) = \overline{\zeta}_{\rm eff}$; we then obtain $q_{\rm av} = q^\star_{\rm av} = (0.27 \pm 0.02)\,\mu$m^{-1}, as indicated by the vertical shaded region. (b) B_0 vs. S_0 corresponding to the $S(q)$ with the same $q_{\rm opt}$ and $q_{\rm av} = q^*_{\rm av}$. The measured roughness amplitude for the same T and H is $\overline{B}_0 = (0.37 \pm 0.02)\,\mu$m^2, illustrated by the horizontal shaded region. S_0 is established as the value $S^\star_0$ that satisfies $B_0(S^\star_0) = \overline{B}_0$; we then obtain $S_0 = S^\star_0 = (1.33 \pm 0.08) \times 10^{-6}\,\mu$m^2, as indicated by the vertical shaded region.

Consequently, the crossover at ℓ_{av} affects ζ_{eff} even for distances r well below this crossover length. Additionally, ℓ_{av} is considerably lower than the characteristic length $L/2$ above which finite-size effects generate a drop of the $B(r)$ dependence. Consequently, we can associate the measured $\overline{\zeta}_{\mathrm{eff}}$ values, which are below the limit $\zeta_{\mathrm{eff}} \simeq 0.9$, to the crossover at ℓ_{av} rather than to finite-size effects. As we have noted for ℓ_{opt}, which is lower than $r_0 = 1.026\,\mu\mathrm{m}$ but may affect ζ_{eff}, ℓ_{av} is higher than $r_1^* \lesssim 10\,\mu\mathrm{m}$ and is shown to affect ζ_{eff}.

Finally, once we have determined both q_{opt} and q_{av}, we may calculate $S(q)$ functions for different S_0 values and evaluate the corresponding $B(r)$ functions in order to obtain B_0. In figure 5.8(b) we plot the resulting B_0 vs. S_0 dependence, which presents a linear behavior. Similarly to how we have chosen the appropriate q_{av} value from comparing $S(q)$ and $B(r)$ calculations with experimental results, we determine S_0 from evaluating where the $B_0(S_0)$ dependence coincides with the experimentally determined $\overline{B}_0$. For the case of the figure, i.e. $T = 275\,\mathrm{K}$ and $H/H_d = 0.31$, $\overline{B}_0 = (0.37 \pm 0.02)\,\mu\mathrm{m}^2$, and thus we obtain $S_0 = S_0^\star = (1.33 \pm 0.08) \times 10^{-6}\,\mu\mathrm{m}^2$.

5.3.4 Resulting parameters and experimental crossover diagram

The procedure for determining q_{av} and S_0 from ℓ_{opt}, $\overline{\zeta}_{\mathrm{eff}}$ and $\overline{B}_0$ that we described above was repeated for all the fields and temperatures for which we have performed roughness measurements. The resulting characteristic lengths ℓ_{opt} and ℓ_{av} are plotted as a function of H/H_d in logarithmic scale for the different temperatures in figure 5.9(a). This plot is analogous to the predicted crossover diagram that we have illustrated in figure 2.16.

The H/H_d-dependence of ℓ_{opt}, which separates the length scales at which the equilibrium roughness exponent ζ_{eq} $(\ell < \ell_{\mathrm{opt}})$ and the depinning roughness exponent ζ_{dep} $(\ell > \ell_{\mathrm{opt}})$ dominate wall morphology, has already been presented in figure 5.7(b). On the other hand, the field dependence of ℓ_{av} shown in figure 5.9(a) constitutes to the best of our knowledge the first experimental determination of this quantity for $H < H_d$, what supports the hypothesis that ℓ_{av} is finite for $T > 0$ even in the creep regime [4]. Remarkably, ℓ_{av} values $\sim 10\,\mu\mathrm{m}$, considerably smaller than L, are necessary in order to interpret our results.

The lack of a complete field dependence for three of the five shown temperatures difficults the evaluation of the temperature dependence of $\ell_{\mathrm{av}}(H/H_d)$. However, the experimental results shown in figure 5.9(a) are roughly consistent with the scenario of a decreasing ℓ_{av} with increasing temperature, also illustrated in figure 2.16.

In figure 5.9(b), we show the H/H_d-dependence of the structure factor amplitude S_0 for the different temperatures. No theoretical prediction has been performed for this quantity; however, the obtained values show that temperature does not impact substantially on the $S_0(H/H_d)$ dependence, while a clear decrease is observed for increasing H/H_d. A roughly linear dependence may be observed in the semi-logarithmic plot, what suggests that $\ln S_0 \sim -H/H_d$.

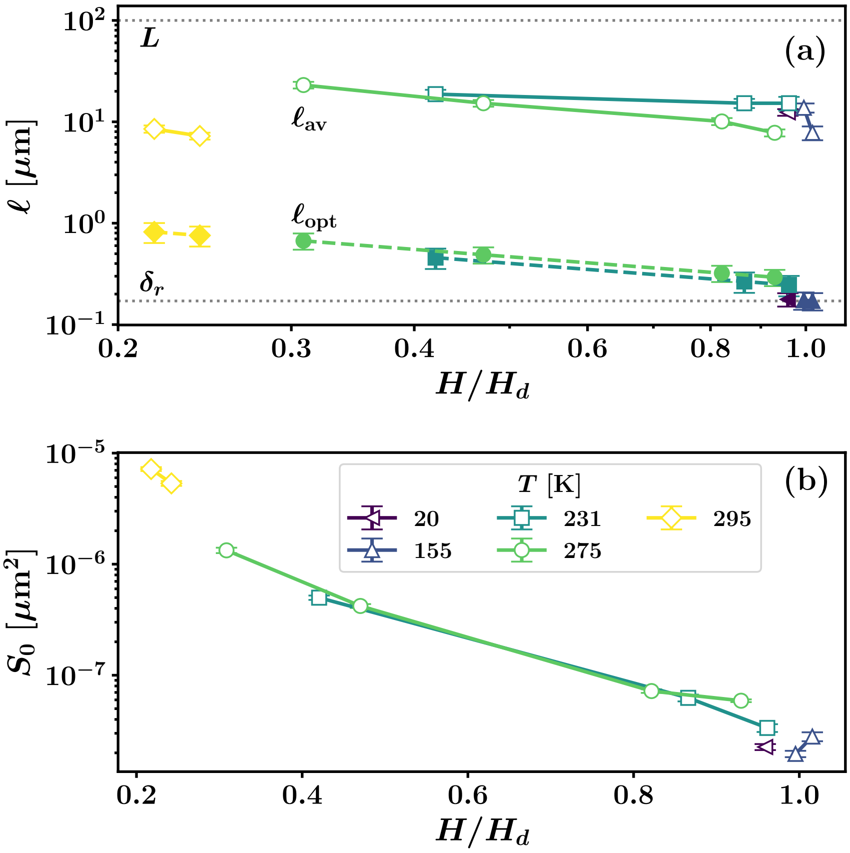

Figure 5.9: **Experimentally determined crossover diagram and structure factor amplitude.** (a) Characteristic lengths ℓ_{opt} (full symbols) and ℓ_{av} (empty symbols) vs. H/H_d for the different considered temperatures in log-log scale. We indicate the pixel size $\delta_r = 0.171\,\mu$m and the considered domain wall size $L = 100\,\mu$m as horizontal dotted lines. (b) Structure factor amplitude S_0 vs. H/H_d for the different temperatures.

Discussion

The analysis of experimental results that we have described above shows that the theoretical scenario presented in 2.4.4 and 5.3.1 may successfully describe the roughness of magnetic domain walls in perpendicularly magnetized thin films. Moreover, the experimental results previously reported in the literature, written in table 5.1, could be interpreted in this framework. We have thus shown that the roughness exponent measurements resulting from computing and fitting the displacement-displacement correlation function $B(r)$ of an experimentally observed domain wall should be carefully interpreted, taking into account that domain wall roughness may be dominated by different exponents at different length scales.

The relevant length scales in the crossover diagram separating regions characterized by the three roughness exponents ζ_{eq}, ζ_{dep} and ζ_{th} are the equilibrium and depinning correlation lengths ℓ_{opt} and ℓ_{av}. Their determination permitted us to plot a crossover diagram, figure

5.9(a), which may be directly compared with the theoretical scenario illustrated in figure 2.16. While the ℓ_{opt} vs. H/H_d dependence had been previously studied [4], no quantitative predictions had been made for the ℓ_{av} vs. H/H_d dependence for $T > 0$, even if finite values of ℓ_{av} were theoretically expected for $H < H_d$ and $T > 0$ [41]. In this context, our results for ℓ_{av} are the first measurements of this quantity for $H < H_d$ and confirm that finite ℓ_{av} values must be considered in order to explain the experimentally obtained effective roughness exponent values.

Particularly, we have found that ℓ_{av} ($\sim 10\,\mu$m) is within the experimentally accessible length scales of magneto-optical microscopy (see figure 5.9(a)). Additionally, ℓ_{opt} (~ 0.1-$1\,\mu$m) is close to the optical resolution $\approx 1\,\mu$m. Consequently, the existence of crossovers at ℓ_{opt} and ℓ_{av} between length scales in which different roughness exponents dominate must be considered and, therefore, the measured roughness exponents cannot be associated to only one of the theoretically predicted exponents. Nevertheless, similar studies have been recently performed in Pt/Co/Pt, in which ℓ_{opt} is shown to be well below experimental access and thus roughness exponent measurements are interpreted in terms of only one crossover at ℓ_{av} and two exponents, ζ_{dep} and ζ_{th} [108].

Other results of our study are the determination of the amplitudes B_0 and S_0. As these quantities are not directly linked to universal parameters, the interpretation of these results is more elusive and there do not exist precise predictions about their magnitude and their temperature and field dependence. However, we have shown rather clear observations that call for deeper studies. On the one hand, the decrease of $\overline{B}_0$ for increasing field H (see figure 5.5(b)), which had already been observed [39] and is consistent with the qualitative observation that domain walls become less rough as pinning force becomes less relevant with respect to the driving force. On the other hand, the clear decrease of S_0 with increasing fields, which might be described as $\ln S_0 \sim -H/H_d$, and the observation that the impact of temperature is not significant (see figure 5.9(b)).

5.4 Chapter summary and conclusions

This chapter has been devoted to the analysis of the roughness properties of magnetic domain walls in a thin GdFeCo sample with perpendicular anisotropy, focusing on the universal critical roughness exponents. We have shown that previous experimental measurements of the roughness exponent ζ are rather disperse and, furthermore, many of them are not consistent with the theoretically predicted exponents.

Consequently, we have pointed out that the distribution of ζ values for elastic lines in a disordered potential is intrinsically wide, what calls for careful studies in order to perform statistically meaningful roughness exponent determinations. We have therefore described the methods that we implement in order to experimentally measure and determine representative values for the roughness exponent ζ_{eff} and the amplitude B_0 obtained from $B(r)$ functions. These measurements were performed for different field and temperature conditions, thus obtaining mean roughness parameters $\overline{\zeta}_{\rm eff}$ and $\overline{B}_0$ spanning over most of the experimentally accessible H - T diagram.

Further on, we have noted that our experimentally measured $\overline{\zeta}_{\rm eff}$ do not coincide with any of the three theoretically predicted roughness exponents. In this context, we have developed the theoretical framework already proposed in section 2.4.4 for the interpretation of experimentally determined roughness exponents. In this hypothetical scenario, we consider that the three exponents $\zeta_{\rm eq}$, $\zeta_{\rm dep}$ and $\zeta_{\rm th}$ predicted for the quenched Edwards-Wilkinson universality class impact on domain wall roughness at different length scales, with crossover characteristic lengths $\ell_{\rm opt}$ and $\ell_{\rm av}$. We have thus proposed an expression for a structure factor $S(q)$ with two crossovers which we would then use for the interpretation of our experimental results.

Our experimental determinations of the mean roughness parameters $\overline{\zeta}_{\rm eff}$ and $\overline{B}_0$ for different fields and temperatures was then combined with the independent determination of $q_{\rm opt}$ in order to find, for each H/H_d and T, the structure factor parameters $q_{\rm av}$ and S_0 which are consistent with those values. This permitted us to plot, as a function of H/H_d and for different T values, the characteristic lengths $\ell_{\rm opt}$ and $\ell_{\rm av}$. We found that both characteristic lengths are within the experimentally accessible length scales, what results on the need of considering two crossovers and three roughness exponents in order to successfully explain the experimentally obtained $\overline{\zeta}_{\rm eff}$ values.

The major results obtained from the studies presented on this chapter are two. On the one hand, the first determination of finite $\ell_{\rm av}$ values for $H < H_d$, what had been suggested only qualitatively for $T > 0$ but had no experimental support. On the other hand, the successful interpretation of experimentally obtained roughness exponents within a new theoretical framework, which calls for more careful domain wall roughness measurements in future investigations and for their interpretation based on the interplay of the three theoretically predicted exponents.

CHAPTER 6

Field- and current-driven domain wall dynamics in (Ga,Mn)(As,P)/(Ga,Mn)As

> *"Hay un mundo real ahí afuera que parece comportarse con reglas propias y en el que ocurren cosas.*
> *Eso que ocurre son hechos, hechos reales.*
> *No existen los 'hechos alternativos'."*
> **Guadalupe Nogués, *Pensar con otros***

In the last two chapters, we have presented the research performed throughout this thesis on field-driven domain walls in a metallic thin film of GdFeCo, focusing both on wall dynamics and morphology. In this chapter, we will present our studies on domain wall dynamics performed in a semiconducting ferromagnet which consists on a bilayer of (Ga,Mn)(As,P)/(Ga,Mn)As with dominant perpendicular magnetic anisotropy and a Curie temperature $T_C = 65\,\mathrm{K}$. The sample characteristics are presented in detail in section 3.4. The key feature of these investigations consists on the application of both field and current within the sample. While the former stimulus, i.e. the magnetic field, pushes domain walls through the Zeeman interaction, the latter induces a spin-transfer torque (STT) over them.

The mechanisms giving rise to the STT have been a subject of intense debate in the last decades [22–24, 26]. Additionally, the STT-driven inversion of perpendicularly magnetized devices has boosted important technological developments, particularly in the field of data-storage applications [11, 196]. As we have discussed in section 2.5.2, STT in diluted magnetic semiconductors as (Ga,Mn)(As,P)/(Ga,Mn)As is particularly efficient, what makes this system an appropriate model in which to study this mechanism.

Several open questions remain regarding STT-driven domain wall dynamics, which arise from some particularities that differentiate it from field-driven dynamics. One of these particularities is the existence of adiabatic [19] and non-adiabatic [22, 23] spin-transfer torques[1]. As these two torques are fundamentally different, the nature of domain wall motion arising from each of them is expected to vary profoundly. While the non-adiabatic STT acts similarly to an applied field, the adiabatic STT has very different properties [197]. Additionally, in contrast with the field-driven force over domain walls, which is isotropic, the STT-driven force depends strongly on the angle between the wall and the flow direction of the polarized current [27].

These particularities have given rise to debates on the universality class of STT-driven domain wall motion [156, 162, 198]. However, as we will further discuss later, the most recent and careful investigations suggest that despite the differences between field- and STT-driven motion, both of them belong to the quenched Edwards-Wilkinson universality class [27]. In this context, our research is focused on the creep regime of domain walls driven by field and STT. On the one hand, we shall compare the magnitudes of these two forces and the wall dynamics induced by each of them in this regime. On the other hand, we will study the dynamics resulting from simultaneously applying field and current. Our studies shed light on the effective action of each of these driving forces and on how the effective pinning parameters are affected by the driving force nature.

This chapter is organized as follows. In section 6.1, we shall motivate our research by briefly reviewing recent studies on the universality class of field- and STT-driven domain wall motion and on the dynamics resulting from the combined application of field and current. In this context, we shall propose some simple ideas which will permit us to analyze the creep motion of magnetic domain walls driven by field and STT. In section 6.2, we will present our methods for simultaneously applying field and current pulses and measuring representative domain wall velocities. Then, in section 6.3 we shall present and discuss our experimental results, analyzing the effect of field and STT on domain wall motion when applied both separately and simultaneously. Finally, in section 6.4 we will present a summary of our main conclusions.

6.1 Motivation and framework

In this section we shall present previous investigations and pose open questions related to the comparison between field- and STT-driven domain wall motion and the effects of combining these two driving forces. The ideas that we shall discuss here will permit us to analyze our experimental results, presented later in this chapter. First, we will discuss the most recent

---

[1] See 2.2.4 for an introduction on the origin and nature of STT mechanisms.

research on the universality class of field- and STT-driven motion. Second, we shall review previous reports on the joint effect of these two driving forces.

6.1.1 Universality class of field-driven and STT-driven domain wall motion

As we have already pointed out in section 2.4.2, the creep exponent $\mu = 1/4$ is well established for field-driven domain wall motion in many thin films with perpendicular anisotropy including (Ga,Mn)As and (Ga,Mn)(As,P) [16]. Even if the determination of other critical exponents as the roughness exponent ζ is more elusive, there exist diverse evidences which support that both the equilibrium and the depinning of field-driven domain walls belong to the quenched Edwards-Wilkinson universality class, as we have thoroughly discussed in previous chapters.

For STT-driven domain wall motion, both μ and ζ values have been under debate in the last years [27, 160, 162, 199]. In these works, μ and ζ are assessed on the one hand for field-driven wall motion and on the other hand for STT-driven wall motion. This analysis has a particular difficulty which consists on the directionality of these forces, already mentioned above. While at any point of the domain wall field-driven force acts in the wall's normal direction, STT acts in the polarized current's direction and its magnitude depends on the angle between $\vec{J}$ and the domain wall, resulting on a non-isotropic force that induces domain wall faceting [27].

This phenomena has been firstly observed by K. W. Moon and collaborators in Pt/Co/Pt thin films [160]. Recently, in a work which constitutes a collaboration in the framework of this thesis [27], Rebeca Díaz Pardo and colleagues carefully analyzed this phenomena in (Ga,Mn)(As,P)/(Ga,Mn)As and provided a plausible interpretation. Figures 6.1(a,b) show a comparison between successive domain wall profiles resulting from the application of field (a) and STT (b). The observed profiles evidence that STT-driven velocities are higher for domain wall segments oriented perpendicularly to the applied current, while they are lower for tilted wall segments, resulting on domain wall faceting. This process is triggered by the pinning of domain wall segments in relatively strong pinning sites, what induces wall tilting and therefore an imbalance of the driving force. In contrast, field-driven motion at similar velocities does not show domain wall faceting due to the uniformity of the driving force.

STT-driven domain wall faceting may distort roughness exponent determination. In the same report [27], Rebeca Díaz Pardo and collaborators showed that the careful measurement of ζ for STT-driven motion shields values which are consistent with those measured for field-driven motion, as shown in figure 6.1(c). Additionally, as it is illustrated in figure 2.21, the creep exponent value was also found to be consistent with $\mu = 1/4$ both for field- and STT-driven motion in (Ga,Mn)(As,P)/(Ga,Mn)As. These findings suggest that, even if directionality of both driving forces result in different behaviors, they both correspond to the quenched Edwards-Wilkinson universality class.

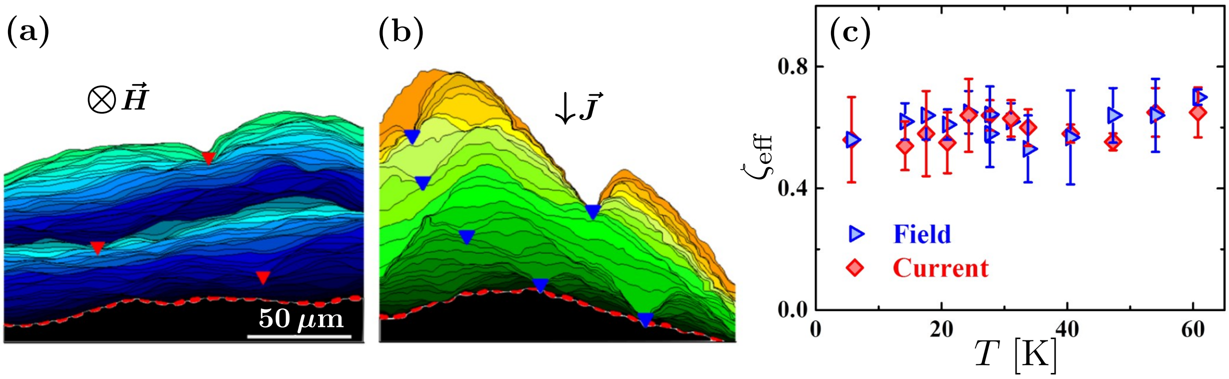

Figure 6.1: **Domain wall faceting and roughness exponent measurements for field- and STT-driven domain walls in (Ga,Mn)(As,P)/(Ga,Mn)As.** (a) Successive wall profiles resulting from field-driven motion with applied field pulses of $\mu_0 H = 0.16\,\text{mT}$ and $\Delta t = 0.5\,\text{s}$. (b) Successive STT-driven wall profiles in the same sample and with the same Δt, for $J = 0.5\,\text{GA/m}^2$. In both (a) and (b), triangles indicate strong pinning sites. (c) Measured roughness exponent ζ_{eff} for field- and STT-driven walls in the same sample, obtained from displacement-displacement correlation functions, as a function of the temperature. The three shown figures are adapted from [27].

As we have just discussed, universality of field- and STT-driven domain wall motion has been studied by applying these stimulus separately and comparing their effects. However, a deep study of the simultaneous field- and STT-driven dynamics is still lacking. In the following, we will review some recent reports on this issue and propose several open questions that we shall try to answer in this chapter.

6.1.2 Combined effect of field and STT on domain wall motion

In order to analyze the field- and STT-driven domain wall dynamics, we shall try to address the following question: which is the effective force over domain walls that is exerted by the applied stimuli? As the field-driven dynamics is much well understood, we may try to find an expression for the effective field $H_{\text{eff}}(H, J)$ arising from a combination of applied field H and current density J. This effective field may be defined as the field which, solely applied, would produce equivalent domain wall dynamics.

Steady and precessional flow regimes

In section 2.2.4, we have presented the adiabatic and non-adiabatic STT mechanisms and their impact on domain wall dynamics in the framework of the micromagnetic 1D model. In this context, disorder and temperature are neglected and thus the model predictions correspond to the flow regime, i.e. $H_{\text{eff}}(H, J) \gg H_d$. Let us consider the steady and the asymptotical precessional flow regimes in order to evaluate the effective field when both H and J are applied.

For the steady flow regime, by comparing equation (2.26) for field-driven motion and equation (2.41) for field- and STT-driven motion, we may write the effective field as

$$\mu_0 H_{\text{eff}}(H,J) = \mu_0 H + \frac{\beta_{\text{ST}}}{\gamma\Delta}\frac{g\mu_B P}{2eM_s}J \ . \tag{6.1}$$

Similarly, for the asymptotical precessional flow regime, we may obtain

$$\mu_0 H_{\text{eff}}(H,J) = \mu_0 H + \left(\beta_{\text{ST}} + \frac{1}{\alpha}\right)\frac{1}{\gamma\Delta}\frac{g\mu_B P}{2eM_s}J \tag{6.2}$$

from a comparison between (2.34) and (2.48).

As evidenced by equations (6.1) and (6.2), in these two flow regimes the effective field may be written as

$$\mu_0 H_{\text{eff}}(H,J) = \mu_0 H + \epsilon J \ . \tag{6.3}$$

In other words, the STT-induced effective field, ϵJ, is proportional to the current density J, and the contributions due to field and current are independent and simply sum up. The proportionality factor ϵ for the steady and asymptotical precessional flow regimes are, respectively,

$$\epsilon_{st} = \frac{\beta_{\text{ST}}}{\gamma\Delta}\frac{g\mu_B P}{2eM_s} \tag{6.4}$$

and

$$\epsilon_{asp} = \left(\beta_{\text{ST}} + \frac{1}{\alpha}\right)\frac{1}{\gamma\Delta}\frac{g\mu_B P}{2eM_s} \ . \tag{6.5}$$

These expressions evidence a key feature of STT-driven domain wall dynamics. If we consider pure current-driven motion and we neglect the non-adiabatic STT, i.e. if $H = 0$ and $\beta_{\text{ST}} = 0$, then no steady motion would occur, and an intrinsic depinning-like threshold would take place at the Walker condition, $J = 2eM_s\gamma\Delta\mu_0 H_w/\alpha g\mu_B P$ according to equation (2.44). For higher J, a precessional regime of motion would take place, induced by the adiabatic STT [23]. This evidences that the adiabatic STT is fundamentally different from the field-induced force over domain walls. Conversely, the non-adiabatic STT, whose magnitude is determined by the parameter β_{ST}, produces a field-like effect over domain walls.

In 2009, J.-P. Adam and collaborators [24] observed the STT-driven steady flow of domain walls in perpendicularly magnetized (Ga,Mn)As. These studies clearly evidenced the importance of the non-adiabatic STT on domain wall motion. Their experiments involved the combined application of current and field, showing a linear change in the velocity as a function of the applied field for a given current in the steady flow regime, as predicted by 2.26 with an effective applied field given by 6.1. However, a study of combined field- and STT-driven dynamics in the thermally activated creep regime was still lacking.

Creep regime

In 2011, J. Ryu and collaborators [197] proposed a theory in order to model the combined effect of applied field and STT on domain wall motion in the creep regime, for relatively small driving forces and below the Walker breakdown threshold, i.e. for

$$\left|\mu_0 H + \frac{\beta_{\mathrm{ST}} - \alpha}{\gamma \Delta} \frac{g \mu_B P}{2 e M_s} J\right| < \mu_0 H_w \tag{6.6}$$

in accordance with (2.44). They thus formulated an expression for the effective field which may be written as [157, 198]

$$\mu_0 H_{\mathrm{eff}}(H, J) = \mu_0 H + \epsilon J + \eta J^2 \ , \tag{6.7}$$

valid for relatively low current densities. In this model, ϵ is associated to the non-adiabatic STT and equal to ϵ_{st}, equation (6.4). The additional quadratic term ηJ^2 proposed by J. Ryu and collaborators results from the adiabatic STT.

The above expression has been shown to successfully describe the thermally activated domain wall motion in metallic thin films with perpendicular anisotropy in several recent studies [156, 157, 198]. In these reports, the dynamics resulting from the simultaneous application of H and J is shown to be consistent with the creep law $\ln v \sim H_{\mathrm{eff}}^{-1/4}$ with an effective field H_{eff} given by (6.7). The reported values for ϵ and η are, respectively, in the range 10^{-2}-10^{-4} mT/(GA/m^2) and 10^{-3}-10^{-5} mT/(GA/m^2)^2. However, several open questions remain; particularly, this expression is yet to be tested in diluted magnetic semiconductors where STT is particularly efficient and thus ϵ is relatively high.

According to the discussion presented above, the effect of simultaneously applying field and current may be modeled by simply considering that an effective field $H_{\mathrm{eff}}(H, J)$ is applied. In this framework, in analogy to (2.75) and (2.76), the creep law may be written as

$$v(H, J) = v_d \exp\left(-\frac{E_p(H, J)}{k_B T}\right) \tag{6.8}$$

with

$$E_p(H, J) = k_B T_d \left[\left(\frac{H_{\mathrm{eff}}(H, J)}{H_d}\right)^{-\mu} - 1\right] \ . \tag{6.9}$$

Several questions, which we shall try to address in this chapter, arise from these expressions.

First, let us consider the case of $H = 0$, i.e. purely STT-driven creep motion. As we have shown in figure 2.21(b) [27], current-driven domain wall motion in perpendicularly magnetized (Ga,Mn)(As,P)/(Ga,Mn)As is consistent with $\ln v \sim J^{-1/4}$, what results inconsistent with the existence of a significative quadratic term ηJ^2 in $H_{\mathrm{eff}}(H, J)$. This suggests that the expression (6.3) rather than (6.7) correctly describes the experimental results. The reason for this could be that $\epsilon J \gg \eta J^2$ in the explored J-range, what is probable due to the high efficiency of non-adiabatic STT [24], or simply that (6.7) is not valid in the studied case. As the Joule heating is expected to produce a temperature rise $\sim J^2$ which strongly affects thermally activated dynamics [164], its effect should be carefully analyzed because it could be the origin of the observed consistence between experiments in metallic thin films and the existence of a quadratic term in $H_{\text{eff}}(H, J)$.

A second key issue that arises from the description of the creep regime in terms of an effective field $H_{\text{eff}}(H, J)$ is the impact of the driving mechanism on the depinning parameters H_d, T_d and v_d. If the driving force is completely described by $H_{\text{eff}}(H, J)$ and expressions (6.8) and (6.9) are valid, then these three parameters should be equivalent for field-driven, STT-driven, or combined field- and STT-driven motion. However, this hypothesis could be incorrect as different driving mechanisms may probably impact on the effective pinning energy barrier $E_p(H, J)$ in different ways.

In the following section we shall describe our methods for domain wall velocity measurements in (Ga,Mn)(As,P)/(Ga,Mn)As. The results of these measurements will be presented and discussed later, in section 6.3. There, we shall address the open questions that we have just proposed by comparing the driving forces due to field and current and analyzing the creep regime dynamics observed when applying field and current separately or simultaneously.

6.2 Methods for velocity measurements

Let us now describe the key features of the measurement methods that permitted us to study the joint effect of field and current on domain wall motion in a perpendicularly magnetized sample of (Ga,Mn)(As,P)/(Ga,Mn)As. All the measurements presented in this chapter were performed using the PMOKE microscope installed at LPS. Firstly, we will show the shape and simultaneity of the applied field and current pulses. Secondly, we shall describe the measurement of domain wall velocities, with the particularity that we evaluate the displacement of two domain walls, the left and right walls, which react differently to the applied stimuli. This particular method will permit us to address the open questions that we have mentioned in the last section.

6.2.1 Shape and simultaneity of applied pulses

In figure 6.2 we show two normalized pulses which were simultaneously measured, corresponding to a field and a current pulse. The field pulse corresponds to the voltage measured in a resistance of $50\,\Omega$ connected in series with the field coil, as explained in section 3.2.4 and illustrated in figure 3.7(a). The applied voltage is $V_h = 120\,\text{V}$ and the pulse time is $\Delta t_{ap} = 2\,\mu\text{s}$. As the rise time is $t_{rise} \approx 0.6\,\mu\text{s}$, the considered effective pulse time is $\Delta t = \Delta t_{ap} - t_{rise} = 1.4\,\mu\text{s}$. The corresponding applied field is $\mu_0 H = 8.5\,\text{mT}$. The current pulse was applied directly in an oscilloscope in order to check its simultaneity with the field

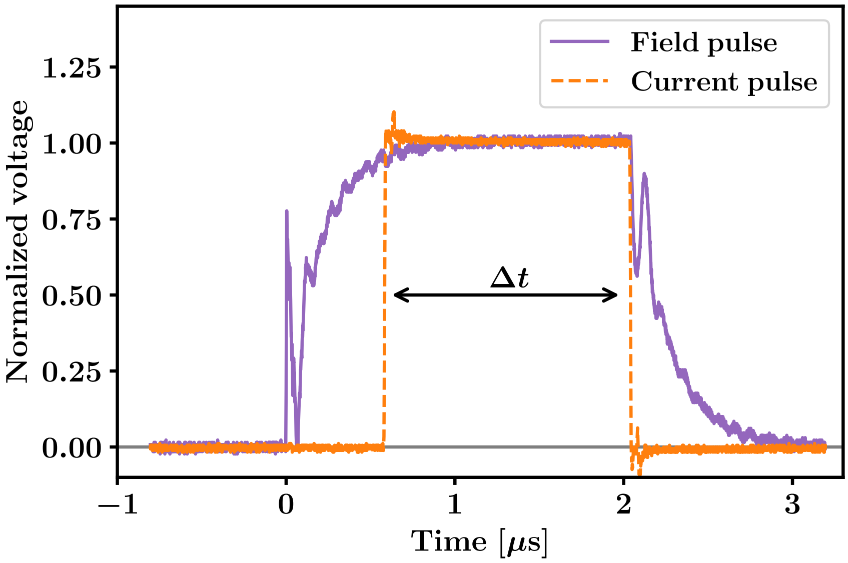

Figure 6.2: **Shape and simultaneity of field and current pulses.** Normalized voltage corresponding to simultaneously measured field and current pulses. The field pulse corresponds to an applied voltage $V_h = 120\,\mathrm{V}$ (field magnitude $\mu_0 H = 8.5\,\mathrm{mT}$) and a pulse time $\Delta t_{ap} = 2\,\mu\mathrm{s}$. The current pulse corresponds to an applied voltage $V_j = 70\,\mathrm{V}$ (current density $J = 7.9\,\mathrm{GA/m^2}$) and a pulse time $\Delta t = 1.4\,\mu\mathrm{s}$, with a delay of $0.6\,\mu\mathrm{s}$ in order to consider the rise time of the field pulse and achieve a good simultaneity.

pulse. As in the experiments this pulse is directly applied on the sample, which behaves as a resistive load, current pulses have a rise time which is negligible at this scale. The shown pulse corresponds to an applied voltage $V_j = 70\,\mathrm{V}$ and a pulse time $\Delta t = 1.4\,\mu\mathrm{s}$ applied with a delay of $0.6\,\mu\mathrm{s}$ in order to consider the rise time of the field pulse and obtain a good simultaneity. The corresponding current density is $J = 7.9\,\mathrm{GA/m^2}$.

The shown pulses correspond to the lowest pulse times that were applied in the experiments discussed in this chapter, as for shorter pulses the rise time of the field coil may considerably affect the measured velocities. In contrast, the domain wall displacement during the $0.6\,\mu\mathrm{s}$ rise time is negligible for $\Delta t_{ap} \geq 2\,\mu\mathrm{s}$ with respect to the displacement due to the stationary field and current values during $\Delta t = \Delta t_{ap} - t_{rise}$.

The same rise time was observed for applied voltages V_h ranging from 5 to 200 V, i.e. from $\mu_0 H = 0.36$ to $14.2\,\mathrm{mT}$, using a unique coil and a resistance of $R = 50\,\Omega$ connected in series. We have used the setup illustrated in figure 3.6(a) for V_h values ranging from 5 to 50 V, and the setup illustrated in figure 3.7(a) for V_h values ranging from 40 to 200 V. This corresponds to all the measurements with applied field presented in this chapter except for some low field measurements which were performed with the big coil for $\Delta t \geq 1\,\mathrm{s}$ with no current. These measurements were used for calibrating the applied field magnitude as explained in section 3.2.4.

The explored range for current injection goes from $V_j = 2$ to 98 V, i.e. from $J = 0.23$ to

11.1 GA/m^2. In this range, and with the corresponding pulse times, approximately ranging from $\Delta t = 900\,\mathrm{ms}$ at $J = 0.23\,\mathrm{GA/m^2}$ to $\Delta t = 1.4\,\mu\mathrm{s}$ at $J \geq 6.2\,\mathrm{GA/m^2}$, Rebeca Díaz Pardo and Vincent Jeudy have verified that Joule heating is negligible [182] (see section 3.4).

6.2.2 Left and right domain wall velocities

In order to perform a fruitful analysis of the joint effect of field and current on domain wall dynamics, we have simultaneously evaluated the displacement of two "different" domain walls. In figure 6.3, we show PMOKE microscopy images obtained at $T = 55\,\mathrm{K}$ in our square-shaped sample, already described in section 3.4. The direction of current flow is always horizontal, and the magnetic field direction is normal to the sample.

The first step for performing wall motion measurements is to nucleate two vertical domain walls, as shown in figure 6.3(a). In order to obtain this state, we proceed as follows. We start with a saturated state with $\odot$ magnetization (light in the figure) and apply a magnetic field in the $\otimes$ direction and a current in the $\leftarrow$ direction (from right to left) in order to nucleate a $\otimes$ (dark) domain in the left side. Then we apply successive current pulses in order to move the nucleated domain wall towards the right side. Finally, we simultaneously apply a field pulse in the $\odot$ direction and a current pulse in the $\leftarrow$ direction in order to nucleate a new domain of $\odot$ (light) magnetization in the left side. The obtained vertical domain walls are thus perpendicular to the current density direction. Both domain walls are subject to an equivalent driving force towards the right direction due to electron flow if the current density is applied in the $\leftarrow$ direction. In contrast, the application of a magnetic field would favor the light or the dark domains, thus generating opposite forces over each of the two domain walls.

In figure 6.3(b), we show the resulting configuration after applying several equivalent simultaneous field and current pulses, similar to those illustrated in figure 6.2, over the configuration shown in (a). In particular, 10 successive pulses of $\Delta t = 1.4\,\mu\mathrm{s}$ were applied between (a) and (b), with field and current magnitudes of $\mu_0 H = 2.1\,\mathrm{mT}$ and $J = 4.5\,\mathrm{GA/m^2}$. While the current density is applied from right to left, inducing the movement of both domain walls towards the right, the field favors the light domains, inducing the approximation of both walls between each other.

In figure 6.3(c), we show the differential image resulting from substracting (a) from (b). This clearly evidences the different mean displacements experienced by the left and the right domain walls, which we define as Δu_L and Δu_R, respectively. Consequently, the left and right domain wall velocities are defined as

$$v_L = \frac{\Delta u_L}{\Delta t} \tag{6.10}$$

and

$$v_R = \frac{\Delta u_R}{\Delta t}\ , \tag{6.11}$$

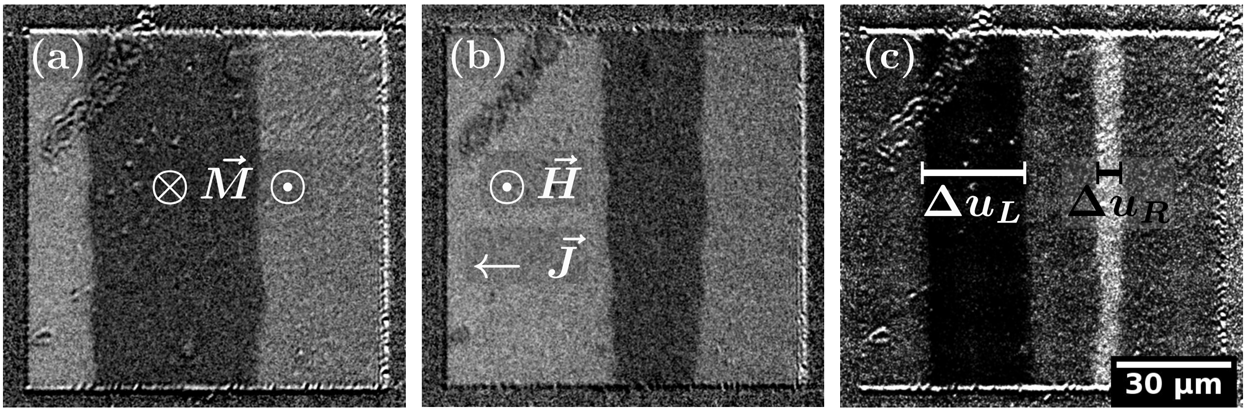

Figure 6.3: **Measurement of left and right domain wall displacements under simultaneous field and current pulses.** (a) PMOKE image of the square-shaped sample with three rectangular domains limited by two vertical domain walls. (b) Resulting image after successively applying 10 simultaneous field and current pulses of $\Delta t = 1.4\,\mu$s and amplitudes $\mu_0 H = 2.1\,\mathrm{mT}$ and $J = 4.5\,\mathrm{GA/m^2}$ over the initial state shown in (a). The current density is applied from right to left and the field favors the light domain, as indicated. (c) Differential image resulting from the substraction of image (b) from image (a) which permits us to measure the mean displacements of the left and the right domain walls, Δu_L and Δu_R, respectively. In this case, both walls have moved towards the right and therefore, both Δu_L and Δu_R are positive.

respectively. According to the relative magnitudes of $\mu_0 H$ and J, Δu_R and v_R may be positive, negative, or even zero if both driving forces are balanced. Conversely, Δu_L and v_L will always be positive for the considered directions of applied field and current.

6.3 Results and discussion

In the following we shall present and discuss our experimental results. These studies are divided in three parts. Firstly, in 6.3.1, we will analyze the conditions in which the field- and current-driven forces over domain walls are balanced in order to establish a comparison between them, at different temperatures. To do so, we will analyze the right wall motion, which in our experimental conditions is subject to opposite forces due to field and STT. Secondly, in 6.3.2, we will present the domain wall velocity curves corresponding to field-driven dynamics on the one hand and current-driven dynamics on the other hand. Hence, we shall analyze and compare the thermally activated creep regimes resulting from each of the two driving forces. Finally, in 6.3.3 we will present our experimental studies on the simultaneous field- and STT-driven domain wall motion. Taking as starting point the results shown in 6.3.1 and 6.3.2, we shall analyze the combined field- and STT-driven dynamics in terms of an effective field $H_{\mathrm{eff}}(H, J)$ and study the impact of the driving forces on H_d, T_d and v_d.

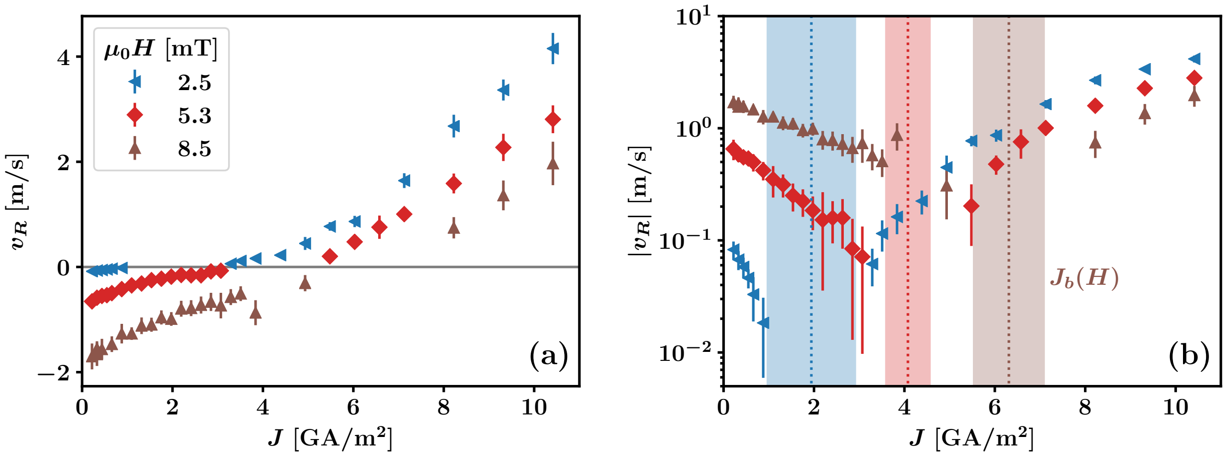

Figure 6.4: **Right domain wall velocity as a function of the current density at $T = 55\,\mathrm{K}$ for different applied fields.** (a) v_R vs. J for three fixed $\mu_0 H$ values´. (b) $|v_R|$ in logarithmic scale vs. J corresponding to the same data. We indicate the ranges $J_b(H)$ at which no displacement is observed. For $\mu_0 H = 2.5\,\mathrm{mT}$, $J_b = (1.9 \pm 0.9)\,\mathrm{GA/m^2}$; for $\mu_0 H = 5.3\,\mathrm{mT}$, $J_b = (4.1 \pm 0.5)\,\mathrm{GA/m^2}$; and for $\mu_0 H = 8.5\,\mathrm{mT}$, $J_b = (6.3 \pm 0.8)\,\mathrm{GA/m^2}$.

6.3.1 Balance of field- and STT-driven forces

Let us now analyze the motion of the right domain wall, whose velocity is measured as explained in 6.2.2 under the application of simultaneous field and current pulses. In figure 6.4 we plot right wall velocity v_R measurements as a function of J for three fixed applied fields $\mu_0 H$ of 2.5, 5.3 and 8.5 mT, at $T = 55\,\mathrm{K}$. As we have discussed above, this domain wall velocity results from the competition between STT, which favors a displacement with positive velocity, and field, which favors motion in the negative direction.

As shown in figure 6.4(a), for each of the applied fields there exists a region of negative velocities, i.e. where the driving force induced by the applied field overcomes the force induced by the STT. For sufficiently high current density J, the inverse situation occurs and $v_R > 0$. Accordingly, there must exist a particular J value for each fixed $\mu_0 H$ where $v_R = 0$. Indeed, for each of the considered $\mu_0 H$ values there exists a range of J for which no right domain wall displacement is observed in our experimental conditions.

Figure 6.4(b) shows the absolute value of v_R in logarithmic scale as a function of J, corresponding to the same data plotted in (a). There, we indicate with shaded areas the ranges $J_b(H)$ for which we do not observe any right wall displacement at each fixed $\mu_0 H$. The center values of these ranges are indicated as vertical dotted lines. As evidenced, for each fixed field, $|v_R|$ falls abruptly as a function of J when approaching $J_b(H)$.

The conditions of field and current that satisfy $v_R = 0$ correspond to a balance of the field- and current-driven forces over domain walls. Thereby, analyzing these conditions permits to establish a comparison between the magnitude of these two stimuli. Particularly,

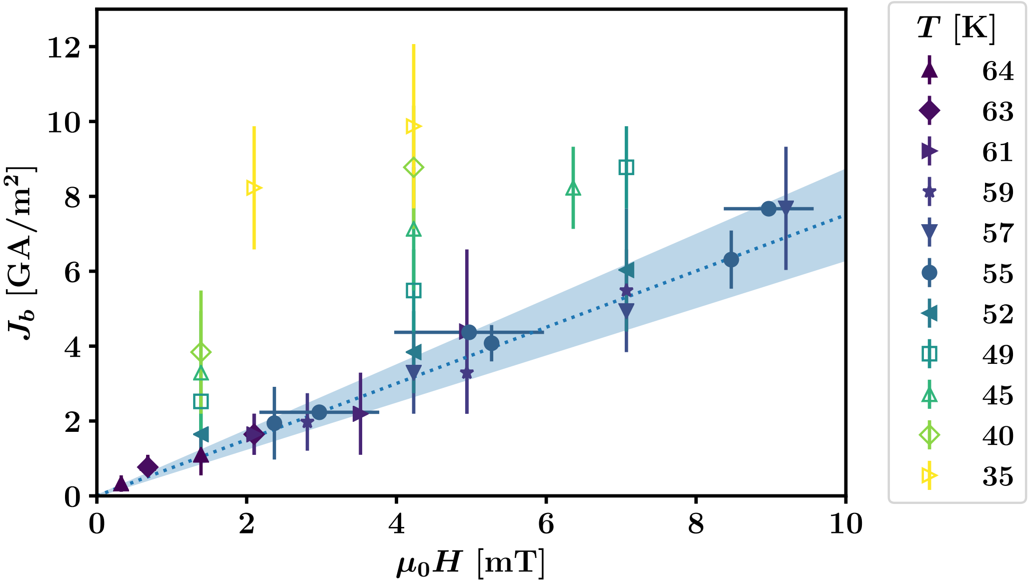

Figure 6.5: **Conditions of balance of the forces induced by field and current.** J_b as a function of $\mu_0 H$ at different temperatures. Full symbols correspond to $T \geq 52\,\mathrm{K}$, empty symbols to $T < 52\,\mathrm{K}$. We indicate the mean slope $\overline{S} = (0.8 \pm 0.1)\,(\mathrm{GA/m^2})/\mathrm{mT}$ obtained for $T \geq 52\,\mathrm{K}$.

for a given $J = J_b(H)$ that balances an applied field $\mu_0 H$, we may deduce that the effective field $\mu_0 H_{\mathrm{eff}}(0, J)$ is equal to $\mu_0 H$. Repeating this analysis at different conditions may shade light on the $\mu_0 H_{\mathrm{eff}}(0, J)$ dependence.

In figure 6.5 we plot the field-dependence of J_b at different temperatures ranging from 35 to 64 K. Note that the highest T is very close to the Curie temperature $T_C = 65\,\mathrm{K}$. If equation 6.3 is valid, then a proportionality between J_b and H is expected, as $H_{\mathrm{eff}}(-H, J_b) = 0$ in order to satisfy $v_R = 0$. Note that, as the applied field pushes the right domain wall towards the left (negative) direction, for this wall we consider $\mu_0 H_{\mathrm{eff}} = \mu_0 H_{\mathrm{eff}}(-H, J)$. In this context, we may write

$$J_b = \frac{1}{\epsilon}\mu_0 H \ . \tag{6.12}$$

From a first glance at the figure we may deduce that if such a proportionality exists, it changes monotonically as a function of temperature, with a decreasing $1/\epsilon$ value for increasing T. Additionally, for all temperatures above $\approx 50\,\mathrm{K}$, the $1/\epsilon$ factor appears to be unique.

In order to test this scenario, we have performed linear fits of the type $y = I + Sx$ with $x = \mu_0 H$ and $y = J_b$ for each temperature. In all cases, the observed $J_b(H)$ dependence may be fairly well described by this fitting relation. In figure 6.6 we plot the obtained slope S and intercept I as a function of the reduced temperature T/T_C.

Let us first analyze the fitting parameters obtained for $T \geq 52\,\mathrm{K}$ (full circles in figure

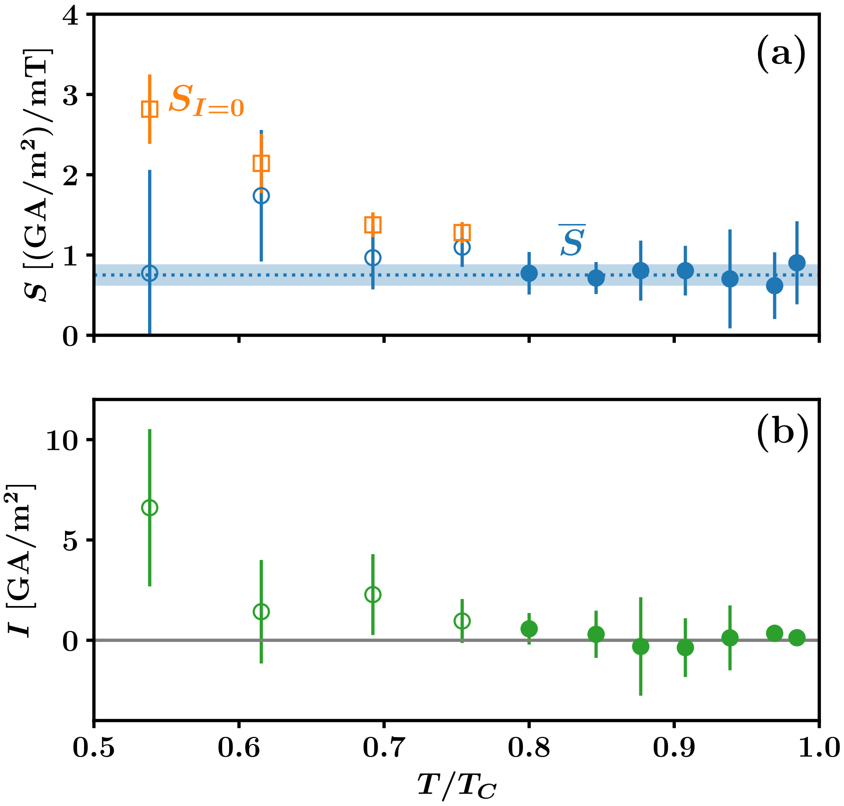

Figure 6.6: **Slope and intercept of the J_b vs. $\mu_0 H$ fits as a function of T/T_C.** Full symbols correspond to $T \geq 52\,\mathrm{K}$ while empty symbols to $T < 52\,\mathrm{K}$. (a) Slope S. Full and empty circles were obtained by fitting both the slope and the intercept, i.e. $J_b = I + S\,\mu_0 H$, while empty squares were obtained with the constraint $I = 0$, i.e. $J_b = S\,\mu_0 H$. The mean value $\overline{S} = (0.8 \pm 0.1)\,(\mathrm{GA/m^2})/\mathrm{mT}$, corresponding to $T \geq 52\,\mathrm{K}$ (full circles), is indicated as a shaded horizontal region. (b) Intercept I. For $T \geq 52\,\mathrm{K}$, $I \simeq 0$; therefore, in this range the obtained data satisfies $J_b = \overline{S}\,\mu_0 H$.

6.6). The slopes, shown in (a), are rather constant and are well described by a mean value $\overline{S} = (0.8 \pm 0.1)\,(\mathrm{GA/m^2})/\mathrm{mT}$. Furthermore, the intercepts I, shown in (b), are practically equal to zero in this temperature range. Consequently, the obtained data may be described by (6.12) with $\epsilon = 1/\overline{S} = (1.3 \pm 0.2)\,\mathrm{mT}/(\mathrm{GA/m^2})$. We may therefore claim that, for $T \geq 52\,\mathrm{K}$ and when both driving forces are balanced, there exists a well defined proportionality between applied current and field which spans over all the experimentally accessible range of J and $\mu_0 H$. The found proportionality factor ϵ is two to four orders of magnitude higher than previously found values for metallic thin films [156, 157, 186, 198], what supports the fact that the non-adiabatic STT is much more efficient in diluted magnetic semiconductors [24, 26].

For $T < 52\,\mathrm{K}$, the lower thermal activation results on wider ranges of undetectable right domain wall motion and therefore wider errorbars for $J_b(H)$ (see figure 6.5). Furthermore, as we have pointed out above, the $J_b/\mu_0 H$ factor increases as T decreases, what drives the J_b

values closer to the experimental limit of $\approx 11\,\mathrm{GA/m^2}$. For these reasons, the uncertainties on the determination of S and I in this range are larger (see empty circles in figure 6.6). Despite this fact, both S and I appear to grow with decreasing temperature. The nonzero values of I suggest that even for $H = 0$ there exists a finite J_b at which the effective force is zero. This result is unphysical, what suggests that the chosen fitting relation might be inappropriate for $T < 52\,\mathrm{K}$. However, it could be an evidence of an increase of the effective pinning at low temperatures which strongly affects current-driven rather than field-driven domain wall motion. Note that the increase of effective pinning for decreasing temperatures is expected independently of the driving force nature, as we have thoroughly studied for field-driven domain walls in GdFeCo (see section 4.2.4). The additional enhance that we observe for current-driven motion could be originated by the phenomena of domain wall faceting [27], which results in a lower effective force over the whole domain wall due to its non-isotropic nature.

As the uncertainties in I for $T < 52\,\mathrm{K}$ are large with respect to its mean values, we may consider that $I = 0$ in order to describe the $J_b(H)$ dependence in terms of a proportionality. Adding this constraint, we obtain the factors $S_{I=0}$ which are shown as empty squares in figure 6.6(a). As noted above, these values decrease with increasing temperature, approaching the $\bar{S}$ value obtained for $T \gtrsim 52\,\mathrm{K}$. Hence, in terms of (6.12), ϵ decreases with decreasing temperature from $(1.3 \pm 0.2)\,\mathrm{mT/(GA/m^2)}$ at $T \geq 52\,\mathrm{K}$ ($T/T_C \geq 0.80$) to $(0.36 \pm 0.06)\,\mathrm{mT/(GA/m^2)}$ at $T = 35\,\mathrm{K}$ ($T/T_C = 0.54$).

Let us now analyze these ϵ values in terms of the physical quantities which, according to the micromagnetic 1D model, determine the proportionality between the forces induced by field and current. Expressions (6.4) and (6.5) indicate, respectively, the expected values for ϵ in the steady and asymptotical precessional regimes. The material- and temperature-dependent quantities are β_{ST}, α, Δ, P and M_s. The gyromagnetic ratio γ and the g-factor are mutually dependent and, for simplicity and due to its relatively slight variations for different materials [147], we consider the values that correspond to free electrons, i.e. $g = 2.0$ and $\gamma = g\mu_B/\hbar = 1.76\times10^{11}\,\mathrm{s/T}$. Using $\beta_{\mathrm{ST}} = \alpha = 0.25$ (typical values for (Ga,Mn)As according to references [24, 26, 81]), $\Delta = 1.5\text{-}3.5\,\mathrm{nm}$ [81], $P = 0.3\text{-}0.4$ [25, 26] and $M_s = 10\,\mathrm{kA/m}$ [26], we obtain $\epsilon_{st} = 0.9\text{-}1.6\,\mathrm{mT/(GA/m^2)}$ and $\epsilon_{asp} = 16\text{-}28\,\mathrm{mT/(GA/m^2)}$.

As evidenced, the estimated value of ϵ_{st} is in very good agreement with the experimentally obtained $\epsilon = (1.3 \pm 0.2)\,\mathrm{mT/(GA/m^2)}$ at $T \geq 52\,\mathrm{K}$. Conversely, the estimated ϵ_{asp} is much larger. This suggests that the observed right domain walls persist in the steady regime for the conditions of force balance at which $v_R = 0$, meaning that the domain wall's internal magnetization does not precess in these conditions. However, if we estimate the Walker field from the same physical quantities using equation (2.30) with the film thickness $t = 4\,\mathrm{nm}$, we obtain $\mu_0 H_w = 0.8\text{-}1.1\,\mathrm{mT}$. According to (6.6) and since we consider that $\beta_{\mathrm{ST}} \simeq \alpha$, this result is inconsistent with the existence of a steady regime of motion for all the $J_b(H)$ values shown in figure 6.5. This inconsistency calls for further studies in order to elucidate the internal state of domain walls in these experimental conditions. However, as the used physical quantities were not obtained strictly for the studied sample, the actual values might differ. Thereby, further studies in this issue require a more reliable determination of relevant

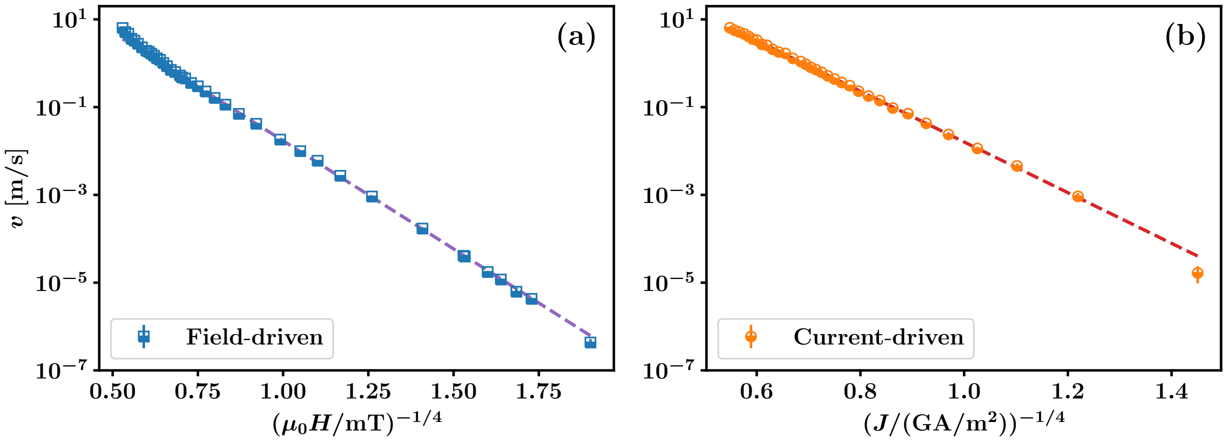

Figure 6.7: **Field-driven and STT-driven domain wall velocity curves in the creep regime at $T = 55\,\mathrm{K}$.** (a) Field-driven v in logarithmic scale vs. $(\mu_0 H/\mathrm{mT})^{-1/4}$. The fit of $\ln(v/(\mathrm{m/s}))$ vs. $(\mu_0 H/\mathrm{mT})^{-1/4}$ for $(\mu_0 H/\mathrm{mT})^{-1/4} > 0.65$, with resulting intercept $I_h = 7.28 \pm 0.03$ and slope $S_h = -11.35 \pm 0.03$, is shown as a dashed line. (b) Current-driven v in logarithmic scale vs. $(J/(\mathrm{GA/m^2}))^{-1/4}$. The fit of $\ln(v/(\mathrm{m/s}))$ vs. $(J/(\mathrm{GA/m^2}))^{-1/4}$ in all the J range, with intercept $I_j = 9.17 \pm 0.06$ and slope $S_j = -13.3 \pm 0.09$, is shown as a dashed line.

physical quantities.

Another feature of the experimentally found ϵ is its temperature dependence, already described above. The observation of a constant value for $T/T_C \geq 0.80$ and its decrease with decreasing temperatures for $T/T_C < 0.80$ is in good agreement with previous experimental studies which have found a similar temperature dependence of the factor P/M_s [25, 26] (note that, according to (6.4) and (6.5), $\epsilon \sim P/M_s$). This result suggests that the temperature dependence of ϵ is dominated by this quantity in our sample and hence, other relevant quantities as β_{ST}, α and Δ present a relatively smooth temperature dependence.

6.3.2 Field-driven and STT-driven creep regimes

In the following, we shall present and analyze the measured field-driven and STT-driven domain wall velocity curves, obtained at $T = 55\,\mathrm{K}$ by applying these two stimuli separately. In figure 6.7, we show these curves in creep-type scales, with the critical exponent $\mu = 1/4$. For the field-driven motion (a), we plot the velocity v in logarithmic scale vs. $(\mu_0 H/\mathrm{mT})^{-1/4}$. For the STT-driven motion (b), we plot v in logarithmic scale vs. $(J/(\mathrm{GA/m^2}))^{-1/4}$.

As evidenced in the figure, both field-driven and STT-driven domain wall dynamics are very well described by the creep law in a velocity range spanning over 6 to 7 orders of magnitude, what supports their belonging to the quenched Edwards-Wilkinson universality class. For the field-driven motion, we have performed a fit of the type $y = I_h + S_h\,x$

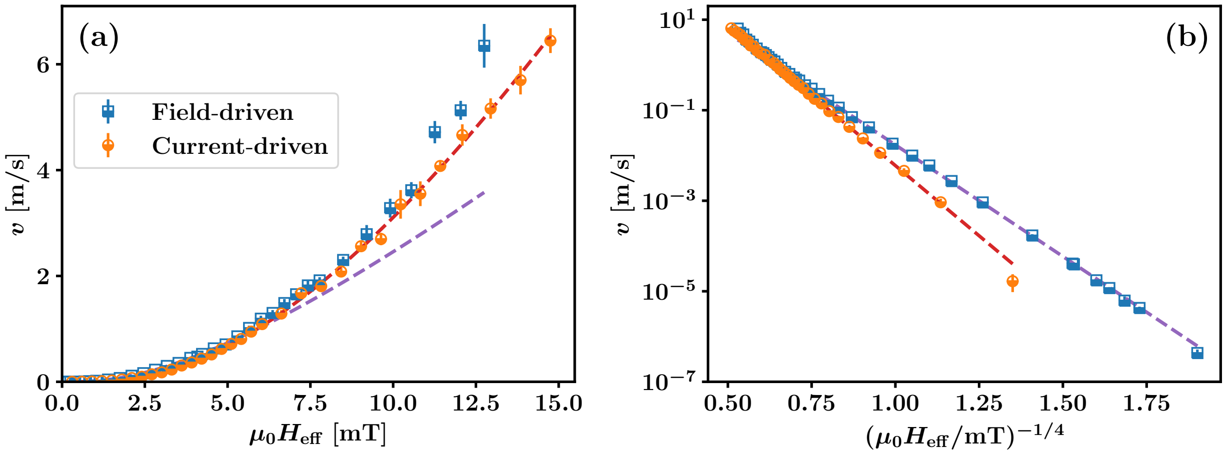

Figure 6.8: **Field-driven and STT-driven domain wall velocity curves as a function of the effective field at $T = 55\,\mathrm{K}$.** For field-driven dynamics, $\mu_0 H_{\text{eff}} = \mu_0 H$, while for current-driven dynamics $\mu_0 H_{\text{eff}} = \epsilon J$ with $\epsilon = 1.3\,\mathrm{mT}/(\mathrm{GA/m^2})$. Corresponding creep fits are shown as dashed lines. (a) v in linear scale vs. $\mu_0 H_{\text{eff}}$. (b) v in logarithmic scale vs. $(\mu_0 H_{\text{eff}}/\mathrm{mT})^{-1/4}$.

with $x = (\mu_0 H/\mathrm{mT})^{-1/4}$ and $y = \ln(v/(\mathrm{m/s}))$, for $x > 0.65$. For lower x values, i.e. for $\mu_0 H > 5.6\,\mathrm{mT}$, we observe a loss of linearity characterized by an excess velocity already observed in other domain wall velocity curves close to the depinning [17]. From this fit we obtained $I_h = 7.28 \pm 0.03$ and $S_h = -11.35 \pm 0.03$. For the current-driven motion, we fitted $y = I_j + S_j\,x$ with $x = (J/(\mathrm{GA/m^2}))^{-1/4}$ and $y = \ln(v/(\mathrm{m/s}))$, obtaining $I_j = 9.17 \pm 0.06$ and $S_j = -13.3 \pm 0.09$. These two fits are shown as dashed lines in figures 6.7(a) and (b).

The fact that the STT-driven domain wall dynamics are well described by the creep scaling relation $\ln v \sim J^{-1/4}$ over several orders of magnitude in v supports the hypothesis that the corresponding effective driving force is proportional to J. This hypothesis corresponds to the proportionality between field and current expressed by equation (6.3) for the effective field $\mu_0 H_{\text{eff}}$ which, in the case of current-driven motion, reads $\mu_0 H_{\text{eff}}(0, J) = \epsilon J$. Conversely, if there existed non-negligible non-linear terms in J, the relation $\ln v \sim J^{-1/4}$ would not prevail if $\ln v \sim H_{\text{eff}}^{-1/4}$.

The study of the conditions of balance of the driving forces induced by field and STT that we have presented in 6.3.1 has allowed us to experimentally obtain $\epsilon = (1.3 \pm 0.2)\,\mathrm{mT}/(\mathrm{GA/m^2})$ for $52\,\mathrm{K} \leq T < T_C = 65\,\mathrm{K}$. Therefore, we may test the equivalence between the field-driven and the current-driven creep regimes in terms of equations (6.8) and (6.9), with the effective field given by (6.3). In figure 6.8, we plot the domain wall velocity v vs. the effective field $\mu_0 H_{\text{eff}}$ for the field-driven and the STT-driven motion. In the former case, the effective field is simply $\mu_0 H$, while in the latter $\mu_0 H_{\text{eff}} = \epsilon J$ with $\epsilon = 1.3\,\mathrm{mT}/(\mathrm{GA/m^2})$.

The plot in linear scale of v vs. $\mu_0 H_{\text{eff}}$ shown in figure 6.8(a) evidences that the independently obtained ϵ factor satisfactorily describes the relation between $\mu_0 H$ and J.

The two experimental curves collapse onto a single curve for velocities of the order $v \sim 1\,\mathrm{m/s}$, what results consistent with the relation (6.3) and strongly supports the result $\epsilon = (1.3 \pm 0.2)\,\mathrm{mT/(GA/m^2)}$ previously obtained at completely different conditions, as explained in 6.3.1. This is one of the main results of this chapter: using two different methods, we have found strong evidences for the validity of (6.3). Furthermore, we have quantified the factor ϵ obtaining one unique value which is consistent both with the balance of the forces induced by field and STT and with the relation between field-driven and current-driven dynamics for $0.1\,\mathrm{m/s} < v < 10\,\mathrm{m/s}$.

However, the creep-type plot shown in figure 6.8(b) evidences that the collapse of field-driven and current-driven velocity curves does not hold in all the velocity range. While for high velocities the description of both curves in terms of $\mu_0 H_{\mathrm{eff}}$ is good, the low-velocity range shows that the corresponding creep fits are different, what results inconsistent with equations (6.8) and (6.9). The ϵ value needed for the coincidence of $\mu_0 H$ and ϵJ at $v \sim 10^{-3}\,\mathrm{m/s}$ is $\approx 0.9\,\mathrm{mT/(GA/m^2)}$. Nevertheless, there is no unique ϵ value that permits the collapse of the two curves in all the velocity range: an ϵ value of $\approx 0.9\,\mathrm{mT/(GA/m^2)}$ generates a mismatch of $\approx 3\,\mathrm{mT}$ between $\mu_0 H$ and ϵJ at $v \sim 1\,\mathrm{m/s}$.

The creep fit of $\ln(v/(\mathrm{m/s}))$ vs. $(\epsilon J/\mathrm{mT})^{-1/4}$ for STT-driven motion, obtained using $\epsilon = 1.3\,\mathrm{mT/(GA/m^2)}$, has an intercept $I_j = 9.17 \pm 0.06$ and a slope $(\epsilon/(\mathrm{mT/(GA/m^2)}))^{1/4} S_j = -14.3 \pm 0.6$, where the slope's uncertainty is obtained considering both the uncertainties of S_j and ϵ. Let us now compare these values with the fitting parameters I_h and S_h corresponding to field-driven motion. In order to establish a fruitful comparison, we may consider two creep laws:

$$\ln\left(\frac{v(H,0)}{\mathrm{m/s}}\right) = \ln\left(\frac{v_{d,h}}{\mathrm{m/s}}\right) + \frac{T_{d,h}}{T} - \frac{T_{d,h}}{T} H_d^{1/4} H^{-1/4} \tag{6.13}$$

for field-driven motion, and

$$\ln\left(\frac{v(0,J)}{\mathrm{m/s}}\right) = \ln\left(\frac{v_{d,j}}{\mathrm{m/s}}\right) + \frac{T_{d,j}}{T} - \frac{T_{d,j}}{T} (\epsilon J_d)^{1/4} (\epsilon J)^{-1/4} \tag{6.14}$$

for current-driven motion, where we have introduced the depinning current J_d. As in none of the cases we are able to see evidences of the depinning transition, we cannot obtain the relevant quantities. However, typical velocities at the depinning field for a nominally equivalent sample [27] are roughly between 5 and $10\,\mathrm{m/s}$ (see figure 2.21). This observation permits us to guess that $\mu_0 H_d = (16 \pm 3)\,\mathrm{mT}$. Additionally, we expect ϵJ_d to be in the same range. Consequently, using $(T_{d,h}/T) H_d^{1/4} = S_h$ and $(T_{d,j}/T)(\epsilon J_d)^{1/4} = \epsilon^{1/4} S_j$, we obtain $T_{d,h} = (310 \pm 20)\,\mathrm{K}$ and $T_{d,j} = (390 \pm 30)\,\mathrm{K}$.

According to the above analysis, the different creep fit slopes observed in figure 6.8(b) may be associated mainly to differences in the depinning temperatures $T_{d,h}$ and $T_{d,j}$. As we have extensively discussed throughout this thesis, this quantity corresponds to the magnitude of the effective energy barriers acting collectively over domain walls in the thermally activated creep regime. Our result $T_{d,h} < T_{d,j}$ suggests that energy barriers are effectively larger for current-driven motion, what could be associated to its non-isotropic nature. As

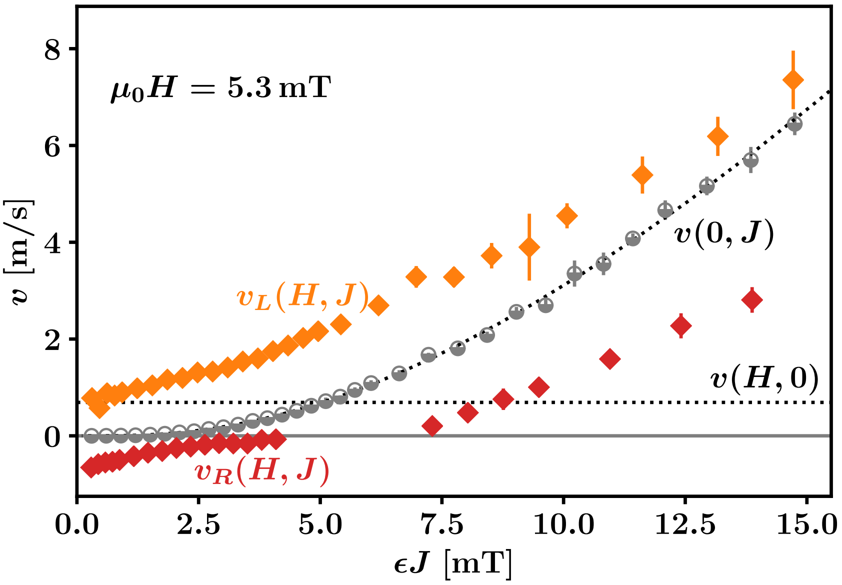

Figure 6.9: **Combined field- and current-driven left and right domain wall dynamics as a function of ϵJ for $\mu_0 H = 5.3\,\mathrm{mT}$ at $T = 55\,\mathrm{K}$.** We indicate as references the current-driven velocity $v(0,J)$ and its corresponding creep fit (dotted curve) and the field-driven velocity $v(H,0)$ for the constant applied field value (horizontal dotted line).

domain wall roughening is more evident for relatively slow motion, current-driven wall faceting is enhanced at low velocities and then the integrated force over walls may be lower, what may effectively impact resulting on a higher T_d. Note that this idea is consistent with the increase of $J_b(H)$ for low temperatures that we have evidenced in section 6.3.1, where we have pointed out its possible relationship with an enhanced pinning for current-driven motion.

6.3.3 Combined field- and STT-driven dynamics

In this third and final part of our studies on domain wall dynamics in the diluted magnetic semiconductor (Ga,Mn)(As,P)/(Ga,Mn)As, we shall present the experimental measurements under combined field and current. In figure 6.9 we plot, for $T = 55\,\mathrm{K}$ and with a fixed applied field $\mu_0 H = 5.3\,\mathrm{mT}$, the left and right domain wall velocity curves as a function of ϵJ, where $\epsilon = 1.3\,\mathrm{mT/(GA/m^2)}$ as determined experimentally for $T \geq 52\,\mathrm{K}$ (see section 6.3.1). We also plot the v vs. ϵJ curve corresponding to current-driven motion, with $H = 0$, i.e. $v(0,J)$. The dotted curve is the creep fit for current-driven motion, already shown in figure 6.8. Additionally, the horizontal dotted line indicated the field-driven domain wall velocity $v(H,0)$ corresponding to $\mu_0 H = 5.3\,\mathrm{mT}$.

As we have already pointed out (see figure 6.4), the right wall velocity is negative for $\epsilon J < \mu_0 H$ and positive for $\epsilon J > \mu_0 H$. In addition, as it is expected due to the opposite action of field with respect to current for this domain wall, $v_R(H,J) < v(0,J)$ in all the J range. On the other hand, the left wall velocity is always positive because both J and H push in the same direction and, as expected, $v_L(H,J) > v(0,J)$ in all the J range. These features are common of all left and right velocity curves with simultaneously applied field and current.

Measurements as the ones shown in figure 6.9 for $\mu_0 H = 5.3\,\mathrm{mT}$ were repeated for different fixed applied fields: $\mu_0 H = 2.5$ and $8.5\,\mathrm{mT}$. Additionally, similar measurements were made as a function of field, for fixed applied currents: $J = 2.3$, 4.5 and $7.9\,\mathrm{GA/m^2}$. As we have discussed in 6.1.2, we are interested on describing the domain wall dynamics under simultaneous field and current in terms of an effective applied field $\mu_0 H_{\mathrm{eff}}(H,J)$. In the following, we will evaluate this description for all our measurements. As the left and right domain walls show different features on their dynamics, we shall present their study separately.

Left wall dynamics

Figure 6.10 shows left domain wall velocity measurements in a creep-type plot, in terms of an effective field defined as $\mu_0 H + \epsilon J$, in accordance with (6.3), with the experimentally determined $\epsilon = 1.3\,\mathrm{mT/(GA/m^2)}$. In (a), we plot the v_L measurements performed with varying H for three different fixed J values and additionally for $J = 0$, namely the field-driven velocity $v(H,0)$. Analogously, in (b) we plot v_L measurements performed with varying J for three different H values and also for $H = 0$, the latter being the current-driven velocity $v(0,J)$.

The simultaneous field- and current-driven left wall velocity for fixed applied current, figure 6.10(a), is rather well described in terms of $\mu_0 H + \epsilon J$, as evidenced by the fairly good collapse of the four shown curves. However, the $v_L(H,J)$ data show a curvature which suggests that there are elements on the underlying physics that are not being considered. The observed curvature could probably be explained by a term of the type ηJ^2, as indicated by equation (6.7). However, the η value needed in order to correct the curvature is of the order $\sim 0.4\,\mathrm{mT/(GA/m^2)^2}$, what would considerably separate the four shown curves. Additionally, as we have pointed out above, the need of a ηJ^2 factor has been verified for metallic films in which ϵ is two to four orders of magnitude lower due to the lower efficiency of non-adiabatic STT. In our sample, conversely, ϵ is high and then any non-linear term in the $\mu_0 H_{\mathrm{eff}}$ vs. J dependence is probably negligible. For these reasons, we consider that the observed v_L vs. $(\mu_0 H + \epsilon J)^{-1/4}$ behavior for fixed J values supports the description in terms of an effective field given by (6.3).

The observed curvature might be associated to the excess velocity of field-driven motion [17] already mentioned above, namely the separation of the $v(H,0)$ dependence from the creep-law behavior at high fields. This is evidenced in figure 6.8 and appears as a slight curvature in the creep-type plot at high fields, similar (but less notorious) than the curvature of the $v_L(H,J)$ vs. $(\mu_0 H + \epsilon J)^{-1/4}$ curves. Additionally, note that we have estimated

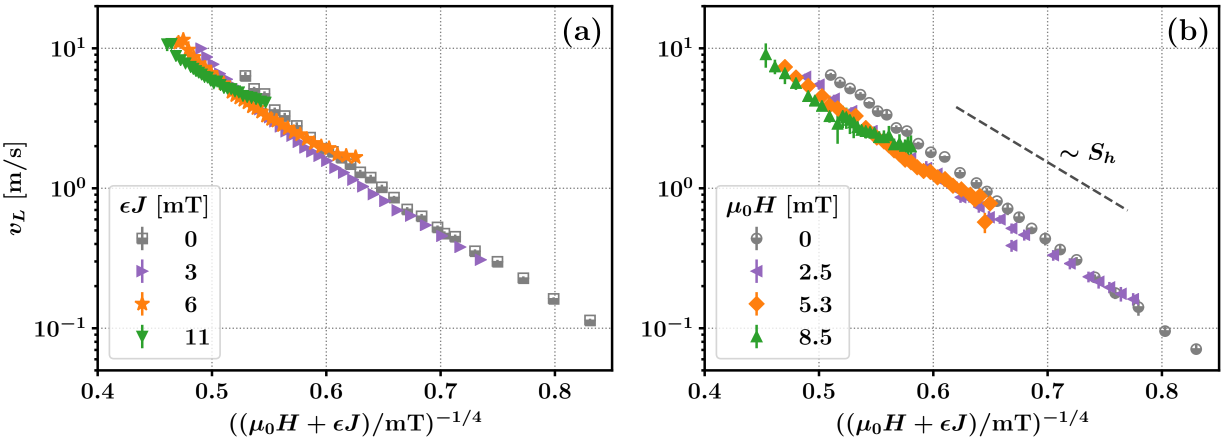

Figure 6.10: **Combined field- and current-driven left domain wall velocity in terms of an effective field at $T = 55\,\mathrm{K}$.** (a) v_L in logarithmic scale as a function of $(\mu_0 H + \epsilon J)^{-1/4}$ for varying H and fixed J values. We also show the field-driven ($J = 0$) curve, i.e. $v(H, 0)$. (b) v_L in logarithmic scale as a function of $(\mu_0 H + \epsilon J)^{-1/4}$ for varying J and fixed H values. We also show the current-driven ($H = 0$) curve, i.e. $v(0, J)$. We indicate as a reference the creep-fit slope S_h corresponding to $v(H, 0)$ for $(\mu_0 H/\mathrm{mT})^{-1/4} > 0.65$.

$\mu_0 H_d = (16 \pm 3)\,\mathrm{mT}$, what corresponds to $(\mu_0 H/\mathrm{mT})^{-1/4} = 0.50 \pm 0.03$. Consequently, the highest velocity range of the shown curves could be affected by the depinning transition, what might induce a lack of coincidence between them in this region. For example, if $\mu_0 H_{d,j} < \mu_0 H_{d,h}$, then the depinning transition could be overcome first by the highest current curve, corresponding to $\epsilon J = 11\,\mathrm{mT}$. In this case, a separation from the creep-law behavior at different values of $(\mu_0 H + \epsilon J)^{-1/4}$ for each of the shown curves in the highest velocity range is possible.

The left wall velocity curves $v_L(H, J)$ for fixed field values, shown in 6.10(b), shows a similar behavior. Accordingly, all curves collapse fairly well on one unique dependence, what also supports the description in terms of the effective field $\mu_0 H_{\mathrm{eff}} = \mu_0 H + \epsilon J$. They show a smaller curvature and present a slightly lower slope in the creep-type plot than the curve corresponding to current-driven dynamics, $v(0, J)$. Remarkably, the observed slope is similar to that corresponding to $v(H, 0)$ for $(\mu_0 H/\mathrm{mT})^{-1/4} > 0.65$, i.e. $S_h = -11.35 \pm 0.03$, as indicated.

The left wall velocity curves that we have measured support the description of domain wall dynamics in terms of the effective field $\mu_0 H + \epsilon J$ in agreement with (6.3). Furthermore, the ϵ value that we have previously obtained, $\epsilon = (1.3 \pm 0.2)\,\mathrm{mT}/(\mathrm{GA/m^2})$ for $T \geq 52\,\mathrm{K}$, is consistent with all the data presented up to now. Note that we have analyzed fundamentally different situations: the balance of field- and current-driven forces over the right domain wall, the comparison between field-driven and current-driven dynamics, and the left domain wall motion, where both field and current push in the same direction. In the following, we will analyze the right wall motion, where field and current push in opposite directions.

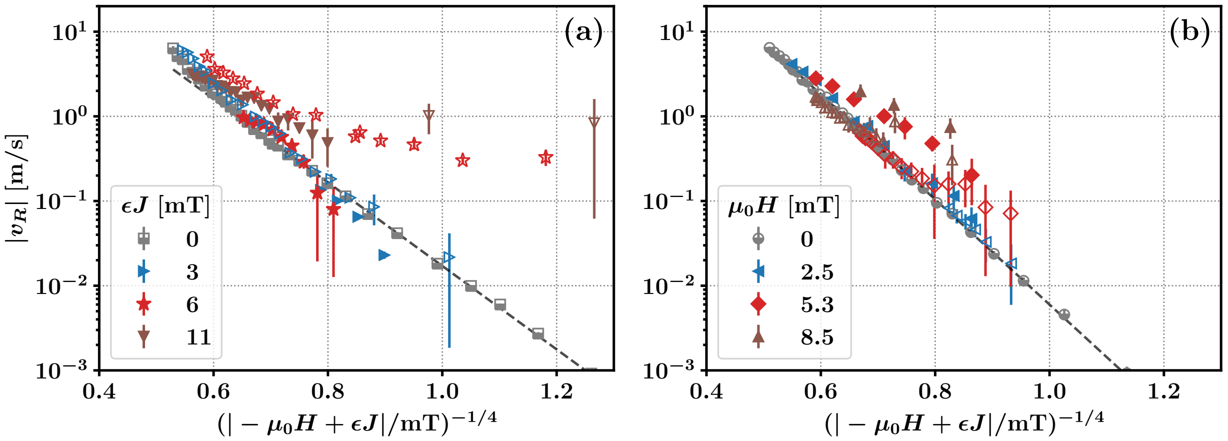

Figure 6.11: **Combined field- and current-driven right domain wall velocity in terms of an effective field at $T = 55\,\mathrm{K}$.** Full symbols correspond to positive velocities, i.e. $v_R > 0$ and $\epsilon J > \mu_0 H$; empty symbols correspond to negative velocities, i.e. $v_R < 0$ and $\epsilon J < \mu_0 H$. (a) $|v_R|$ in logarithmic scale as a function of $|-\mu_0 H + \epsilon J|^{-1/4}$ for varying H and fixed J values. We also show the field-driven ($J = 0$) curve, i.e. $v(H, 0)$, and the corresponding creep fit. (b) $|v_R|$ in logarithmic scale as a function of $|-\mu_0 H + \epsilon J|^{-1/4}$ for varying J and fixed H values. We also show the current-driven ($H = 0$) curve, i.e. $v(0, J)$, and the corresponding creep fit.

Right wall dynamics

The right domain wall velocity $v_R(H, J)$ measurements are shown in creep-type plots in figure 6.11. As field and current push this domain wall in opposite directions, v_R is negative for $\mu_0 H > \epsilon J$. We thus plot the absolute value $|v_R|$ as a function of $|-\mu_0 H + \epsilon J|^{-1/4}$. In the figure, we distinguish between positive v_R, corresponding to $\mu_0 H < \epsilon J$, and negative v_R, corresponding to $\mu_0 H > \epsilon J$. The former are indicated as full symbols while the latter are represented as empty symbols. In (a), we plot these measurements for fixed J values, while in (b) we plot them for fixed H values.

Let us firstly discuss the results for fixed J. For $\epsilon J = 3.0\,\mathrm{mT}$, both negative and positive v_R follow notoriously well the creep-type dependence in accordance with the zero-current curve $v(H, 0)$. However, for higher applied current other elements appear, as evidenced in the figure. The most notorious observation is the difference between measurements corresponding to $v_R > 0$ and to $v_R < 0$. Particularly, $|v_R|_{\mu_0 H > \epsilon J} > |v_R|_{\epsilon J > \mu_0 H}$, and this effect is more notorious for relatively low values of $|-\mu_0 H + \epsilon J|$. Additionally, both curves separate from the zero-current curve $v(H, 0)$, what suggests that the description in terms of the effective field given by (6.3) is no longer valid.

The results for fixed applied field values, figure 6.11(b), show both similarities and differences with the curves for fixed current values. For the lowest value, $\mu_0 H = 2.5\,\mathrm{mT}$, both positive and negative right wall velocities are in very good agreement with the zero-field curve, $v(0, J)$, when described in terms of $|-\mu_0 H + \epsilon J|$. For higher applied fields, the results for $v_R > 0$ and for $v_R < 0$ differentiate in this description, with the particularity that $|v_R|_{\mu_0 H > \epsilon J} < |v_R|_{\epsilon J > \mu_0 H}$, i.e. the observed behavior is roughly opposite to the one illustrated in (a) for fixed J. However, the curvature of the plotted curves for fixed J and for fixed H is consistent between each other. Namely, positive v_R data show a negative concavity while negative v_R data show a positive concavity.

This last observation indicates that the balance of field- and current-induced forces is achieved more abruptly for $\mu_0 H < \epsilon J$, in the limit $\mu_0 H \to (\epsilon J)^-$ (or $\epsilon J \to (\mu_0 H)^+$) than for $\mu_0 H > \epsilon J$, in the limit $\mu_0 H \to (\epsilon J)^+$ (or $\epsilon J \to (\mu_0 H)^-$). This may also be observed in figure 6.4. Remarkably, for fixed $\epsilon J = 6$ and $11\,\mathrm{mT}$ and sufficiently low $|-\mu_0 H + \epsilon J|$ (see figure 6.11(a)), negative velocities tend to stabilize towards an apparently constant $|v_R|$ value. However, the detailed measurement of the region of low $|-\mu_0 H + \epsilon J|$ values was not possible due to the experimental conditions, in which both left and right domain walls move simultaneously at different velocities.

In the region of relatively high velocities, $|v_R|$ generally tends to a linear behavior consistent with the creep law, see figure 6.11. However, the slope of this creep law is in some cases significantly different to the reference slopes corresponding to $v(H, 0)$ or $v(0, J)$, S_h and $\epsilon^{1/4} S_j$ respectively. For fixed J, panel (a), negative velocities (empty symbols) separate more notoriously from the reference slope S_h, towards lower slopes. In contrast, for fixed H, panel (b), positive velocities (full symbols) separate from the reference slope $\epsilon^{1/4} S_j$ while, remarkably, negative velocities for all finite field values are in very good accordance with the reference data for $|-\mu_0 H + \epsilon J|^{-1/4} < 0.8$.

The observed discrepancies between the creep-law description in terms of $\mu_0 H_{\text{eff}} = \mu_0 H + \epsilon J$ and the left and right wall velocities under simultaneous field and current, shown in figures 6.10 and 6.11, cannot be explained by the existence of an additional term in the effective field of the type ηJ^2, as proposed by J. Ryu and collaborators [197] and expressed by equation (6.7). Even if several studies on metallic samples [156, 157, 198] show the validity of this expression, our results in (Ga,Mn)(As,P)/(Ga,Mn)As are not consistent with it. As we have already mentioned, this may be due to the high efficiency of non-adiabatic STT in diluted magnetic semiconductors and the resultant high ϵ value, which rules out any non-linear term in the $\mu_0 H_{\text{eff}}$ vs. J dependence.

We may therefore highlight two main observations. On the one hand, we have shown that the simple expression (6.3) successfully describes domain wall dynamics in a variety of situations with a unique value $\epsilon = (1.3 \pm 0.2)\,\mathrm{mT/(GA/m^2)}$: in the conditions of balance of the field- and current-induced forces over domain walls for $T \geq 52\,\mathrm{K}$, when comparing field-driven and current-driven dynamics at velocities in the range $0.1\,\mathrm{m/s} < v < 10\,\mathrm{m/s}$, and for most of the simultaneous field- and current-driven dynamics of left and right domain walls in the range $|\mu_0 H_{\text{eff}}|^{-1/4} < 0.8$. On the other hand, we have shown that in some situations, generally for relatively low values of $|\mu_0 H_{\text{eff}}|$, the description in terms of an effective field is not enough to account for the observed domain wall dynamics if we consider equations (6.8) and (6.9) with unique values of v_d, H_d and T_d. Rather than this, the effective pinning parameters could depend on the driving force nature, or another regime which cannot be described by these equations could appear. The obtained results, which up to now could not be completely understood in the framework of the present theories, call for further studies.

6.4 Chapter summary and conclusions

In this chapter, we have presented and discussed our studies on the field- and STT-driven domain wall dynamics in a diluted ferromagnetic semiconductor. Specifically, we have studied a bilayer of (Ga,Mn)(As,P)/(Ga,Mn)As with a thickness $t = 4\,\mathrm{nm}$. The particularities of the experimental investigations which constitute the core of this chapter are the material properties (different from the metallic ferrimagnet studied in chapters 4 and 5) and the study of domain wall dynamics under two different driving forces.

We have started this chapter by presenting the most recent investigations on this topic and posing some open questions. Firstly, we have shown that the most recent evidences support the hypothesis that both field- and STT-driven domain wall motion belongs to the quenched Edwards-Wilkinson universality class, what has permitted us to analyze all our results in this framework. Secondly, we have reviewed some previous investigations in which field and current are combined in order to drive domain walls. In this context, we have presented some ideas which permit to analyze domain wall dynamics in the creep regime in terms of an effective field H_{eff} which considers both the effect of the applied field H and the current density J.

Then, in section 6.2, we have described the experimental methods that we have implemented in order to study combined field- and current-driven domain wall dynamics. We have discussed about the simultaneity of the applied field and current pulses, and we have described our velocity measurements, in which we consider the motion of two domain walls: the “left” wall, which is pushed in the same direction both by field and current, and the “right” wall, which is pushed in opposite directions by these two stimuli.

In section 6.3, we have presented and discussed our experimental results. Firstly, we have analyzed the right domain wall velocity and the conditions in which both forces over domain walls are balanced, as a function of the temperature, in the range $0.5 < T/T_C < 1$, where $T_C = 65\,\mathrm{K}$. These studies have permitted us to compare the forces induced by field and current over domain walls. We have found that, for $T \geq 52\,\mathrm{K}$, there exists a proportionality between these two stimuli with a value $\epsilon = (1.3 \pm 0.2)\,\mathrm{mT/(GA/m^2)}$, two to four orders of magnitude higher than the value obtained for metallic samples in which STT efficiency is much lower.

Secondly, we have compared the pure field-driven motion with the pure current-driven motion, both in the creep regime. Remarkably, we have observed that in the range $0.1\,\mathrm{m/s} < v < 10\,\mathrm{m/s}$, the same ϵ factor permits to successfully compare the field-driven and current-driven domain wall dynamics. In other words, the effective field for current-driven motion may be calculated as ϵJ. However, we have found that for lower velocities, this relation is no longer valid and the creep slopes are considerably different.

Finally, we have studied the simultaneous field- and current-driven domain wall dynamics when field and current push both in equal or opposite directions. Even if most of the results also show a rather good consistency with the description in terms of the effective field $\mu_0 H_{\text{eff}} = \mu_0 H + \epsilon J$, some systematic discrepancies have been observed, specially when the two driving forces act oppositely and at low domain wall velocities. As this expression for $\mu_0 H_{\text{eff}}$ is very robust and non-linear terms are expected to be negligible due to the high ϵ value, our results suggest that other regimes of motion which cannot be described by the creep law appear. These observations call for further research in this field, both theoretical and experimental.

CHAPTER 7

General conclusions and perspectives

“Creo que la palabra nos hace libres.
Creo que la palabra nos hace bellos.
Creo que la palabra nos hace luminosos.
Y creo que si alguna vez nos toca
quedarnos sin palabras,
es bueno que sea porque estamos maravillados
y no porque estamos vacíos.”
Liliana Bodoc

THROUGHOUT this thesis work, we have explored the dynamics and morphology of magnetic domain walls in thin films with perpendicular anisotropy. We have noted that, as domain walls have an associated energy arising fundamentally from contributions of the exchange and anisotropy energies, they can be treated as elastic objects. In addition, they lie in magnetic materials with intrinsic inhomogeneities and therefore, we may consider that domain walls lie in a disordered energy landscape. On this basis, we have addressed the study of magnetic domain walls in thin films with the Statistical Physics approach, i.e. using the theory of elastic manifolds in disordered media. Particularly, as the thickness of the studied magnetic thin films is comparable to the domain wall width, we have considered that walls may be seen as elastic lines in a two-dimensional disordered medium.

Keeping in mind this theoretical framework, we have experimentally studied domain wall dynamics and morphology by using the polar magneto-optical Kerr effect (PMOKE) microscopy, in two fundamentally different materials. On the one hand, the ferrimagnetic GdFeCo, which presents particular temperature-dependent magnetic properties due to the antiferromagnetic coupling of rare-earth and transition metal sub-lattices. On the other hand, a ferromagnetic and semiconducting bilayer of (Ga,Mn)(As,P)/(Ga,Mn)As, which presents an efficient spin-transfer torque mechanism and is therefore suitable for the study of both field-driven and current-driven domain wall motion.

In our experimental studies, we have observed domain walls in the creep and depinning regimes of motion. In this context, we have measured their dynamic and morphological properties for different conditions of temperature and driving force magnitude. Based on these measurements, we have addressed fundamental questions related to the universality class to which domain walls in thin films belong, the length scales that are involved in the statistical properties of domain walls, and the nature of the driving forces that induce wall motion.

For the ferrimagnetic GdFeCo sample, we have firstly performed a careful study of field-driven domain wall dynamics in the creep and depinning regimes in a wide range of temperatures, from $T = 10\,\mathrm{K}$ to $T = 353\,\mathrm{K}$. For $T > 100\,\mathrm{K}$, we have verified the existence of a creep regime of motion with the expected creep exponent $\mu = 1/4$, and we have found evidences of the depinning transition for domain wall velocities of the order $v \sim 100\,\mathrm{m/s}$. This allowed for the quantification of key parameters which permit to describe these dynamical regimes as a function of T; particularly, the depinning field H_d and the depinning temperature T_d. We have observed a divergence of the depinning field H_d when approaching the magnetic compensation temperature of the sample at $T_M = (190 \pm 4)\,\mathrm{K}$. This divergence is directly linked to the temperature-dependence of the saturation magnetization M_s. In addition, we have observed an increase of T_d for decreasing T, what evidences that the effective pinning energy barrier grows for decreasing temperature. Remarkably, magnetic compensation does not seem to affect this T_d vs. T dependence. Additionally, from the joint analysis of the temperature-dependence of H_d, M_s and T_d, we have compared the Zeeman energy $\varepsilon_Z(H_d)$ associated to domain wall displacement at depinning with the effective pinning energy barrier $k_B T_d$, what has shed light over fundamental length scales associated to disorder, namely the Larkin length L_c and the pinning correlation length ξ_p. The found magnitudes of these characteristic lengths are consistent with theoretical predictions, what validates our approach for the interpretation of domain wall dynamics measurements.

Future studies regarding the temperature-dependence of domain wall dynamics in GdFeCo could focus on the effects of angular compensation in the creep and depinning regime. Even if we have not observed any evidence of the angular compensation temperature T_A in our experimental studies, we have not characterized it by means of other techniques. A characterization of dynamic magnetic properties which could be made, for example, with ferromagnetic resonance, time-resolved MOKE magnetometry or domain wall velocity measurements in the flow regime, would be appropriate in order to determine T_A and carefully investigate its effects in the creep and depinning regimes.

The depinning transition of field-driven domain walls in GdFeCo, which resulted rather difficult to analyze in the range of high temperatures due to thermal effects, appeared to be increasingly clear for decreasing temperatures. This notorious fact may be associated with the increase of T_d for decreasing T, what results on a significant decrease of the reduced temperature T/T_d quantifying the effective thermal activation. Moreover, the T_d values that we have found for temperatures close to $T = 100\,\mathrm{K}$ are surprisingly high, what results in an extremely reduced thermal energy in the range of low temperatures. Particularly, in the range $10\,\mathrm{K} \leq T < 100\,\mathrm{K}$, we have measured domain wall velocity vs. applied field curves which may be directly analyzed in terms of the theoretically expected depinning transition at zero-temperature. This allowed us to directly determine the parameters associated to this transition. In particular, for each velocity vs. field curve, we determined the value of the critical exponent β associated to the power-law behavior of domain wall velocity. As theoretically expected for universal critical exponents, we have found that the obtained β values are consistent with a unique mean value $\overline{\beta} = 0.30 \pm 0.03$. Furthermore, we have analyzed the spatial correlation of domain wall velocities in this range of low temperatures, what permitted us to estimate the velocity-dependence of the depinning correlation length ℓ_{av} at different temperatures. As theoretically expected, we have found a power-law dependence from which we obtained the critical exponent of the depinning correlation length, ν_{dep}. Remarkably, we have found a mean value $\overline{\nu}_{\mathrm{dep}} = 1.3 \pm 0.3$ which is representative of all the values obtained for the analyzed temperatures. To the best of our knowledge, the direct experimental determination of β and ν_{dep} had never been performed for magnetic domain walls in thin films. The obtained values of these universal critical exponents of the depinning transition are in very good agreement with the theoretically calculated values for the quenched Edwards-Wilkinson (qEW) universality class with random-bond disorder and short-range elasticity, and they are clearly inconsistent with the expected values for the other usually considered universality class, the quenched Kardar-Parisi-Zhang (qKPZ) class. Therefore, our results permit us to claim that the depinning of magnetic domain walls in GdFeCo thin films belongs to the qEW universality class. Furthermore, this strongly suggests that this is the case for all domain walls in perpendicularly magnetized thin films, as expected for universal phenomena.

Future experimental research in this issue could be devoted to experimentally characterize β and ν_{dep} in other materials in order to test our result. An open question in this context is why the studied GdFeCo sample shows such large values of the depinning temperature T_d, what allows for our direct observation of the depinning regime and associated power-laws. Another open issue from the experimental point of view is the determination of other critical exponents of the depinning transition. Regarding the relationship between our results and theoretical predictions, an interesting discussion remains on the possibility of theoretically predicting, based on fundamental properties, when the KPZ term is relevant enough to change the universality class to which domain walls or other interface phenomena belong to.

Regarding the morphological properties of domain walls, we have carefully quantified the roughness parameters of magnetic domain walls in the same GdFeCo sample for different temperatures and driving fields. This quantification is performed by computing and fitting the displacement-displacement correlation function $B(r)$ of domain wall profiles observed by PMOKE microscopy. A particularity of our analysis is that we consider multiple wall profiles at each field and temperature condition in order to obtain statistically representative mean values of the measured roughness exponent ζ_{eff} and the roughness amplitude B_0. As the obtained mean values of ζ_{eff} result inconsistent with any of the three theoretically expected values for the qEW universality class, $\zeta_{\text{eq}} = 2/3$, $\zeta_{\text{dep}} = 1.25$ and $\zeta_{\text{th}} = 0.5$, we propose that the measured exponent may be interpreted as an effective value given by contributions of these three expected exponents, each of them dominating at different length scales. We consider that below the correlation length ℓ_{opt}, which is associated to the equilibrium reference point at $H \to 0$, ζ_{eq} dominates the power-law behavior of domain wall roughness, while between ℓ_{opt} and the depinning correlation length $\ell_{\text{av}} > \ell_{\text{opt}}$, ζ_{dep} dominates. Finally, for length scales above ℓ_{av}, the thermal roughness exponent ζ_{th} dominates. We have therefore analyzed our results in terms of this scenario, taking into account that the different power-law behaviors corresponding to different length scales are appropriately modeled in terms of the structure factor $S(q)$. Consequently, based on this ideas and on previously determined physical quantities we have obtained the temperature-dependence of ℓ_{opt} and ℓ_{av}. Remarkably, both characteristic lengths are within the working range of the PMOKE microscope: $\ell_{\text{opt}} \lesssim 1\,\mu\text{m}$ and $\ell_{\text{av}} \gtrsim 10\,\mu\text{m}$. This supports the idea that the three different theoretically predicted exponents can impact on the effective measured roughness exponent ζ_{eff}. Furthermore, we have experimentally quantified for the first time ℓ_{av} as a function of H for driving fields below H_d, what is in agreement with qualitative theoretical arguments suggesting that ℓ_{av} is finite even below the depinning transition at $T > 0$. Moreover, the proposed interpretation of experimentally measured roughness exponents permits to successfully reinterpret previously reported experimental roughness determinations.

Several open questions remain regarding domain wall roughness and the characteristic correlation lengths. Even if we have experimentally quantified ℓ_{av} below the depinning transition, its detailed field-dependence for finite temperatures is not clear and it has never been theoretically obtained. As domain wall roughness is not easy to experimentally quantify and an important statistical analysis is needed, a very careful research should be made in order to obtain more detailed results in this subject. Moreover, the field- and temperature-dependence of the roughness amplitude B_0 that we have obtained still needs to be successfully interpreted. Even if this parameter is not universal, it clearly decreases for increasing domain wall velocities, what is consistent with the direct naked-eye observation that domain walls are less rough as they move faster. Since the roughness amplitude might be related with pinning parameters, a detailed study of this relation is still lacking.

For the diluted magnetic semiconductor (Ga,Mn)(As,P)/(Ga,Mn)As, we have performed measurements of domain wall dynamics driven both by field and current. These investigations were motivated by open questions regarding the effective nature of these two driving forces on domain wall motion when applied both separately and simultaneously. We have firstly analyzed the dynamics of magnetic domain walls when the driving forces induced by field and current are opposed and act simultaneously. In this context, we have focused on the conditions in which these two forces are balanced and thus no domain wall motion is detected. We have analyzed these conditions as a function of temperature in a large range which spans between $T = 35\,\mathrm{K}$ and the sample's Curie temperature $T_C = 65\,\mathrm{K}$. Remarkably, for $T/T_C \geq 0.8$, we have observed that the balance of field- and current-driven forces over domain walls occurs for a current density $J = J_b(H) = \mu_0 H/\epsilon$ with $\epsilon = (1.3 \pm 0.2)\,\mathrm{mT}/(\mathrm{GA}/\mathrm{m}^2)$ for all the experimentally accessible field magnitudes. This accounts for a proportionality between the two driving forces in the studied conditions and evidences a high efficiency of the spin-transfer torque (STT) mechanism. Furthermore, we have analyzed and compared the creep regimes resulting from applying field and current separately at $T = 55\,\mathrm{K}$. Notably, in the range of relatively high velocities, i.e. close to the depinning transition, the domain wall velocity resulting from applying a field $\mu_0 H$ is equal to the velocity that results from applying a current J such that $\epsilon J = \mu_0 H$ with $\epsilon = (1.3 \pm 0.2)\,\mathrm{mT}/(\mathrm{GA}/\mathrm{m}^2)$. Consequently, the comparison between field- and current-driven forces yields a proportionality that is equivalent in two fundamentally different situations. Nevertheless, in the range of velocities $v < 10^{-1}\,\mathrm{m/s}$, this proportionality is no longer valid. Instead, field-driven motion is more efficient. This difference might be associated to the non-isotropic nature of current-driven motion, which may result in a reduced effective force over the whole domain wall. Finally, we have analyzed the effect of simultaneously applying field and current at $T = 55\,\mathrm{K}$, both when they push domain walls oppositely and when they push in the same sense. Remarkably, most of our results are consistent with describing domain wall dynamics in terms of an effective field $\mu_0 H_{\mathrm{eff}} = \mu_0 H + \epsilon J$ with the same ϵ value we have previously found. However, some systematic discrepancies have been observed, specially for oppositely acting driving forces and in the range of low wall velocities.

These observations call for further theoretical and experimental research in this field. An open question remains regarding the state of domain wall's internal magnetization in the conditions of balance between field- and current-driven forces and also for simultaneous drive. This could be addressed by characterizing the static and dynamic magnetic properties of the studied sample, what would permit to determine the theoretically expected ϵ value. Furthermore, a detailed investigation of the influence of different driving forces on effective pinning parameters as H_d, T_d and v_d would be appropriate. In addition, a thorough characterization of the global effective force over domain walls that considers the non-isotropic nature of the force induced by current is lacking. These investigations would allow for a correct evaluation of both the effective force and the effective pinning as a function of the combination of field and current that acts over domain walls.

The studies presented in this thesis make contributions to our knowledge about the nature of magnetic domain walls in thin films with perpendicular anisotropy. While a deep understanding of the microscopic mechanisms that give rise to magnetic domain walls and their behavior under diverse stimuli has been achieved by considering the tools of micromagnetism, in this thesis we have focused on their statistical properties and universal features, which are common to many other interface phenomena in nature. Our studies shed light on the universality class to which domain wall depinning belongs, on the basic features of wall roughness and the length scales that are involved in their motion and morphology, and on the effective nature of field-driven motion and current-driven motion via the STT mechanism. While these investigations push the limits of our knowledge in this area, they call for further studies permitting to test our ideas and to achieve an increasingly deep insight on domain walls and other interface phenomena. Furthermore, they motivate further research on the relationship between effective models of statistical physics for interface phenomena and more fundamental approaches focused on the basic principles that govern them.

List of publications

- **Lucas J. Albornoz**, Ezequiel E. Ferrero, Alejandro B. Kolton, Vincent Jeudy, Sebastian Bustingorry, and Javier Curiale, *Universal critical exponents of the magnetic domain wall depinning transition*, Physical Review B **104**, L060404 (2021).
- **Lucas J. Albornoz**, Pamela C. Guruciaga, Vincent Jeudy, Javier Curiale, and Sebastian Bustingorry, *Domain-wall roughness in GdFeCo thin films: Crossover length scales and roughness exponents*, Physical Review B **104**, 024203 (2021).
- Cynthia P Quinteros, María José Cortés Burgos, **Lucas J Albornoz**, Javier E Gómez, Pablo Granell, Federico Golmar, María Luján Ibarra, Sebastian Bustingorry, Javier Curiale, and Mara Granada, *Impact of growth conditions on the domain nucleation and domain wall propagation in Pt/Co/Pt stacks*, Journal of Physics D: Applied Physics **54**, 015002 (2020).
- D. Jordán , **L. J. Albornoz**, J. Gorchon , C. H. Lambert, S. Salahuddin, J. Bokor, J. Curiale, and S. Bustingorry, *Statistically meaningful measure of domain-wall roughness in magnetic thin films*, Physical Review B **101**, 184431 (2020).
- R. Díaz Pardo, N. Moisan, **L. J. Albornoz**, A. Lemaître, J. Curiale, and V. Jeudy, *Common universal behavior of magnetic domain walls driven by spin-polarized electrical current and magnetic field*, Physical Review B **100**, 184420 (2019).
- Nirvana B. Caballero, Iván Fernández Aguirre, **Lucas J. Albornoz**, Alejandro B. Kolton, Juan Carlos Rojas-Sánchez, Sophie Collin, Jean Marie George, Rebeca Díaz Pardo, Vincent Jeudy, Sebastián Bustingorry, and Javier Curiale, *Excess velocity of magnetic domain walls close to the depinning field*, Physical Review B **96**, 224422 (2017).

List of Figures

2.1 Ferromagnetic, anti-ferromagnetic and ferrimagnetic configurations. 8

2.2 Demagnetizing field in a uniformly magnetized material. 10

2.3 Magnetic domains structure minimizing dipolar energy. 12

2.4 Bloch and Néel Walls in a thin film with perpendicular anisotropy. 13

2.5 Static profile of a one-dimensional domain wall. 15

2.6 Analytical solution for the static profile of a one-dimensional domain wall. . 16

2.7 Schematic representation of magnetization dynamics according to the Landau-Lifshitz-Gilbert equation. 17

2.8 Velocity vs. field dependence and Walker breakdown of a one-dimensional domain wall. 22

2.9 Examples of elastic interfaces in disordered media. 27

2.10 Elastic line in a two-dimensional disordered medium and notion of self-affinity. 28

2.11 Dynamical regimes and associated critical exponents of an elastic interface in the quenched Edwards-Wilkinson model. 34

2.12 Illustration of the coherent and fast displacement of one segment in a driven elastic line. 36

2.13 Domain wall velocity versus applied field in Pt/Co/Pt thin films. 40

2.14 Reduced effective pinning energy barrier as a function of the reduced applied field in the whole creep regime. 42

2.15 Universality of the depinning transition at finite temperature. 44

2.16 Crossover diagram showing the field-dependence of characteristic length-scales and associated roughness exponents. 46

2.17 Electronic states, band structure and exchange interactions giving rise to ferrimagnetism in a GdCo compound. 51

2.18 Mean-field calculation of magnetization as a function of temperature in a ferrimagnetic GdCo alloy. 52

2.19 Domain wall velocity peak associated to the angular momentum compensation in GdFeCo. 54

2.20 Crystalline structure and temperature dependence of magnetization in (Ga,Mn)As. 56

2.21 Field- and STT-driven domain wall motion in perpendicularly magnetized (Ga,Mn)(As,P)/(Ga,Mn)As. 57

3.1 Geometry of the polar Kerr effect. 62

3.2 Polar magneto-optical Kerr effect (PMOKE) image of a GdFeCo sample. . . 65

3.3 Optical setup of the used PMOKE microscopes. 67

3.4 Domain wall velocity measurement. 72

3.5 Domain wall displacement as a function of the pulse time. 73

3.6 Application of field pulses and measurement of their shape when using the medium sized coil. 75

3.7 Application of short field pulses and measurement of their shape. 76

3.8 Domain wall profile detection. 78

3.9 Saturation magnetization as a function of temperature in GdFeCo. 80

3.10 Polar Kerr effect hysteresis cycles as a function of the field for different temperatures. 82

3.11 Anomalous Hall effect measurement of hysteresis cycles with in-plane applied field at different fixed temperatures. 83

3.12 Coercive field and anisotropy energy as a function of the temperature. 84

3.13 Studied (Ga,Mn)(As,P)/(Ga,Mn)As sample. 86

4.1 Effect of the depinning field on domain wall velocity in GdFeCo close to the angular compensation. 92

4.2 Domain wall velocity as a function of the applied field for $T = 353\,\mathrm{K}$. 96

4.3 Domain wall velocity as a function of the applied field above the magnetic compensation temperature. 98

4.4 Creep-type plot of domain wall velocity curves above the magnetic compensation temperature. 99

4.5 Creep fit parameters above T_M as a function of the temperature. 100

4.6 Depinning field determination for velocity curves above T_M. 102

4.7 Depinning field vs. temperature for $T > T_M$. 103

4.8 Depinning temperature vs. temperature for $T > T_M$. 104

4.9 Domain wall velocity as a function of the applied field below the magnetic compensation temperature. 106

4.10 Creep-type plot of domain wall velocity curves below the magnetic compensation temperature. 107

4.11 Effect of different magnetic field amplitudes on domain walls at $T = 102\,\mathrm{K}$. . 108

4.12 Creep fit parameters as a function of the temperature in the whole temperature range. 110

4.13 Depinning field determination for velocity curves below T_M and above $100\,\mathrm{K}$. 112

4.14 Depinning field as a function of T for $T > 100\,\mathrm{K}$. 113

4.15 Depinning temperature T_d and reduced temperature T/T_d as a function of T. 114

4.16 Temperature dependence of obtained physical quantities characterizing the pinning of magnetic domain walls. 116

4.17 Thermally activated v vs. $\mu_0 H$ curve at $T = 295\,\mathrm{K}$ and athermal curve at $T = 20\,\mathrm{K}$. . . . 118

4.18 PMOKE microscopy images in the vicinity of the depinning transition at $T = 20\,\mathrm{K}$. . . . 121

4.19 Depinning transition in the velocity vs. field curve for $T = 20\,\mathrm{K}$. . . . 122

4.20 Depinning fit parameters as a function of $\mu_0 H_d$ in the range $(\mu_0 H_{d,\mathrm{min}}, H_{d,\mathrm{max}})$ for $T = 20\,\mathrm{K}$. . . . 124

4.21 Log-log velocity vs. reduced field dependence corresponding to the athermal depinning transition for $T = 20\,\mathrm{K}$. . . . 125

4.22 Master curve showing the good agreement of velocity-field curves below $T = 100\,\mathrm{K}$ with the theoretically predicted zero-temperature depinning transition. 126

4.23 Depinning parameters $\mu_0 H_d$, β and v_H as a function of T, obtained for all studied temperatures below $T = 100\,\mathrm{K}$. . . . 127

4.24 Successive domain wall profiles considered for calculating the depinning correlation length at $T = 20\,\mathrm{K}$. . . . 128

4.25 Normalized velocity correlation functions for different applied fields at $T = 20\,\mathrm{K}$.130

4.26 Mean domain wall velocity vs. depinning avalanche size for $T = 20\,\mathrm{K}$. . . . 131

4.27 Common dependence of reduced parameters relating the mean domain wall velocity and the depinning avalanche length for different temperatures. . . . 132

4.28 Depinning correlation length parameters ν_{dep} and ξ_0 as a function of T for the lowest temperatures.. . . . 133

5.1 Displacement-displacement correlation function for a single domain wall profile.143

5.2 Protocol for determining roughness parameters and their uncertainties for a single domain wall profile. . . . 145

5.3 Statistics of roughness parameters for a particular field and temperature condition. . . . 147

5.4 Velocity vs. field curves corresponding to temperatures for which we performed domain wall roughness measurements. . . . 149

5.5 Mean roughness parameters as a function of the reduced field for different temperatures. . . . 150

5.6 Structure factor and displacement-displacement correlation function of an elastic line with two crossovers between different roughness exponents. 152

5.7 Calculated Larkin length L_c and optimal event size ℓ_{opt}. 155

5.8 Determination of structure factor parameters q_{av} and S_0 in accordance with measured roughness parameters $\overline{\zeta}_{\text{eff}}$ and $\overline{B}_0$. 157

5.9 Experimentally determined crossover diagram and structure factor amplitude. 159

6.1 Domain wall faceting and roughness exponent measurements for field- and STT-driven domain walls in (Ga,Mn)(As,P)/(Ga,Mn)As. 166

6.2 Shape and simultaneity of field and current pulses. 170

6.3 Measurement of left and right domain wall displacements under simultaneous field and current pulses. 172

6.4 Right domain wall velocity as a function of the current density at $T = 55\,\text{K}$ for different applied fields. 173

6.5 Conditions of balance of the forces induced by field and current. 174

6.6 Slope and intercept of the J_b vs. $\mu_0 H$ fits as a function of T/T_C. 175

6.7 Field-driven and STT-driven domain wall velocity curves in the creep regime at $T = 55\,\text{K}$. 177

6.8 Field-driven and STT-driven domain wall velocity curves as a function of the effective field at $T = 55\,\text{K}$. 178

6.9 Combined field- and current-driven left and right domain wall dynamics as a function of ϵJ for $\mu_0 H = 5.3\,\text{mT}$ at $T = 55\,\text{K}$. 180

6.10 Combined field- and current-driven left domain wall velocity in terms of an effective field at $T = 55\,\text{K}$. 182

6.11 Combined field- and current-driven right domain wall velocity in terms of an effective field at $T = 55\,\text{K}$. 183

List of Tables

4.1 Universal depinning critical exponents. 94

4.2 Experimentally determined depinning critical exponents. 135

5.1 Experimentally determined roughness exponents reported in the literature, corresponding to field-driven domain walls. 141

5.2 Relevant material- and temperature-dependent parameters at selected temperatures. 154

Bibliography

[1] A. Hubert and R. Schäfer. *Magnetic Domains: the analysis of magnetic nanostructures*. Springer-Verlag, Berlin Heidelberg, 1998.

[2] A. P. Malozemoff and J. C. Slonczewski. *Magnetic Domain Walls in Bubble Materials*. Academic Press, New York, 1979.

[3] A.-L. Barabási and H. E. Stanley. *Fractal Concepts in Surface Growth*. Cambridge University Press, Cambridge, 1995.

[4] E. E. Ferrero, S. Bustingorry, A. B. Kolton, and A. Rosso. Numerical approaches on driven elastic interfaces in random media. *Comptes Rendus Physique*, 14(8):641–650, 2013.

[5] E. E. Ferrero, L. Foini, T. Giamarchi, A. B. Kolton, and A. Rosso. Creep Motion of Elastic Interfaces Driven in a Disordered Landscape. *Annual Review of Condensed Matter Physics*, 12(1):111–134, 2021.

[6] John M. D. Coey. *Magnetism and Magnetic Materials*. Cambridge University Press, Cambridge, 2010.

[7] Blas Cabrera. *El Magnetismo de la Materia*. Institución Cultural Española, Buenos Aires, 1944.

[8] Hideo Ohno. A window on the future of spintronics. *Nature Materials*, 9(12):952–954, 2010.

[9] Teruya Shinjo. *Nanomagnetism and Spintronics*. Elsevier, London, 2013.

[10] Yongbing Xu, David D. Awschalom, and Junsaku Nitta. *Handbook of spintronics*. Springer Science+Business Media, New York London, 2016.

[11] Bernard Dieny, Ronald B. Goldfarb, and Kyung-Jin Lee. *Introduction to magnetic random-access memory.* John Wiley & Sons, Inc., Hoboken, New Jersey, 2016.

[12] Atsufumi Hirohata, Keisuke Yamada, Yoshinobu Nakatani, Lucian Prejbeanu, Bernard Diény, Philipp Pirro, and Burkard Hillebrands. Review on spintronics: Principles and device applications. *Journal of Magnetism and Magnetic Materials*, 509:166711, 2020.

[13] S Lemerle, J Ferré, C Chappert, V Mathet, T Giamarchi, and P Le Doussal. Domain Wall Creep in an Ising Ultrathin Magnetic Film. *Physical Review Letters*, 80(4):849–852, 1998.

[14] P J Metaxas, J P Jamet, A Mougin, M Cormier, J Ferré, V Baltz, B Rodmacq, B Dieny, and R L Stamps. Creep and flow regimes of magnetic domain-wall motion in ultrathin Pt/Co/Pt films with perpendicular anisotropy. *Physical Review Letters*, 99(21):217208, 2007.

[15] J Gorchon, S Bustingorry, J Ferré, V Jeudy, A B Kolton, and T Giamarchi. Pinning-dependent field-driven domain wall dynamics and thermal scaling in an ultrathin Pt/Co/Pt magnetic film. *Physical Review Letters*, 113(2):027205, 2014.

[16] V Jeudy, A Mougin, S Bustingorry, W Savero Torres, J Gorchon, A B Kolton, A Lemaître, and J P Jamet. Universal Pinning Energy Barrier for Driven Domain Walls in Thin Ferromagnetic Films. *Physical Review Letters*, 117(5):057201, 2016.

[17] Nirvana B. Caballero, Iván Fernández Aguirre, Lucas J. Albornoz, Alejandro B. Kolton, Juan Carlos Rojas-Sánchez, Sophie Collin, Jean Marie George, Rebeca Diaz Pardo, Vincent Jeudy, Sebastian Bustingorry, and Javier Curiale. Excess velocity of magnetic domain walls close to the depinning field. *Physical Review B*, 96(22):224422, 2017.

[18] R Díaz Pardo, W Savero Torres, A B Kolton, S Bustingorry, and V Jeudy. Universal depinning transition of domain walls in ultrathin ferromagnets. *Physical Review B*, 95(18):184434, 2017.

[19] J C Slonczewski. Current-driven excitation of magnetic multilayers. *Journal of Magnetism and Magnetic Materials*, 159(1-2):L1–L7, 1996.

[20] S Zhang, P M Levy, and A Fert. Mechanisms of spin-polarized current-driven magnetization switching. *Physical Review Letters*, 88(23):2366011–2366014, 2002.

[21] A. Yamaguchi, T. Ono, S. Nasu, K. Miyake, K. Mibu, and T. Shinjo. Real-Space Observation of Current-Driven Domain Wall Motion in Submicron Magnetic Wires. *Physical Review Letters*, 92(7):077205, 2004.

[22] S Zhang and Z Li. Roles of nonequilibrium conduction electrons on the magnetization dynamics of ferromagnets. *Physical Review Letters*, 93(12):127204, 2004.

[23] A Thiaville, Y Nakatani, J Miltat, and Y Suzuki. Micromagnetic understanding of current-driven domain wall motion in patterned nanowires. *Europhysics Letters*, 69(March):990–996, 2005.

[24] J P Adam, N Vernier, J Ferré, A Thiaville, V Jeudy, A Lemaître, L Thevenard, and G Faini. Nonadiabatic spin-transfer torque in (Ga,Mn)As with perpendicular anisotropy. *Physical Review B - Condensed Matter and Materials Physics*, 80(19):193204, 2009.

[25] V. Jeudy, J. Curiale, J. P. Adam, A. Thiaville, A. Lemaître, and G. Faini. Current induced domain wall motion in GaMnAs close to the Curie temperature. *Journal of Physics: Condensed Matter*, 23(44):446004, 2011.

[26] J Curiale, A Lemaître, C Ulysse, G Faini, and V Jeudy. Spin drift velocity, polarization, and current-driven domain-wall motion in (Ga,Mn)(As,P). *Physical Review Letters*, 108(7):076604, 2012.

[27] R. Díaz Pardo, N. Moisan, L. J. Albornoz, A. Lemaître, J. Curiale, and V. Jeudy. Common universal behavior of magnetic domain walls driven by spin-polarized electrical current and magnetic field. *Physical Review B*, 100(18):184420, 2019.

[28] F. J.A. den Broeder, W. Hoving, and P. J.H. Bloemen. Magnetic anisotropy of multilayers. *Journal of Magnetism and Magnetic Materials*, 93:562–570, 1991.

[29] V. G. Harris, K. D. Aylesworth, B. N. Das, W. T. Elam, and N. C. Koon. Structural origins of magnetic anisotropy in sputtered amorphous Tb-Fe films. *Physical Review Letters*, 69(13):1939, 1992.

[30] H. Ohno, A. Shen, F. Matsukura, A. Oiwa, A. Endo, S. Katsumoto, and Y. Iye. (Ga,Mn)As: A new diluted magnetic semiconductor based on GaAs. *Applied Physics Letters*, 69(3):363, 1996.

[31] F. Keffer and C. Kittel. Theory of antiferromagnetic resonance. *Physical Review*, 85(2):329, 1952.

[32] P. Hansen, C. Clausen, G. Much, M. Rosenkranz, and K. Witter. Magnetic and magneto-optical properties of rare-earth transition-metal alloys containing Gd, Tb, Fe, Co. *Journal of Applied Physics*, 66(2):756–767, 1989.

[33] Tadashi Kobayashi, Hideaki Hayashi, Yuji Fujiwara, and Shigeru Shiomi. Damping parameter and wall velocity of RE-TM films. *IEEE Transactions on Magnetics*, 41(10):2848–2850, 2005.

[34] C. D. Stanciu, A. V. Kimel, F. Hansteen, A. Tsukamoto, A. Itoh, A. Kirilyuk, and Th Rasing. Ultrafast spin dynamics across compensation points in ferrimagnetic GdFeCo: The role of angular momentum compensation. *Physical Review B - Condensed Matter and Materials Physics*, 73(22):220402(R), 2006.

[35] Kab Jin Kim, Se Kwon Kim, Yuushou Hirata, Se Hyeok Oh, Takayuki Tono, Duck Ho Kim, Takaya Okuno, Woo Seung Ham, Sanghoon Kim, Gyoungchoon Go, Yaroslav Tserkovnyak, Arata Tsukamoto, Takahiro Moriyama, Kyung Jin Lee, and Teruo Ono. Fast domain wall motion in the vicinity of the angular momentum compensation temperature of ferrimagnets. *Nature Materials*, 16:1187–1192, 2017.

[36] Lucas Caretta, Maxwell Mann, Felix Büttner, Kohei Ueda, Bastian Pfau, Christian M. Günther, Piet Hessing, Alexandra Churikova, Christopher Klose, Michael Schneider, Dieter Engel, Colin Marcus, David Bono, Kai Bagschik, Stefan Eisebitt, and Geoffrey S.D. Beach. Fast current-driven domain walls and small skyrmions in a compensated ferrimagnet. *Nature Nanotechnology*, 13(12):1154–1160, 2018.

[37] Eloi Haltz, Sachin Krishnia, Léo Berges, Alexandra Mougin, and João Sampaio. Domain wall dynamics in antiferromagnetically coupled double-lattice systems. *Physical Review B*, 103(1):14444, 2021.

[38] L J Albornoz, E E Ferrero, A B Kolton, V Jeudy, S Bustingorry, and J Curiale. Universal critical exponents of the magnetic domain wall depinning transition. *Physical Review B*, 104(6):L060404, 2021.

[39] D. Jordán, L. J. Albornoz, J. Gorchon, C. H. Lambert, S. Salahuddin, J. Bokor, J. Curiale, and S. Bustingorry. Statistically meaningful measure of domain-wall roughness in magnetic thin films. *Physical Review B*, 101(18):184431, 2020.

[40] Lucas J Albornoz, Pamela C Guruciaga, Vincent Jeudy, Javier Curiale, and Sebastian Bustingorry. Domain-wall roughness in GdFeCo thin films: Crossover length scales and roughness exponents. *Physical Review B*, 104(2):24203, 2021.

[41] A B Kolton, A Rosso, T Giamarchi, and W Krauth. Creep dynamics of elastic manifolds via exact transition pathways. *Physical Review B - Condensed Matter and Materials Physics*, 79(18):184207, 2009.

[42] T Dietl and H Ohno. Dilute ferromagnetic semiconductors: Physics and spintronic structures. *Reviews of Modern Physics*, 86(1):187–251, 2014.

[43] T. Jungwirth, X. Marti, P. Wadley, and J. Wunderlich. Antiferromagnetic spintronics. *Nature Nanotechnology*, 11:231–241, 2016.

[44] V. Baltz, A. Manchon, M. Tsoi, T. Moriyama, T. Ono, and Y. Tserkovnyak. Antiferromagnetic spintronics. *Reviews of Modern Physics*, 90(1):015005, 2018.

[45] Yuushou Hirata, Duck Ho Kim, Se Kwon Kim, Dong Kyu Lee, Se Hyeok Oh, Dae Yun Kim, Tomoe Nishimura, Takaya Okuno, Yasuhiro Futakawa, Hiroki Yoshikawa, Arata Tsukamoto, Yaroslav Tserkovnyak, Yoichi Shiota, Takahiro Moriyama, Sug Bong Choe, Kyung Jin Lee, and Teruo Ono. Vanishing skyrmion Hall effect at the angular momentum compensation temperature of a ferrimagnet. *Nature Nanotechnology*, 14:232–236, 2019.

[46] Joachim Stöhr and Hans Christoph Siegmann. *Magnetism: From fundamentals to nanoscale dynamics.* Springer-Verlag, Berlin Heidelberg, 2006.

[47] Olivier Darrigol. *Electrodynamics from Ampère to Einstein.* Oxford University Press, New York, 2003.

[48] P Weiss. L ' hypothèse du champ moléculaire et la propriété ferromagnétique. *Journal de Physique Théorique*, 6(1):661–690, 1907.

[49] G. E. Uhlenbeck and S. Goudsmit. Spinning Electrons and the Structure of Spectra. *Nature*, 117:264–265, 1926.

[50] Aníbal Guillermo Bibiloni, Enrique Osvaldo Civitarese, and María Cecilia von Reichenbach. Richard Gans y la cuantificación del momento dipolar magnético. *Anales de la Asociación de Física Argentina*, 14:11–14, 2002.

[51] N. W. Ashcroft and N. D. Mermin. *Solid state physics.* Harcourt College Publishers, Orlando, 1976.

[52] Charles Kittel. *Introduction to Solid State Physics.* John Wiley & Sons, Inc., 8th edition, 1957.

[53] Wolfgang Pauli. Über den Zusammenhang des Abschlusses der Elektronengruppen im Atom mit der Komplexstruktur der Spektren. *Zeitschrift für Physik*, 31(1):765–783, 1925.

[54] Werner Heisenberg. Zur Theorie des Ferromagnetismus. *Zeitschrift fur Physik*, 49(9-10):619–636, 1928.

[55] Igor Dzyaloshinsky. A thermodynamic theory of "weak" ferromagnetism of antiferromagnetics. *Journal of Physics and Chemistry of Solids*, 4(4):241–255, 1958.

[56] Tôru Moriya. Anisotropic superexchange interaction and weak ferromagnetism. *Physical Review*, 120:91–98, 1960.

[57] M. Bode, M. Heide, K. Von Bergmann, P. Ferriani, S. Heinze, G. Bihlmayer, A. Kubetzka, O. Pietzsch, S. Blügel, and R. Wiesendanger. Chiral magnetic order at surfaces driven by inversion asymmetry. *Nature*, 447:190–193, 2007.

[58] C. M. Hurd. Varieties of magnetic order in solids. *Contemporary Physics*, 23(5):469–493, 1982.

[59] S. L. Zhang, I. Stasinopoulos, T. Lancaster, F. Xiao, A. Bauer, F. Rucker, A. A. Baker, A. I. Figueroa, Z. Salman, F. L. Pratt, S. J. Blundell, T. Prokscha, A. Suter, J. Waizner, M. Garst, D. Grundler, G. Van Der Laan, C. Pfleiderer, and T. Hesjedal. Room-temperature helimagnetism in FeGe thin films. *Scientific Reports*, 7:123, 2017.

[60] Mathias Getzlaff. *Fundamentals of magnetism.* Springer-Verlag, Berlin Heidelberg, 2008.

[61] R. Soucaille, M. Belmeguenai, J. Torrejon, J. V. Kim, T. Devolder, Y. Roussigné, S. M. Chérif, A. A. Stashkevich, M. Hayashi, and J. P. Adam. Probing the Dzyaloshinskii-Moriya interaction in CoFeB ultrathin films using domain wall creep and Brillouin light spectroscopy. *Physical Review B*, 94(10):104431, 2016.

[62] Anjan Soumyanarayanan, Nicolas Reyren, Albert Fert, and Christos Panagopoulos. Emergent phenomena induced by spin-orbit coupling at surfaces and interfaces. *Nature*, 539:509–517, 2016.

[63] S G Je, D H Kim, S C Yoo, B C Min, K Ji. Lee, and S B Choe. Asymmetric magnetic domain-wall motion by the Dzyaloshinskii-Moriya interaction. *Physical Review B - Condensed Matter and Materials Physics*, 88(21):214401, 2013.

[64] R Lavrijsen, D M F Hartmann, A Van Den Brink, Y Yin, B Barcones, R A Duine, M A Verheijen, H J M Swagten, and B Koopmans. Asymmetric magnetic bubble expansion under in-plane field in Pt/Co/Pt: Effect of interface engineering. *Physical Review B - Condensed Matter and Materials Physics*, 91(10):104414, 2015.

[65] E Jué, C K Safeer, M Drouard, A Lopez, P Balint, L Buda-Prejbeanu, O Boulle, S Auffret, A Schuhl, A Manchon, I M Miron, and G Gaudin. Chiral damping of magnetic domain walls. *Nature Materials*, 15(3):272–277, 2016.

[66] J. P. Pellegren, D. Lau, and V. Sokalski. Dispersive Stiffness of Dzyaloshinskii Domain Walls. *Physical Review Letters*, 119(2):027203, 2017.

[67] J. H. Van Vleck. On the anisotropy of cubic ferromagnetic crystals. *Physical Review*, 52(11):1178–1198, 1937.

[68] M T Johnson, P J H Bloemen, F J A den Broeder, and J J de Vries. Magnetic anisotropy in metallic multilayers. *Reports on Progress in Physics*, 59:1409–1458, 1996.

[69] B. Dieny and M. Chshiev. Perpendicular magnetic anisotropy at transition metal/oxide interfaces and applications. *Reviews of Modern Physics*, 89(2):025008, 2017.

[70] André Thiaville. The demagnetizing field inside a domain wall. *Journal of Magnetism and Magnetic Materials*, 140-144:1877–1878, 1995.

[71] A. Hrabec, N. A. Porter, A. Wells, M. J. Benitez, G. Burnell, S. McVitie, D. McGrouther, T. A. Moore, and C. H. Marrows. Measuring and tailoring the Dzyaloshinskii-Moriya interaction in perpendicularly magnetized thin films. *Physical Review B - Condensed Matter and Materials Physics*, 90(2):020402(R), 2014.

[72] M Vanatka, J C Rojas-Sánchez, J Vogel, M Bonfim, M Belmeguenai, Y Roussigné, A Stashkevich, A Thiaville, and S Pizzini. Velocity asymmetry of Dzyaloshinskii domain walls in the creep and flow regimes. *Journal of Physics Condensed Matter*, 27(32):326002, 2015.

[73] Andre Thiaville, Stanislas Rohart, Emilie Jue, Vincent Cros, and Albert Fert. Dynamics of Dzyaloshinskii domain walls in ultrathin magnetic films. *EPL (Europhysics Letters)*, 100(5):57002, 2012.

[74] Thomas L. Gilbert. A Lagrangian Formulation of the Gyromagnetic Equation of the Magnetization Field. *Physical Review*, 100:1243, 1955.

[75] L Landau and E Lifshits. On the Theory of the Dispersion of Magnetic Permeability in Ferromagnetic Bodies. *Physikalische Zeitschrift der Sowjetunion*, 8:153–169, 1935.

[76] André Thiaville and Yoshinobu Nakatani. Domain-Wall Dynamics in Nanowires and Nanostrips. In *Spin Dynamics in Confined Magnetic Structures III. Topics in Applied Physics*. Springer, Berlin Heidelberg, 2006.

[77] A. Thiaville, Y. Nakatani, J. Miltat, and N. Vernier. Domain wall motion by spin-polarized current: A micromagnetic study. *Journal of Applied Physics*, 95(11):7049, 2004.

[78] N L Schryer and L R Walker. The motion of 180° domain walls in uniform dc magnetic fields. *Journal of Applied Physics*, 45(12):5406–5421, 1974.

[79] A Mougin, M Cormier, J P Adam, P J Metaxas, and J Ferré. Domain wall mobility, stability and Walker breakdown in magnetic nanowires. *EPL (Europhysics Letters)*, 78(5):57007, 2007.

[80] G S D Beach, C Nistor, C Knutson, M Tsoi, and J L Erskine. Dynamics of field-driven domain-wall propagation in ferromagnetic nanowires. *Nature Materials*, 4:741–744, 2005.

[81] A Dourlat, V Jeudy, A Lemaître, and C Gourdon. Field-driven domain-wall dynamics in (Ga,Mn)As films with perpendicular anisotropy. *Physical Review B - Condensed Matter and Materials Physics*, 78(16):161303(R), 2008.

[82] Mark D. Stiles and Jacques Miltat. Spin-Transfer Torque and Dynamics. In *Spin Dynamics in Confined Magnetic Structures III. Topics in Applied Physics*. Springer, Berlin Heidelberg, 2006.

[83] L Berger. Emission of spin waves by a magnetic multilayer traversed by a current. *Physical Review B*, 54(13):9353–9358, 1996.

[84] M Kläui, C A F Vaz, J A C Bland, W Wernsdorfer, G Faini, E Cambril, and L J Heyderman. Domain wall motion induced by spin polarized currents in ferromagnetic ring structures. *Applied Physics Letters*, 83(1):105–107, 2003.

[85] J. Grollier, P. Boulenc, V. Cros, A. Hamzić, A. Vaurès, A. Fert, and G. Faini. Switching a spin valve back and forth by current-induced domain wall motion. *Applied Physics Letters*, 83(3):509, 2003.

[86] N. Vernier, D. A. Allwood, D. Atkinson, M. D. Cooke, and R. P. Cowburn. Domain wall propagation in magnetic nanowires by spin-polarized current injection. *EPL (Europhysics Letters)*, 65(4):526–532, 2004.

[87] Michele Voto, Luis Lopez-Diaz, Luis Torres, and Simone Moretti. Disorder-induced domain wall velocity shift at high fields in perpendicularly magnetized thin films. *Physical Review B*, 94(17):174438, 2016.

[88] L. D. Geng and Y. M. Jin. Domain wall creep in magnetic thin films near the depinning transition. *EPL (Europhysics Letters)*, 116(3):36002, 2016.

[89] J. Leliaert, M. Dvornik, J. Mulkers, J. De Clercq, M. V. Milošević, and B. Van Waeyenberge. Fast micromagnetic simulations on GPU - Recent advances made with mumax3. *Journal of Physics D: Applied Physics*, 51(12):123002, 2018.

[90] Nirvana B. Caballero, Ezequiel E. Ferrero, Alejandro B. Kolton, Javier Curiale, Vincent Jeudy, and Sebastian Bustingorry. Magnetic domain wall creep and depinning: A scalar field model approach. *Physical Review E*, 97(6):062122, 2018.

[91] Pamela C. Guruciaga, Nirvana B. Caballero, Vincent Jeudy, Javier Curiale, and Sebastian Bustingorry. Ginzburg-Landau micromagnetic model to study domain wall dynamics in thin ferromagnetic systems. *Journal of Statistical Mechanics: Theory and Experiment*, 2021(3):033211, 2021.

[92] Nirvana Caballero, Elisabeth Agoritsas, Vivien Lecomte, and Thierry Giamarchi. From bulk descriptions to emergent interfaces: Connecting the Ginzburg-Landau and elastic-line models. *Physical Review B*, 102(10):104204, 2020.

[93] Nikolas Provatas, Tapio Ala-Nissila, Martin Grant, K. R. Elder, and Luc Piché. Scaling, propagation, and kinetic roughening of flame fronts in random media. *Journal of Statistical Physics*, 81(3-4):737–759, 1995.

[94] P. G. De Gennes. Wetting: Statics and dynamics. *Reviews of Modern Physics*, 57(3):827–863, 1985.

[95] P. Le Doussal, K. J. Wiese, S. Moulinet, and E. Rolley. Height fluctuations of a contact line: A direct measurement of the renormalized disorder correlator. *EPL (Europhysics Letters)*, 87(5):56001, 2009.

[96] Juan A. Bonachela, Carey D. Nadell, João B. Xavier, and Simon A. Levin. Universality in Bacterial Colonies. *Journal of Statistical Physics*, 144(2):303–315, 2011.

[97] M. A.C. Huergo, M. A. Pasquale, A. E. Bolzán, A. J. Arvia, and P. H. González. Morphology and dynamic scaling analysis of cell colonies with linear growth fronts. *Physical Review E - Statistical, Nonlinear, and Soft Matter Physics*, 82(3):031903, 2010.

[98] N. E. Muzzio, M. A. Pasquale, P. H. González, and A. J. Arvia. Influence of individual cell motility on the 2D front roughness dynamics of tumour cell colonies. *Journal of Biological Physics*, 40(3):285–308, 2014.

[99] E. Bouchaud, J. P. Bouchaud, D. S. Fisher, S. Ramanathan, and J. R. Rice. Can crack front waves explain the roughness of cracks? *Journal of the Mechanics and Physics of Solids*, 50(8):1703–1725, 2002.

[100] D. Bonamy, S. Santucci, and L. Ponson. Crackling dynamics in material failure as the signature of a self-organized dynamic phase transition. *Physical Review Letters*, 101(4):045501, 2008.

[101] E. A. Jagla and A. B. Kolton. A mechanism for spatial and temporal earthquake clustering. *Journal of Geophysical Research: Solid Earth*, 115(B5):B05312, 2010.

[102] Patrycja Paruch and Jill Guyonnet. Nanoscale studies of ferroelectric domain walls as pinned elastic interfaces. *Comptes Rendus Physique*, 14(8):667–684, 2013.

[103] Jacques Ferré, Peter J Metaxas, Alexandra Mougin, Jean Pierre Jamet, Jon Gorchon, and Vincent Jeudy. Universal magnetic domain wall dynamics in the presence of weak disorder. *Comptes Rendus Physique*, 14(8):651–666, 2013.

[104] J. Guyonnet, E. Agoritsas, P. Paruch, and S. Bustingorry. Statistics of roughness for fluctuating interfaces: A survey of different scaling analyses. *arXiv:1904.11726 [cond-mat.dis-nn]*, 2020.

[105] S Bustingorry, J Guyonnet, P Paruch, and E Agoritsas. A numerical study of the statistics of roughness parameters for fluctuating interfaces. *Journal of Physics: Condensed Matter*, 33(34):345001, 2021.

[106] P Meakin. The growth of rough surfaces and interfaces. *Physics Reports*, 235(4-5):189–289, 1993.

[107] J M López, M A Rodriguez, and R Cuerno. Superroughening versus intrinsic anomalous scaling of surfaces. *Physical Review E - Statistical, Nonlinear, and Soft Matter Physics*, 56(4):3993–3998, 1997.

[108] María José Cortés Burgos, Pamela C. Guruciaga, Daniel Jordán, Cynthia P. Quinteros, Elisabeth Agoritsas, Javier Curiale, Mara Granada, and Sebastian Bustingorry. Field-dependent roughness of moving domain walls in a Pt/Co/Pt magnetic thin film. *Physical Review B*, 104(14):144202, 2021.

[109] P Chauve, T Giamarchi, and P Le Doussal. Creep and depinning in disordered media. *Physical Review B - Condensed Matter and Materials Physics*, 62(10):6241–6267, 2000.

[110] M Kardar, G Parisi, and Y C Zhang. Dynamic Scaling of Growing Interfaces. *Physical Review Letters*, 56(9):889, 1986.

[111] A Rosso and W Krauth. Origin of the Roughness Exponent in Elastic Strings at the Depinning Threshold. *Physical Review Letters*, 87(18):187002, 2001.

[112] A Rosso, A Hartmann, and W Krauth. Depinning of elastic manifolds. *Physical Review E*, 67(2):21602, 2003.

[113] Onuttom Narayan and Daniel S Fisher. Threshold critical dynamics of driven interfaces in random media. *Physical Review B*, 48(10):7030–7042, 1993.

[114] S Bustingorry, A B Kolton, and T Giamarchi. Thermal rounding of the depinning transition. *EPL (Europhysics Letters)*, 81(16):260005, 2008.

[115] S Bustingorry, A B Kolton, and T Giamarchi. Thermal rounding exponent of the depinning transition of an elastic string in a random medium. *Physical Review E - Statistical, Nonlinear, and Soft Matter Physics*, 85(2):021144, 2012.

[116] S Bustingorry, A B Kolton, and T Giamarchi. Thermal rounding of the depinning transition in ultrathin Pt/Co/Pt films. *Physical Review B - Condensed Matter and Materials Physics*, 85(21):214416, 2012.

[117] K J Kim, J C Lee, S M Ahn, K S Lee, C W Lee, Y J Cho, S Seo, K H Shin, S B Choe, and H W Lee. Interdimensional universality of dynamic interfaces. *Nature*, 458(7239):740–742, 2009.

[118] W. Savero Torres, R. Díaz Pardo, S. Bustingorry, A. B. Kolton, A. Lemaître, and V. Jeudy. Universal dimensional crossover of domain wall dynamics in ferromagnetic films. *Physical Review B*, 99(20):201201(R), 2019.

[119] E E Ferrero, S Bustingorry, and A B Kolton. Nonsteady relaxation and critical exponents at the depinning transition. *Physical Review E - Statistical, Nonlinear, and Soft Matter Physics*, 87(3):032122, 2013.

[120] Vincent Jeudy, Rebeca Díaz Pardo, Williams Savero Torres, Sebastian Bustingorry, and Alejandro Kolton. Pinning of domain walls in thin ferromagnetic films. *Physical Review B - Condensed Matter and Materials Physics*, 98(5):054406, 2018.

[121] A. I. Larkin and Yu N. Ovchinnikov. Pinning in type II superconductors. *Journal of Low Temperature Physics*, 34:409–428, 1979.

[122] G Blatter, M V Feigel'Man, V B Geshkenbein, A I Larkin, and V M Vinokur. Vortices in high-temperature superconductors. *Reviews of Modern Physics*, 66(4):1125–1388, 1994.

[123] S Bustingorry, A B Kolton, and T Giamarchi. Random-manifold to random-periodic depinning of an elastic interface. 82(9):094202, 2010.

[124] Hyung Keun Gweon, Seok Jin Yun, and Sang Ho Lim. A very large perpendicular magnetic anisotropy in Pt/Co/MgO trilayers fabricated by controlling the MgO sputtering power and its thickness. *Scientific Reports*, 8:1266, 2018.

[125] D. Mergel, H. Heitmann, and P. Hansen. Pseudocrystalline model of the magnetic anisotropy in amorphous rare-earth transition-metal thin films. *Physical Review B*, 47(2):882–891, 1993.

[126] Jean-Paul Adam. *Du renversement sous champ de l'aimantation d'un nano-plot au déplacement sous courant d'une paroi de domaines dans une nano-piste par microscopie Kerr polaire.* PhD thesis, Université Paris-Sud, 2008.

[127] T. Shono, T. Hasegawa, T. Fukumura, F. Matsukura, and H. Ohno. Observation of magnetic domain structure in a ferromagnetic semiconductor (Ga, Mn)As with a scanning Hall probe microscope. *Applied Physics Letters*, 77(9):1363, 2000.

[128] Stuart S P Parkin, Masamitsu Hayashi, and Luc Thomas. Magnetic Domain-Wall Racetrack Memory. *Science*, 320(5873):190–194, 2008.

[129] Stuart Parkin and See-Hun Yang. Memory on the racetrack. *Nature Nanotechnology*, 10:195–198, 2015.

[130] Jacob Torrejon, Mathieu Riou, Flavio Abreu Araujo, Sumito Tsunegi, Guru Khalsa, Damien Querlioz, Paolo Bortolotti, Vincent Cros, Kay Yakushiji, Akio Fukushima, Hitoshi Kubota, Shinji Yuasa, Mark D. Stiles, and Julie Grollier. Neuromorphic computing with nanoscale spintronic oscillators. *Nature*, 547:428–431, 2017.

[131] A Fert, V Cros, and J Sampaio. Skyrmions on the track. *Nature Nanotechnology*, 8(3):152–156, 2013.

[132] Kamil Olejník, Tom Seifert, Zdenek Kašpar, Vít Novák, Peter Wadley, Richard P. Campion, Manuel Baumgartner, Pietro Gambardella, Petr Nemec, Joerg Wunderlich, Jairo Sinova, Petr Kužel, Melanie Müller, Tobias Kampfrath, and Tomas Jungwirth. Terahertz electrical writing speed in an antiferromagnetic memory. *Science Advances*, 4(3):eaar3566, 2018.

[133] See Hun Yang, Kwang Su Ryu, and Stuart Parkin. Domain-wall velocities of up to 750 m s-1 driven by exchange-coupling torque in synthetic antiferromagnets. *Nature Nanotechnology*, 10:221–226, 2015.

[134] I. A. Campbell. Indirect exchange for rare earths in metals. *Journal of Physics F: Metal Physics*, 2(3):L47, 1972.

[135] Eloi Haltz. *Domain Wall Dynamics driven by spin-current in Ferrimagnetic alloys.* PhD thesis, Université Paris-Saclay, 2019.

[136] Edmund C Stoner. Collective electron ferromagnetism. *Proceedings of the Royal Society of London. Series A. Mathematical and Physical Sciences*, 165(922):372–414, 1938.

[137] Aleš Hrabec. *Domain wall dynamics in magnetic nanostructures: Effect of magnetic field and electric current.* PhD thesis, Université de Grenoble, 2011.

[138] S. K. Malik, F. J. Arlinghaus, and W. E. Wallace. Spin-polarized energy-band structure of YCo5, SmCo5, and GdCo5. *Physical Review B*, 16(3):1242, 1977.

[139] Hiroshi Tanaka and Shinji Takayama. Electronic structure calculations for Gd32Co68 and Gd18Co82 amorphous alloys. *Journal of Applied Physics*, 70(10):6577, 1991.

[140] Hiroshi Tanaka, Shinji Takayama, and Takeo Fujiwara. Electronic-structure calculations for amorphous and crystalline Gd33Fe67 alloys. *Physical Review B*, 46(12):7390–7394, 1992.

[141] A. Gangulee and R. C. Taylor. Mean field analysis of the magnetic properties of vapor deposited amorphous Fe-Gd thin films. *Journal of Applied Physics*, 49(3):1762, 1978.

[142] Felix Büttner, Ivan Lemesh, and Geoffrey S.D. Beach. Theory of isolated magnetic skyrmions: From fundamentals to room temperature applications. *Scientific Reports*, 8:4464, 2018.

[143] Roald K. Wangsness. Sublattice effects in magnetic resonance. *Physical Review*, 91(5):1085–1091, 1953.

[144] Yuushou Hirata, Duck Ho Kim, Takaya Okuno, Tomoe Nishimura, Dae Yun Kim, Yasuhiro Futakawa, Hiroki Yoshikawa, Arata Tsukamoto, Kab Jin Kim, Sug Bong Choe, and Teruo Ono. Correlation between compensation temperatures of magnetization and angular momentum in GdFeCo ferrimagnets. *Physical Review B*, 97(22):220403(R), 2018.

[145] Yuushou Hirata, Duck Ho Kim, Takaya Okuno, Tomoe Nishimura, Yasuhiro Futakawa, Hiroki Yoshikawa, Wooseung Ham, Sanghoon Kim, Arata Tsukamoto, Yoichi Shiota, Takahiro Moriyama, Kab Jin Kim, and Teruo Ono. Effect of depinning field on determination of angular-momentum-compensation temperature of ferrimagnets. *Applied Physics Express*, 11(6):063001, 2018.

[146] E. Haltz, J. Sampaio, S. Krishnia, L. Berges, R. Weil, and A. Mougin. Measurement of the tilt of a moving domain wall shows precession-free dynamics in compensated ferrimagnets. *Scientific Reports*, 10:16292, 2020.

[147] Charles Kittel. On the gyromagnetic ratio and spectroscopic splitting factor of ferromagnetic substances. *Physical Review*, 76(6):743–748, 1949.

[148] G. G. Scott. Review of gyromagnetic ratio experiments. *Reviews of Modern Physics*, 34:102–109, 1962.

[149] Kab Jin Kim, Se Kwon Kim, Yuushou Hirata, Se Hyeok Oh, Takayuki Tono, Duck Ho Kim, Takaya Okuno, Woo Seung Ham, Sanghoon Kim, Gyoungchoon Go, Yaroslav Tserkovnyak, Arata Tsukamoto, Takahiro Moriyama, Kyung Jin Lee, and Teruo Ono. Supplementary information for "Fast domain wall motion in the vicinity of the angular momentum compensation temperature of ferrimagnets". *Nature Materials*, 16(12):1187–1192, 2017.

[150] Tomoe Nishimura, Duck Ho Kim, Yuushou Hirata, Takaya Okuno, Yasuhiro Futakawa, Hiroki Yoshikawa, Arata Tsukamoto, Yoichi Shiota, Takahiro Moriyama, and Teruo Ono. Correlation between magnetic properties and depinning field in field-driven domain wall dynamics in GdFeCo ferrimagnets. *Applied Physics Letters*, 112(17):172403, 2018.

[151] K Edmonds, G Van Der Laan, and G Panaccione. Electronic structure of (Ga,Mn)As as seen by synchrotron radiation. *Semiconductor Science and Technology*, 30(4):043001, 2015.

[152] T Ishii, T Kawazoe, Y Hashimoto, H Terada, I Muneta, M Ohtsu, M Tanaka, and S Ohya. Electronic structure near the Fermi level in the ferromagnetic semiconductor GaMnAs studied by ultrafast time-resolved light-induced reflectivity measurements. *Physical Review B*, 93(24):2413031(R), 2016.

[153] A. Yamaguchi, S. Nasu, H. Tanigawa, T. Ono, K. Miyake, K. Mibu, and T. Shinjo. Effect of Joule heating in current-driven domain wall motion. *Applied Physics Letters*, 86(1):012511, 2005.

[154] G. S. D. Beach, C. Knutson, C. Nistor, M. Tsoi, and J. L. Erskine. Nonlinear domain-wall velocity enhancement by spin-polarized electric current. *Physical Review Letters*, 97(5):057203, 2006.

[155] M. Hayashi, L. Thomas, Ya B. Bazaliy, C. Rettner, R. Moriya, X. Jiang, and S. S.P. Parkin. Influence of current on field-driven domain wall motion in permalloy nanowires from time resolved measurements of anisotropic magnetoresistance. *Physical Review Letters*, 96(19):197207, 2006.

[156] J C Lee, K.-J. Kim, J Ryu, K.-W. Moon, S.-J. Yun, G H Gim, K.-So. Lee, K H Shin, H W Lee, and S B Choe. Universality Classes of Magnetic Domain Wall Motion. *Physical Review Letters*, 107(6):67201, 2011.

[157] S Le Gall, N Vernier, F Montaigne, A Thiaville, J Sampaio, D Ravelosona, S Mangin, S Andrieu, and T Hauet. Effect of spin transfer torque on domain wall motion regimes in [Co/Ni] superlattice wires. *Physical Review B*, 95(18):184419, 2017.

[158] D. Ravelosona, D. Lacour, J. A. Katine, B. D. Terris, and C. Chappert. Nanometer scale observation of high efficiency thermally assisted current-driven domain wall depinning. *Physical Review Letters*, 95(11):117203, 2005.

[159] D. Ravelosona, S. Mangin, J. A. Katine, Eric E. Fullerton, and B. D. Terris. Threshold currents to move domain walls in films with perpendicular anisotropy. *Applied Physics Letters*, 90(7):072508, 2007.

[160] K W Moon, D H Kim, S C Yoo, C G Cho, Hwang S., B Kahng, Min B C., Shin K H., and Choe S. Distinct universality classes of domain wall roughness in two-dimensional Pt/Co/Pt films. *Physical Review Letters*, 110(10):107203, 2013.

[161] M. Yamanouchi, D. Chiba, F. Matsukura, T. Dietl, and H. Ohno. Velocity of domain-wall motion induced by electrical current in the ferromagnetic semiconductor (Ga,Mn)As. *Physical Review Letters*, 96(9):096601, 2006.

[162] M Yamanouchi, J Ieda, F Matsukura, S E Barnes, S Maekawa, and H Ohno. Universality Classes for Domain Wall Motion in the Ferromagnetic Semiconductor (Ga,Mn)As. 317:1726–1729, 2007.

[163] J Curiale, A Lemaître, G Faini, and V Jeudy. Track heating study for current-induced domain wall motion experiments. *Applied Physics Letters*, 97(24):243505, 2010.

[164] J Curiale, A Lemaître, T Niazi, G Faini, and V Jeudy. Joule heating and current-induced domain wall motion. *Journal of Applied Physics*, 112(10):103922, 2012.

[165] Wolfgang Kuch, Rudolf Schäfer, Peter Fischer, and Franz Ulrich Hillebrecht. *Magnetic Microscopy of Layered Structures.* Springer-Verlag, Berlin Heidelberg, 2015.

[166] Michael Faraday. On the magnetization of light and the illumination of magnetic lines of force. *Philosophical Transactions of the Royal Society*, 136:1–20, 1846.

[167] John Kerr. On Rotation of the Plane of Polarization by reflection from the Pole of a Magnet. *Philosophical Magazine and Journal of Science*, 3(19):321–343, 1877.

[168] Hendrik Antoon Lorentz. *Le Phénomène Découvert Par Hall et la Rotation Électromagnétique du Plan de Polarisation de la Lumière*, pages 136–163. Springer, Dordrecht, 1936.

[169] Woldemar Voigt. Doppelbrechung von im Magnetfelde befindlichem Natriumdampf in der Rischtung normal zu den Kraftlinien. *Nachrichten von der Gesellschaft der Wissenschaften zu Göttingen, Mathematisch-Physikalische Klasse*, 1898:355–359, 1898.

[170] A Cotton and H Mouton. Sur les propriétés magnétooptiques des colloides et des liqueurs hétérogenes. *Ann Chim Phys*, 11:145–203, 1907.

[171] R Schäfer and A Hubert. A new magnetooptic effect related to non-uniform magnetization on the surface of a ferromagnet. *physica status solidi (a)*, 118(1):271–288, 1990.

[172] Pieter Zeeman. XXXII. On the influence of magnetism on the nature of the light emitted by a substance. *The London, Edinburgh, and Dublin Philosophical Magazine and Journal of Science*, 43(262):226–239, 1897.

[173] F Schmidt, W Rave, and A Hubert. Enhancement of magneto-optical domain observation by digital image processing. *IEEE Transactions on Magnetics*, 21(5):1596–1598, 1985.

[174] Jon Gorchon. *Current and field induced magnetization reversal in Pt/Co/Pt and (Ga,Mn)(As,P) ferromagnetic films.* PhD thesis, Université Paris-Sud, 2014.

[175] Daniel Jordán Ringgold. *Estudio de la rugosidad de paredes de dominio en GdFeCo*. Tesis carrera de maestría en ciencias físicas, Instituto Balseiro - Universidad Nacional de Cuyo, 2018.

[176] P Domenichini, F Paris, M G Capeluto, M Granada, J.-M. George, G Pasquini, and A B Kolton. Curvature-driven ac-assisted creep dynamics of magnetic domain walls. *Physical Review B*, 103(22):L220409, 2021.

[177] L. Herrera Diez, M. Voto, A. Casiraghi, M. Belmeguenai, Y. Roussigné, G. Durin, A. Lamperti, R. Mantovan, V. Sluka, V. Jeudy, Y. T. Liu, A. Stashkevich, S. M. Chérif, J. Langer, B. Ocker, L. Lopez-Diaz, and D. Ravelosona. Enhancement of the Dzyaloshinskii-Moriya interaction and domain wall velocity through interface intermixing in Ta/CoFeB/MgO. *Physical Review B*, 99(5):054431, 2019.

[178] L Berger and G Bergmann. The Hall Effect of Ferromagnets. In *The Hall Effect and Its Applications*, pages 55–76. Springer, Boston, 1980.

[179] A Lemaître, A Miard, L Travers, O Mauguin, L Largeau, C Gourdon, V Jeudy, M Tran, and J M George. Strain control of the magnetic anisotropy in (Ga,Mn) (As,P) ferromagnetic semiconductor layers. *Applied Physics Letters*, 93(2):211231–211233, 2008.

[180] T Niazi, M Cormier, D Lucot, L Largeau, V Jeudy, J Cibert, and A Lemaître. Electric-field control of the magnetic anisotropy in an ultrathin (Ga,Mn)As/(Ga,Mn)(As,P) bilayer. *Applied Physics Letters*, 102(12):122403, 2013.

[181] M Cormier, V Jeudy, T Niazi, D Lucot, M Granada, J Cibert, and A Lemaître. Electric-field-induced magnetization reorientation in a (Ga,Mn)As/(Ga,Mn)(As,P) bilayer with out-of-plane anisotropy. *Physical Review B - Condensed Matter and Materials Physics*, 90(17):174418, 2014.

[182] Rebeca Díaz Pardo. *Universal behaviors of magnetic domain walls in thin ferromagnets*. PhD thesis, Université Paris-Saclay, 2018.

[183] Lei Han Tang, Mehran Kardar, and Deepak Dhar. Driven depinning in anisotropic media. *Physical Review Letters*, 74(6):920–923, 1995.

[184] Olaf Duemmer and Werner Krauth. Critical exponents of the driven elastic string in a disordered medium. *Physical Review E - Statistical, Nonlinear, and Soft Matter Physics*, 71(6):061601, 2005.

[185] E E Ferrero, L Foini, T Giamarchi, A B Kolton, and A Rosso. Spatiotemporal Patterns in Ultraslow Domain Wall Creep Dynamics. *Physical Review Letters*, 118(14):147208, 2017.

[186] E Haltz, J Sampaio, R Weil, Y Dumont, and A Mougin. Strong current actions on ferrimagnetic domain walls in the creep regime. *Physical Review B*, 99(10):104413, 2019.

[187] A Kirilyuk, J Ferré, V Grolier, J P Jamet, and D Renard. Magnetization reversal in ultrathin ferromagnetic films with perpendicular anisotropy. *Journal of Magnetism and Magnetic Materials*, 171(1):45–63, 1997.

[188] Keisuke Yamada, Jean-Pierre Jamet, Yoshinobu Nakatani, Alexandra Mougin, André Thiaville, Teruo Ono, and Jacques Ferré. Influence of Instabilities on High-Field Magnetic Domain Wall Velocity in (Co/Ni) Nanostrips. *Applied Physics Express*, 4(11):113001, 2011.

[189] S. Le Gall, N. Vernier, F. Montaigne, M. Gottwald, D. Lacour, M. Hehn, D. Ravelosona, S. Mangin, S. Andrieu, and T. Hauet. Thermally activated domain wall motion in [Co/Ni](111) superlattices with perpendicular magnetic anisotropy. *Applied Physics Letters*, 106(6):062406, 2015.

[190] Duck Ho Kim, Takaya Okuno, Se Kwon Kim, Se Hyeok Oh, Tomoe Nishimura, Yushou Hirata, Yasuhiro Futakawa, Hiroki Yoshikawa, Arata Tsukamoto, Yaroslav Tserkovnyak, Yoichi Shiota, Takahiro Moriyama, Kab Jin Kim, Kyung Jin Lee, and Teruo Ono. Low Magnetic Damping of Ferrimagnetic GdFeCo Alloys. *Physical Review Letters*, 122(12):127203, 2019.

[191] T Shibauchi, L Krusin-Elbaum, Valerii M. Vinokur, B E Argyle, D Weller, and B D Terris. Deroughening of a 1D Domain Wall in an Ultrathin Magnetic Film by a Correlated Defect. *Physical Review Letters*, 87(26):267201, 2001.

[192] M. Huth, P. Haibach, and H. Adrian. Scaling properties of magnetic domain walls in Pt/Co/Pt trilayers on MgO (1 1 1). *Journal of Magnetism and Magnetic Materials*, 240(1-3):311–313, 2002.

[193] P. Domenichini, C. P. Quinteros, M. Granada, S. Collin, J. M. George, J. Curiale, S. Bustingorry, M. G. Capeluto, and G. Pasquini. Transient magnetic-domain-wall ac dynamics by means of magneto-optical Kerr effect microscopy. *Physical Review B*, 99(21):214401, 2019.

[194] Kang Soo Lee, Chang Won Lee, Young Jin Cho, Sunae Seo, Dong Hyun Kim, and Sug Bong Choe. Roughness exponent of domain interface in CoFe/Pt multilayer films. *IEEE Transactions on Magnetics*, 45(6):2548–2550, 2009.

[195] Matías Pablo Grassi, Alejandro B. Kolton, Vincent Jeudy, Alexandra Mougin, Sebastian Bustingorry, and Javier Curiale. Intermittent collective dynamics of domain walls in the creep regime. *Physical Review B*, 98(22):224201, 2018.

[196] S. Mangin, D. Ravelosona, J. A. Katine, M. J. Carey, B. D. Terris, and Eric E. Fullerton. Current-induced magnetization reversal in nanopillars with perpendicular anisotropy. *Nature Materials*, 5(3):210–215, 2006.

[197] J Ryu, S B Choe, and H W Lee. Magnetic domain-wall motion in a nanowire: Depinning and creep. *Physical Review B - Condensed Matter and Materials Physics*, 84(7):075469, 2011.

[198] Kab Jin Kim, Jae Chul Lee, Kyung Ho Shin, Hyun Woo Lee, and Sug Bong Choe. Universal classes of magnetic-field- and electric-current-induced magnetic domain-wall dynamics in one and two dimensional regimes. *Current Applied Physics*, 13(1):228–236, 2013.

[199] S DuttaGupta, S Fukami, C Zhang, H Sato, M Yamanouchi, F Matsukura, and H Ohno. Adiabatic spin-transfer-torque-induced domain wall creep in a magnetic metal. *Nature Physics*, 12(4):333–336, 2015.

université
PARIS-SACLAY

ÉCOLE DOCTORALE
Ondes et matière
(EDOM)

Titre : Dynamique et morphologie des parois des domaines magnétiques dans les films minces du point de vue de la physique statistique

Mots clés : systèmes désordonnés, transition de dépiégeage, dynamique de l'aimantation, parois de domaines magnétiques, systèmes nano-structurés

Résumé : L'étude des parois de domaines magnétiques (PD) dans les films minces est d'un grand intérêt pour la compréhension de la dynamique de l'aimantation et pour le développement de dispositifs spintroniques. En raison de ses caractéristiques, les PD peuvent être étudiés dans le cadre de la théorie des interfaces élastiques dans les milieux désordonnés. Dans cette thèse, nous étudions les propriétés dynamiques et morphologiques des PD à partir de ce point de vue. Notre principal outil expérimental est la microscopie par effet Kerr magnéto-optique polaire (PMOKE). Les échantillons étudiés sont un film ferrimagnétique de GdFeCo de 10 nm d'épaisseur, et une bicouche semi-conductrice ferromagnétique de (Ga,Mn)(As,P)/(Ga,Mn)As de 4 nm d'épaisseur.

Pour l'échantillon de GdFeCo, nous avons étudié la dynamique des PD déplacées par champ magnétique, sur une large gamme de températures (10-353 K), dans les régimes de reptation et de dépiégeage. Nous avons constaté une divergence du champ de dépiégeage à la température de compensation magnétique, et une augmentation de l'énergie caractéristique de piégeage k_BT_d lorsque la température T diminue, ce qui se traduit par des effets thermiques exceptionnellement faibles en dessous de 100 K. Cela nous a permis d'observer une transition de dépiégeage quasi athermique à basse température et de déterminer les exposants critiques. Nous avons indépendamment déterminé les valeurs de l'exposant de paramètre d'ordre β=0.30±0.03 et l'exposant de longueur de corrélation ν=1.3±0.3, qui sont tous deux compatibles avec les prédictions théoriques pour la classe d'universalité Edwards-Wilkinson pour un système avec un désordre figé.

Une autre étude de cette thèse est l'analyse statistique de la morphologie des PD en GdFeCo. Nous avons obtenu des valeurs représentatives pour l'exposant de rugosité ς et l'amplitude de rugosité B_0. Les valeurs de ς obtenues ne peuvent pas être directement identifiées avec les valeurs théoriquement prédites.

Afin d'expliquer ce désaccord, nous considérons que les exposants prédits gouvernent la rugosité des PD à différentes échelles de longueur séparées par deux longueurs de croisement : la longueur de corrélation L_{opt} associée aux sauts au-dessus des barrières énergie d'ancrage, et la longueur de corrélation L_{av} associée à la taille caractéristique des avalanches. Sur la base de ces idées, nous interprétons l'exposant ς mesuré comme une valeur effective et quantifions expérimentalement pour la première fois la longueur de corrélation L_{av} pour différents champs et températures. En outre, nous avons constaté que L_{av} restait fini au-dessous de la transition de dépiégeage (pour $H<H_d$) conformément aux propositions théoriques.

Avec le film de (Ga,Mn)(As,P)/(Ga,Mn), nous avons étudié le mouvement des PD induit simultanément ou séparément par un champ magnétique et un courant électrique polarisé en spin. Afin de comparer la contribution de ces deux forces motrices, nous avons analysé les conditions d'équilibre d'une paroi lorsque que ces deux forces agissent en direction opposée. Nous montrons que ces deux contributions sont proportionnelles avec un facteur (1.3±0.2) mT/(GA/m2) sur une grande plage de température proche du point de Curie. Nous constatons que ce même facteur décrit avec succès la dynamique des PD dans le régime de reptation au voisinage de la transition dépiégeage. Cela suggère que la force effective exercée sur les PD peut être décrite par une somme des forces dues au champ et au courant. Cependant, ce n'est plus valable dans le régime de reptation à plus faible vitesse, ce qui pourrait être associé à la nature non isotrope du mouvement des PD induit par le courant. Les résultats présentés dans cette thèse jettent un éclairage sur la nature universelle du déplacement des PD de domaines magnétiques et élargissent nos connaissances sur les caractéristiques de base des forces motrices qui produisent leur mouvement.

université
PARIS-SACLAY

ÉCOLE DOCTORALE
Ondes et matière
(EDOM)

Title: Dynamics and morphology of driven domain walls in magnetic thin films from the standpoint of statistical physics

Keywords: depinning transition, disordered systems, magnetic domain walls, dynamics of magnetization, nanostructured systems

Abstract: Studying magnetic domain walls (DWs) in thin films is of great interest for the understanding of magnetization inversion mechanisms and for the development of spintronics devices. As DWs have an associated energy and lie in a material with intrinsic inhomogeneities, they can be studied within the theory of elastic interfaces in disordered media. In this thesis, we investigate the dynamic and morphological properties of DWs in thin films from this viewpoint. Our main experimental tool is the polar magneto-optical Kerr-effect (PMOKE) microscopy, which permits the direct observation of DWs. The studied samples are a ferrimagnetic 10nm-thick film of GdFeCo, and a ferromagnetic 4nm-thick semiconducting bilayer of (Ga,Mn)(As,P)/(Ga,Mn)As, both of them presenting perpendicular magnetic anisotropy.

For the GdFeCo sample, we have studied the dynamics of field-driven DWs in a wide temperature range, from 10 K to 353 K, in the creep and depinning regimes. We have found that the depinning field H_d diverges at the magnetic compensation temperature T_M, and that the characteristic pinning energy barrier $k_B T_d$ grows in magnitude for decreasing temperature, what results in exceptionally low thermal effects below 100 K. This has allowed for the direct observation of the depinning transition at low temperatures and the subsequent determination of associated critical exponents. We have independently determined values of the order-parameter exponent $\beta=0.30\pm0.03$ and the correlation length exponent $\nu=1.3\pm0.3$, both of them being consistent only with the quenched Edwards-Wilkinson universality class.

Another investigation of this thesis concerns the statistical analysis of DW morphology in the GdFeCo sample. For different temperatures and applied fields, we have obtained representative values for the roughness exponent ς and the roughness amplitude B_0. We have found that the obtained ς values cannot be directly identified with any of the theoretically predicted roughness exponents. In order to explain this disagreement, we propose a quantitative interpretation based on previous theoretical studies. We consider that the predicted exponents govern DW roughness at different length scales separated by two crossover lengths: the correlation length L_{opt} associated to jumps over characteristic energy barriers, and the correlation length L_{av} associated to the characteristic size of depinning avalanches. Based on these ideas, we interpret the measured ς exponents as effective values and experimentally quantify for the first time the depinning correlation length L_{av} for different fields and temperatures. Moreover, we have found that L_{av} is finite even for $H<H_d$ in accordance with previous theoretical ideas for DW dynamics at finite temperatures.

For the (Ga,Mn)(As,P)/(Ga,Mn)As sample, we have studied the field- and current-driven DW motion when both stimuli are applied separately and simultaneously. In order to compare the strength of these two driving forces, we have analyzed the conditions of balance between them when they push oppositely. We show that there is a constant proportionality factor (1.3±0.2) mT/(GA/m^2) over a large temperature range close to the Curie point. We find that this same factor successfully describes the DW dynamics in the creep regime close to the depinning transition both when field and current are applied separately and simultaneously. This suggests that the effective force exerted on DWs can be described by a sum of the forces due to field and current. However, this relation does not stand at relatively low velocities, which could be associated with the non-isotropic nature of current-driven DW motion. The results presented in this thesis shed light on the universal nature of driven DWs and broadens our knowledge on the effective features of the driving forces.

ÉCOLE DOCTORALE
Ondes et matière
(EDOM)

Título: Dinámica y morfología de paredes de dominios magnéticos en láminas delgadas desde el punto de vista de la física estadística

Palabras clave: dinámica de la magnetización, paredes de dominios magnéticos, sistemas nanoestructurados, transición de desanclaje, sistemas desordenados

Resumen: El estudio de paredes de dominios magnéticos (PDM) en láminas delgadas es de gran interés para la comprensión de los mecanismos de inversión de la magnetización y para el desarrollo de dispositivos de electrónica de spin. Debido a sus características, las PDM pueden ser estudiadas en el marco de la teoría de interfases elásticas en medios desordenados. En esta tesis, investigamos la dinámica y la morfología de PDM en láminas delgadas con anisotropía magnética perpendicular desde dicho enfoque. La técnica experimental principal que utilizamos es la microscopía magneto-óptica por efecto Kerr polar (PMOKE), que permite la observación directa de las PDM. Las muestras estudiadas son una lámina ferrimagnética de GdFeCo de 10 nm de espesor, y una bicapa ferromagnética de (Ga,Mn)(As,P)/(Ga,Mn)As de 4 nm de espesor.

En la muestra de GdFeCo, estudiamos la dinámica de PDM impulsadas por campo magnético en un rango amplio de temperaturas, 10K-353K, en los regímenes de *creep* (reptación) y *depinning* (desanclaje). Encontramos que el campo de *depinning* H_d diverge en la temperatura de compensación magnética T_M, y que la barrera de energía de anclaje característica k_BT_d crece al bajar la temperatura. Esto último resulta en efectos térmicos excepcionalmente débiles por debajo de 100K, y permite la observación directa de la transición de *depinning* a bajas temperaturas y la determinación de exponentes críticos asociados. Determinamos independientemente los valores del exponente del parámetro de orden $\beta=0.30\pm0.03$ y del exponente de la longitud de correlación $\nu=1.3\pm0.3$. Ambos son consistentes sólo con la clase de universalidad de *quenched Edwards-Wilkinson*.

Por otro lado, estudiamos las propiedades estadísticas de la morfología de PDM en la muestra de GdFeCo. Para diferentes temperaturas y campos aplicados, obtuvimos valores representativos del exponente de rugosidad ς y de la amplitud de la rugosidad B_0. Encontramos que los valores de ς obtenidos no pueden ser identificados directamente con ninguno de los exponentes teóricamente predichos. Para explicar esta discordancia, proponemos una interpretación cuantitativa basada en estudios teóricos previos. Consideramos que los exponentes predichos dominan la rugosidad de PDM a distintas escalas de longitud separadas por dos longitudes características: la longitud de correlación L_{opt} asociada a saltos sobre barreras de energía características, y la longitud de correlación L_{av} asociada al tamaño característico de las avalanchas en la transición de *depinning*. En base a estas ideas, interpretamos los exponentes ς medidos como valores efectivos y cuantificamos experimentalmente por primera vez la longitud de correlación L_{av} para distintos campos y temperaturas. Asimismo, encontramos que L_{av} es finita incluso para $H<H_d$, de acuerdo con ideas teóricas previas para temperaturas finitas.

En la muestra de (Ga,Mn)(As,P)/(Ga,Mn)As, estudiamos la dinámica de PDM impulsadas tanto por campo como por corriente. Para comparar la magnitud de estas dos fuerzas de empuje, analizamos las condiciones tales que, al empujar en direcciones opuestas, ambas fuerzas están balanceadas. Mostramos que existe un factor de proporcionalidad (1.3 ± 0.2) mT/(GA/m^2) en un amplio rango de temperaturas cercano al punto de Curie de la muestra. Encontramos que este mismo factor describe satisfactoriamente la dinámica de PDM en el régimen de *creep* cerca de la transición de *depinning*. Esto sugiere que la fuerza efectiva que actúa sobre las PDM puede ser descrita como una suma de las fuerzas debidas al campo y a la corriente. Sin embargo, esta relación no se mantiene a velocidades relativamente bajas, lo cual puede ser asociado a la naturaleza anisotrópica de la fuerza inducida por corriente. Los resultados presentados en esta tesis amplían nuestro conocimiento sobre la naturaleza universal de las PDM y sobre las propiedades efectivas de las fuerzas de empuje.